博　士　論　文

Doctoral Thesis

論　　文　　題　　目

Thesis Theme

Low-Temperature Catalytic Methane Conversion Using Carbon Dioxide in an Electric Field

電場印加反応場における二酸化炭素を用いた触媒的低温メタン転換

February, 2017

Tomohiro	YABE
矢部	智宏

論　文　題　目

Thesis Theme

Low-Temperature Catalytic Methane Conversion Using Carbon Dioxide in an Electric Field

電場印加反応場における二酸化炭素を用いた触媒的低温メタン転換

February, 2017

Waseda University

Graduate School of Advanced Science and Engineering

Department of Advanced Science and Engineering

Research on Applied Chemistry B

Tomohiro	YABE
矢部	智宏

Table of contents

Chapter 1 General introduction

1.1 Features of the natural gas as energy resources

In the 1960s, large oil fields such as the Khafji and Raudhatain oilfields commenced one after another in Saudi Arabia and Kuwait, and the consumption of oil as an energy source exceeded that for coal. This was the time when the primary fuel changed from coal to oil, that is to say, the energy revolution. Oil has been produced at a low price thanks to the abundant reserves. In addition, oil had an advantage over coal from the viewpoints of transportation and storage because oil is liquid and coal is solid. Therefore, oil has acquired the initiative of energy resources. However, from the viewpoints of the limiting amounts of oil reserve and global environmental issues, departure from an oil-dependent economy has been desired in recent years. In this respect, natural gas has been attracting a great deal of attention. The natural gas consumption has increased by about 2,000 MMBTU (Million British Thermal Unit) from 1971 to 2014. The steps to increasing energy consumption in Asian countries has increased every year and the ratio of energy consumption in Asian countries to the world's energy consumption will keep increasing.

Natural gas, which is mainly composed of methane, is flammable gas produced from oil and gas fields. Typical uses of natural gas are for power generation and city gas. The primary global energy consumption resource in 2015 was 13.1 billion tonnes of oil equivalent: 33% is oil, 30% is coal and 24% is natural gas. On the other hand, in 1971, 48% was oil, 29% was coal and 18% was natural gas. This means that the global energy consumption has shifted from oil to natural gas and natural gas has become the third primary energy resource in the last 40 years.

Natural gas has been distributed evenly all over the world, while oil is not. [1] The total area of confirmed natural gas reserves was 187 trillion m^3 with 24.8% in the Middle East, 30.4% in Europe and Eurasia, 8.4% in the Asian Pacific, 7.5% in Africa, 6.8% in North America and 4.1% in Middle and South America. This means that about 55 % of the confirmed natural gas reserves are located in the Middle East, Europe and Eurasia. The reason for natural gas being distributed evenly all over the world is that oil can be deposited only up to 473 K and 2000 m depth to retain the structure, whereas natural gas is stable at higher temperatures and can be deposited in a stratum deeper than 2000 m.

R/P ratio (R: reserves, P: productions), which indicates how long the production can continue, was prospected to last 53 years for natural gas according to the BP Statistical Review of World Energy 2016, but has been expected to last further in recent years because

an excavation technology of oil fields has progressed and unconventional natural gas, which was difficult to mine, has become available. [1] Recently, unconventional natural gas, with shale gas in the lead, has become an energy reserve option, and the demand and supply balance for natural gas has changed mainly around North America. Due to the increase in shale gas reserves in North America, the natural gas production was 11% higher than the production in 2015, or the natural gas production will become 11% higher than the consumption in 2035. This situation enables the following: the energy dependency in North America on foreign countries will decrease and the domestic energy demands will be able to be covered by the natural gas production. [2, 3] Also, the developments for other conventional natural gas such as tight sand gas and coal bed methane, has progressed and the R/P ratio will continue to increase. In addition, it will become important to keep a balance with the excavation cost. Therefore, the energy policy centering on natural gas is expected to break the largely oil-dependent economy in the Middle East. In addition, from the perspective of an environmental burden, natural gas is a green reserve compared to oil and coal, because the carbon dioxide emissions are low in combustion and natural gas contains little N and S atom, resulting in emitting little thermal NO_x and SO_x.

Efficiency for the transportation and storage of natural gas is not as good as that of oil because the energy density per unit volume is lower for natural gas. Natural gas is transported usually by pipelines to a remote place. However, when natural gas is transported to an island place such as Japan, it has been transported as liquefied natural gas (LNG), in a tank which is filled at a low temperature (111 K) and under high pressure conditions near the gas fields. The volume of LNG is a 600^{th} part of the gas condition. Now, all the natural gas has been imported as LNG in Japan. The natural gas imports in 2014 was 892 million tonnes with 20.6% from Australia, 18.5% from Qatar, 17.2% from Malaysia, and 9.6% from Russia. However, the natural gas transportation as LNG is inefficient because large costs and energy are required in the liquefying and transportation process. Since the LNG process requires vast capital investment to construct the gas liquefying plant and the receiving terminal, it is only applicable to a huge gas field. In a medium/small gas field far from the demand area, the infrastructure cost such as a pipeline and LNG base is not economically viable. Elsewhere, the natural gas converts into the syngas, mix gases of CO and H_2, from steam reforming *et al.* and the syngas converts into the liquid fuel from Fischer-Tropsch synthesis (FT synthesis); this process is called Gas-To-Liquid (GTL) technology. However, GTL is inefficient due to the multistage process.

In these situations, the compensate for chemical products synthesized from the naphtha, which is separated from oil, by natural gas is attracting attention currently. Converting natural

gas into chemical products can heighten an added value, not using it only in combustion as thermal power generation. Though utilizing natural gas, which is the gaseous state and fluid energy, as an energy resource is short-term, utilizing it as chemical raw materials and products can be immobilized. In addition, effectively utilizing the medium/small gas fields at a lower cost is expected, thanks to the conversion of natural gas into chemical products. Ethylene, propylene and the syngas are important for chemical raw materials. Ethylene is a source of polyethylene, ethylene glycol, ethanol, acetaldehyde and acetic acid. Propylene is a source of polypropylene, glycerin and acrylonitrile. Syngas is a source of methanol, acetic acid, FT oil and dimethyl ether. The processes of producing ethylene and propylene from the naphtha are as follow: mixed gas with the naphtha and water is degraded at a high temperature from 1073–1173 K and is separated by distillation. The plants for producing ethylene and propylene from the naphtha are very large and require vast amounts of energy and costs due to composing many processes.

This study focuses on the direct ethylene synthesis via oxidative coupling of methane (OCM) and the syngas production via dry reforming of methane (DRM), adding high values to the natural gas as chemical conversion technologies. Accordingly, this study aimed at the establishment of new catalytic reaction system applying an electric field, adapting to OCM and DRM reactions, and showing high selectivity and product yields even at lower temperatures.

1.2 Methane utilizations via chemical conversion

In order to utilize methane, a major component of natural gas, via chemical conversion, various catalytic processes aiming at industrialization have been reported and there have been many reviews in this topic. [4–10] Havran *et al.* noted the thermodynamic reactivity for methane and reported that the chemical reactions using methane was thermodynamically unfavorable except for methane oxidation. [4] Alvarez-Galvan *et al.* reported that in order to convert methane to high value-added products, catalyst designs for avoiding the reaction with water, which progressed more easily than other reactions, are important and the method for using chloromethane was effective for activating methane. [5] Vora *et al.* summarized the previous reports in methane conversion technology focused on using silicoaluminophosphate zeolite catalysts such as SAPO–34, which had water resistance and a large particle size. [7]

The outline about methane conversion technologies is shown as Figure 1-1. Methane conversion technologies are generally divided into two paths: indirect and direct conversion process. Indirect conversion processes are as follows: methane converts the syngas, a mixed

gas of carbon monoxide and hydrogen, and syngas converts into various chemical products such as FT oil and methanol. [8–10] Main process for producing the syngas are steam reforming (SR), dry reforming (DR) and partial oxidation (PO_x). Direct conversion process will be more simple and economic process than indirect ones because the syngas production plant is not required.

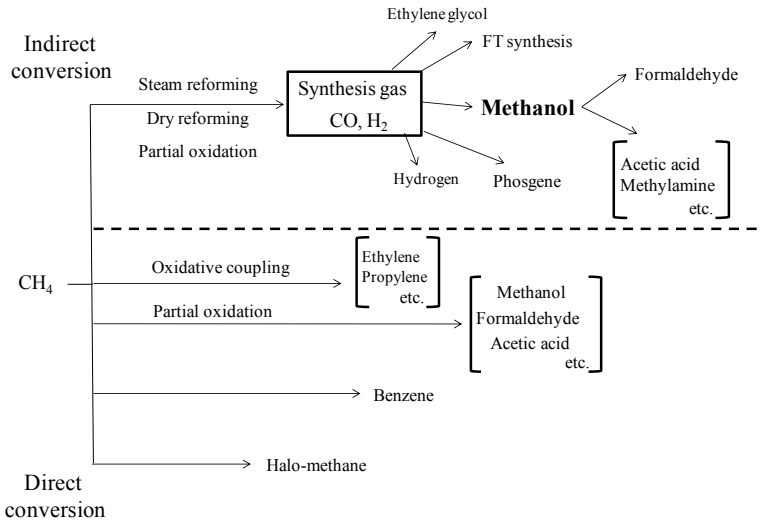

Figure 1-1 The scheme of methane conversion.

1.2.1 Indirect methane conversion technology

As the first step, methane reforming using oxidizing agents such as oxygen, carbon dioxide and water is important for indirect methane conversion. Hydrogen, a part of syngas, has been utilized by a number of methods such as agents for refining crude oil and the clean energy carrier in recent years, and the demand for it has been increasing. Additionally, syngas itself has been utilized as a raw material for synthesizing various chemical products such as methanol and ammonia. However, hydrogen does not exist as a natural resource on the earth and must be produced artificially from water, oil, natural gas, plant resources *etc*. The role of catalysts for the reforming process is particularly more important than other indirect conversion processes because the reforming process cost is a majority of the overall costs. In this section, indirect methane conversion technologies via syngas production are summarized.

1.2.1.1 Hydrogen and syngas production from methane

The most major syngas and hydrogen production from methane has been steam reforming of methane (SRM) for the last 80 years. The reaction equation of SRM is the following

(eq. 1) :

$$CH_4 + H_2O \rightarrow CO + 3H_2 \qquad \Delta H^0_{298} = 206.1\ kJ{\cdot}mol^{-1} \qquad \text{(eq. 1)}$$

Carbon monoxide obtained from SRM (eq. 1) can further produce hydrogen via a water gas shift reaction. (WGS: shown in eq. 2)

$$CO + H_2O \rightarrow CO_2 + H_2 \qquad \Delta H^0_{298} = -42.1\ kJ{\cdot}mol^{-1} \qquad \text{(eq. 2)}$$

The price of hydrogen produced via SRM is about 0.2–0.3 dollars per m^3. The energy capacity of hydrogen is strongly dependent on the reformer efficiency. The efficiency of the overall reformer process is estimated to be 60–75%. [2, 3]

Also, dry reforming of methane (DRM: as shown in eq. 3) has been attracting attention from the perspective of reducing environmental footprints due to a decrease in both methane and carbon dioxide, which are known for creating greenhouse gases. [11]

$$CH_4 + CO_2 \rightarrow 2CO + 2H_2 \qquad \Delta H^0_{298} = 247.2\ kJ{\cdot}mol^{-1} \qquad \text{(eq. 3)}$$

Noble metals supported oxide catalysts such as Pt, but Ni are known to be catalysts suitable to DRM from the viewpoints of economic efficiency. Although the previous reported Ni supported catalysts have a high DRM activity, the catalyst sintered and lose its catalytic activity soon after the carbon deposition. [12] Recently, the Chiyoda Corporation developed a catalyst that is stable and has high DRM activity, and implemented to practical use. In addition, research and development for DRM have become prosperous again with a combination of carbon dioxide capture and storage (CCS) technologies around Europe.

In addition to the two reforming reactions, partial oxidation of methane (POx: eq. 4) is a promising technology for producing the syngas.

$$CH_4 + \frac{1}{2}O_2 \rightarrow CO + 2H_2 \qquad \Delta H^0_{298} = -35.6\ kJ{\cdot}mol^{-1} \qquad \text{(eq. 4)}$$

The energy efficiency of POx is estimated as 50%, inferior to SRM. However, the POx plant can be simpler and smaller than the other two reforming plants because POx is an exothermic reaction and does not need to continuously heat the reactor. Besides, the heat recovery is very important in POx reactor due to produce a large heat value at a front end part of the catalyst

bed. [8, 9] Ni supported oxide catalysts are known to be suitable catalysts as similarly to DRM. [13]

Also, auto thermal reforming (ATR), which is a combination of SRM and PO_x, is a promising technology because heat generated via POx is controlled by heat adsorbed via SRM. This complementary reaction in the same reactor results in restraining the hot-spot integration and the carbon deposition. In addition, the H_2/CO ratio can be controlled by changing the flow rate of oxygen and water. [14, 16]

Otherwise, though syngas and hydrogen are synthesized from off-gas purification, water electrolysis, pyrolysis of water and hydrocarbons *etc.*, SRM is the best way for meeting the recent industrial demand from the perspective of energy efficiency and economic balance. [2, 3]

Due to the increasing hydrogen demand in recent years, the research and developments for producing the hydrogen-rich syngas has been attracting an attention. Lisboa *et al.* reported that as a result of the screening tests over Ni supported various oxide catalysts, a 10wt% $Ni/Ce_{0.75}Zr_{0.25}O_2$ catalyst showed high stability, low coke formation and high H_2 selectivity (>50%). [14] Palmer *et al.* reported that various metal supported honeycomb and foamed monolith structure catalysts (Al_2O_3, oxygen bonded silicon carbide, denoted as OBSiC, and ZrO_2) were found to be suitable catalytic systems for indicating flatter and lower temperature distribution and higher H_2 selectivity than conventional catalytic systems, and they analyzed in detail on the basis of the internal temperature distribution of the reactor. [16] Also, they reported that the temperature profile and methane conversion became constant over any catalysts soon after the raw gas flowed, and H_2 selectivity indicated about 45%.

1.2.1.2 Methane conversion via halogenated hydrocarbons

Research on methane conversion via halogenated hydrocarbons, expected to show higher C_2 selectivity than a conventional system, has been conducted since the 1980s. [17, 18] For example, olefins synthesis via methane coupling used halogenated methane was composed of the following four routes: [19]

$$CH_4 + HX + \frac{1}{2}O_2 \rightarrow CH_3X + H_2O \quad \text{(eq. 5)}$$

$$CH_4 + X_2 \rightarrow CH_3X + HX \quad \text{(eq. 6)}$$

$$n\,CH_3X \rightarrow C_nH_{2n} + n\,HX \quad \text{(eq. 7)}$$

$$4HX + O_2 \rightarrow 2X_2 + 2H_2O \quad \text{(eq. 8)}$$

(denoted X as halogen species)

Eqs. 5 and 6 represents the halogenated methane synthesis process, and the reaction of eq. 5 is named "oxyhydrohalogenation," which is generally more progressed than acid zeolite catalysts. [18] Also, the reaction of eq. 6 is generally more progressed over Pt supported super acid oxide catalysts. These reactions are weak exothermic reactions and the reaction selectivity is relatively high. [20] The reaction of eq. 7 is generally more progressed than microporous acid oxide catalysts, and leads to the synthesis of the olefin and halogenated hydrogen. Eq. 8 represents the oxidative recovery reaction for halogens. If halogens are efficiently recovered, the separation and detoxifying processes for halogenated hydrogen will not be required and these processes will become more economic. [21] However, the products from these reactions have toxicity and corrosiveness, and this situation results in a high cost for preparing these systems because of the safety issue. Technological developments of a corrosion preventive measure will make the halogenated methane synthesis process more attractive. [22]

1.2.1.3 Syngas conversion technology

Syngas can be converted into various chemical products depending on the H_2/CO ratio. The following are examples of several H_2/CO ratios: [23]

•When the H_2/CO ratio is 1, syngas can be converted into dimethyl ether (DME). (shown in eq. 9)

$$3CO + 3H_2 \rightarrow CH_3OCH_3 + CO_2 \qquad \text{(eq. 9)}$$

•When the H_2/CO ratio is 2, syngas can be converted into methanol synthesis and Fischer-Tropsch synthesis. (shown in eqs. 10–12)

$$2CO + 4H_2 \rightarrow CH_3OCH_3 + H_2O \qquad \text{(eq. 10)}$$
$$CO + 2H_2 \rightarrow CH_3OH \qquad \text{(eq. 11)}$$
$$CO + 2H_2 \rightarrow -CH_2- + H_2O \qquad \text{(eq. 12)}$$

Fischer-Tropsch synthesis and methanol synthesis are described in the following sections.

1.2.1.3.1 Fischer-Tropsch synthesis

Many syngas conversion technologies into various value-added chemical products such as methanol and ethylene glycol have been reported and Gharibi summarized the previous research. [6] Fischer-Tropsch synthesis (FTS) for producing lower olefins (C_2–C_4), whose demands have been rapidly increasing, are promising examples. Lower olefins have been synthesized via naphtha cracking and fluid catalytic cracking (FCC). However, lower olefins have expected to be synthesized from natural gas from the perspectives of oil price increases and country risks. FTS is the multistep reaction in which CH_x species derived from adsorbed carbon monoxide on the catalytic surface are polymerized and grown as hydrocarbons of various chain lengths. [24, 25] Many reviews have been published on this reaction. [26–34] The reaction mechanism is proposed as follows: first, methyl added surface alkyl groups form straight-chain α-olefins via β-desorption. Next, the straight-chain α-olefins form n-paraffins, added to hydrogens. Finally, CH species are added to α-olefins as the new surface alkyl groups again and form longer hydrocarbons. [35, 36] FTS products can be converted into various paraffins and oxygen-containing compounds via the secondary reaction such as hydrogenation, hydrocracking and hydroformylation and, among them, Fe, Co, Ni and Ru supported catalysts have been reported as suitable catalysts for FTS, Fe and Co supported catalysts have been practically used for industrial productions because larger amounts of methane are produced as by-products than Ni supported catalysts, and Ru is an expensive noble metal. Several plants were operated: the Shell Corporation operated an SMDS (Shell Middle Distillate Synthesis) process in Bintulu, Malaysia, and Pearl, Qatar; the Oryx GTL Corporation, a joint venture with The QP Corporation and an SASOL, operated SSPD (Sasol Slurry Phase Distillate) process in Ras Laffan, Qatar.

The FTS process can be categorized into two areas depending on its major products: the HTFT (High Temperature Fischer-Tropsch) process and LTFT (Low Temperature Fischer-Tropsch) process. In an HTFT process using Fe supported catalysts at a higher temperature (573–623 K), the primary products are gasoline and small straight-chain olefins and the secondary products are oxygen containing compounds. On the other hand, in an LTFT process using Fe or Co supported catalysts at a lower temperature (473–513 K), the primary products are large straight-chain waxes. The LTFT process based on a Co supported catalyst has been the major stream in recent years. [33] The products distribution in FTS are dominated by Anderson-Schulz-Flory (ASF) kinetics due to a polymerized reaction. (as shown in eq. 13)

$$W_n = n \cdot \alpha^{n-1} (1-\alpha)^2 \qquad \text{(eq. 13)}$$

(*Wn* is a weight ratio of hydrocarbons composed of *n* carbons and α is a chain propagation rate)

Most previously reported catalysts obeyed ASF kinetics and high selective hydrocarbons cannot be synthesized by these catalysts. Accordingly, developments of catalysts which do not follow ASF kinetics by nano spatial controls using zeolites *etc.* have been expected. [37, 38] Bessel *et al.* compared the catalytic activities for an FTS reaction among 10 wt%Co-supported porous alumina, silica, *Kieselguhr* (diatomite) and various zeolites such as Y zeolite, Mordenite and ZSM-5, in order to break away ASF kinetics. [37] As a result, the secondary reaction for FTS products did not progress and gasoline components, that is, high octane level hydrocarbons, were not synthesized over silica and Kieselguhr catalysts which did not have acid sites or porous structure. On the other hand, the major products were gasoline components over three above-mentioned zeolite which had large amounts of acid sites, especially over ZSM-5 with the highest hydrocarbons selectivity. The major products were not gasoline components over porous alumina which had relatively large amounts of acid sites. From the results above, they indicated the importance of the accessibility for FTS products to the acid sites over catalysts.

Martínez *et al.* compared the catalytic activities for the secondary FTS reaction over hybrid catalysts, physically mixed with 20 wt%Co/SiO_2 and four different topological zeolites such as USY, Beta, Mordenite and ZSM-5. [39] For USY, they compared the catalytic activities over different acidity catalysts by changing the Si/Al ratio (2.6 and 15.0) They found that USY of the largest porous size produced aromatic hydrocarbons such as alkyl naphthalene and alkyl phenanthlene in fine pores. On the other hand, USY of the smallest porous size produced long-chained n-paraffin. From these results, they indicated the relationship between the second reaction selectivity for FTS light olefins produced over the Co/SiO_2 surface and topology in acid sites distribution for zeolites. Furthermore, they indicated the relationship between the product distribution and the accessibility of acid sites on catalysts because the product distribution was not changed in different acidity USY.

Galvis *et al.* reported that an Fe/Na/α-Al_2O_3 catalyst with a small amount of sulfur showed high C_2–C_4 selectivity (≥50%-C) for an FTS reaction while methanation was suppressed (<20%-C.) [43] They also indicated that increasing olefin selectivity originated from the suppression of the methanation, which is caused by the covering of the active sites for hydrogenation by sulfur.

Recently, Tsubaki and Nishiyama groups reported *capsule catalyst* (core–shell catalyst), which is a hybrid catalyst of Co/SiO_2 and ZSM-5. [40, 41] They reported that when syngas passed over the capsule catalyst through the zeolite membrane to the Co/SiO_2 shell, all the hydrocarbons produced on the core part were hydrogenated and isomerized within the zeolite pore and the amounts of unreacted products decreased. He *et al.* compared the FTS activity over the catalyst physically mixed with Co/SiO_2 and ZSM-5 to that over the capsule catalysts of various ZSM-5 pore sizes, and found that iso-paraffin selectivity was higher and C_{11+} products were more suppressed over the *capsule catalysts* than those over the physically mixed catalyst. [42] They discussed the reason that the sequential reactions, and the space and shape selectivity functioned well over two reaction sites on each layer. Their group also reported that the core-shell catalyst, such as the hybrid catalyst of Co/SiO_2 and H-Beta, showed high selectivity for iso-paraffin and suppressed the C_{15+} products formation. [40] They also reported that the hybrid core-shell catalyst suppressed methanation, more than the catalyst of ZSM-5 shell did, and the product distribution can be controlled by choosing a suitable shell catalyst.

1.2.1.3.2 Methanol synthesis and its application for fuel

Methanol has been utilized as the liquid fuel, and the direct methanol fuel cell (DMFC) has been developed for electric energy storage in recent years. Additionally, methanol was focused on for MTG (methanol-to-gasoline) technology in the 1980s but has been dismissed as a liquid fuel when effects of the oil shock had been weakened. Olah proposed a renewable methanol society, as the background of technological innovation and the shale gas emergence in recent years, in order to support the increasing population and advanced industrialization while keeping the quality of the global environment, not depending on oil which had a limit on the reserve amounts. [68] Renewable methanol is produced via *bireforming*, that is, the process of methanol synthesis from carbon dioxide and methane, different from the conventional process via syngas conversion, and shown as the following eqs. 14–15:

$$3CH_4 + CO_2 + 2H_2O \rightarrow 4CO + 8H_2 \quad \text{(eq. 14)}$$

$$4CO + 8H_2 \rightarrow 4CH_3OH \quad \text{(eq. 15)}$$

The first step (eq. 14) is producing *metgas* (H_2/CO ratio is 2) from methane and carbon dioxide and the metgas are directly converted into methanol. The suitable catalyst for bireforming was Ni-supported catalyst and the reported reaction conditions were the

temperature as 1073−1273 K and the pressure as about 40 atm.

MTG (methanol-to-gasoline) and MTO (methanol-to-olefins) have been focused on and developed in the 1970s, as the background of twice oil shocks. The representative catalysts were H-ZSM-5 developed by the Mobil Corporation and H-SAPO-34 developed by the Union Carbide Company (present UOP; Universal Oil Products Company) and many reviews have been published on these catalysts. [44–48] These reviews indicated the reaction mechanism of forming intermediates such as $(:CH_2)_n$ species over solid oxide catalysts. The oxonium ylide mechanism, carbene mechanism, carbocation mechanism and free radical mechanism were indicated as the mechanisms of olefin formations. After that, Dahl and Kolboe advocated the "hydrocarbon-pool" mechanism in the 1990s. [49, 50] Finally, the "dual-cycle" mechanism, which is the modified version of the previous mechanism, has been the mainstream. [19, 51] The "hydrocarbon-pool" mechanism was the olefin formation by carbon-increasing sequentially from the adsorbed $(CH_2)_n$ species on the catalyst surface. However, the theoretically expected hydrogen consumption were different from the experimental data and detail characteristics of the active sites remained unknown. After that, Mikkelsen *et al.* reported that the intermediate derived from a kind of allene were synthesized from which methanol were reacted with benzene and toluene, and these allene compounds were important for propene formations, based on the "aromatic co-catalysis" mechanism [52], proposed by Mole *et al.*, of increasing olefin yields by adding a little toluene and p-xylene. [53] Additionally, Arstad *et al.* reported that stably trapped methylbenzene within the pole of H-SAPO-34 catalysts was important for this mechanism. [54] Haw *et al.* reported that methyl cyclopentenyl cations were important intermediates in olefin formations over H-ZSM-5 catalysts. [55, 56] Next, two hypotheses of the detailed mechanism for olefin formations from the methylbenzene intermediates were advocated. One is the "paring model" [57], proposed by Sullivan *et al.*, and the other is the "side chain methylation scheme" [52, 58], proposed by Mole *et al.* and modified by Haw *et al.* (as shown in Figure 1-2)

In these models, when the produced olefins were emitted to the gas phase, the products distribution derived from both the pore topology and the diffusion gradient was reported. [60] For example, Svelle groups conducted an MTO reaction over 4 zeolites of various pore topologies. [61] They reported that ethylene and propylene were main products over H-SAPO-34 catalysts, which had relatively small pores (about 4 Å diameter) and the products of the largest molecules were straight-chain pentene. On the other side, products of high propylene/ethylene ratio were obtained over a TON type zeolite, H-ZEM-22, which had a 10-membered ring and the one-dimension pore.

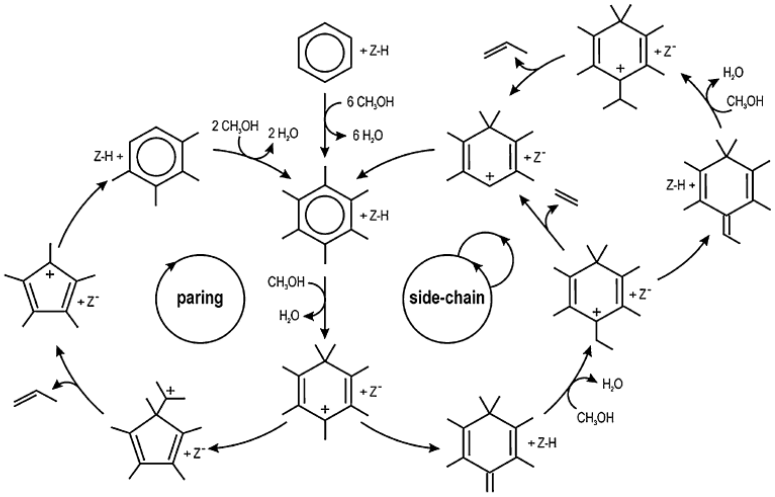

Figure 1-2 The proposed two mechanism of the "paring model" (Left cycle) and "side chain methylation scheme" (Right cycles). (Reprinted with permission from Ref. [59] Copyright 2009 John Wiley & Sons Inc.)

Therefore, they indicated that the MTO reaction was not progressed in the aromatics-based cycle mechanism. Additionally, methylbenzene was produced over H-ZSM-5 and H-beta, which had relatively large three-dimensional pores. They indicated that the MTO reaction was not progressed in "dual-cycle mechanism", which was the hybrid mechanism with an aromatics-based cycle mechanism and the cycle reaction of propylene intermediates. (as shown in Figure 1-3) Song *et al.* reported that propylene was easily produced by trapping 4–6 methyl groups to methyl benzene and ethylene was easily produced by trapping 2–3 methyl groups to methyl benzene. [62]

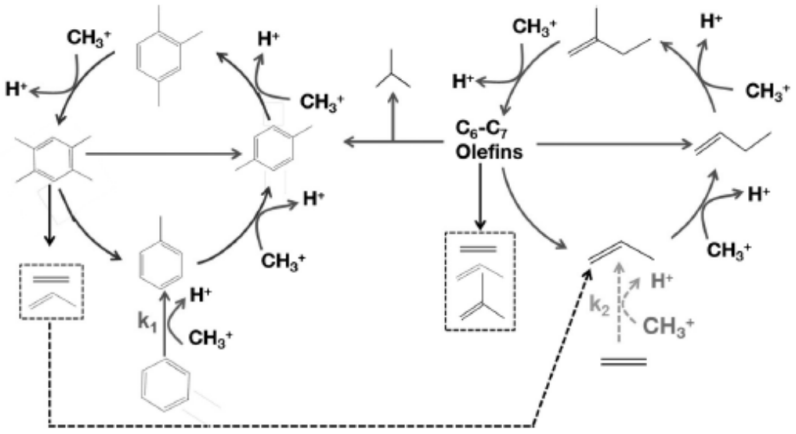

Figure 1-3 "Dual-cycle mechanism" over H-ZSM-5 catalysts. (Reprinted with permission from Ref. [63] Copyright 2014 Elsevier)

1.2.1.3.3 DME synthesis and this application

Olefin synthesis by DME conversion has been reported since the 2000s. [64] DME has a high cetane number and high possibility for diesel fuels because DME does not have C-C bonds and smoky gas was not easily produced in combustion. Additionally, DME can be utilized as various petroleum chemical products by converting it into olefins (DTO: DME-to-olefin) in the same mechanism as methanol conversions, and as a hydrogen carrier. Therefore, DME has come to be the representative starting materials for C1 chemistry and many reviews has been published in recent years. [65]

Zhou conducted DTO over H-Beta zeolite with large pore (7.6×6.4 Å) and Pd-Beta prepared by an ion-exchange method. [66] They reported that, when the Si/Al ratio was 200, olefins of more than C_6 were not produced and C_3–C_5 olefins were selectively produced. They also indicated the reason for high olefin selectivity in spite of a large pore zeolite that the vertical (7.6×6.4 Å) and horizontal (5.5×5.5 Å) channels were located in pores and the direction of the [001] angle, and olefins were produced in smaller channels. Tsubaki groups reported that relatively heavy olefins were produced over H-ZSM-5, which was widely used in the MTO reaction, due to the acid sites and topology of the zeolite, and conducted DTO reaction over H_3PO_4/12.5%ZrO_2/H-ZSM-5 catalyst. [67] They also reported that high propylene selectivity was obtained because the pore size of H-ZSM-5 support shrank from 5.5 Å to 5.3 Å, the acid site density increased, and weak acid structures such as Zr-OH and P-OH formed on the catalyst surface.

1.2.1.4 Combined process for natural gas and biomass

As a background of increasing the natural gas productions, a combination process with biomass and natural gas has been focused on. However, present issues in biomass utilization are the limited amount of energy production, and low yields and high costs in FTS using biomass. Accordingly, the efficient process for syngas and liquid fuel in combination with shale gas and biomass have been designed. Martin *et al.* attempted to optimize the above process using five different parts of switchgrass, and shale gas. [69] First, the shale gas was converted into syngas via the SRM and the switchgrass was converted into the syngas via vaporization, SRM and POx. H_2/CO ratio of this obtained syngas changed from 1 to 2 via WGS, PSA (pressure swing adsorption) and membrane separation. Next, the purified syngas components were converted into liquid hydrocarbons via FTS under pressure as about 30 atm. Finally, FT oil productions were separated from the water by gravity and fractionated by

distillation. If the shale gas cost was less than $11.5/MMBTU, these processes can meet the liquid fuels demands even if the biomass cost was $100/t. Additionally, the cost of these liquid fuel was estimated to be $1/gal, equivalent to existing gasoline and diesel engine oils.

1.2.2 Direct methane conversion technology

Direct methane conversion to high value-added olefins and oxygen containing compounds such as methanol, not through the high cost syngas, will be beneficial financially. However, direct methane conversion technology has two major problems. One is that oxygen, a source of direct methane oxidation, needs to be separated from the air. The other is that the process of sufficient product yield at a commercialized stage still has not existed. This is because the product yield was still very small and large cost for products separation was required due to one-pot process. [6, 9]

The process of direct methane conversion into high value-added ethylene via partial oxidative dehydrogenation is known as oxidative coupling of methane (OCM) and has been focused on in recent years. However, in the OCM reaction, the sequential oxidation is difficult to control because ethane and ethylene, products in OCM, more easily reacted with oxygen than methane. Lunsford and Choudhary groups conducted OCM over various oxide catalysts so far but the results of showing high C_2 yields as more than 30% have been hardly reported. [70]

Direct methanol conversion technology has been anticipated in the realm of economics due to increasing methanol demands in recent years. [71, 72] Arutyunov indicated the reaction mechanism in direct methanol synthesis and what technology will be required. [71] Also, he indicated the reasons for a low methanol yield in previous catalytic systems that products were sequentially oxidized, nearly equal amounts of methanol and carbon monoxide resulted in 50% methanol selectivity at most. Palkovits conducted direct methanol conversion over a Pt-bipyridine complex CTF (covalent triazine-based framework) catalyst in sulphuric acid solution and reported a high methanol yield (1.8 methanol conc. mol L^{-1}). [73] They also reported that the methanol yield was the same as the Pt-bipyridine complex catalyst previously reported by Periana *et al.* [72], but the catalyst stability of the CTF catalyst was higher than the reported catalyst and the catalyst recycle was possible.

Aromatization has been focused on as non-oxidative direct methane conversion technology as well. BTX (benzene, toluene, xylene) are very important raw chemical materials and direct BTX synthesis technology from natural gas will contain a large economic impact. However,

BTX yields were about 7% so far over a Mo supported micro-nano scale H-ZSM-5 catalyst, reported by Zhang et al. [74]

MTB (methane-to-benzene) is direct and a one-pass methane conversion into benzene, and the reaction equation of this reaction is the following (eq. 16) :

$$6CH_4 \rightarrow C_6H_6 + 9H_2 \qquad \Delta H^0_{298} = 532\ \text{kJ·mol}^{-1} \qquad \text{(eq. 16)}$$

This reaction is largely endothermic and a high temperature reaction condition is required, which is a thermodynamic disadvantage. Bijani analyzed in thermodynamic methane conversion at 1000 K as about 15%. [75] Therefore, more research on catalysts of high benzene yields are required in order to develop MTB processes in a commercialized stage. Many reviews on MTB reaction have been reported. [76–78] The most promising catalyst is a Mo supported H-ZSM-5 catalyst because Wang *et al.* reported a high benzene yield and selectivity over the catalyst. [23] Shu *et al.* indicated the reason for high benzene selectivity over a H-ZSM-5 catalyst that H-ZSM-5 had the same pore size as a benzene molecule and reported other MCM-22 catalysts for high benzene selectivity in these points. [79] The reaction mechanism in MTB has been widely known as follows: firstly, methane was activated on Mo metal to produce ethylene. Ethylene was oligomerized and cyclized by Brønsted acid sites on zeolite. Some advocated that the intermediate in MTB was acetylene and the Brønsted acid sites were not relatively important. [80–83] The Mo states on Mo supported H-ZSM-5 were reported by Iglesia groups in detail. [84–87]

The induction period of MoOx to MoCx were indicated to exist in the initial stage of activating methane over Mo supported H-ZSM-5. [88–90] Kim *et al.* reported that Mo outside the surface of ZSM-5 formed Mo_2C and $Al_2(MoO_4)_3$, decreasing the MTB yield. [84] The issue of the Mo/HZSM-5 catalyst indicated low catalytic activity and easily sintering by carbon deposition. Ma *et al.* indicated that the deposited carbon was derived from the reaction on the Mo surface or the Brønsted acid site in pores and the deposited carbon on the Brønsted acid site in pores deteriorated the catalytic activity. [91–93] In order to suppress the carbon deposition, secondary metal addition, zeolite modification and different reactant introduction were conducted. Liu *et al.* reported that the suitable secondary metal added to Mo/HZSM-5 were Fe, Co, Ga, Ag and Pt. [94–98] Xu *et al.* reported that zeolite modifications were tested by silanation in order to remove the excessive Brønsted acid sites [99, 100] and the mesopore introduction. [101–103] Otherwise, Li *et al.* conducted MTB over the GaN catalyst and reported high benzene selectivity as 89.8% and the equilibrium conversion as 0.56% at 723 K. [104]

1.3 Oxidative coupling of methane

As described in section 1.2.2, oxidative coupling of methane (OCM), directly converting methane into ethane and ethylene via partial oxidative dehydrogenation, have been focused on as the future important technology for the effective chemical utilization of natural gas. [10, 105–109] The reaction equation of this reaction is the following (eq. 17):

$$CH_4 + \frac{1}{2}O_2 \rightarrow \frac{1}{2}C_2H_4 + H_2O \qquad \Delta H^0_{298} = \text{-}140.4\ \text{kJ}\cdot\text{mol}^{-1} \qquad \text{(eq. 17)}$$

Pitchai and Lunsford groups reported several papers on kinetic analysis covering the wide range of activity tests for methane oxidative coupling. [106] In these papers, a lot of kinetic analyses over La_2O_3 and CeO_2 catalysts were conducted. As a result, La_2O_3 catalysts showed high C_2 yield because the ability of abstracting hydrogen from methane and activating oxygen were higher than that of oxidizing methyl radicals. On the other hand, CeO_2 catalysts showed low C_2 selectivity because the rate for methyl radical oxidation was fast and the sequential oxidation were unavoidable. Methane conversion and C_2 selectivity were fallen the limiting range over most of reported catalysts: $16\pm3\%$ and $70\pm8\%$. Additionally, the catalytic activities were more dependent on the physical properties such as specific surface area and particle size over rare earth catalysts than on the chemical properties.

An OCM reaction (eq. 17) is an exothermic reaction but higher temperature is required because of methyl radical formation, the rate determining step of this reaction. The related equations for this reaction are the following (eqs. 17–20) :

$$CH_4 + \frac{1}{4}O_2 \rightarrow \frac{1}{2}C_2H_6 + \frac{1}{2}H_2O \qquad \text{(eq. 18)}$$

$$CH_4 + \frac{1}{2}O_2 \rightarrow \frac{1}{2}C_2H_4 + H_2O \qquad \text{(eq. 17)}$$

$$CH_4 + \frac{3}{2}O_2 \rightarrow CO + 2H_2O \qquad \text{(eq. 19)}$$

$$CH_4 + 2O_2 \rightarrow CO_2 + 2H_2O \qquad \text{(eq. 20)}$$

Otherwise, more than 50 reactions as gas phase radical reactions are related to the OCM reaction. Therefore, the reaction analyses are considered to be difficult due to complex behaviors and interactions with each product. Next, the equations of methyl radical formation

are the following (eqs. 21–25). Accordingly, the equations (eqs. 21–23) are shown as methyl radical formations via homogeneous dissociation:

$$CH_4 + O_s' \rightarrow CH_3\cdot + OH_s' \quad \text{(eq. 21)}$$

$$2OH_s' \rightleftarrows H_2O + O_s'' + V_O^{\cdot\cdot} \quad \text{(eq. 22)}$$

$$\frac{1}{2}O_2 + V_O^{\cdot\cdot} + O_s'' \rightarrow 2O_s' \quad \text{(eq. 23)}$$

O_s expresses as the surface oxygen species and other writes are followed by the Kröger-Vink method. From these equations, methane reacts with adsorbed oxygen species on the catalyst surface and dissociated to form methyl radicals. On the other hand, the equations (eqs. 24 and 25) are shown as methyl radical formations via heterogeneous dissociation:

$$CH_4 + M^{n+} + \frac{1}{2}O_2^- \rightarrow CH_3 - M^{n+} + OH^- \quad \text{(eq. 24)}$$

$$CH_3^- \rightarrow CH_3\cdot + e^- \quad \text{(eq. 25)}$$

(denoted M^{n+} as a metal cation)

From these equations, methane receives electrons from the surface oxygen and combines with metal cations, and C–H bonds are separated to form methyl radicals. Finally, the above produced methyl radicals via homogeneous and heterogeneous dissociation are coupled with each other to form ethane.

In eq. 17, ethane via OCM, shown as eq. 18, is sequentially oxidative dehydrogenated to form ethylene. When the reaction temperature is very high, ethylene is sequentially oxidative dehydrogenated to form acetylene. Additionally, ethylene is produced via simple ethane dehydrogenation at a high temperature: (as shown in eq. 26)

$$C_2H_6 \rightarrow C_2H_4 + H_2 \quad \text{(eq. 26)}$$

Eq. 19 and eq. 20 show the reactions of carbon monoxide and carbon dioxide formations in which methyl radicals do not couple and react with gas phase oxygen. In this scheme, peroxy radicals ($CH_3O_2\cdot$) form as activated oxygen species. Peroxy radicals form methoxy radicals ($CH_3O\cdot$) via dehydrogenation and hydroxyl group elimination. Methoxy radicals form formaldehydes via dehydrogenation. Formaldehyde is dehydrogenated to form $CHO\cdot$ radicals due to its high reactivity. Finally, $CHO\cdot$ radicals form carbon monoxide and carbon dioxide.

This sequential non-selective oxidation decreases C_2 selectivity in an OCM reaction. [110] The following sentences describe the representative catalysts: $Mn/Na_2WO_4/ SiO_2$ and rare earth oxide catalysts.

Fang *et al.* reported at first that the $Mn\text{-}Na_2WO_4/SiO_2$ catalyst indicated high and stable OCM activity at high temperature conditions. [111] The reason has been known as stabilizing alkali metal, which is weak in high temperature conditions, by including W in the structure. [112] The strong point of a $Mn\text{-}Na_2WO_4/SiO_2$ catalyst is its simple and high reproducible preparation method. $Mn\text{-}Na_2WO_4/SiO_2$ catalysts do not require a unique precursor, $Mn(NO_3)_2$ and Na_2WO_4 are impregnated to SiO_2 in a water solution at 358-363 K (incipient wetness method) and dried in the O_2 flow (it is also possible in the air flow) at 353-403 K. After that, many studies have been reported by Lunsford and other groups. [113, 114] Tiemersma *et al.* reported that they remarked previous kinetic reports had discussed the heterogeneous catalytic surface and homogeneous gas phase at the same time, so they separated from the rates of the heterogeneous catalytic surface and homogeneous gas phase and analyzed the main and side reactions in detail. [115] As a result, they proposed the following 5 hypotheses:

a. Oxidation to form carbon monoxide are mainly in the gas phase.
b. Under any condition, carbon dioxide is mainly produced from methane.
c. The main product for an OCM reaction is ethane.
d. Ethylene is produced via ethane oxidative dehydrogenation.
e. The rates of side reactions are mostly negligible in certain conditions.

Around the same time as Tiemersma *et al.*, Ahari *et al.* pointed out the same issues, optimized the reaction algorithm over an $Mn/Na_2WO_4/SiO_2$ catalyst by using an analogy of another catalytic reaction system and calculated the reaction rate parameters. [116] Additionally, they indicated that the rate determining step is methyl radicals formation from methane (as shown in eq. 27) and summarized, by using these algorithm, the main gas phase elementary reactions to 39 reactions and the surface catalytic reactions to 11 reactions.

$$CH_4 + O^* \rightarrow CH_3\cdot + OH^* \qquad \text{(eq. 27)}$$

(denoted * as chemically adsorbed species on the surface catalytic active sites)

They also indicated by simulation method that ethylene was produced in the order of ethane, ethyl radicals and ethylene.

Elkins *et al.* analyzed in detail, by using XPS, XRD and TEM measurement, WO_4^{2-} tetragonal structure and the interaction for W-O-Si, that is, WO_4^{2-} and α-cristobalite SiO_2, considered to be the main factor of high OCM activity over an $Mn/Na_2WO_4/SiO_2$ catalyst. [117] They also conducted detail characterization over $Mn/Na_2WO_4/MgO$ catalyst as a comparison in order to investigate the SiO_2 support effects. As a result, Mn_2O_3 played an important role in the electron transfer and the redox cycle occurred between W^{6+} and W^{5+}, Mn^{3+} and Mn^{2+}. The intermediates sequentially oxidized to form CO_x over MnO_2 catalyst due to its higher redox performance. Accordingly, methane conversion decreased over MgO supports and the Mn state existed as Mn^{4+}, that is, Mg_6MnO_8. On the other hand, high C_2 selectivity was indicated over SiO_2 supports due to the presence of stable Mn_2O_3.

The pioneering research on OCM over rare earth oxide catalysts have been conducted by Otsuka *et al.* [118] and Lunsford *et al.* [119], and they investigated most of oxide catalysts except for CeO_2, Pr_6O_{11} and Tb_4O_7. High C_2 selectivity over rare earth oxide catalysts were indicated due to the presence of stable CH_3· by MIESR (matrix isolation electron spin resonance) measurement. Additionally, Dedov *et al.* reported that high C_2 selectivity over these catalysts were indicated thanks to relatively weak redox performance rather than transition metal oxides and suppression for the sequential oxidation or reduction. [120]

Tong *et al.* reported that the formation rates for methyl radical were relatively high over lanthanoid oxide catalysts, especially over the La_2O_3 catalyst. [121] Figure 1-4 showed the formation rates for methyl radicals over light rare earth and ytterbium oxide catalysts at 873 K.

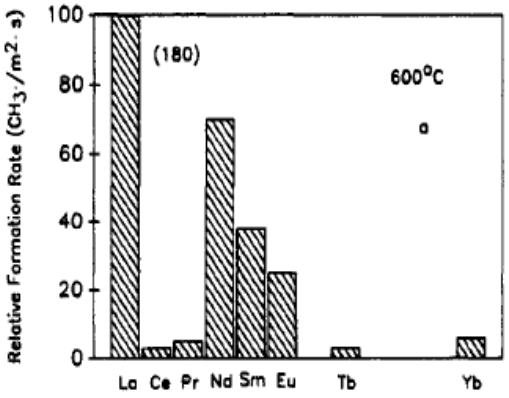

Figure 1-4 Comparison of CH_3· formation rate with selected members of the lanthanide oxide series. (Reprinted with permission from Ref. [121] Copyright 1989 American Chemical Society)

Choudhary *et al.* reported that the OCM and ODE (oxidative dehydrogenation of ethane) yield increased by doping Sr into various rare earth oxide catalysts, as shown in Figure 1-5. [122]

Palmer *et al.* indicated that the active site for OCM was adsorbed oxygen species, especially electron-rich oxygen species such as O_2^{2-} or O^-. [123] The equation of equilibrium reactions is the following (eq. 17) :

$$O_{2(g)} \rightleftharpoons O_{2(ads)} \overset{+e^-}{\rightleftharpoons} O_2^- \overset{+e^-}{\rightleftharpoons} O_2^{2-} \rightleftharpoons 2O^- \overset{+2e^-}{\rightleftharpoons} 2O^{2-} \qquad \text{(eq. 28)}$$

Palmer *et al.* also indicated that the OCM yield increased by doping Sr into La_2O_3 and increasing adsorbed O^- sites.

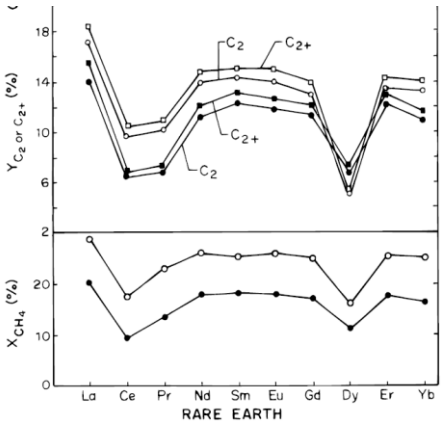

Figure 1-5 Effect of rare earth in Sr-promoted rare earth oxide catalyst on its methane conversion (X) activity, yield (Y) for C_2 and C_2^+ hydrocarbons. (Reprinted with permission from Ref. [122] Copyright 2004 Plenum Publishing Corporation)

Dedov *et al.* investigated the relationship between the specific surface area of before/after the reaction and OCM activities over various rare earth oxide catalysts, as shown in Table 1-1. [120] Table 1-1 indicates that the specific surface area of before/after the reaction and C_2 yields have a correlation over most catalysts except for the Sm_2O_3 catalyst. Additionally, increasing the specific surface area resulted in increasing the surface active sites and CH_4 conversions, but the catalyst stability became worse and C_2 selectivity decreased.

Choudhary *et al.* pointed out the previous study on which basic sites played an important role in OCM reactions [124] and investigated how basic sites and the surface carbonates for different temperatures affected on the C_2 formations over strong basic alkali earth metal (M=Be, Mg, Ca, Sr) doped Nd_2O_3 catalysts. [125] They also reported that basic sites (A) and

active sites which had an affinity for carbon dioxide (B) existed over the M-Nd_2O_3 catalyst. At a lower reaction temperature, C_2 formation was hindered by CO_2 covering (A) sites.

Table 1-1 Catalytic activity of the individual rare earth oxide and rare earth oxide mixtures. (Reprinted with permission from Ref. [120] Copyright 2003 Elsevier)

Catalyst	CH_4 conversion / %	C_2 selectivity / %	C_2 Yield / %	Temp / K	Specific surface / $m^2 \cdot g^{-1}$
10mol%Ce-LaO_2	31	66.0	22.3	1048	9.4 → 8.6
Eu_2O_3	23	72.4	17.7	998	6.0 → 5.1
10mol%Nd-La_2O_3	21	73.0	16.6	1043	7.9 → 7.0
Sm_2O_3	20	65.4	14.2	1053	3.6 → 2.3
La_2O_3	19	67.6	13.9	1073	9.4 → 8.6
La-Pr-Nd-CeOx	19	64.1	13.3	1108	12.0 → 10.7

On the other hand, the sequential methane oxidation proceeded on the acid (B) sites. Therefore, they indicated that the control of (B) sites was important for suppressing the sequential oxidation.

Ferreira *et al.* investigated the effect of both doped ion radius and formed surface oxygen species on OCM activities over alkali earth metal (Mg, Ca, Sr) doped CeO_2 catalysts. [126] They reported that many electrophilic oxygen species such as O_2^{2-} formed on CeO_2 surface by alkali earth metal ion penetrating into the structure of CeO_2. Additionally, they also indicated the reason for showing the highest C_2 yield over $Ca_{0.5}Ce_{0.5}O_2$ catalyst that the structure strain of CeO_2 was large because the ion radius of Ca^{2+} was close to that of Ce^{4+} and many O_2^{2-} species formed.

Elkins *et al.* attempted to improve the C_2 yield by decomposing the oleic acid complex precursor of Sm_2O_3, which had been reported by Otsuka [118] for indicating relatively high C_2 yield among rare earth oxide catalysts, and nanocrystalizing them. [127] Additionally, in the perspective of the elements strategy, they also optimized the supporting method of Sm on Al_2O_3. As a result, decreasing the particle size of Sm_2O_3 resulted in increasing both methane conversion and C_2 selectivity; the highest C_2 yield was obtained in the particle size as 14 nm. They also indicated that, though Al_2O_3 support had Lewis acid sites and the sequential oxidation was easily occurred, supporting Sm_2O_3 nano particles on Al_2O_3 suppressed the function of acid sites and a high C_2 yield was obtained.

Investigations for the characteristics of active oxygen species in OCM reaction have attempted using computational chemistry method such as DFT (density functional theory) in recent years. Neurock groups investigated the methane activation by specific oxygen species such as O^{2-}, O^- and O_2^{2-} on the (001) face of La_2O_3 using DFT. [122, 128] As a result, they

indicated that the methane activation by O_2^{2-} on La_2O_3 played an important role in C_2 formations. Additionally, Chu *et al.* investigated the additional effect of the mechanism of recovering the active site by water on the above-mentioned Neurock's mechanism. [129] As a result, they indicated that O_2^{2-} species were not very important for the active site of methane activation and O^{2-} played an important role in the perspective of computational chemistry.

1.4 Oxidative coupling of methane using carbon dioxide

As described in Section1.3, a stable methane molecule can be activated by specific oxygen species. However, because OCM using oxygen as an oxidizing agent is an exothermic reaction, the temperature of the gas phase increases and the formations of carbon monoxide and carbon dioxide are not suppressed due to the gas phase sequential and non-selective oxidation. Therefore, methane activation using carbon dioxide as an oxidizing agent have been focused on. The reaction equation of oxidative coupling of methane using carbon dioxide (CO_2-OCM) is the following (eq. 29) :

$$CH_4 + CO_2 \rightarrow \frac{1}{2}C_2H_4 + CO + H_2O \qquad \Delta H^0_{298} = 142.1\ \mathrm{kJ \cdot mol^{-1}} \qquad \text{(eq. 29)}$$

Different from OCM, CO_2-OCM is an endothermic reaction. The thermodynamic equilibrium methane conversion is about 10% at 900 K. Additionally, gas phase radical reaction are expected to be suppressed as described in Section 1.3 and the sequential oxidation on the catalyst will be controlled, because the reactivity of carbon dioxide is lower than that of oxygen. In a CO_2-OCM reaction, carbon dioxide, which is a by-product in an OCM reaction, is utilized as a raw material and only carbon monoxide is regarded as a by-product in the CO_2-OCM reaction. In these viewpoints, though this reaction is more difficult than OCM due to high bond energy of carbon dioxide (C=O bond energy is 526.1 kJ mol^{-1}), high C_2 selectivity are expected.

Kuo *et al.* reported that, though oxygen existed, increasing the CO_2/CH_4 ratio resulted in a C_2 yield and the C_2 yield indicated 25% to the maximum in the condition of the ratio as 2 at 1073 K. [130] However, a C_2 yield has not exceeded 30% up to the present time and catalysts for activating both methane and carbon dioxide have been required. Additionally, C_2 hydrocarbons were hardly produced in the absence of oxygen and effective catalysts have been required.

Asami *et al.* conducted CO_2-OCM in the absence of oxygen over more than 30 oxide catalysts [131–133] and reported that Pr and Tb oxide catalysts indicated high OCM activity at 1123 K: C_2 yield was 1.5% and C_2 selectivity was 50%. [133] They also reported that CO_2-OCM reacted over most of catalysts in the condition of CO_2/CH_4 ratio as 2. [131] They investigated the relationship between carbon dioxide conversion and methane conversion (left figure) and yield of C_2 hydrocarbons (right figure) over various metal oxide catalysts, as shown in Figure 1-6. Broken lines in Figure 1-6 denotes ratio 2.

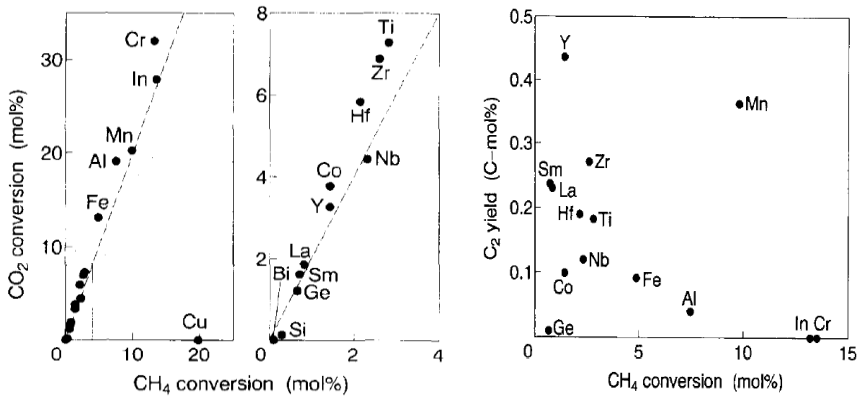

Figure 1-6 Relationship between carbon dioxide conversion and methane conversion (Left side) and yield of C_2 hydrocarbons (Right side). Broken lines denotes ratio 2. (Reprinted with permission from Ref. [131] Copyright 1995 Elsevier.)

Wang *et al.* conducted CO_2-OCM over various alkali metal and alkali earth metal doped CeO_2 catalysts in the absence of oxygen, as catalytic activities shown in Figure 1-7. [134] The Ca doped CeO_2 catalyst of the Ca/Ce ratio as 0.5 showed the highest catalytic activities: C_2 selectivity was 62% and the C_2 yield was 6.1%. They also investigated the reaction mechanism in detail that methane mainly reacted with the lattice oxygen to form carbon monoxide and hydrogen (dry reforming of methane: DRM) in the condition of carbon dioxide desorption, and the catalysts were reduced by DRM products. After that, carbon dioxide oxidized the catalysts, known as the redox mechanism. On the other hand, Ca sites on the CaO-CeO_2 catalyst adsorbed carbon dioxide (CO_2 pool mechanism) in the condition of carbon dioxide adsorption, and pooled carbon dioxide hindered desorbing carbon dioxide and promoting redox cycle, that is, progressing DRM reaction. They indicated that this mechanism resulted in high C_2 yield over the Ca doped CeO_2 catalyst. [134] They also indicated that carbon dioxide adsorbed on Ca was activated by Ce^{3+} to form O^-, which had an ability for methyl radical formation. Therefore, closely existing Ca^{2+} and Ce^{3+} was important

to produce the CO_2-OCM reaction. Additionally, they reported that CO_2-OCM proceeded over the Ca doped Cr_2O_3 catalyst in the same mechanism as mentioned above. [135]

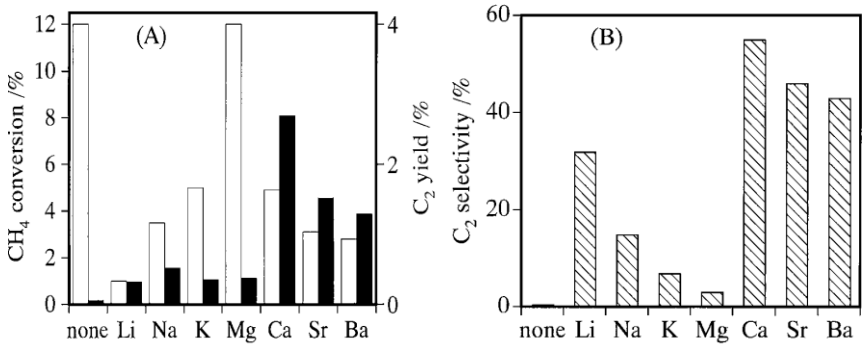

Figure 1-7 Effect of the addition of alkali and alkaline earth metal oxides to CeO_2 on the reaction of CH_4 and CO_2. (A) CH_4 conversion (open) and C_2 yield (closed); (B) C_2 selectivity. Reaction conditions: T=1123 K, $P(CH_4)=P(CO_2)=30$ kPa (Reprinted with permission from Ref. [134] Copyright 1999 Elsevier.)

Wang *et al.* reported that high CO_2-OCM activity over the CaO-ZnO catalyst of a Ca/Zn ratio as 0.5: the C_2 yield was 4.3% and the C_2 selectivity was 80%. [136] In only methane flows, oxygen species on the CaO-ZnO catalyst reacted with methane to produce hydrogen and carbon monoxide. Carbon dioxide adsorption on Ca suppressed the lattice oxygen reactivity and formed oxygen species from carbon dioxide dissociation such as O^- resulted in high C_2 selectivity.

Wang *et al.* also systematically investigated on CO_2-OCM over various Mn-mixed oxide catalysts. As a result, Sr-MnO_2 of the Sr/Mn ratio as 1 and Ba-MnO_2 of Ba/Mn ratio as 1 catalysts showed relatively high C_2 selectivity: 85%. [137] Additionally, the initial catalytic activity over the Ca-MnO_2 catalyst was the same as over the previously reported Ca-CeO_2 catalyst but the catalyst sintered to form $CaCO_3$ soon after the reaction. On the other hand, the catalytic activities over Sr-MnO_2 and Ba-MnO_2 catalysts were stable. These oxides reacted with carbon dioxide to form $SrCO_3$ or $BaCO_3$, and these carbonates reacted with MnO_2 to form $SrMnO_{2.5}$ or $BaMnO_{2.5}$. Mn^{3+} ion over $SrMnO_{2.5}$ and $BaMnO_{2.5}$ catalysts activated methane and resulted in a high C_2 yield. Cai *et al.* investigated the reaction mechanism in CO_2-OCM over Mn-$SrCO_3$. They reported that $SrCO_3$ degraded into SrO and $CO_2{}^*_{(a)}$, $CO_2{}^*_{(a)}$ reacted with Mn^{2+} to form O^- species, which were known to the active sites on OCM, and SrO reacted with gas phase carbon dioxide to re-form $SrCO_3$. [138]

Asami *et al.* proposed two kinds of reaction mechanisms on CO_2-OCM depending on catalysts: via heterogeneous and homogeneous disaggregation. [133] In the mechanism

including heterogeneous disaggregation, carbon dioxide adsorbed and eliminated to form the active oxygen species on the oxide catalysts (eq. 30), produced active oxygen removed hydrogen from methane to form methyl radicals (eq. 31) and these methyl radicals combined with each other to form ethane (eq. 32).

$$CO_2 + M^{n+} \rightarrow CO + O\text{-}M^{n+} \quad \text{(eq. 30)}$$

$$O\text{-}M^{n+} + CH_4 \rightarrow CH_3\cdot + OH' + M \quad \text{(eq. 31)}$$

$$2CH_3\cdot \rightarrow C_2H_6 \quad \text{(eq. 32)}$$

On the other hand, in the mechanism including homogeneous disaggregation, methane were activated by lattice oxygen on metal oxide catalysts to form methyl radicals (eq. 33), produced methyl radicals combined with each other to form ethane (eq. 32) and carbon dioxide adsorbed the remaining lattice vacancy, dissociating to carbon monoxide.

$$O_s'' + 2CH_4 \rightarrow 2CH_3\cdot + H_2O + V_O^{\cdot\cdot} \quad \text{(eq. 33)}$$

$$V_O^{\cdot\cdot} + CO_2 \rightarrow CO + O_s' \quad \text{(eq. 34)}$$

The difference between two reported mechanisms was the catalyst structure after reactions. In the mechanism including homogeneous disaggregation, the catalyst was reduced by methane and the structure was changed after the reaction. On the other hand, in the mechanism including heterogeneous disaggregation, the structure change was not observed. Therefore, they reported the reaction mechanism could be predicted by observing the catalyst structure after the reaction. For example, the structural change was not observed over rare earth metal oxide and zirconium oxide catalysts, indicating heterogeneous disaggregation proceeding, and iron oxides and manganese oxide catalysts were reduced after the reaction, indicating homogeneous disaggregation proceeding.

Chen *et al.* conducted CO_2-OCM over a La_2O_3/ZnO catalyst, which was known for not forming carbonates even at high temperatures in the condition of producing the OCM reaction. [139] As a result, the 20wt%La_2O_3/ZnO catalyst indicated high catalytic activities: C_2 selectivity was 90.6% and the C_2 yield was 2.8%. They also reported that the test for comparison between over only the La_2O_3 catalyst and various rare earth oxide (La_2O_3, Y_2O_3, Sm_2O_3) supported ZnO catalysts was conducted and the interaction between La_2O_3 and ZnO played an important role in producing the CO_2-OCM reaction.

Eliasson groups reported several pieces of research in CO_2-OCM using discharge. An application for non-equilibrium discharge, which had a very high electron temperature, such

as 10,000–100,000 K and retained the gas phase temperature at room temperature, have been expected because of a lower reaction temperature than the conventional reaction system. [140] Eliasson *et al.* conducted CO_2-OCM over zeolite catalysts (NaA, NaX, NaY) using DBD (dielectric barrier discharge), a kind of non-equilibrium discharge. [141] A silica tube was used as a dielectric. They also reported that simultaneously using zeolites with DBD resulted in decreasing methane and carbon dioxide conversions, light hydrocarbons (C_2–C_4) selectivity and methanol selectivity increased, and carbon black formation and hydrocarbon polymerization were suppressed. Additionally, they investigated the additional effect of carbon dioxide because light hydrocarbons concentrated on acetylene were produced in only methane flow. As a result, they also reported that increasing the partial pressure of carbon dioxide resulted in increasing methane and carbon dioxide conversions, a complication of RWGS reaction promoted carbon monoxide formation and light hydrocarbon selectivity increased. Energy efficiency (conversion per kWh) increased depending on the increasing discharge power, exceeding 5 g kWh^{-1}. They indicated the reason for such high energy efficiency that the concentration of intermediates such as methyl radical was relatively high. Liu *et al.* conducted CO_2-OCM not using any catalysts and investigated the effect of discharge because large variety of products including oxygen containing compounds such as methanol and aldehyde were synthesized from methane and carbon dioxide using DBD. [31] As a result, they also reported that the main products were not acetylene but ethane and propane using other discharge processes (thermal plasma, corona discharge, microwave discharge) of the same as DBD. Increasing applied voltage resulted in increasing the H_2/CO ratio because, though imposed voltage increased, carbon monoxide formation from RWGS were constant and the H/C ratio of produced hydrocarbon decreased. Zhang *et al.* conducted CO_2-OCM over La_2O_3/γ-Al_2O_3 and Pd/γ-Al_2O_3 catalysts using pulse discharge, low temperature plasma. [142] As a result, they reported that C_2 selectivity was high but the main product was acetylene over the La_2O_3/γ-Al_2O_3 catalyst; on the other hand, ethylene selectivity was high but C_2 selectivity was low over the Pd/γ-Al_2O_3 catalyst. Accordingly, they investigated CO_2-OCM over the Pd-La_2O_3/γ-Al_2O_3 catalyst, which was synthesized from palladium chloride and lanthanum acetate co-impregnated to γ-Al_2O_3 and high catalytic activities demonstrated thanks to the synergistic effect of Pd and La_2O_3: C_2 selectivity was 70.4% and ethylene selectivity was 65.4%. Thus, though the catalytic processes using discharge are variously available in reactions for methane and carbon dioxide, higher efficiency is expected due to its high input energy.

1.5 Dry reforming of methane

DRM (dry reforming of methane) is the process to produce the syngas from methane and carbon dioxide, and the reaction equation of this reaction is the following (eq. 3, shown again) :

$$CH_4 + CO_2 \rightarrow 2CO + 2H_2 \qquad \Delta H^0_{298} = 247.2\ \text{kJ·mol}^{-1} \qquad \text{(eq. 3)}$$

Eq. 3 is a large endothermic reaction and the number of moles increased. Therefore, high temperature and high pressure conditions are advantages in thermodynamic equilibrium. In this section, thermodynamic analysis, the roles of supported metal and supports as catalysts, the carbon deposition mechanism, reaction kinetics, proposed reaction mechanism and the discharge reaction for DRM reaction are summarized.

1.5.1 Thermodynamic analysis

The temperature dependence on changing free Gibbs energy is the following (eq. 35) :

$$\Delta G_T\left(\text{kJ·mol}^{-1}\right) = 2.31\times10^{7} - 0.0702T\cdot\ln T + 0.185T + 5.19\times10^{-5}T^2 + 5.65\times10^{-9}T^3 \qquad \text{(eq. 35)}$$

The equilibrium conversions depending on the temperature in the condition of the total pressure as 1 atm and the CO_2/CH_4 ratio as 1 were calculated from eq. 35. (shown as Figure 1-8)

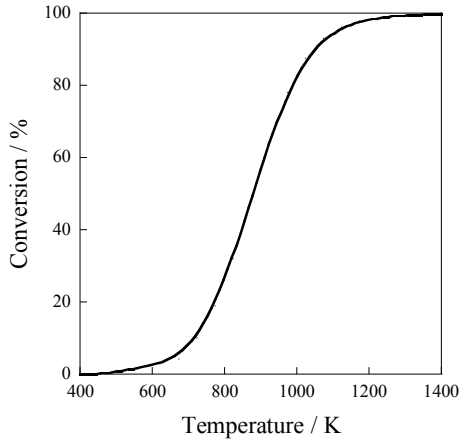

Figure 1-8 Equilibrium Conversion at various temperature for DRM, total pressure: 1.0 atm; $P_{CH4}/P_{CO2}=1$

Figure 1-8 indicates that DRM is required to have high reaction temperature and disadvantage in the perspective of reaction engineering and energy. [143] Additionally, the theoretical H_2/CO ratio of the production in DRM (eq. 3) is 1, but the experimental H_2/CO ratio is under 1 because RWGS (eq. 36) proceeds at the same time. However, the experimental H_2/CO ratio sometimes exceeds 1 due to the sequential carbon deposition (eq. 37, eq.38) depending on the reaction condition and catalysts.

$$CO_2 + H_2 \rightleftarrows CO + H_2O \qquad \Delta H^0_{298} = 41.2\ \text{kJ·mol}^{-1} \qquad \text{(eq. 36)}$$

$$CH_4 \rightleftarrows C(S) + 2H_2 \qquad \Delta H^0_{298} = 74.0\ \text{kJ·mol}^{-1} \qquad \text{(eq. 37)}$$

$$2CO \rightleftarrows C(S) + CO_2 \qquad \Delta H^0_{298} = -172.5\ \text{kJ·mol}^{-1} \qquad \text{(eq. 38)}$$

Eq. 37 indicates methane dissociation to form solid carbon (deposited carbon) and hydrogen; eq. 38 indicates carbon monoxide disproportionation to form surface carbon and carbon dioxide, named as the Boudouard reaction.

Pakhare *et al.* calculated the equilibrium conversions and composition from reactions of methane and carbon dioxide by a simulation using HSC Chemistry 7.1 software, named as Gibbs free energy minimization algorithm. [144, 145] Figure 1-9 shows the thermodynamic equilibrium plots for DRM depending on the temperature. Figure 1-9(a) indicates the plots in the condition of no carbon deposition and Figure 1-9(b) indicates the plots in the condition of carbon deposition. As shown in Figure 1-9(a), RWGS did not proceed at 673–1073 K. As shown in Figure 1-9(b), the H_2/CO ratio increased due to carbon deposition and the carbon deposition did not occur at more than 1173 K. These calculations coincided with the previous report. [146]

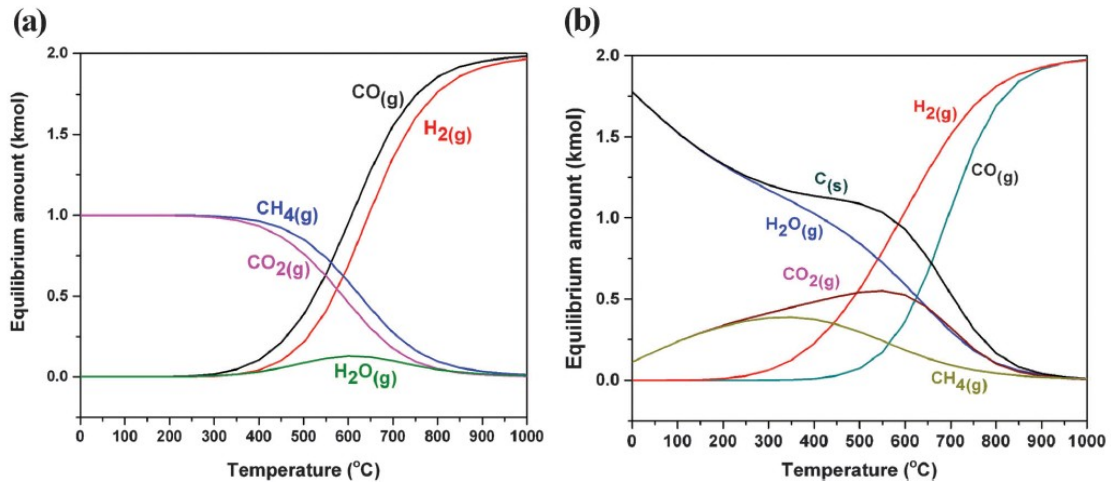

Figure 1-9 Thermodynamic equilibrium plots for DRM from 0 to 1000 °C and at feed ratio of CO_2 and CH_4 as 1: (a) Assuming no carbon formation occurs; (b) Assuming carbon formation occurs. (Reprinted with permission from Ref. [144, 145] Copyright 2013 Elsevier, and 2014 Royal Society of Chemistry.)

1.5.2 The role of supported metals

Generally, methane is adsorbed only on metal sites and forms hydrogen and CH_x species by dissociation. Supporting metal on the supports plays an important role for producing a DRM reaction because a large majority of H species were recombined to form hydrogen. [147] In order to produce the DRM reaction, a high temperature condition as above 1173 K is required from thermodynamic analysis as described in section 1.5.1. However, the supported metal sintering and support structure change are evitable at such high temperature. Therefore, many catalysts using noble metals such as Pt, Rh and Ru have been investigated. [143, 148, 149–153] Nakamura *et al.* investigated the comparison of DRM activities at 973 K among various metal (Ni, Ru, Rh, Pd, Pt) supported SiO_2 and MgO catalysts. [143] The order of catalytic activities was Ru>Rh>Ni>Pt>Pd on SiO_2 support and Ru>Rh>Ni>Pd>Pt on MgO support. Aparicio *et al.* also reported that the order of catalytic activities on Al_2O_3 support was Rh>Ni>Pt>Ir>Ru>Co. [148] However, Ni or Co supported catalyst has been focused on in recent years because noble metals are expensive. [154–163] García-Diéguez *et al.* reported that Rh addition to a Ni supported catalyst promoted a Ni reduction and suppressed sintering by hydrogen spillover from Rh to Ni. [160] Nagaoka *et al.* also reported the same trends over Pt or Ru doped Co supported catalysts. [164]

1.5.3 The role of supports

In the perspective of economics, Ni supported catalysts are expected as described in section 1.5.2, but carbon deposition and sintering easily occurred and the catalytic activities do not sustain for a long time. Therefore, the modification for supports has been investigated. There are strong agreements in the former literatures that methane dissociation occurs on the supported metal and carbon dioxide are affected by the acidity and basicity of supports. [165] On the other hand, both methane and carbon dioxide are possibly activated on supported metals over neutral supports such as SiO_2. On acidic supports, carbon dioxide is activated by formate species produced from hydroxyl species and, on basic supports, carbon dioxide is activated by forming oxy-carbonate. [166, 167] On the other hand, over neutral supports, carbon dioxide is activated by hydrogen species from methane dissociation but sintering the catalyst easily occurs due to carbon deposition. Therefore, the stabilization for catalytic activities over neutral supports have been explored in the perspective of metal-metal interaction over bi-metallic catalysts. [168, 169] Wu *et al.* reported higher DRM activity and stability over Rh and Ni supported boron nitride (BN) catalysts, rather than the γ-Al_2O_3 support. [168] They indicated that metal-metal interaction was weak and the Rh-Ni bimetallic cluster did not form over γ-Al_2O_3 support. On the other hand, Miguel *et al.* reported that the bimetallic cluster formed over Pt and Ni catalysts supported on γ-Al_2O_3. [169] Therefore, the interaction between the metal-metal interaction and the acidity in the DRM reaction is still being discussed.

Mixed oxide support catalysts also have been studied. Reddy *et al.* investigated the interaction between the support and Pt over Pt supported mixed oxide supports by comparing the mixed ratio of ZrO_2 and SiO_2. [170] Over only the ZrO_2 catalyst, carbon dioxide was highly activated but the interaction between Pt and the support was weak due to a large particle of Pt. Addition of a small portion of SiO_2 to ZrO_2 resulted in increasing the interfacial site on Pt-ZrO_2 and suppressing the carbon deposition. Additionally, Stagg-Williams *et al.* investigated DRM activities over La or Ce doped Pt/ZrO_2 catalysts. [171] La or Ce addition to Pt/ZrO_2 stabilized tetragonal ZrO_2, promoted carbon dioxide adsorption and the density of adsorbed carbon dioxide increased. As a result, they indicated that oxygen species from dissociated carbon dioxide near the Pt particle cleaned the deposited carbon. Thus, increasing interfacial active sites between metal and support over mixed oxide support has been focused on.

1.5.4 Carbon deposition

In the DRM reaction, the suppression of carbon deposition is very important along with catalytic activities. The ternary diagram is useful for thermodynamic prediction for carbon deposition. [172] Figure 1-10 shows the Ni–C–H–O diagram by Sacco *et al.* and indicates the phase of carbide deposition, carbon deposition and Ni metal. The line between methane and carbon dioxide is very close to the carbon deposition phase and the carbon deposition thermodynamically easily occurs. Additionally, Figure 1-10 indicates that the addition of hydrogen and water is valid for avoiding the carbon deposition. Bartholomew also reported the same figure. [173] Gadalla and Bower reported the figure of the CO_2/CH_4 feed ratio and temperature, in which the carbon deposition phase in DRM reaction can be experimentally predicted. (as shown in Figure 1-11) [174] The origin of inactive carbon during the DRM reaction is derived from methane decomposition (eq. 37) and carbon monoxide disproportionation (eq. 38). Carbon monoxide disproportionation is an exothermic reaction and the equilibrium constant decreases by increasing the temperature. On the other hand, methane decomposition is an endothermic reaction and the equilibrium constant increases with increasing the temperature.

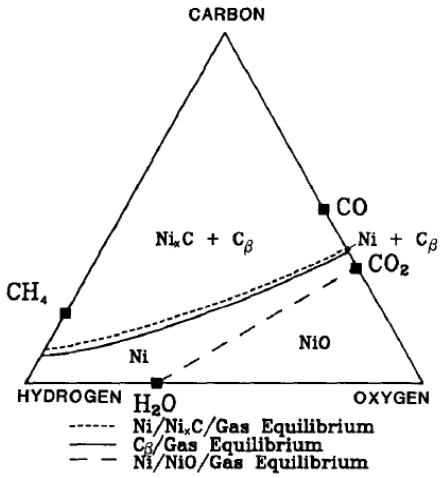

Figure 1-10 Ni–C–H–O phase diagram (900 K, 1 bar pressure) (Reprinted with permission from Ref. [172] Copyright 1989 Elsevier.)

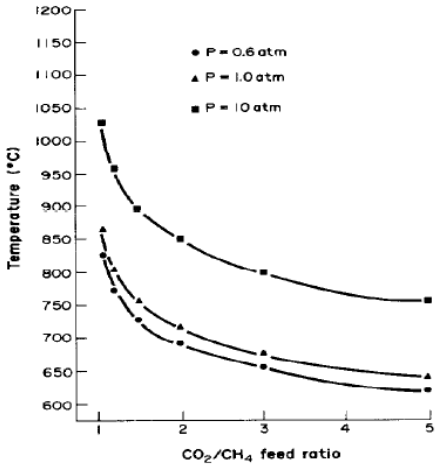

Figure 1-11 Effect of feed ratio on the temperature below which carbon deposits at various pressures. (Reprinted with permission from Ref. [174] Copyright 1988 Elsevier.)

Rodriguez mentioned that the shape of inactive carbon in the DRM reaction was often whisker carbon and the rate determining step in this whisker carbon formation was the diffusion of carbon atoms through a metal particle. [175] He also indicated that the driving force for this carbon diffusion process was heat generation from exothermic steps, such as carbon monoxide adsorption and disproportionation. There have been strong agreements for the process of carbon monoxide dissociation and carbon fiber formation in former literature as follows: firstly, carbon monoxide adsorbed the multiple coordination on transition metals, proceeding through a bent transition state before dissociation [176, 179]; adsorbed carbon monoxide species on C/Ni induced the migration of carbon atoms to subsurface Ni layers. [180]; this migration induced the reconstruction of the Ni surface, thereby lengthening nearby Ni-Ni bonds and penetrating a deeper carbon particle into the Ni lattice; finally, graphitic layer formed on the back side of the metal crystallite by carbon diffusion through the metal lattice and inactive carbon matured.

Tavares *et al.* investigated the effect of anisotropic crystallinity on the carbon deposition using TEM measurement by the reaction for mix gases of carbon monoxide, carbon dioxide, methane and hydrogen. [181] As a result, the carbon deposition formed as the encapsulating type on rough crystallinity. However, isotropic filamentous carbon was deposited on high crystallinity. Chesnokov *et al.* also investigated the interaction between carbon morphology and crystallinity in only methane feed over Ni supported catalysts. [182] These results indicate that methane decomposition formed on Ni (100) and (110) faces, diffused across the Ni surface and graphitic layer formed on the (111) face. The driving force of these process has assumed to be a carbon concentration gradient. In order to clarify whether the carbon deposition in a DRM reaction derived from methane decomposition or carbon monoxide

disproportionation, Swaan and Tsipouriari independently evaluated the carbon deposition by the reaction of ^{13}C isotopic labeling methane and carbon dioxide using TPO measurement. [183, 184] As a result, carbon deposition occurred from both steps but primarily from carbon monoxide derived from carbon dioxide.

1.5.5 Kinetics

Activation energies E_a in the DRM reaction were investigated over various catalysts, summarized in Table 1-2. [186-192] Beebe *et al.* reported that activation energies of methane dissociation were 55.7±6 kJ mol^{-1} on Ni (110) face and 52.8±5 kJ mol^{-1} on Ni (111) face. [193] It is interesting that the number of listed catalysts which the rate determining step was methane dissociation in Table 1-2 is small because many listed catalysts indicates high activation energy exceeding the value of methane dissociation. On the other hand, the activation energies from methane over many listed catalysts are higher than those from carbon dioxide. These results assume that the rate determining step over many listed catalysts is the elementary process related to methane.

Activation sites for methane and carbon dioxide are thought to be dependent on a combination of the supported metal and support because Table 1-2 shows various activation energies depending on a combination of the supported metal and support. For example, both methane and carbon dioxide were activated on the Pt surface over the Pt/SiO_2 catalyst and carbon dioxide was activated on ZrO_2 over ZrO_2 catalysts and TOF of carbon dioxide increased due to its lattice defects and basicity. [194–195] Bitter *et al.* investigated the electron state of Pt over the Pt/ZrO_2 catalyst in a carbon dioxide feed by *in-situ* XANES measurement. [194] As a result, they also reported that, though carbon dioxide dissociated to carbon monoxide and oxygen, oxygen became a part of ZrO_2 because the electron state of Pt unchanged. On the other hand, Aparicio and Schuurman reported that, over Rh or Ru supported the SiO_2 catalyst, carbon dioxide oxidized metals. [167, 195] Therefore, the reaction on metal-support interfacial over various catalysts plays an important role in determining the activation energy.

Table 1-2 Kinetic parameter (activation energy) for DRM: TOFs extrapolated to reaction condition of the total pressure as 1 atm; P_{CH4}/P_{CO2}=1; 723K. (Ref from [186–192])

Catalyst	TOF / s^{-1}		E_a / kJ mol^{-1}		Catalyst	TOF / s^{-1}		E_a / kJ mol^{-1}	
	CH_4	CO_2	CH_4	CO_2		CH_4	CO_2	CH_4	CO_2
Co/C	0.06	0.1	46	38	Pd/MgO	0.03	–	113	–
Co/SiO_2	0.16	0.26	42	33	Pd/SiO_2	0.23	0.34	117	96
Ni/Al_2O_3	–	–	42	33	Pd/Al_2O_3	0.07	0.10	84	92
Ni/C	–	–	84	92	Pd/TiO_2	1.1	2.3	75	63
Ni/ZrO_2	–	–	59	42	Ir/Al_2O_3	0.01	0.01	113	130
Ni/SiO_2	–	–	96	88	Ir/MgO	0.03	–	159	–
Ni/MgO	–	–	88	88	Ir/TiO_2	11	22	88	75
Ni/TiO_2	–	–	109	88	Pt/Al_2O_3	0.06	0.12	63	50
Ni foil	–	–	29	–	Pt/Cr_2O_3	0.42	1.08	67	63
Ru/Al_2O_3	0.08	0.10	92	96	Pt/ZrO_2	0.52	0.98	100	84
Ru/C	0.10	0.21	109	88	Pt/SiO_2	0.45	0.85	63	80
Ru/TiO_2	4.3	7.2	75	71	Pt/TiO_2	2.3	4.4	96	80
Rh/Al_2O_3	0.06	0.11	67	54	Pt foil	–	–	75	75
Rh/SiO_2	0.12	0.14	84	96					
Rh/MgO	0.26	–	117	–					
Rh/TiO_2	15	25	88	75					

Several rate expressions to describe the reaction kinetics were reported. One of earliest rate expressions was the following Langmuir-Hinshelwood type equation over Cu/SiO_2 by Lewis *et al.* (as shown in eq. 39) [196]

$$r = \frac{kP_{CH4}\cdot(P_{CO2}+P_{H2O})}{[1+24\cdot(P_{CO2}+P_{H2O})+8P_{H2}]^2} \qquad \text{(eq. 39)}$$

Eq. 39 ignored the parameter related to the temperature and was in partial contradiction with the experimental data reported by Clarke *et al.* [197] Bodorov *et al.* reported the other rate expression in DRM reaction, referred to kinetic analysis in SRM reaction over Ni foil (as shown in eq. 40) [185]

$$r = \frac{kP_{CH4}}{1+a\cdot(P_{H2O}/P_{H2})+b\cdot P_{CO}} \qquad \text{(eq. 40)}$$

Richardson *et al.* provided the other rate expression based on Langmuir-Hinshelwood type equation including the redox mechanism. [198]

$$r = \frac{kK_{CO2} \cdot K_{CH4} \cdot P_{CO2} \cdot P_{CH4}}{(1+K_{CO2} \cdot P_{CO2}+K_{CH4} \cdot P_{CH4})^2} \quad \text{(eq. 41)}$$

Otherwise, Mark (eq. 42), Horiuchi (eq. 43) and Verykios(eq. 44) provided the rate expression but these equations were in partial contradiction with the experimental data of adsorption enthalpy or kinetic parameters from other reports. Therefore, discussions over the rate expressions in DRM reaction will possibly remain. [188, 199, 200]

$$r = \frac{k_R \cdot [P_{CH4} - (P_{H2}^2 \cdot P_{CO}^2 / K_R \cdot P_{CO2})]}{1+(P_{CO}^2 / K_{R,C} \cdot P_{CO2})} \quad \text{(eq. 42)}$$

$$r = \frac{k \cdot \sqrt{K_1 \cdot K_2 \cdot P_{CH4} \cdot P_{CO2}}}{(1+\sqrt{K_1 \cdot P_{CO2}}+\sqrt{K_2 \cdot P_{CH4}})^2} \quad \text{(eq. 43)}$$

$$r = \frac{a \cdot P_{CH4} \cdot P_{CO2}^2}{(P_{CO2}+b \cdot P_{CO2}^2+c \cdot P_{CH4})^2} \quad \text{(eq. 44)}$$

In relatively recent reports, Verykios *et al.* provided the rate expressions based on the rate determining step as methane decomposition over the Ni/La_2O_3 catalyst and mentioned that this equation coincided well with other experimental data. [201]

$$r = \frac{K_1 \cdot k_2 \cdot K_3 \cdot k_4 \cdot P_{CH4} \cdot P_{CO2}}{K_1 \cdot k_2 \cdot K_3 \cdot P_{CH4} \cdot P_{CO2}+K_1 \cdot k_2 \cdot P_{CH4}+K_3 \cdot k_4 \cdot P_{CO2}} \quad \text{(eq. 45)}$$

(denoted K_1 as rate constant for methane adsorption, k_2 as rate constant for methane surface reaction, K_3 as rate constant for carbon dioxide adsorption and k_4 as rate constant for carbon dioxide surface reaction)

Quiroga *et al.* provided the other rate expressions based on a different rate determining step from eq. 45 and mentioned that this equation coincided well with other experimental data, especially over Pt or Rh supported catalysts. (as shown in eq. 46) [202] They assumed in eq. 46 that methane absorption and decomposition reached an equilibrium value. Additionally,

they also considered the carbon deposition and hydrogen formation in eq. 46. Therefore, this equation possibly expresses the apparent reaction rate.

$$r_{\cdot} = \frac{k_1 \cdot K_{CH4} \cdot K_{CO2} \cdot \left(P_{CH4} \cdot P_{CO2} \Big/ P_{H2}^{0.5} - P_{H2}^{0.5} \cdot P_{CO2}^{2} \Big/ K_{ref} \right)}{\left(1 + P_{CH4} \Big/ P_{H2}^{0.5} \cdot K_{CH4} + P_{CO2} \cdot K_{CO2} \right)^{2}} \qquad \text{(eq. 46)}$$

(denoted k_1 as rate constant for surface reaction between methane and carbon dioxide on active sites over the support and the metal surface)

1.5.6 Reaction mechanism

The reaction mechanism in DRM were investigated about 50 years ago and the first reported mechanism, called Bodorov-Apel'baum mechanism, was as follows: [185]

$CH_4 + M \rightarrow CH_2\text{-}M + H_2$ (eq. 47)

$CO_2 + M \rightleftarrows CO + O\text{-}M$ (eq. 48)

$O\text{-}M + H_2 \rightleftarrows H_2O + M$ (eq. 49)

$CH_2\text{-}M + H_2O \rightleftarrows CO\text{-}M + 2H_2$ (eq. 50)

$CO\text{-}M \rightleftarrows CO + M$ (eq. 51)

(denoted M as metal active sites)

Nakamura *et al.* experimentally confirmed these mechanisms. [147] Firstly, methane was decomposed to form CH_2 species on the active site as the rate determining step. Subsequently, carbon dioxide and hydrogen reacted in the RWGS reaction to form carbon monoxide and water. Finally, water and CH_2 species reacted to form hydrogen and carbon monoxide. Bodorov indicated that the SRM reaction more rapidly proceeded than the DRM reaction thanks to efficiently shift the equilibrium by direct water addition in eq. 47 and eq. 48. [185]

Rostrup-Nielsen and Erdöhelyi *et al.* provided modified a Bodorov-Apel'baum mechanism. [187, 203] Firstly, they modified the methane dissociative adsorption process (eq. 46) to the following equations (eqs. 51 and 52) because CH_x species except for CH_2 were observed on metal active sites.

$CH_4 + 2M \rightarrow CH_3\text{-}M + H\text{-}M$ (eq. 52)

$$CH_3\text{-}M + (3\text{-}x)M \rightarrow CH_x\text{-}M + (3\text{-}x)H\text{-}M \quad \text{(eq. 53)}$$

Next, they modified carbon dioxide elimination (eq. 47) to the following equations (eqs. 53 and 54) because adsorbed hydrogen species reacted with carbon dioxide by FT-IR measurement.

$$CO_2 + H\text{-}M \rightleftarrows CO + HO\text{-}M \quad \text{(eq. 54)}$$

$$2HO\text{-}M \rightleftarrows H_2O + O\text{-}M + M \quad \text{(eq. 55)}$$

Finally, they modified the adsorbed oxygen reaction with hydrogen to form water (eq. 48) to the following equations (eqs. 55 and 56) because adsorbed oxygen reacted with surface CH_x species to form carbon monoxide and hydrogen.

$$CH_x + O\text{-}M + (x\text{-}2)M \rightleftarrows CO + xH\text{-}M \quad \text{(eq. 56)}$$

$$2H\text{-}M \rightleftarrows H_2 + 2M \quad \text{(eq. 57)}$$

1.5.7 DRM using plasma technology

The first plasma utilization for DRM reaction was 40 years ago by Capezzuto *et al.* [204] They reported that acetylene was the main product in DRM reactions using radiofrequency (RF) plasma reactor in the condition of the pressure under 20 Torr. Later, the Jorgensen group conducted DRM reactions using gliding arc discharge in atmospheric pressure conditions because the cost of vacuum discharge was too expensive in the vacuuming process and reported that the syngas and water were produced other than acetylene. [205] Additionally, they reported that the production distribution was dependent on the P_{CH4}/P_{CO2} ratio. In atmospheric pressure plasma, energy for the first step of electronic ionization is very high and the secondary electron productions are easily induced. Therefore, the excitation and dissociation energy in the electron collision step play an important role in DRM reaction using plasma. Morgan *et al.* reported that electronic ionization energy of methane and carbon dioxide were 9 eV and 11 eV. [206, 207] The following electron collision process in carbon dioxide decomposition were reported in previous studies [207–209] :

$$e + CO_2\left(X^1\sum_g^+\right) \rightarrow e + CO_2\left(1^1\sum_u^+\right) \quad \text{(eq. 58)}$$

$$e + CO_2\left(1^1\sum_g^+\right) \rightarrow e + CO\left(X^1\sum^+\right) + O(^1S) \quad \text{(eq. 59)}$$

$$e + CO_2\left(X^1\sum_g^+\right) \rightarrow e + CO(a^3\Pi) + O(^3P) \quad \text{(eq. 60)}$$

$$e + CO_2\left(X^1\sum_g^+\right) \rightarrow e + CO(a^3\Pi) + O(^5S) \quad \text{(eq. 61)}$$

$$e + CO_2\left(X^1\sum_g^+\right) \rightarrow e + CO_2(001) \quad \text{(eq. 62)}$$

$$e + CO_2(001) \rightarrow e + CO\left(X^1\sum^+\right) + O(^1S) \quad \text{(eq. 63)}$$

Excitation of vibrational carbon dioxide is an important step in carbon dioxide decomposition thanks to its low threshold energy. Nakatsuji *et al.* reported that carbon dioxide vibration mode was composed of symmetric stretching, bending and asymmetric stretching, and long-life asymmetric stretching was the main mode. [210] They also investigated excited electron states of carbon dioxide in the electron collision process, as listed in Table 1-3. The electron collision process in methane decomposition is more complicated than that in carbon dioxide decomposition because methane has complicated vibration modes. [206] Four C-H bonds in methane molecules has a higher bond energy than the C=O bond and methane decomposition by direct electron collision is difficult. Removal hydrogen atom from methane was reported to be 9–11 eV.

Table 1-3 Excited electron states of carbon dioxide (Reprinted with permission from Ref. [210] Copyright 1983 Elsevier)

State	Excitation energy (eV)
$^1\Pi_u$	11.39
$^3\Pi_u$	11.31
$^1\Sigma_u^+$	11.00
$^1\Delta_u$	9.32
$^1\Sigma_u^+$	9.27
$^3\Sigma_u^-$	9.19
$^1\Pi_g$	8.93
$^3\Delta_u$	8.80
$^3\Pi_g$	8.73
Σ_u^+	8.15

Electron collision process in hydrogen production from methane were reported as follows:

$$e + CH_4 \rightarrow e + CH_3 + H \quad \text{(eq. 64)}$$

$$e + CH_4 \rightarrow e + CH_2 + H_2 \quad \text{(eq. 65)}$$

$$e + CH_4 \rightarrow e + CH + H_2 + H \quad \text{(eq. 66)}$$

The following paragraphs summarize 5 types of plasma applied in the DRM reaction by various forming methods: corona discharge, dielectric barrier discharge, glow discharge, arc discharge and spark discharge.

Corona discharge, which is a persistent discharge, forms by an unevenly distributed electric field around a pointed needle-shaped electrode. The light emitting area around the needle-shaped electrode is called the corona. The current by corona discharge is very small: several μA. When applying corona discharge, carbon monoxide was produced more than hydrogen in the DRM reaction. [211, 212] Acetylene was also produced as a by-product. Yang *et al.* reported that increasing the flow rate of raw gas resulted in increasing the energy efficiency. [211]

Dielectric barrier discharge (DBD) is generated in inserting the dielectric between two electrodes. [213] During DBD, electrons have high kinetic energy in the filament and relatively higher energy density than other non-thermal plasma. Zou *et al.* reported that, when applying DBD, the same amounts of carbon monoxide were produced as hydrogen and acetylene was also produced as a by-product. [214, 215]

Glow discharge is a kind of Townsend discharge and emits visible light. Townsend discharge is the phenomenon that supplied charge particles to the gap between two electrodes causes the secondary electron emission in positive ion collision to the anode (γ process) and the gas phase molecules ionization by electrons transferring between the cathode and anode (α process), increasing electron conductivity of the gas phase by an electron avalanche phenomenon. As increasing applied current, dark current discharge, glow discharge and arc plasma are generated. Li *et al.* reported that DRM using atmospheric pressure glow discharge (APGD), which had a large discharge volume, was more efficient in high flow rate conditions than using corona discharge. As a result, they also reported that decreasing conversion resulted in acetylene formation. [216, 217]

Arc plasma can be divided into two modes: control arc and gliding arc. Control arc was the earliest investigated among plasma DRM processes and generates higher gas temperatures than DBD and APGD because the control arc has thermal plasma characteristics. [218] Additionally, the gas temperature in arc plasma is known to be dependent on the electrode gap

length and applied voltage. [219, 220] They also reported that syngas selectivity and energy efficiency using arc plasma were lower than using DBD and APGD.

Spark discharge is the transition state between corona discharge and glow discharge, and has the intermediate characteristic of filament discharge and flame discharge. [221, 222] Li *et al.* reported that applied voltage and the consumed energy was lower than APGD in the same current. However, they also reported that the application for spark discharge in DRM reactions was few because the operating rage of spark discharge was limited, and the products distribution was the same as using APGD.

In the above paragraphs, DRM reactions using plasma applied to the reactor are mentioned. Otherwise, a lot of research on catalysts valid for DRM reaction using plasma preparation methods have been reported. [223–230] Liu *et al.* reported that plasma was widely used for the surface treating method on materials and altering the durability and basicity of catalysts were expected to enhance DRM activities. [223] They also indicated that both charged and neutral particles gained kinetic energy by applying plasma. However, a clear model on the prediction for physicochemical variation has not been reported due to the thermal diffusion effects. Several effects on plasma preparation methods have been reported: (a) smaller metal cluster formation, (b) active sites reduction, (c) oxygen vacancy formation and (d) pore structure variation effects. Wu *et al.* reported that electron transfer on catalysts resulted in concentrating thermal energy and generating local hot spots of very high temperatures, promoting re-agglomeration of metal clusters. (a) [224, 225] Zhang *et al.* reported that discharge generated both positively and negatively charged particles, and these particles generated the surface of various oxidizing states as oxidizing or reducing agent. They also indicated that hydrogen plasma easily reduced the surface metal by hydrogen atoms and retained the reducing state of metal in DRM reactions. (b) [226, 227] Zhu *et al.* reported that local high temperatures in plasma preparation promoted the interaction between the support and supported metal, and oxides of high oxygen ion mobility such as perovskite oxides formed on the interfacial phase to generate oxygen vacancy and higher oxygen affinity. (c) [225, 228] Shang *et al.* reported that, on pore structure materials, the complicated discharge distribution on catalysts and metal-support interfaces were generated depending on the pore size and shape due to various pore structures. (d) [229, 230]

1.6 Catalytic reaction in an electric field

The catalytic reaction in an electric field promotes the catalytic activities by applying voltage, lower voltage than in discharge and higher voltage than in electrolysis and NEMCA

(non-Faradic electrochemical modification of catalytic activity). [231] NEMCA is a kind of non-Faradaic reaction, that is, the process which activates several 1,000–10,000 molecules per electron, providing by Vayenas *et al.* [232–236] Solid electrolytes such as yttria stabilized zirconia (YSZ) are used as a base disk catalyst, and Ag or Pt is coated with the disk surface as both electrode and catalyst. Applying a weak current to the disk catalyst decreases an activation energy of reactions and improves the reaction rate. A catalytic reaction in an electric field has the following strong points, rather than other electrical processes: lower reaction temperature, which is not required to the exterior heat supply, and high electron efficiency, which can activate several 100 molecules per an electron. [231] The specific feature of the electric field in the process is to control the applied voltage by current cut-off. The electric field is controlled by imposing several mA current to the catalyst bed and the voltage in the electric field is determined by the electric characteristic of the catalyst, the electrode gap and the reaction condition such as the gas component and temperature in catalytic reactions. The applied voltage is several 100–2,000 V.

Our laboratory conducted SRM (eq. 1) in the electric field (*electreforming*) and the screening tests to find high catalytic activities at low temperatures, as shown in Figure 1-12 and Figure 1-13. [231, 237–239] Figure 1-12 indicated high catalytic activity at low temperatures over Pt, Pd, Rh and Ni supported catalysts, which was known to indicate high catalytic activity in conventional reactions (not applying the electric field). [240–243] Sekine *et al.* reported that catalytic characteristics in the electric field was the same as those in conventional reactions. They also indicated higher methane conversion over Rh/CeO_2 and Ni/CeO_2 catalysts: 13% at about 500 K. As a result, the reaction temperature decreased to about 150 K due to applying the electric field because the reaction temperature of 650 K with thermodynamic equilibrium was required to indicate the same conversion as in the electric field. [231]

Sekine *et al.* reported that CeO_2 and $Ce_XZr_{1-X}O_2$ solid solution supports of high oxygen mobility indicated high SRM activity, as shown in Figure 1-13. Additionally, the $Pd/Ce_{0.25}Zr_{0.75}O_2$ catalyst of higher oxygen ion conductivity than CeO_2 indicated higher methane conversion at 550 K applying the imposed power as 3.5 W: 40%. Hydrogen production per electron in *electreforming* exceeded 400 $mol_{\text{-}H2}$ $mol_{\text{-}e}^{-1}$ and that in the conventional electrochemical two- electron reaction was 0.5, that is, the electron efficiency in the electric field was about 800 times as high as in conventional electrochemical reaction. [237] Therefore, *electreforming* can convert hydrogen from methane in imposing relatively low power with high electron efficiency.

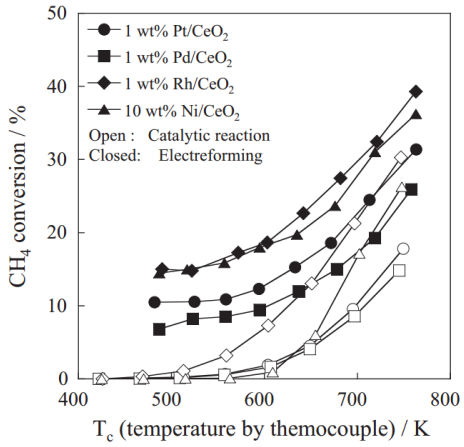

Figure 1-12 Catalytic activities for e*lectreforming* over various metal supported CeO_2 catalysts. (Reprinted with permission from Ref.[237] Copyright 2011 Elsevier)

Our laboratory reported high catalytic activities at a lower temperature in steam reforming of ethanol, ethanol degradation, water gas shift reaction and OCM, other than *electreforming*. [231, 244–248] Haraguchi *et al.* conducted steam reforming of ethanol over Pd, Rh and Pt supported CeO_2 catalysts in the electric field and compared to the conventional catalytic reaction (not applying the electric field). [231] They reported that all catalysts did not indicate the catalytic activities at 423 K in the conventional reaction but indicated high methane conversion in the electric field: 20–60%. They also indicated that applying the electric field changed the reaction path, suppressed acetaldehyde degradation and promoted steam reforming of acetaldehyde and methane, increasing hydrogen production.

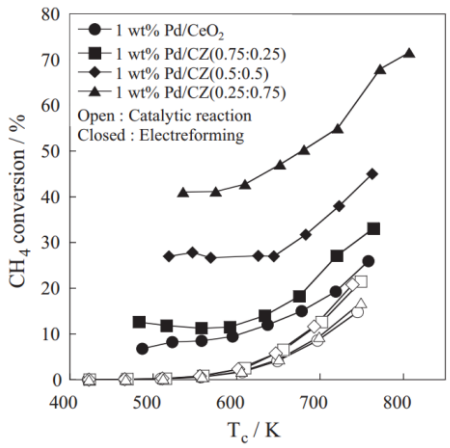

Figure 1-13 Catalytic activities for *electreforming* over various Rh supported $Ce_XZr_{1-X}O_2$ catalysts. (Reprinted with permission from Ref.[237] Copyright 2011 Elsevier)

Sakurai *et al.* conducted steam reforming of ethanol over the Pt/CeO_2 catalyst in the electric field and investigated the effect of applying the electric field. [244] They also indicated that the increasing imposed current resulted in high ethanol conversion and hydrogen yield in *electreforming* because the apparent activation energy of ethanol dehydrogenation and steam reforming of acetaldehyde decreased by increasing the imposed current. They also conducted *in-situ* DRIFT (diffuse reflectance infrared fourier transform spectroscopy) measurement in *electreforming* and indicated that conversion of ethoxide species to the acetate species proceeded even at low temperatures, increasing hydrogen production by applying the electric field.

Tomioka *et al.* conducted ethanol degradation over a Pt supported CeO_2 catalyst in the electric field, lowering the reaction temperature as proceeding 100 K. [245] They reported that, though ethanol degradation did not proceed at such a low temperature as 423 K in the conventional reaction (not applying the electric field), ethanol degradation in the electric field indicated relatively high ethanol conversion: about 8%. They also indicated that the percentage of input energy by applying an electric field as 36% contributed to the ethanol degradation at 423 K.

Tanaka *et al.* conducted OCM over various La_2O_3 catalysts in the electric field, lowering the reaction temperature to 500 K. [246] Oshima *et al.* reported that the structure of the $Sr\text{-}La_2O_3$ (Sr/La = 1/20) catalyst did not change after the OCM reaction in the electric field by XRD (x-ray diffraction) measurement. [247] They also evaluated the heating value and the temperature of the hot spots in the electric field by Plank's radiant law (as shown in eq. 66) using emission spectrum measurement. Results of the emission spectrum measurement in discharge and applied the electric field are shown in Figure 1-14.

$$\mathrm{P}(\lambda,\mathrm{T}) = \frac{2\pi \mathrm{hc}^2}{\lambda^5} \cdot \frac{1}{exp(\mathrm{ch}/\lambda \mathrm{kT}) - 1} \qquad \Delta P(T) = \frac{P(900,T) - P(880,T)}{P(900,T)} \qquad \text{(eq. 67)}$$

As a result, the calculated temperature by emission spectrum measurement was about 1300 K, higher than the external temperature as 900 K. Oshima *et al.* conducted CO_2-OCM over 10 mol%$La\text{-}ZrO_2$ catalyst in the electric field at a low external temperature of 423 K, lowering the reaction temperature as exceeding 700 K. [248]

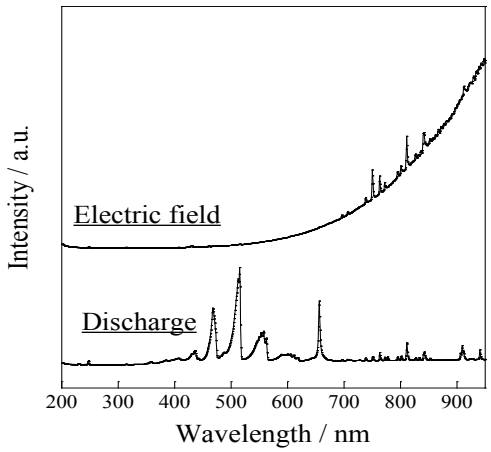

Figure 1-14 Emission spectrum of LEP discharge and electric field.
(CH_4:O_2:Ar = 25:5:100, total flow rate: 130 mL min^{-1})

They reported that the ZrO_2 catalyst indicated low C_2 selectivity and increasing doping amounts of La into ZrO_2 resulted in increasing C_2 selectivity by 5 mol%, decreasing in exceeding 5 mol%. They also investigated the stability of the La-ZrO_2 catalyst structures by XRD measurement, as shown in Figure 1-15. As a result, the monoclinic phase was seen over ZrO_2 and increasing the doping amounts of La into ZrO_2 resulted in appearing for the peak of tetragonal phase and disappearing for the peak of monoclinic phase. On the other hand, a comparison stabilized zirconia of 10 mol%Y-ZrO_2 did not indicate CO_2-OCM activities in the electric field, though the tetragonal ZrO_2 phase was seen. Therefore, they mentioned that the synergetic effect with La and tetragonal ZrO_2 played an important role in CO_2-OCM in the electric field.

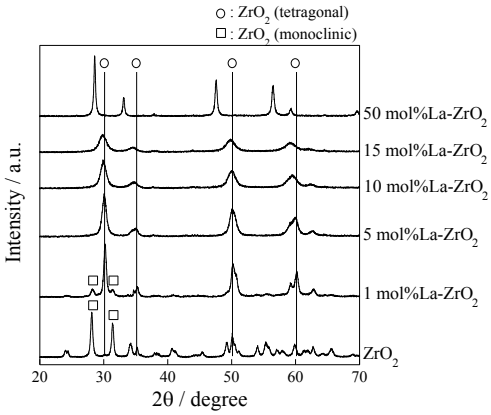

Figure 1-15 XRD patterns of various doping amounts of La into ZrO_2 catalysts. (denoted circle symbol as tetragonal structure and square symbol as monoclinic structure) (Reprinted with permission from Ref. [248] Copyright 2013 Elsevier)

References:

[1] British Petroleum, BP statistical review of world energy 2016 (2016).

[2] Y.P. Upadhyay, R. Bansal, R.B. Sharma, Effects of greenhouse & global warming on environment and uses the hydrogen as an alternative fuel, Int. J. Innov. Res. Develop. 2(2) (2013) 699–718.

[3] N. Pelletier, G. Shahani, Steam reformers for hydrogen and synthesis gas, Petro. Tech. Quarterly 18(1) (2013) 79–83.

[4] V. Havran, M.P. Duduković, C.S. Lo, Conversion of methane and carbon dioxide to higher value products, Ind. Eng. Chem. Res. 50 (2011) 7089–7100.

[5] M.C. Alvarez-Galvan, N. Mota, M. Ojeda, S. Rojas, R.M. Navarro, J.L.G. Fierro, Direct methane conversion routes to chemicals and fuels, Catal. Today 171 (2011) 15–23.

[6] M. Gharibi, F.T. Zangeneh, F. Yaripour, S. Sahebdelfar, Nanocatalysts for conversion of natural gas to liquid fuels and petrochemical feedstocks, Appl. Catal. A: General 443–444 (2012) 8–26.

[7] B. Vora, J.Q. Chen, A. Bozzano, B. Glover, P. Barger, Various routes to methane utilization–SAPO-34 catalysis offers the best option, Catal. Today 141 (2009) 77–83.

[8] J. Zaman, Oxidative processes in natural gas conversion, Fuel Proc. Technol. 58 (1999) 61–81.

[9] J.H. Lunsford, Catalytic conversion of methane to more useful chemicals and fuels: a challenge for the 21st century, Catal. Today 63 (2000) 165–174.

[10] J.R.H. Ross, A.N.J. van Keulen, M.E.S. Hegarty, K. Seshan, The catalytic conversion of natural gas to useful products, Catal. Today 30 (1996) 193–199.

[11] M. García-Diéguez, C. Herrera, M. Ángeles Larrubia, L.J. Alemany, CO_2–reforming of natural gas components over a highly stable and selective $NiMg/Al_2O_3$ nanocatalyst, Catal. Today 197 (2012) 50–57.

[12] M.-S. Fan, A.Z. Abdullah, S. Bhatia, Utilization of greenhouse gases through dry reforming: screening of nickel-based bimetallic catalysts and kinetic studies, Chem. Sus. Chem. 4 (2011) 1643–1653.

[13] Y. Kobayashi, J. Horiguchi, S. Kobayashi, Y. Yamazaki, K. Omata, D. Nagao, M. Konno, M. Yamada, Effect of NiO content in mesoporous $NiO–Al_2O_3$ catalysts for high pressure partial oxidation of methane to syngas, Appl. Catal. A: Gen. 395 (2011) 129–137.

[14] J.S. Lisboa, L.E. Terra, P.R.J. Silva, H. Saitovitch, F.B. Passos, Investigation of $Ni/Ce–ZrO_2$ catalysts in the autothermal reforming of methane, Fuel. Proc. Technol. 92 (2011) 2075–2082.

[15] D. Scognamiglio, L. Russo, P.L. Maffettone, L. Salemme, M. Simeone, S. Crescitelli,

Modelling and simulation of a catalytic autothermal methane reformer with Rh catalyst, Int. J. Hydrogen Energy 37 (2012) 263–275.

[16] V. Palma, A. Ricca, P. Ciambelli, Methane auto-thermal reforming on honeycomb and foam structured catalysts: The role of the support on system performances, Catal. Today 216 (2013) 30–37.

[17] G.A. Olah, B. Gupta, J.D. Felberg, W.M. Ip, A. Husain, R. Karpeles, K. Lammertsma, A.K. Melhotra, N.J. Trivedi, Selective monohalogenation of methane over supported acidic or platinum metal catalysts and hydrolysis of methyl halides over γ-alumina-supported metal oxide/hydroxide catalysts. A feasible path for the oxidative conversion of methane into methyl alcohol/dimethyl ether, J. Am. Chem. Soc. 107(24) (1985) 7097–7105.

[18] L.A. Noronha, E.F. Souza-Aguiar, C.J.A Mota, Conversion of chloromethane to light olefins catalyzed by ZSM-5 zeolites, Catal. Today 101 (2005) 9–13.

[19] S. Svelle, S. Aravinthan, M. Bjørgen, K.-P. Lillerud, S. Kolboe, I.M. Dahl, U. Olsbye, The methyl halide to hydrocarbon reaction over H-SAPO-34, J. Catal. 241 (2006) 243–254.

[20] P. Lersch, F. Bandermann, Conversion of chloromethane over metal-exchanged ZSM-5 to higher hydrocarbons, Appl. Catal. 75 (1991) 133–152.

[21] J. He, T. Xu, Z. Wang, Q. Zhang, W. Deng, Y. Wang, Transformation of methane to propylene: A two-step reaction route catalyzed by modified CeO_2 nanocrystals and zeolites, Angew. Chem. Int. Ed. 51 (2012) 2438–2442.

[22] E. McFarland, Unconventional chemistry for unconventional natural gas, Science, 338 (2012) 340–342.

[23] L. Wang, L. Tao, M. Xie, G. Xu, J. Huang, Y. Xu, Dehydrogenation and aromatization of methane under non-oxidizing conditions, Catal. Lett. 21 (1993) 35–41.

[24] P. Biloen, J.N. Helle, W.M.H. Sachtler, Incorporation of surface carbon into hydrocarbons during Fischer-Tropsch synthesis: Mechanistic implications, J. Catal. 58 (1979) 95–107.

[25] R.C. Brady III, R. Pettit, On the mechanism of the Fischer-Tropsch reaction. The chain propagation step, J. Am. Chem. Soc. 103 (1981) 1287–1289.

[26] H. Kölbel, M. Ralek, The Fischer-Tropsch synthesis in the liquid phase, Catal. Rev. Sci. Eng. 21 (1980) 225–274.

[27] M.E. Dry, J.C. Hoogendoorn, Technology of the Fischer-Tropsch process, Catal. Rev. Sci. Eng. 23 (1981) 265–278.

[28] E. Iglesia, Design, synthesis, and use of cobalt-based Fischer-Tropsch synthesis catalysts, Appl. Catal. A: Gen. 161 (1997) 59–78.

[29] A.K. Dalai, B.H. Davis, Fischer–Tropsch synthesis: A review of water effects on the

performances of unsupported and supported Co catalysts, Appl. Catal. A: Gen. 348 (2008) 1–15.

[30] O.O. James, A.M. Mesubi, T.C. Ako, S. Maity, Increasing carbon utilization in Fischer–Tropsch synthesis using H_2-deficient or CO_2-rich syngas feeds, Fuel Proc. Technol. 91 (2010) 136–144.

[31] J.R. Rostrup-Nielsen, Fuels and energy for the future: The role of catalysis, Catal. Rev. Sci. Eng. 46(3–4) (2004) 247–270.

[32] H.M.T. Galvis, K.P. de Jong, Catalysts for production of lower olefins from synthesis gas: A review, ACS Catal. 3 (2013) 2130–2149.

[33] E. Jin, Y. Zhang, L. He, H.G. Harris, B. Teng, M. Fan, Indirect coal to liquid technologies, Appl. Catal. A: Gen. 476 (2014) 158–174.

[34] J. Yang, W. Ma, D. Chen, A. Holmen, B.H. Davis, Fischer–Tropsch synthesis: A review of the effect of CO conversion on methane selectivity, Appl. Catal. A: Gen. 470 (2014) 250–260.

[35] E. Iglesia, S.C. Reyes, R.J. Madon, Transport-enhanced α-olefin readsorption pathways in Ru-catalyzed hydrocarbon synthesis, J. Catal. 129 (1991) 238–256.

[36] R.J. Madon, S.C. Reyes, E. Iglesia, Primary and secondary reaction pathways in ruthenium-catalyzed hydrocarbon synthesis, J. Phys. Chem. 95 (1991) 7795–7804.

[37] S. Bessell, Support effects in cobalt-based Fischer-Tropsch catalysis, Appl. Catal. A: Gen. 96 (1993) 253–268.

[38] V. Udaya., S. Rao, R.J. Gormley, Bifunctional catalysis in syngas conversions, Catal. Today 6 (1990) 207–234.

[39] A. Martínez, J. Rollán, M.A. Arribas, H.S. Cerqueira, A.F. Costa, E.F. S.-Aguiar, A detailed study of the activity and deactivation of zeolites in hybrid Co/SiO_2-zeolite Fischer–Tropsch catalysts, J. Catal. 249 (2007) 162–173.

[40] J. Bao, J. He, Y. Zhang, Y. Yoneyama, N. Tsubaki, A core/shell catalyst produces a spatially confined effect and shape selectivity in a consecutive reaction, Angew. Chem. Int. Ed. 47 (2008) 353–356.

[41] J. He, Y. Yoneyama, B. Xu, N. Nishiyama, N. Tsubaki, Designing a capsule catalyst and its application for direct synthesis of middle isoparaffins, Langmuir 21 (2005) 1699–1702.

[42] J. He, Z. Liu, Y. Yoneyama, N. Nishiyama, N. Tsubaki, Multiple- functional capsule catalysts: A tailor-made confined reaction environment for the direct synthesis of middle isoparaffins from syngas, Chem. A Eur. J. 12 (2006) 8296–8304.

[43] H.M.T. Galvis, A.C.J. Koeken, J.H. Bitter, T. Davidian, M. Ruitenbeek, A.I. Dugulan, K.P. de Jong, Effects of sodium and sulfur on catalytic performance of supported iron

catalysts for the Fischer-Tropsch synthesis of lower olefins, J. Catal. 303 (2013) 22–30.
[44] C.D. Chang, Methanol conversion to light olefins, Catal. Rev.-Sci. Eng. 26 (1984) 323–345.
[45] C.D. Chang, MTG revisited, Stud. Surf. Sci. Catal. 61 (1991) 393–404.
[46] M. Stöcker, Methanol-to-hydrocarbons: Catalytic materials and their behavior, Micropor. Mesopor. Mat. 29 (1999) 3–48.
[47] F.J. Keil, Methanol-to-hydrocarbons: Process technology, Micropor. Mesopor. Mat. 29 (1999) 49–66.
[48] U. Olsbye, S. Svelle, M. Bjørgen, P. Beato, T.V.W. Janssens, F. Joensen, S. Bordiga, K.P. Lillerud, Conversion of methanol to hydrocarbons: How zeolite cavity and pore size controls product selectivity, Angew. Chem. Int. Ed. 51 (2012) 5810–5831.
[49] I.M. Dahl, S. Kolboe, On the reaction mechanism for propene formation in the MTO reaction over SAPO-34, Catal. Lett. 20 (1993) 329–336.
[50] I.M. Dahl, S. Kolboe, On the reaction mechanism for hydrocarbon formation from methanol over SAPO-34: I. Isotopic labeling studies of the co-reaction of ethene and methanol, J. Catal. 149 (1994) 458–464.
[51] M. Bjørgen, S. Svelle, F. Joensen, J. Nerlov, S. Kolboe, F. Bonino, L. Palumbo, S. Bordiga, U. Olsbye, Conversion of methanol to hydrocarbons over zeolite H-ZSM-5: On the origin of the olefinic species, J. Catal. 248 (2007) 195–207.
[52] T. Mole, G. Bett, Conversion of methanol to hydrocarbons over ZSM-5 zeolite: An examination of the role of aromatic hydrocarbons using ^{13}carbon- and deuterium-labeled feeds, J. Catal 84 (1983) 435–445.
[53] Ø. Mikkelsen, P.O. Rønning, S. Kolboe, Use of isotopic labeling for mechanistic studies of the methanol-to-hydrocarbons reaction. Methylation of toluene with methanol over H-ZSM-5, H-mordenite and H-beta, Micropor. Mesopor. Mat. 40 (2000) 95–113.
[54] B. Arstad, S. Kolboe, The reactivity of molecules trapped within the SAPO-34 cavities in the methanol-to-hydrocarbons reaction, J. Am. Chem. Soc. 123 (2001) 8137–8138.
[55] J.F. Haw, J.B. Nicholas, W. Song, F. Deng, Z. Wang, T. Xu, C.S. Heneghan, Roles for cyclopentenyl cations in the synthesis of hydrocarbons from methanol on zeolite catalyst HZSM-5, J. Am. Chem. Soc. 122 (2000) 4763–4775.
[56] J.F. Haw, Zeolite acid strength and reaction mechanisms in catalysis, Phys. Chem. Chem. Phys. 4 (2002) 5431–5441.
[57] R.F. Sullivan, C.J. Egan, G.E. Langlois, R.P. Sieg, A new reaction that occurs in the hydrocracking of certain aromatic hydrocarbons, J. Am. Chem. Soc. 83 (1961) 1156–1160.
[58] A. Sassi, M.A. Wildman, H.J. Ahn, P. Prasad, J.B. Nicholas, J.F. Haw, Methylbenzene

chemistry on zeolite HBeta: Multiple insights into methanol-to-olefin catalysis, J. Phys. Chem. B 106 (2002) 2294–2303.

[59] D. Lesthaeghe, A. Horré, M. Waroquier, G.B. Marin, V. van Speybroeck, Theoretical insights on methylbenzene side-chain growth in ZSM-5 zeolites for methanol-to-olefin conversion, Chem. Eur. J. 15 (2009) 10803–10808.

[60] M. Bjørgen, U. Olsbye, D. Petersen, S. Kolboe, The methanol-to- hydrocarbons reaction: Insight into the reaction mechanism from [^{12}C]benzene and [^{13}C]methanol coreactions over zeolite H-beta, J. Catal. 221 (2004) 1–10.

[61] S. Teketel, U. Olsbye, K.-P. Lillerud, P. Beato, S. Svelle, Selectivity control through fundamental mechanistic insight in the conversion of methanol to hydrocarbons over zeolites, Micropor. Mesopor. Mat. 136 (2010) 33–41 (2010).

[62] W. Song, H. Fu, J.F. Haw, Supramolecular origins of product selectivity for methanol-to-olefin catalysis on HSAPO-34, J. Am. Chem. Soc. 123 (2001) 4749–4754.

[63] X. Sun, S. Mueller, Y. Liu, H. Shi, G.L. Haller, M. Sanchez-Sanchez, A.C. van Veen, J.A. Lercher, On reaction pathways in the conversion of methanol to hydrocarbons on HZSM-5, J. Catal. 317 (2014) 185–197.

[64] W. Song, D.M. Marcus, H. Fu, J.O. Ehresmann, J.F. Haw, An oft-Studied reaction that may never have been: Direct catalytic conversion of methanol or dimethyl ether to hydrocarbons on the solid acids HZSM-5 or HSAPO-34, J. Am. Chem. Soc. 124 (2002) 3844–3845.

[65] J. Sun, G. Yang, Y. Yoneyama, N. Tsubaki, Catalysis chemistry of dimethyl ether synthesis, ACS Catal. 4 (2014) 3346–3356.

[66] W. Zhu, X. Li, H. Kaneko, K. Fujimoto, Selective transformation of dimethyl ether into small molecular hydrocarbons over large-pore beta zeolite, Catal. Lett. 120 (2008) 95–99.

[67] T.-S. Zhao, T. Takemoto, N. Tsubaki, Direct synthesis of propylene and light olefins from dimethyl ether catalyzed by modified H-ZSM-5, Catal. Commun. 7 (2006) 647–650.

[68] G.A. Olah, Towards oil independence through renewable methanol chemistry, Angew. Chem. Int. Ed. 52 (2013) 104–107.

[69] M. Martin, I.E. Grossmann, Optimal use of hybrid feedstock, switchgrass and shale gas for the simultaneous production of hydrogen and liquid fuels, Energy 55 (2013) 378–391.

[70] V.R. Choudhary, V.H. Rane, Acidity/basicity of rare-earth oxides and their catalytic activity in oxidative coupling of methane to C_2–hydrocarbons, J. Catal. 130 (1991) 411–422.

[71] V. Arutyunov, Low-scale direct methane to methanol–Modern status and future prospects, Catal. Today 215 (2013) 243–250.

[72] R.A. Periana, G. Bhalla, W.J. Tenn III, K.J.H. Young, X.Y. Liu, O. Mironov, CJ Jones,

V.R. Ziatdinov, Perspectives on some challenges and approaches for developing the next generation of selective, low temperature, oxidation catalysts for alkane hydroxylation based on the CH activation reaction, J. Mol. Catal. 220 (2004) 7–25.

[73] R. Palkovits, M. Antonietti, P. Kuhn, A. Thomas, F. Schüth, Solid catalysts for the selective low-temperature oxidation of methane to methanol, Angew. Chem. Int. Ed. 48 (2009) 6909–6912.

[74] W. Zhang, D. Ma, X. Han, X. Liu, X. Bao, X. Guo, X. Wang, Methane dehydro-aromatization over Mo/HZSM-5 in the absence of oxygen: A multinuclear solid-state NMR study of the interaction between supported Mo species and HZSM-5 zeolite with different crystal sizes, J. Catal. 188 (1999) 393–402.

[75] P.M. Bijani, M. Sohrabi, S. Sahebdelfar, Thermodynamic analysis of nonoxidative dehydroaromatization of methane, Chem. Eng. Technol. 35(10) (2012) 1825–1832.

[76] Y. Xu, X. Bao, L. Lin, Direct conversion of methane under nonoxidative conditions, J. Catal. 216(1–2) (2003) 386–395.

[77] Z.R. Ismagilov, E.V. Matus, L.T. Tsikoza, Direct conversion of methane on Mo/ZSM-5 catalysts to produce benzene and hydrogen: Achievements and perspectives, Energy Environ. Sci. 1 (2008) 526–541.

[78] J.J. Spivey, G. Hutchings, Catalytic aromatization of methane, Chem. Soc. Rev. 43 (2014) 792–803.

[79] Y. Shu, D. Ma, L. Xu, Y. Xu, X. Bao, Methane dehydro‐aromatization over Mo/MCM‐22 catalysts: A highly selective catalyst for the formation of benzene, Catal. Lett. 70 (2000) 67–73.

[80] S. Liu, L. Wang, R. Ohnishi, M. Ichikawa, Bifunctional catalysis of Mo/HZSM-5 in the dehydroaromatization of methane to benzene and naphthalene XAFS/TG/DTA/MASS/FTIR characterization and supporting effects, J. Catal. 181 (1999) 175–188.

[81] K.S. Wong, J.W. Thybaut, E. Tangstad, M.W. Stöcker, G.B. Marin, Methane aromatisation based upon elementary steps: Kinetic and catalyst descriptors, Micropor. Mesopor. Mat. 164 (2012) 302–312.

[82] P. Mériaudeau, V.T.T. Ha, L.V. Tiep, Methane aromatization over Mo/H-ZSM-5: On the reaction pathway, Catal. Lett. 64 (2000) 49–51.

[83] V.T.T. Ha, L.V. Tiep, P. Meriaudeau, C. Naccache, Aromatization of methane over zeolite supported molybdenum: Active sites and reaction mechanism, J. Mol. Catal. A: Chem. 181 (2002) 283–290.

[84] Y. Kim, R. W Borry III, E. Iglesia, Genesis of methane activation sites in Mo-exchanged H–ZSM-5 catalysts, Micropor. Mesopor. Mat. 35-36 (2000) 495–509.

[85] W. Li, G.D. Meitzner, R. W Borry III, E. Iglesia, Raman and x-ray absorption studies of Mo species in Mo/H-ZSM5 catalysts for non-oxidative CH_4 reactions, J. Catal. 191 (2000) 373–383.

[86] W. Ding, S. Li, G.D. Meitzner, E. Iglesia, Methane conversion to aromatics on Mo/H-ZSM5: Structure of molybdenum species in working catalysts, J. Phys. Chem. B 105 (2001) 506–513.

[87] H.S. Lacheen, E. Iglesia, Stability, structure, and oxidation state of Mo/H-ZSM-5 catalysts during reactions of CH_4 and CH_4–CO_2 mixtures, J. Catal. 230 (2005) 173–185.

[88] D. Wang, J.H. Lunsford, M.P. Rosynek, Characterization of a Mo/ZSM-5 catalyst for the conversion of methane to benzene, J. Catal. 169 (1997) 347–358.

[89] D. Ma, Y. Shu, M. Cheng, Y. Xu, X. Bao, On the induction period of methane aromatization over Mo-based catalysts, J. Catal. 194 (2000) 105–114.

[90] H. Liu, W. Shen, X. Bao, Y. Xu, Methane dehydroaromatization over Mo/HZSM-5 catalysts: The reactivity of MoC_x species formed from MoO_x associated and non-associated with Brönsted acid sites, Appl. Catal. A: Gen. 295 (2005) 79–88.

[91] D. Ma, D. Wang, L. Su, Y. Shu, Y. Xu, X. Bao, Carbonaceous deposition on Mo/HMCM-22 catalysts for methane aromatization: A TP technique investigation, J. Catal. 208 (2002) 260–269.

[92] H. Liu, L. Su, H. Wang, W. Shen, X. Bao, Y. Xu, The chemical nature of carbonaceous deposits and their role in methane dehydro-aromatization on Mo/MCM-22 catalysts, Appl. Catal. A: Gen. 236 (2002) 263–280.

[93] Y. Song, A clue to exploration of the pathway of coke formation on Mo/HZSM-5 catalyst in the non-oxidative methane dehydroaromatization at 1073 K, Appl. Catal. A: Gen. 482 (2014) 387–396.

[94] B. Liu, Y. Yang, A. Sayari, Non-oxidative dehydroaromatization of methane over Ga-promoted Mo/HZSM-5-based catalysts, Appl. Catal. A: Gen. 214 (2001) 95–102.

[95] M.W. Ngobeni, A.F. Carley, M.S. Scurrell, C.P. Nicolaides, The effects of boron and silver on the oxygen-free conversion of methane over Mo/H-ZSM-5 catalysts, J. Mol. Catal. A: Chem. 305 (2009) 40–46.

[96] Y. Xu, J. Wang, Y. Suzuki, Z.-G. Zhang, Effect of transition metal additives on the catalytic stability of Mo/HZSM-5 in the methane dehydro- aromatization under periodic CH_4–H_2 switch operation at 1073 K, Appl. Catal. A: Gen. 409-410 (2011) 181–193.

[97] T.E. Tshabalala, N.J. Coville, M.S. Scurrell, Dehydroaromatization of methane over doped Pt/Mo/H-ZSM-5 zeolite catalysts: The promotional effect of tin, Appl. Catal. A: Gen. 485 (2014) 238–244.

[98] V. Abdelsayed, D. Shekhawat, M.W. Smith, Effect of Fe and Zn promoters on Mo/HZSM-5 catalyst for methane dehydroaromatization, Fuel 139 (2015) 401–410.

[99] Y. Xu, J. Wang, Y. Suzuki, Z.-G. Zhang, Improving effect of Fe additive on the catalytic stability of Mo/HZSM-5 in the methane dehydroaromatization, Catal. Today 185 (2012) 41–46.

[100] W. Ding, G.D. Meitzner, E. Iglesia, The effects of silanation of external acid sites on the structure and catalytic behavior of Mo/H-ZSM5, J. Catal. 206 (2002) 14–22.

[101] H. Liu, Yong Li, W. Shen, X. Bao, Y. Xu, Methane dehydroaromatization over Mo/HZSM-5 catalysts in the absence of oxygen: effects of silanation in HZSM-5 zeolite, Catal. Today 93–95 (2004) 65–73.

[102] L. Su, L. Liu, J. Zhuang, H. Wang, Y. Li, W. Shen, Y. Xu, X. Bao, Creating mesopores in ZSM-5 zeolite by alkali treatment: A new way to enhance the catalytic performance of methane dehydroaromatization on Mo/HZSM-5 catalysts, Catal. Lett. 91 (2003) 155–168.

[103] A. Martínez, E. Peris, M. Derewinski, A. Burkat-Dulak, Improvement of catalyst stability during methane dehydroaromatization (MDA) on Mo/HZSM-5 comprising intracrystalline mesopores, Catal. Today 169 (2011) 75–84.

[104] L. Li, X. Mu, W. Liu, X. Kong, S. Fan, Z. Mi, C.-J. Li, Thermal non-oxidative aromatization of light alkanes catalyzed by gallium nitride, Angew. Chem. Int. Ed. 53(51) (2014) 14106–14109.

[105] G.E. Keller, M.M. Bhasin, Synthesis of ethylene via oxidative coupling of methane: I. Determination of active catalysts, J. Catal. 73 (1982) 9–19.

[106] R. Pitchai, K. Klier, Partial oxidation of methane, Catal. Rev. Sci. Eng. 28 (1986) 13–88.

[107] J.S. Lee, S.T. Oyamat, Oxidative coupling of methane to higher hydrocarbons, Catal. Rev.-Sci. Eng. 30(2) (1988) 249–280.

[108] Y. Amenomiya, V.I. Birss, M. Goledzinowski, J. Galuszka, A.R. Sanger, Conversion of methane by oxidative coupling, Catal. Rev.-Sci. Eng. 32(3) (1990) 163–227.

[109] S. Arndt, T. Otremba, U. Simon, M. Yildiz, H. Schubert, R. Schomäcker, Mn–Na_2WO_4/SiO_2 as catalyst for the oxidative coupling of methane. What is really known?, Appl. Catal. A: Gen. 425 (2012) 53–61.

[110] J.H. Lunsford, The catalytic conversion of methane to higher hydrocarbons, Catal. Today 6(3) (1990) 235–259.

[111] X.P. Fang, S.B. Li, J.Z. Lin, J.F. Gu, D.X. Yang, Oxidative coupling of methane, Mn-Na_2WO_4/SiO_2, dispersion, XRD/XPS/PASCA, J. Mol. Catal. (China) 6 (1992) 255.

[112] J. Wu, S. Li, Role of distorted WO_4 in the oxidative coupling of methane on tungsten

oxide supported catalysts, J. Phys. Chem. 99 (1995) 4566–4568.

[113] S. Pak, P. Qiu, J.H. Lunsford, Elementary reactions in the oxidative coupling of methane over $Mn/Na_2WO_4/SiO_2$ and $Mn/Na_2WO_4/MgO$ catalysts, J. Catal. 179 (1998) 222–230.

[114] U. Simon, O. Görke, A. Berthold, S. Arndt, R. Schomäcker, H. Schubert, Fluidized bed processing of sodium tungsten manganese catalysts for the oxidative coupling of methane, Chem. Eng J. 168 (2011) 1352–1359.

[115] T.P. Tiemersma, M.J. Tuinier, F. Gallucci, J.A.M. Kuipers, M. van S. Annaland, A kinetics study for the oxidative coupling of methane on a $Mn/Na_2WO_4/SiO_2$ catalyst, Appl. Catal. A: Gen. 433 (2012) 96–108.

[116] J.S. Ahari, S. Zarrinpashne, M.T. Sadeghi, Micro-kinetic modeling of OCM reactions over $Mn/Na_2WO_4/SiO_2$ catalyst, Fuel Proc. Technol. 115 (2013) 79–87.

[117] T.W. Elkins, H.E. Hagelin-Weaver, Characterization of $Mn–Na_2WO_4/SiO_2$ and $Mn–Na_2WO_4/MgO$ catalysts for the oxidative coupling of methane, Appl. Catal. A: Gen. 497 (2015) 96–106.

[118] K. Otsuka, K. Jinno, A. Morikawa, Active and selective catalysts for the synthesis of C_2H_4 and C_2H_6 via oxidative coupling of methane, J. Catal. 100(2) (1986) 353–359.

[119] K.D. Campbell, H. Zhang, J.H. Lunsford, Methane activation by the lanthanide oxides, J. Phys. Chem. 92 (1988) 750–753.

[120] A.G. Dedov, A.S. Loktev, I.I. Moiseev, A. Aboukais, J.-F. Lamonier, I.N. Filimonov, Oxidative coupling of methane catalyzed by rare earth oxides: Unexpected synergistic effect of the oxide mixtures, Appl. Catal. A. 245 (2003) 209–220.

[121] Y. Tong, M.P. Rosynek, J.H. Lunsford, Secondary reactions of methyl radicals with lanthanide oxides: Their role in the selective oxidation of methane, J. Phys. Chem. 93 (1989) 2896–2898.

[122] V.R. Choudhary, B.S. Uphade, Oxidative conversion of methane/natural gas into higher hydrocarbons, Catal. Surv. Asia 8 (2004) 15–25.

[123] M.S. Palmer, M. Neurock, M.M. Olken, Periodic density functional theory study of methane activation over La_2O_3: Activity of O^{2-}, O^-, O_2^{2-}, oxygen point defect, and Sr^{2+}–doped surface sites, J. Am. Chem. Soc. 124 (2002) 8452–8461.

[124] V.R. Choudhary, V.H. Rane, R.V. Gadre, Influence of precursors used in preparation of MgO on its surface properties and catalytic activity in oxidative coupling of methane, J. Catal. 145 (1994) 300–311.

[125] F. Papa, D. Gingasu, L. Patron, A. Miyazaki, I. Balint, On the nature of active sites and catalytic activity for OCM reaction of alkaline-earth oxides-neodymia catalytic systems, Appl.

Catal. A: Gen. 375 (2010) 172–178.
[126] V.J. Ferreira, P. Tavares, J.L. Figueiredo, J.L. Faria, Effect of Mg, Ca, and Sr on CeO_2 based catalysts for the oxidative coupling of methane: Investigation on the oxygen species responsible for catalytic performance, Ind. Eng. Chem. Res. 51 (2012) 10535–10541.
[127] T.W. Elkins, H.E. Hagelin-Weaver, Oxidative coupling of methane over unsupported and alumina-supported samaria catalysts, Appl. Catal. A: Gen. 454 (2013) 100–114.
[128] M.S. Palmer, M. Neurock, Periodic density functional theory study of the dissociative adsorption of molecular oxygen over La_2O_3, J. Phys. Chem. B 106 (2002) 6543–6547.
[129] C. Chu, Y. Zhao, S. Li, Y. Sun, Role of peroxides on La_2O_3 catalysts in oxidative coupling of methane, J. Phys. Chem. C 118 (2014) 27954–27960.
[130] J.C.W. Kuo, C.T. Kresge, R.E. Palermo, Evaluation of direct methane conversion to higher hydrocarbons and oxygenates, Catal Today 4 (1989) 463–470.
[131] K. Asami, T. Fujita, K. Kusakabe, Y. Nishiyama, Y. Ohtsuka, Conversion of methane with carbon dioxide into C_2 hydrocarbons over metal oxides, Appl. Catal. A. 126 (1995) 245–255.
[132] K. Asami, K. Kusakabe, N. Ashi, Y. Ohtsuka, Formation of ethane and ethylene by the reaction of methane and carbon dioxide over unsupported metal oxides, Stud. Surf. Sci. Catal. 107 (1997) 279–283.
[133] K. Asami, K. Kusakabe, N. Ashi, Y. Ohtsuka, Synthesis of ethane and ethylene from methane and carbon dioxide over praseodymium oxide catalysts, Appl. Catal. A. 156 (1997) 43–56.
[134] Y. Wang, Y. Takahashi, Y. Ohtsuka, Carbon dioxide as oxidant for the conversion of methane to ethane and ethylene using modified CeO_2 catalysts, J. Catal. 186 (1999) 160–168.
[135] Y. Wang, Y. Takahashi, Y. Ohtsuka, Effective catalysts for conversion of methane to ethane and ethylene using carbon dioxide, Chem. Lett. 27(12) (1998) 1209–1210.
[136] Y. Wang, Y. Ohtsuka, CaO-ZnO catalyst for selective conversion of methane to C_2 hydrocarbons using carbon dioxide as the oxidant, J. Catal. 192 (2000) 252–255.
[137]Y. Wang, Y. Ohtsuka, Mn-based binary oxides as catalysts for the conversion of methane to C_2 hydrocarbons with carbon dioxide as oxidant, Appl. Catal. A. 219 (2001) 183–193.
[138] Y. Cai, L. Chou, S. Li, B. Zhang, J. Zhao, Selective conversion of methane to C_2 hydrocarbons using carbon dioxide over Mn-$SrCO_3$ catalysts, Catal. Lett. 86(4) (2003) 191–195.
[139] C. Chen, Y. Xu, G. Li. X. Guo, Oxidative coupling of methane by carbon dioxide: A highly C_2 selective La_2O_3/ZnO catalyst, Catal. Lett. 42 (1996) 149–153.
[140] L.M. Zhou, B. Xue, U. Kogelschatz, B. Eliasson, Nonequilibrium plasma reforming of

greenhouse gases to synthesis gas, Energ. Fuel. 12 (1998) 1191–1199.
[141] B. Eliasson, C.-J. Liu, U. Kogelschatz, Direct conversion of methane and carbon dioxide to higher hydrocarbons using catalytic dielectric-barrier discharges with zeolites, Ind. Eng. Chem. Res. 39 (2000) 1221–1227.
[142] X. Zhang, B. Dai, A. Zhu, W. Gong, C.-J. Liu, The simultaneous activation of methane and carbon dioxide to C_2 hydrocarbons under pulse corona plasma over La_2O_3/γ-Al_2O_3 catalyst, Catal. Today 72(3-4) (2002) 223–227.
[143] J. Nakamura, T. Uchijima, Catalytic reforming of methane using CO_2, Catalysts and Catalysis 35 (1993) 478–484.
[144] D. Pakhare, C. Shaw, D. Haynes, D. Shekhawat, J. Spivey, Effect of reaction temperature on activity of Pt- and Ru-substituted lanthanum zirconate pyrochlores ($La_2Zr_2O_7$) for dry (CO_2) reforming of methane (DRM), J. CO_2 Util. 1 (2013) 37–42.
[145] D. Pakhare, J. Spivey, A review of dry (CO_2) reforming of methane over noble metal catalysts, Chem. Soc. Rev. 43 (2014) 7813–7837.
[146] S. Wang, G.Q.M. Lu, G.J. Miller, Carbon dioxide reforming of methane to produce synthesis gas over metal-supported catalysts: State of the art, Energy fuels 10 (1996) 896–904.
[147] J. Nakamura, K. Aikawa, K. Sato, T. Uchijima, Role of support in reforming of CH_4 with CO_2 over Rh catalysts, Catal. Lett. 25 (1994) 265–270.
[148] P. Ferreira-Aparicio, A. Guerrero-Ruiz, I. Rodríguez-Ramos, Comparative study at low and medium reaction temperatures of syngas production by methane reforming with carbon dioxide over silica and alumina supported catalysts, Appl. Catal. A: Gen. 170 (1998) 177–187.
[149] J. Kehres, J.G. Jakobsen, J.W. Andreasen, J.B. Wagner, H. Liu, A. Molenbroek, J. Sehested, I. Chorkendorff, T. Vegge, Dynamical properties of a $Ru/MgAl_2O_4$ catalyst during reduction and dry methane reforming, J. Phys. Chem. 116 (2012) 21407–21415.
[150] C. Carrara, J. Múnera, E.A. Lombardo, L.M. Cornaglia, Kinetic and stability studies of Ru/La_2O_3 used in the dry reforming of methane, Top. Catal. 51 (2008) 98–106.
[151] P. Ferreira-Aparicio, C. Márquez-Alvarez, I. Rodríguez-Ramos, Y. Schuurman, A. Guerrero-Ruiz, C. Mirodatos, A transient kinetic study of the carbon dioxide reforming of methane over supported Ru catalysts, J. Catal. 184 (1999) 202–212.
[152] K. Sutthiumporn, S. Kawi, Promotional effect of alkaline earth over $Ni-La_2O_3$ catalyst for CO_2 reforming of CH_4: Role of surface oxygen species on H_2 production and carbon suppression, Int. J. Hydrogen Energy 36 (2011) 14435–14446.
[153] Z. Zhang, X.E. Verykios , S.M. MacDonald , S. Affrossman, Comparative study of carbon dioxide reforming of methane to synthesis gas over Ni/La_2O_3 and conventional

nickel-based catalysts, J. Phys. Chem. 100 (1996) 744–754.
[154] Z. Hou, T. Yashima, Small amounts of Rh-promoted Ni catalysts for methane reforming with CO_2, Catal. Lett. 89 (2003) 193–197
[155] K. Takanabe, K.I. Nagaoka, K. Aika, Improved resistance against coke deposition of titania supported cobalt and nickel bimetallic catalysts for carbon dioxide reforming of methane, Catal. Lett. 102 (2005) 153–157.
[156] B. Pawelec, S. Damyanova, K. Arishtirova, J.L.G. Fierro, L. Petrov, Structural and surface features of PtNi catalysts for reforming of methane with CO_2, Appl. Catal. A: Gen.323 (2007) 188–201.
[157] J. Zhang, H. Wang, A.K. Dalai, Development of stable bimetallic catalysts for carbon dioxide reforming of methane, J. Catal. 249 (2007) 300–310.
[158] B. Steinhauer, M.R. Kasireddy, J. Radnik, A. Martin, Development of Ni-Pd bimetallic catalysts for the utilization of carbon dioxide and methane by dry reforming, Appl. Catal. A: Gen. 366 (2009) 333–341.
[159] D. San-José-Alanso, J. Juan-Juan, M.J. Illán-Gómez, M.C. Román-Martínez, Ni, Co and bimetallic Ni-Co catalysts for the dry reforming of methane, Appl. Catal. A: Gen. 371 (2009) 54–59.
[160] M. García- Diéguez, I.S. Pieta, M.C. Herrera, M.A. Larrubia, L.J. Alemany, Improved Pt-Ni nanocatalysts for dry reforming of methane, Appl. Catal A: Gen. 377 (2010) 191–199.
[161] I. Luisetto, S. Tuti, E.D. Bartolomeo, Co and Ni supported on CeO_2 as selective bimetallic catalyst for dry reforming of methane, Int. J. Hydrogen Energy 37 (2012) 15992–15999.
[162] S. Özkara-Aydınoğlu, A.E. Aksoylu, A comparative study of the kinetics of carbon dioxide reforming of methane over Pt-Ni/Al_2O_3 catalyst: Effect of Pt/Ni ratio, Chem. Eng. J. 215-216 (2013) 542–549.
[163] H. Ay, D. Üner, Dry reforming of methane over CeO_2 supported Ni, Co and Ni-Co catalysts, Appl. Catal. B: Environ. 179 (2015) 128–138.
[164] K. Nagaoka, K. Takanabe, Modification of Co/TiO_2 for dry reforming of methane at 2 MPa by Pt, Ru or Ni, K. Aika, Appl. Catal. A:Gen. 268 (2004) 151–158.
[165] A.C. Luntz, J. Harris, CH_4 dissociation on metals: A quantum dynamics model, Surf. Sci. 258 (1991) 397–426.
[166] J.H. Bitter, K. Seshan, J.A. Lercher, Mono and bifunctional pathways of CO_2/CH_4 reforming over Pt and Rh based catalysts, J. Catal. 176 (1998) 93–101.
[167] P. Ferreira-Aparicio, A. Guerrero-Ruiz, I. Rodríguez-Ramos, Mechanistic aspects of the dry reforming of methane over ruthenium catalysts, Appl. Catal. A: Gen. 202 (2000) 183–196.

[168] J.C.S Wu, H.C. Chou, Bimetallic Rh-Ni/BN catalyst for methane reforming with CO_2, Chem. Eng. J. 148 (2009) 539–545.
[169] S.R. de Miguel, I.M.J. Vilella, S.P. Maina, D.S. Jose-Alonso, M.C. Roman-Martinez, M.J. Illan-Gomez, Influence of Pt addition to Ni catalysts on the catalytic performance for long term dry reforming of methane, Appl. Catal. A: Gen. 435 (2012) 10–18.
[170] G.K. Reddy, S. Loridant, A. Takahashi, P. Delichere, B.M. Reddy, Reforming of methane with carbon dioxide over $Pt/ZrO_2/SiO_2$ catalysts – Effect of zirconia to silica ratio, Appl. Catal. A: Gen. 389 (2010) 92–100.
[171] S.M. Stagg-Williams, F.B. Noronha, G. Fendley, D.E. Resasco, CO_2 reforming of CH_4 over Pt/ZrO_2 catalysts promoted with La and Ce oxides, J. Catal 194 (2000) 240–249.
[172] A. Sacco Jr., F.W.A.H. Geurts, G.A. Jablonski, S. Lee, R.A. Gately, Carbon deposition and filament growth on Fe, Co, and Ni foils using $CH_4 \cdot H_2 \cdot H_2O \cdot CO \cdot CO_2$ gas mixtures, J. Catal. 119 (1989) 322–341.
[173] C.H. Bartholomew, Carbon deposition in steam reforming and methanation, Catal. Rev. Sci. Eng. 24(1) 1982 67–112.
[174] A.M. Gadalla, B. Bower, The role of catalyst support on the activity of nickel for reforming methane with CO_2, Chem. Eng. Sci. 43 (1988) 3049–3062.
[175] N.M. Rodriguez, A review of catalytically grown carbon nanofibers, J. Mater. Res. 8 (1993) 3233–3250.
[176] G. Blyholder, A theoretical study of the site of CO dissociation on Fe(100), M. Lawless, Surf. Sci. 290(1–2) (1993) 155–162.
[177] F. Zaera, E. Kollin, J.L. Gland, Observation of an unusually low CO stretching frequency: CO chemisorption on a Mo(100) surface, Chem. Phys. Lett. 121 (1985) 464–468.
[178] S. Johnson, R.J. Madix, Desorption of hydrogen and carbon monoxide from Ni(100), Ni(100)p(2×2)S, and Ni(100)c(2×2)S surfaces, Surf. Sci. 108 (1981) 77–98.
[179] X. Yin-Sheng, H. Xiao-Le, EHMO calculations for CO dissociation on supported metal catalysts, J. Mol. Catal. 33 (1985) 179–188.
[180] E.O.F. Zdansky, A. Nilsson, N. Mårtensson, CO-induced reversible surface to bulk transformation of carbidic carbon on Ni(100), Surf. Sci. 310 (1994) L583–L588.
[181] M.T. Tavares, I. Alstrup, C.A. Berriardo, J.R. Rostrup-Nielsen, CO disproportionation on silica-supported nickel and nickel-copper catalysts, J. Catal. 147 (1994) 525–534.
[182] V.V. Chesnokov, V.I. Zaikovskii, R.A. Buyanov, V.V. Molchanov, L.M. Plyasova, Morphology of carbon from methane on nickel-containing catalysts, Catal. Today 24 (1995) 265–267.
[183] H.M. Swaan, V.C.H. Kroll, G.A. Martin, C. Mirodatos, Deactivation of supported nickel

catalysts during the reforming of methane by carbon dioxide, Catal. Today 21 (1994) 571–578.

[184] V.A. Tsipouriari, A.M. Efstathiou, Z.L. Zhang, X.E. Verykios, Reforming of methane with carbon dioxide to synthesis gas over supported Rh catalysts, Catal. Today 21 (1994) 579–587.

[185] M.C.J. Bradford, M.A. Vannice, CO_2 reforming of CH_4, Catal. Rev. Sci. Eng. 41(1) (1999) 1–42.

[186] F. Solymosi, Gy. Kustán, A. Erdöhelyi, Catalytic reaction of CH_4 with CO_2 over alumina-supported Pt metals, Catal. Lett. 11 (1991) 149–156.

[187] J.R. Rostrup-Nielsen, J.-H. Bak Hansen, CO_2-reforming of methane over transition metals, J. Catal 144 (1993) 38–49.

[188] Z. Zhang, X.E. Verykios, Carbon dioxide reforming of methane to synthesis gas over supported Ni catalysts, Catal. Today 21 (1994) 589–595.

[189] A. Guerrero-Ruiz, A. Sepúlveda-Escribano, I. Rodríguez-Ramos, Cooperative action of cobalt and MgO for the catalyzed reforming of CH_4 with CO_2, Catal. Today 21 (1994) 545–550.

[190] M.C.J. Bradford, M.A. Vannice, Catalytic reforming of methane with carbon dioxide over nickel catalysts II. Reaction kinetics, Appl. Catal. A: Gen. 142 (1996) 97–112.

[191] M.C.J. Bradford, M.A. Vannice, Metal-support interactions during the CO_2 reforming of CH_4 over model TiO_x/Pt catalysts, Catal. Lett. 48 (1997) 31–38.

[192] M.C.J. Bradford, M.A. Vannice, CO_2 reforming of CH_4 over supported Pt catalysts, J. Catal. 173 (1998) 157–171.

[193] T.P. Beebe Jr., D.W. Goodman, B.D. Kay, J.T. Yates, Kinetics of the activated dissociative adsorption of methane on the low index planes of nickel single crystal surfaces, J. Chem. Phys. 87 (1987) 2305–2315.

[194] J.H. Bitter, K. Seshan, J.A. Lercher, On the contribution of X-ray absorption spectroscopy to explore structure and activity relations of Pt/ZrO_2 catalysts for CO_2/CH_4 reforming, Top. Catal. 10 (2000) 295–305.

[195] Y. Schuurman, V.C.H. Kroll, P. Ferreira-Aparicio, C. Mirodatos, Use of transient kinetics techniques for studying the methane reforming by carbon dioxide, Catal. Today 38 (1997) 129–135.

[196] W.K. Lewis, E.R. Grilliland, W.A. Reed, Reaction of methane with copper oxide in a fluidized bed, Ind. Eng. Chem. 41 (1949) 1227–1237.

[197] D.B. Clarke, I. Suzuki, A.T. Bell, An infrared study of the interactions of CO and CO_2 with Cu/SiO_2, J. Catal. 142 (1993) 27–36.

[198] J.T. Richardson, S.A. Paripatyadar, Carbon dioxide reforming of methane with supported rhodium, Appl. Catal. 61 (1990) 293–309.

[199] M.F. Mark, W.F. Maier, CO_2–reforming of methane on supported Rh and Ir catalysts, J. Catal. 164 (1996) 122–130.

[200] T. Horiuchi, K. Sakuma, T. Fukui, Y. Kubo, T. Osaki, T. Mori, Suppression of carbon deposition in the CO_2–reforming of CH_4 by adding basic metal oxides to a Ni/Al_2O_3 catalyst, Appl. Catal. A: Gen. 144 (1996) 111–120.

[201] X.E. Verykios, Catalytic dry reforming of natural gas for the production of chemicals and hydrogen, Int. J. Hydrogen Energy 28 (2003) 1045–1063.

[202] M.M.B. Quiroga, A.E.C. Luna, Kinetic analysis of rate data for dry reforming of methane, Ind. Eng. Chem. Res. 46 (2007) 5265–5270.

[203] A. Erdöhelyi, J. Cserényi, E. Papp, F. Solymosi, Catalytic reaction of methane with carbon dioxide over supported palladium, Appl. Catal. A. 108 (1994) 205–219.

[204] P. Capezzuto, F. Cramarossa, R. D'Agostino, E. Molinari, Contribution of vibrational excitation to the rate of carbon dioxide dissociation in electrical discharges. J. Phys. Chem. 80(8) (1976) 882–888.

[205] A. Czernichowski, Electrically assisted conversion of carbon dioxide into synthesis gas, Green Gas Control Technol. (1999) 385–443.

[206] W.L. Morgan, A critical evaluation of low–energy electron impact cross sections for plasma processing modeling. II: Cl_4, SiH_4 and CH_4, Plasma Chem. Plasma Process. 12 (1992) 477–493.

[207] J.W. McConkey, C.P. Malone, P.V. Johnson, C. Winstead, V. McKoy, I. Kanik, Electron impact dissociation of oxygen-containing molecules–A critical review, Phy. Rep. 466 (2008) 1–103.

[208] R.S. Freund, Dissociation of CO_2 by electron impact with the formation of metastable CO(a $^3\Pi$) and O(^{5}S), J. Chem. Phys. 55 (1971) 3569–3577.

[209] L.R. LeClair, J.W. McConkey, On O(^{1}S) and CO(a $^3\Pi$) production from electron impact dissociation of CO_2, J. Phys. B 27 (1994) 4039–4055.

[210] H. Nakatsuji, Cluster expansion of the wavefunction, valence and rydberg excitations, ionizations, and inner-valence ionizations of CO_2 and N_2O studied by the sac and sac CI theories, Chem. Phys. 75 (1983) 425–441.

[211] Y. Yang, Methane conversion and reforming by nonthermal plasma on pins, Ind. Eng. Chem. Res. 41(24) (2002) 5918–5926.

[212] M. Li, G. Xu, Y. Tian, L. Chen, H. Fu, Carbon dioxide reforming of methane using DC corona discharge plasma reaction, J. Phys. Chem. A 108 (2004) 1687–1693.

[213] U. Kogelschatz, Dielectric-barrier discharges: Their history, discharge physics, and industrial applications, Plasma Chem. Plasma Proc. 23(1) (2003) 1–46.
[214] J.-J. Zou, Y.-P. Zhang, C.-J. Liu, Y. Li, B. Eliasson, Starch-enhanced synthesis of oxygenates from methane and carbon dioxide using dielectric-barrier discharges, Plasma Chem. Plasma Proc. 23(1) (2003) 69–82.
[215] Q. Wang, B.-H. Yan, Y. Jin, Y. Cheng, Dry reforming of methane in a dielectric barrier discharge reactor with Ni/Al_2O_3 catalyst: Interaction of catalyst and plasma, Energy Fuels, 23(8) (2009) 4196–4201.
[216] D. Li, X. Li, M. Bai, X. Tao, S. Shang, X. Dai, Y. Yin, CO_2 reforming of CH_4 by atmospheric pressure glow discharge plasma: A high conversion ability, Int. J. Hydrogen Energy 34 (2009) 308–313.
[217] X. Tao, M. Bai, X. Li, H. Long, S. Shang, Y. Yin, X. Dai, CH_4–CO_2 reforming by plasma – challenges and opportunities, Prog. Energ. Combust. Sci. 37 (2011) 113–124.
[218] W.-C. Chung, M.-B. Chang, Review of catalysis and plasma performance on dry reforming of CH_4 and possible synergistic effects, Renew. Sust. Energ. Rev. 62 (2016) 13–31.
[219] Z. Bo, J. Yan, X. Li, Y. Chi, K. Cen, Plasma assisted dry methane reforming using gliding arc gas discharge: Effect of feed gases proportion, Int. J. Hydrogen Energy 33 (2008) 5545–5553.
[220] X. Tu, J.C. Whitehead, Plasma dry reforming of methane in an atmospheric pressure AC gliding arc discharge: Co-generation of syngas and carbon nanomaterials, Int. J. Hydrogen Energy 39 (2014) 9658–9669.
[221] X.-S. Li, B. Zhu, C. Shi, Y. Xu, A.-M. Zhu, Carbon dioxide reforming of methane in kilohertz spark-discharge plasma at atmospheric pressure, AlChE J. 57 (2011) 2854–2860.
[222] B. Zhu, X.-S. Li, C. Shi, J.-L. Liu, T.-L. Zhao, A.-M. Zhu, Pressurization effect on dry reforming of biogas in kilohertz spark-discharge plasma, Int. J. Hydrogen Energy 37 (2012) 4945–4954.
[223] C.-J. Liu, G.P. Vissokov, B.W.-L. Jang, Catalyst preparation using plasma technologies, Catal. Today 72(3–4) (2002) 173–184.
[224] Y.-W. Wu, W.-C. Chung, M.-B. Chang, Modification of Ni/γ-Al2O3 catalyst with plasma for steam reforming of ethanol to generate hydrogen Int. J. Hydrogen Energy 40 (2015) 8071–8080.
[225] X. Zhu, P. Huo, Y.-P. Zhang, D.-G. Cheng, C.-J. Liu, Structure and reactivity of plasma treated Ni/Al_2O_3 catalyst for CO_2 reforming of methane, Appl. Catal. B: Environ. 81 (2008) 132–140.
[226] M. Zhang, X. Zhu, X. Liang, Z. Wang, Preparation of highly efficient Au/C catalysts for

glucose oxidation via novel plasma reduction, Catal. Commun. 25 (2012) 92–95.
[227] X. Tu, H.J. Gallon, J.C. Whitehead, Plasma-assisted reduction of a NiO/Al_2O_3 catalyst in atmospheric pressure H_2/Ar dielectric barrier discharge, Catal. Today 211 (2013) 120–125.
[228] H.S. Kim, C.H. Lee, C.E. Lee, Y.H. Jeong, N.H. Hur, Charge transport in oxygen-plasma-treated $La_{0.7}Ca_{0.3}MnO_{3-\delta}$, Solid State Commun. 127 (2003) 609–612.
[229] S. Shang, G. Liu, X. Chai, X. Tao, X. Li, M. Bai, W. Chu, X. Dai, Y. Zhao, Y. Yin, Research on Ni/γ-Al_2O_3 catalyst for CO_2 reforming of CH_4 prepared by atmospheric pressure glow discharge plasma jet, Catal. Today 148 (2009) 268–274.
[230] X. Tang, F. Gao, Y. Xiang, H. Yi, , S. Zhao, Low temperature catalytic oxidation of nitric oxide over the Mn–CoO_x catalyst modified by nonthermal plasma, Catal. Commun. 64 (2015) 12–17.
[231] Y. Sekine, M. Haraguchi, M. Tomioka, M. Matsukata, E. Kikuchi, Low-temperature hydrogen production by highly efficient catalytic system assisted by an electric field, J. Phys. Chem. A 114 (2010) 3824–3833.
[232] M. Stoukides, C.G. Vayenas, The effect of electrochemical oxygen pumping on the rate and selectivity of ethylene oxidation on polycrystalline silver, J. Catal. 70 (1981) 137–146.
[233] I.V. Yentekakis, Y. Jiang, S. Neophytides, S. Bebelis, C.G. Vayenas, Catalysis, electrocatalysis and electrochemical promotion of the steam reforming of methane over Ni film and Ni-YSZ cermet anodes, Ionics 1 (1995) 491–498.
[234] C. Kokkofitis, M. Ouzounidou, A. Skodra, M. Stoukides, Catalytic and electrocatalytic production of H_2 from the water gas shift reaction over Pd in a high temperature proton-conducting cell-reactor, Solid State Ionics 178 (2007) 475–480.
[235] C.G. Vayenas, S. Bebelis, S. Ladas, Dependence of catalytic rates on catalyst work function, Nature 343 (1990) 625–627.
[236] C. G. Vayenas, S. Bebelis, S. Neophytides, Non-faradaic electro- chemical modification of catalytic activity, J. Phys. Chem. 92 (1988) 5083–5085.
[237] Y. Sekine, M. Haraguchi, M. Matsukata, E. Kikuchi, Low temperature steam reforming of methane over metal catalyst supported on $Ce_xZr_{1-x}O_2$ in an electric field, Catal. Today 171 (2011) 116–125.
[238] K. Oshima, T. Shinagawa, M. Haraguchi, Y. Sekine, Low temperature hydrogen production by catalytic steam reforming of methane in an electric field, Int. J. Hydrogen Energy 38 (2013) 3003–3011.
[239] K. Oshima, T. Shinagawa, Y. Sekine, Methane conversion assisted by plasma or electric field, J. Jpn. Petrol. Inst. 56(1) (2013) 11–21.
[240] J.R. Rostrup-Nielsen, Activity of nickel catalysts for steam reforming of hydrocarbons,

J. Catal. 31 (1973) 173–199.
[241] J.R. Rostrup-Nielsen, Sulfur-passivated nickel catalysts for carbon-free steam reforming of methane, J. Catal. 85 (1984) 31–43.
[242] S.A. Bernardo, I. Alstrup, J.R. Rostrup-Nielsen, Carbon deposition and methane steam reforming on silica-supported Ni・Cu catalysts, J. Catal. 96 (1985) 517–534.
[243] J. Wei, E. Iglesia, Mechanism and site requirements for activation and chemical conversion of methane on supported Pt clusters and turnover rate comparisons among noble metals, J. Phys. Chem. B 108 (2004) 4094–4103.
[244] S. Sakurai, S. Ogo, Y. Sekine, Hydrogen production by steam reforming of ethanol over Pt/CeO_2 catalyst in electric field at low temperature, J. Jpn. Petrol. Inst. 59(5), 174–183, 2016.
[245] T. Sekine, M. Tomioka, M. Matsukata, E. Kikuchi, Catalytic degradation of ethanol in an electric field, Catal. Today 146 (2009) 183–187.
[246] K. Tanaka, Y. Sekine, K. Oshima, Y. Tanaka, M. Matsukata, E. Kikuchi, Catalytic oxidative coupling of methane assisted by electric power over a semiconductor catalyst, Chem. Lett. 41 (2012) 351–353.
[247] K. Oshima, K. Tanaka, T. Yabe, Y. Tanaka, Y. Sekine, Catalytic oxidative coupling of methane with a dark current in an electric field at low external temperature, Int. J. Plasma Environ. Sci. Technol. 6(3) (2012) 266–271.
[248] K. Oshima, K. Tanaka, T. Yabe, E. Kikuchi, Y. Sekine, Oxidative coupling of methane using carbon dioxide in an electric field over $La\text{-}ZrO_2$ catalyst at low external temperature, Fuel 107 (2013) 879–881.

Chapter 2 Low-temperature oxidative coupling of methane in an electric field using carbon dioxide as an oxidizing agent over Ca-doped $LaAlO_3$ perovskite oxide catalysts

2.1 Introduction

Considering safe and reliable energy supplies for the future, natural gas conversion technologies converting methane to value-added products have been the subject of intensive academic and industrial research, especially for the development of direct conversion methods. Methane, the main component of natural gas (and also shale gas), can be converted to C_2 hydrocarbons by coupling of methane. The most important starting material of petrochemicals, ethylene, can be synthesized by coupling. Nevertheless, direct and selective synthesis from methane is extremely difficult to accomplish in an economically feasible manner because methane has a stable tetrahedral structure.

Oxidative coupling of methane (OCM) to C_2 products (ethane and ethylene) is a promising direct methane conversion technology that has been investigated extensively during the last three decades [1–13]. The OCM reaction formula is shown below.

$$CH_4 + \frac{1}{2}O_2 \rightarrow \frac{1}{2}C_2H_4 + H_2O \qquad \Delta H^0_{298} = -140.4\ \text{kJ·mol}^{-1} \qquad \text{(eq. 1)}$$

Although OCM is an exothermic reaction, it requires temperatures higher than 900 K because of the high dissociation energy of CH_3-H. In such high-temperature conditions, C_2 products that are more reactive than methane will be consumed non-selectively by sequential oxidation by oxygen in the gas phase. Therefore, achieving high OCM yield is difficult. To prevent the sequential reaction of C_2 products in the gas phase, OCM reaction with carbon dioxide as an oxidant (CO_2-OCM) has been proposed [14–20]. The reaction formula of CO_2-OCM is the following:

$$CH_4 + CO_2 \rightarrow \frac{1}{2}C_2H_4 + CO + H_2O \qquad \Delta H^0_{298} = 142.1\ \text{kJ·mol}^{-1} \qquad \text{(eq. 2)}$$

Asami *et al.* repeated the CO_2-OCM reaction over various oxide catalysts [14]. Higher CO_2-OCM activity was obtained over rare earth metal oxide catalysts. Especially on Pr and Tb oxide catalysts, C_2 yield of 1.5% and C_2 selectivity of 50% were reported. Wang *et al.*

conducted CO_2-OCM over various catalysts, especially on CaO-CrO_x [17], CaO-CeO_2 [18], and CaO-ZnO [19].

To achieve higher methane conversion at low temperatures, non-conventional catalytic systems have also been reported, including catalytic reactions in an electric field [21–29], catalytic reactions with discharge [30–36], and non-Faradaic electrochemical modification of catalytic activity (NEMCA) [37–41]. Among them, the catalytic reaction in the electric field has two characteristic features: high catalytic activity at low temperatures (even at 423 K of external temperature) can be accomplished in the electric field. Moreover, the operation condition is milder than other electrical processes such as discharge. Furthermore, the selectivity to products on the catalytic reaction in the electric field is determined by the catalyst characteristics.

Therefore, we investigated catalytic activity of methane in an electric field at low temperatures to obtain C_2 hydrocarbon by CO_2-OCM. In this work, $La_{0.7}Ca_{0.3}AlO_{3-\delta}$ (LCAO) catalyst, in which the A site of $LaAlO_3$ perovskite oxide was partially substituted with Ca, indicated the highest C_2 yield among various oxide catalysts. We investigated the effects of the electric field on methane activation, comparing them with the conventional catalytic reactions. The effects of different doping amounts of Ca in $LaAlO_3$ on the catalytic activity were investigated, along with the relation between OCM activity, effects of electric factors on the catalytic activity in the electric field, and the catalytic reaction mechanism of CO_2-OCM in the electric field over LCAO catalyst.

From the results of screening tests, $La_{0.7}Ca_{0.3}AlO_{3-\delta}$ catalyst showed high CO_2-OCM activity. The highest CO_2-OCM activity, C_2 yield of 7.4%, was obtained even at 348 K, that value was higher than those of other earlier reports. Dry reforming of methane to produce syngas (H_2+CO) proceeded simultaneously. No other byproduct was observed. Results of *in-situ* IR, XRD and TG measurements demonstrated that CO_2 adsorption on the catalyst surface and formation of $La_2O_2CO_3$ intermediate are important for progress of the CO_2-OCM reaction, even at low temperature in an electric field. Ca atom incorporated in $LaAlO_3$ perovskite played an important role in C_2 hydrocarbon formation.

2.2 Experimental

2.2.1 Synthesis of various metal-doped $LaAlO_3$ catalysts

Various oxide catalysts including $LaAlO_3$, $La_{0.7}M_{0.3}AlO_{3-\delta}$ (M=Mg, Ca, Sr, Ba), $LaAl_{0.7}M'_{0.3}AlO_{3-\delta}$ (M'=Ti, Cr, Mn, Fe, Co), and $La_{1-x}Ca_xAlO_{3-\delta}$ (X=0.1–0.5) were prepared

using a complex polymerized method. The obtained powder was calcined at 1123 K for 10 h in air flow. Various *y*-wt%Ca/LCAO (*y*=0, 1, 2) catalysts were prepared by an impregnation method on LCAO using aqueous solution of Ca nitrate.

2.2.2 Reaction conditions for activity tests and changing the Ca amount in $LaAlO_3$

Catalytic activity tests were performed in the electric field using a quartz tube (6 mm o.d.) reactor [24]. The charged amount of catalyst was 200 mg. The reaction temperature was maintained at 423 K using an external furnace. To measure the catalyst bed temperature, a thermocouple was attached to the lower edge of the catalyst bed. The flow rate of raw gas was set up as CH_4:CO_2:Ar = 25:25:50, total flow rate 100 mL min^{-1} insofar as there is no particular remark stating otherwise. In the test for comparison between conventional catalytic reactions and CO_2-OCM in the electric field, the temperature was changed from 1173 K to 1348 K for conventional reactions, and from 423 K to 633 K for CO_2-OCM in the electric field. For the test conducted with different amounts of doped Ca in $LaAlO_3$, the field intensity, which was expressed as applied voltage per catalyst bed height, was fixed to 94 V mm^{-1} to make the reaction condition uniform. Because, when catalysts were filled as the same weight, the catalyst bed height and applied voltage differed depending on the substitution amount of Ca in the $LaAlO_3$. The imposed current was fixed at 3 mA or 5 mA. The applied voltage was 1.2–2.5 kV. To assess the effect of changing the imposed current, the current was fixed at 2–9 mA, and applied voltage changed based on the reaction conditions, as described previously.

2.2.3 Evaluation for electrical factors on CO_2-OCM in the electric field

To reveal electrical factors such as imposed current on CO_2-OCM in the electric field, we conducted activity tests by changing imposed currents, measured applied voltage, and calculated imposed power. In the test for changing amounts of supported Ca on LCAO, imposed current was fixed to 3 mA. The other conditions were the same as those described in section 2.2.

2.2.4 Elucidation of reaction mechanisms in CO_2-OCM in the electric field

To reveal the reaction mechanism in CO_2-OCM in the electric field, catalytic activity tests were conducted by changing the CH_4 and CO_2 partial pressures (P_{CH4} and P_{CO2}), and the contact times (W/F_{CH4}). During these tests, the imposed current was fixed to 3 mA. Other

conditions were the same as those described in section 2.2. In the tests for changing CH_4 partial pressure (P_{CH4}) in CO_2-OCM in the electric field, P_{CH4} was changed from 0.06 atm to 0.35 atm, and the CO_2 partial pressure (P_{CO2}) was fixed to 0.25 atm. In tests for changing P_{CO2} in CO_2-OCM in the electric field, P_{CO2} was changed from 0.17 atm to 0.44 atm and P_{CH4} was fixed to 0.25 atm. In the case of P_{CO2} = 0.06 atm, the electric field was not applicable. Reaction orders for CO_2-OCM in the electric field were calculated based on the formation rates per unit of imposed power. In tests for changing contact times (W/F_{CH4}) for CO_2-OCM in the electric field over LCAO, the gas composition was fixed to CH_4:CO_2:Ar = 1:1:2, and total gas flow rate was changed while the charged catalyst amount was fixed.

2.2.5 Analyses of product gases and characterization techniques

After products were dried in a cold trap, they were analyzed using a GC-FID (GC-2014; Shimadzu Corp.) with a Porapak N-packed column after methanation by Ru/Al_2O_3 catalyst for analyses of CO, CH_4, and CO_2, C_{2+}hydrocarbons, and by a GC-TCD (GC-2014; Shimadzu Corp.) with a molecular sieve 5A packed column for analyses of H_2 and CH_4. The electric field was applied on the catalyst using a DC high-voltage power supply. The field was controlled by an imposed current. The impressed voltage depended on the electric characteristics of the catalyst and the dielectric properties of the supplied gas.
Conversion and selectivity were calculated using eqs. 3–6 shown below.

$$CH_4 \text{ conv.} = \Sigma (F_{CO*} + F_{C2H4} + F_{C2H6}) / S_{CH4} \times 100 \quad \text{(eq. 3)}$$

$$CO_2 \text{ conv.} = (F_{CO} - F_{CO*}) / S_{CO2} \times 100 \quad \text{(eq. 4)}$$

$$X \text{ yield} = \text{formation rate of } X / S_{CH4} \times 100 \quad \text{(eq. 5)}$$

$$\text{OCM sel.} = \Sigma (F_{C2H4} + F_{C2H6}) / \Sigma (F_{CO*} + F_{C2H4} + F_{C2H6} + F_{C2H2}) \quad \text{(eq. 6)}$$

In these equations, F denotes the product formation rate, S denotes the supply rate of the reactant, and "CO*" denotes the produced amount of CO derived from CH_4. The formation rate of "CO*" was calculated based on a method reported by Asami *et al.* [14] as presented below.

$$F_{CO*} = (F_{H2} + F_{CO} - F_{C2H6} - 2 \times F_{C2H4}) / 4 \quad \text{(eq. 7)}$$

For calculation of the formation rate of CO from CO_2 (denoted as $F_{CO \text{ from } CO2}$) and H_2O (r_{H2O}), eqs. 8 and 9 are used.

$$F_{CO\ from\ CO2} = F_{CO\ total} - F_{CO*} \quad \text{(eq. 8)}$$

$$F_{H2O} = (F_{C2H6} + 2*F_{C2H4} - F_{H2} + F_{CO}) / 2 \quad \text{(eq. 9)}$$

X-ray diffractometry (SmartLab III; Rigaku Corp.) was used to ascertain the catalyst crystallinity. Anode voltage and anode current values were set, respectively, to 40 kV and 40 mA. Diffractograms were taken at 2θ angles for 10–90° with steps of 0.01°. All diffraction patterns were indexed using SmartLab Studio II. Most catalysts were identified as having a perovskite structure. Impurity phases were found in $La_{0.7}Ca_{0.3}AlO_{3-\delta}$, $La_{0.7}Sr_{0.3}AlO_{3-\delta}$, $La_{0.7}Ba_{0.3}AlO_{3-\delta}$, $La_{0.6}Ca_{0.4}AlO_{3-\delta}$, and $La_{0.5}Ca_{0.5}AlO_{3-\delta}$. These phases were assigned as a melilite structure.

The amount of carbon deposited on the catalyst after the reaction was measured using temperature programmed oxidation (TPO) in 10% O_2/N_2 with the total flow rate of 100 mL min^{-1}, using an infrared gas analyzer (CGT-700; Shimadzu Corp.). For all experiments, the amount of deposited carbon was negligibly small: less than 10 mg g_{-cat}^{-1}.

The BET specific surface area of catalysts was measured (Gemini VII 2390; Shimadzu Corp.). Before carrying out measurements, each sample was purged using He gas at 573 K for 1 hr. The specific surface areas of the samples were calculated following the multi-point Brunauer–Emmett–Teller (BET) procedure.

To compare the characteristics of CO_2 desorption between Ca doped-$LaAlO_3$ and Ca supported-$LaAlO_3$, thermogravimetry (TG) was conducted using an infrared gas analyzer (CGT-700; Shimadzu Corp.). Before carrying out the measurement, each sample was heated in Ar gas to 1073 K with rising temperature by 30 K min^{-1}. Then each was cooled to room temperature. Subsequently, CO_2 was adsorbed on each sample by CO_2 in CO_2:Ar = 10:90, the total flow rate 100 mL min^{-1} at room temperature for 1 hr: and the CO_2 desorption behavior was measured in Ar gas, rising temperature to 1073 K with the ramping rate of 10 K min^{-1}. In addition, background measurements were conducted using Ar gas in the manner described above.

To elucidate the adsorbed species on CO_2 adsorption over LCAO catalysts, DRIFTS measurements were conducted using FT-IR (FT-IR/6100; Jasco Corp.) with an MCT detector and a diffuse reflectance infrared Fourier transform spectroscopy reactor cell (DR-600Ai; Jasco Corp.) with ZnSe windows for 20 times with resolution of 4 cm^{-1}. To remove impurities from the surface of LCAO catalyst before carrying out measurements, the sample was heated in Ar gas, the flow rate was 50 mL min^{-1} at 773 K for 30 min. After cooling to 423 K, the background spectra were measured. Subsequently, CO_2 was adsorbed on the sample in

CO_2:Ar = 5:45, overall flow rate of 50 mL min^{-1} at 423 K for 30 min and the spectra were measured in Ar gas at 423 K after Ar purge. The sample was heated to 473 K, with the temperature retained for 10 min. In addition, the spectra were measured at 423, 523, 573, and 623 K. To elucidate the adsorbed species on catalysts with and without an electric field, *in-situ* DRIFTS measurements were conducted using the same FT-IR apparatus with a DRIFTS cell made of Teflon and MACOR® for catalytic reaction in an electric field. LCAO oxide was used for the catalyst sample, and it was molded as a disk with 7 mm outer diameter. To remove impurities from the LCAO catalyst surface, the sample was heated in Ar gas, the flow rate was 50 mL min^{-1}, at 673 K for 30 min and was cooled to 523 K (same as the reaction condition). Then the background spectra were measured. Subsequently, spectra were measured at 523 K in CH_4:CO_2 = 1:1, with the total flow rate of 50 mL min^{-1} before reaction and in the electric field. The imposed current was fixed to 10 mA in this case. In addition, to elucidate the effect of partial pressure of CO_2, the flow rate was changed in only CH_4 with the total flow rate of 50 mL min^{-1}.

2.3 Results and discussion

2.3.1 Screening of suitable catalysts for methane conversion in an electric field

First, to discover suitable catalysts for methane conversion by CO_2-OCM in an electric field, various rare earth oxides, alkali earth metal oxides, transition metal oxides (TiO_2, Nb_2O_3, HfO_2, Ta_2O_5, and WO_3), and perovskite oxides were investigated to assess their catalytic activities. These oxides have been reported previously as good candidates for methane conversion. Perovskite oxides, expressed as ABO_3, can be designed as various structures when tolerance factor *t* and the electrical neutrality condition are satisfied. As perovskite oxides, we selected La as the A site element because La-containing oxide showed high OCM activity in the electric field in our earlier studies [24, 25]. Additionally, we selected Cr, Mn, Fe, Co, Ni, Al, Ga, and In as B sites of perovskite oxide. Results show that most of these catalysts exhibited formation of a spark discharge because of their low electric conductivities, or caused formation of a short circuit because of their high electric conductivities. We have reported already that suitable electric conductivity of the catalyst (10^{-6}-10^{-3} Ω m^{-1}) is necessary for application of the electric field to the catalyst bed [24]. Over TiO_2, ZrO_2, CeO_2, Sm_2O_3, and Gd_2O_3 catalysts, the electric field was applicable but the methane conversion was extremely low. Less C_2 compound formation was observed. Both BaO and Pr_6O_{11} catalysts exhibited high activities. The CO_2-OCM yields over BaO and Pr_6O_{11} catalysts were,

respectively, 2.7% and 1.0%. However, the activities over these two catalysts degraded soon after starting the reaction. We also tried to use $La_{0.7}M_{0.3}AlO_{3-\delta}$ (M=Mg, Ca, Sr, Ba) catalysts, partly substituted A site of $LaAlO_3$ with alkali earth metal and $LaAl_{0.7}M'_{0.3}O_{3-\delta}$ (M'=Ti, Cr, Mn, Fe, Co) catalysts, partly substituted B site with transition metal. Table 2-1 presents experimentally obtained results on various perovskite catalysts. Over $La_{0.7}Mg_{0.3}AlO_{3-\delta}$ catalyst, the electric field was not applicable, and CH_4 and CO_2 conversions were low. Over $La_{0.7}Ca_{0.3}AlO_{3-\delta}$, $La_{0.7}Sr_{0.3}AlO_{3-\delta}$ and $La_{0.7}Ba_{0.3}AlO_{3-\delta}$ catalysts, the electric field was applicable and C_2 products were obtained because the substitution of a part of La^{3+} with divalent alkali earth metal cations increased the carrier mobility such as holes and oxygen ions. Over $LaAl_{0.7}B_{0.3}AlO_{3-\delta}$ catalysts, the electric field was applicable stably but C_2 products were not obtained. In addition, over $LaAl_{0.7}Ti_{0.3}AlO_{3-\delta}$, $LaAl_{0.7}Fe_{0.3}AlO_{3-\delta}$ and $LaAl_{0.7}Co_{0.3}AlO_{3-\delta}$ catalysts, dry reforming of methane (DR) proceeded dominantly. Both syngas by DR and C_2 hydrocarbons by CO_2-OCM are useful chemical feedstocks, but C_2 hydrocarbon is more important considering the value of the products. From this viewpoint, we assumed that $La_{0.7}Ca_{0.3}AlO_{3-\delta}$ (LCAO) catalyst was the most appropriate catalyst among these oxides in this reaction system. In addition, substitution with 30% Ca at the A site showed the highest OCM yield of 2.0%. That value was comparable to the value presented in an earlier report [18]. C_2 hydrocarbon and syngas were dominant products and no other byproduct such as oxygenates or carbon was obtained on the LCAO catalyst. Moreover, as a result of a survey for the highest C_2 yield in CO_2-OCM in the electric field over the LCAO catalyst, 7.4% C2 yield, the highest among previous reports, was obtained in CH_4:CO_2:Ar = 5:25:70, total flow rate of 100 mL min^{-1} at 348 K (furnace temperature).

The effect of the electric field on the reaction was investigated through comparison of catalytic activity on the conventional catalytic reaction using LCAO catalyst. Figure 2-1 presents results of CH_4 and CO_2 conversions and C_2 selectivity in a conventional catalytic reaction (i.e. no electric field; right side) and in the catalytic reaction with the electric field (left side). Reaction temperatures were 1173–1348 K in conventional catalytic reactions and 423–633 K (furnace temperature) in the catalytic reaction with the electric field. As presented in Figure 2-1, the CH_4 and CO_2 conversions on the catalytic reaction in the electric field on 3 mA were comparable to that in the conventional reaction at 1323 K. The reaction progressed at markedly low temperatures because of the application of the electric field. In addition, although the temperature rose in the electric field, CH_4 and CO_2 conversion, and C_2 selectivity were constant. Therefore, Joule heat did not affect the catalytic activity in the electric field and electrical modification to the catalyst affected the catalytic activity.

2.3.2 Effects of electrical factors on catalytic activity in the electric field

To elucidate the catalytic activity tests described above, we investigated the effect of imposed current, and calculated imposed power on the catalytic activity. We also confirmed the effect of applied voltage, and no importance for the voltage was found in this system. Figure 2-2 presents results of CH_4 and CO_2 conversion, as well as those for C_2 selectivity for changing imposed current, calculated imposed power and applied voltage. As presented in Figure 2-2, CH_4 and CO_2 conversion, and C_2 selectivity were changed depending on the imposed current and imposed power, not on applied voltage. These electrical factors possibly affected CO_2-OCM in the electric field. CH_4 and CO_2 conversion and C_2 selectivity were unchanged by changes in applied voltage. Therefore, the key electrical factor in CO_2-OCM in the electric field was imposed current to the catalyst bed. In addition, the interaction between imposed current and applied voltage (I–V profile) in CO_2-OCM in the electric field was investigated. Results are described in Figure 2-3. The electric field was unstable when the imposed current was 2 mA, and when CH_4 and CO_2 conversion were very low, and the applied voltage was not stable. On the other hand, when the imposed current was changed from 3 mA to 9 mA, the relation between imposed current and applied voltage did not follow the Ohmic law. The imposed current presumably affected various adsorbed species and carriers on the catalyst.

2.3.3 Catalytic reaction mechanism in CO_2-OCM in the electric field

To elucidate the catalytic reaction mechanism in CO_2-OCM in the electric field over LCAO catalyst, activity tests by changing CH_4 and CO_2 partial pressure (P_{CH4} and P_{CO2}) were investigated. Then the reaction order was calculated. The left side of Fig. 4 shows the logarithmic plots for the formation rate by changing P_{CH4}. As a result, when P_{CH4} was increased, the formation rate in OCM reaction (calculated from the formation rate for C_2H_4 and C_2H_6 products) per unit of imposed power increased. The formation rate in the DR reaction (as calculated from CO from DR and H_2 products) per unit of imposed power was constant from 0.06 atm to 0.25 atm. On the other hand, the right side of Figure 2-4 shows logarithmic plots for the formation rate by changing P_{CO2}; consequently, when P_{CO2} was increased, the formation rate in OCM reaction and reverse water gas shift (RWGS) reaction per unit of imposed power increased. The formation rate in the DR reaction per unit of imposed power increased at lower CO_2 partial pressure, and became constant above 0.25 atm. The results of the activity tests for changing the partial pressure showed that the formation

rate r in CO_2-OCM in the electric field can be expressed as the following equation using rate constant k and partial pressure P.

$$r = k\, P_{CO2}^{0.70} \qquad \text{(eq. 10)}$$

In this way, we showed that the formation rate in CO_2-OCM in the electric field is strongly dependent on the CO_2 partial pressure.

Next, the effect of contact time (W/F_{CH4}) on CO_2-OCM activity in the electric field over LCAO was investigated. Figure 2-5 portrays the result of these tests; the left side of plots shows the result obtained using $La_{0.7}Ca_{0.3}AlO_{3-\delta}$ catalyst; the right side of plots shows the result obtained using $La_{0.9}Ca_{0.1}AlO_{3-\delta}$ catalyst. When W/F_{CH4} was increased, CH_4 and CO_2 conversion increased; C_2 selectivity decreased. In the higher W/F_{CH4} range, C_2 selectivity remained at a lower value. Therefore, the DR reaction was dominant in this range. Regarded from the viewpoint of the difference of amounts of Ca-doped into $LaAlO_3$ catalyst, CH_4 and CO_2 conversion increased more drastically using $La_{0.7}Ca_{0.3}AlO_{3-\delta}$ catalyst than using $La_{0.9}Ca_{0.1}AlO_{3-\delta}$ catalyst. Therefore, as the amounts of Ca-doped into $LaAlO_3$ catalyst increase, the active site for CO_2-OCM in the electric field is presumed to increase.

Next, to elucidate the characterization for the adsorbed species from CO_2 on LCAO catalysts, CO_2-temperature programmed desorption (TPD) was conducted using FT-IR. Figure 2-6 presents results obtained for CO_2-TPD using FT-IR from 423 K to 623 K. Four peaks were measured at 423 K: they were the peak at 1781 cm^{-1} derived from bicarbonate, the peak at 1581 cm^{-1} derived from bidentate carbonate, the peak at 1338 cm^{-1} derived from unidentate carbonate, and the peak at 1086 cm^{-1} derived from $La_2O_2CO_3$ oxide [42, 43]. Bicarbonate, bidentate carbonate, and unidentate carbonate are derived from the CO_2 adsorbed species. As for the $La_2O_2CO_3$ oxide, Au *et al.* reported that the presence of the $La_2O_2CO_3$ phase over $BaCO_3$/LaOBr catalyst appeared to have a promoting effect on the catalytic activity in OCM reaction, Taylor *et al.* reported that the catalytic activity of the $La_2O_2CO_3$ catalysts was better than that of La_2O_3, $La(OH)_3$ and $La_2(CO_3)_3$ catalysts, and Dubois *et al.* reported that O_2^- ion was stabilized, and the C_2 selectivity increased in OCM thanks to $La_2O_2CO_3$ oxide [44-46]. In addition, the formation of $La_2O_2CO_3$ oxide from CO_2 adsorption on LCAO at room temperature is an interesting result because $La_2O_2CO_3$ oxide on La_2O_3 was reported to form at high temperature of 723 K [43, 47]. From the result of CO_2-TPD using FT-IR, when the temperature increased, the intensities for these four peaks were decreased. They disappeared at 623 K. Considering that CO_2-OCM in the electric field proceeds at 423 K, the CO_2 adsorbent and formed $La_2O_2CO_3$ are important for the progress of CO_2-OCM in the electric

field.

Next, *in-situ* IR was conducted to elucidate the adsorbed species from CO_2 on LCAO catalysts in the electric field. Figure 2-7 shows the result of *in-situ* IR: two new peaks appeared at 844 cm^{-1} and 1040 cm^{-1} imposing the electric field. These peaks are also derived from $La_2O_2CO_3$ as described above. The fluctuation for the baseline was derived from the imposed current. The imposed electric field caused formation of $La_2O_2CO_3$ on LCAO. This intermediate remained on the catalyst when the current was turned off and the electric field was imposed again. In order to elucidate the interaction between the formation of $La_2O_2CO_3$ and partial pressures for CO_2, *in-situ* IR for changing partial pressures for CO_2 in the electric field was conducted (as shown in Figure 2-8 and Figure 2-9). Figure 2-9 shows the base-line compensated intensity of Figure 2-8, the intensity at 900 cm^{-1} and 1200 cm^{-1} was set as baseline. As a result from these two figures, the peaks from $La_2O_2CO_3$ were not mostly depended on partial pressure of CO_2. Therefore, the rate determining step in CO_2-OCM in the electric field is supposed to be desorption of intermediates. In addition, from the result of CO_2-TPD using FT-IR, $La_2O_2CO_3$ was degraded at 623 K, but conventional catalytic CO_2-OCM (not imposed the electric field) did not proceed at 623 K. Repeatedly, in the raw gas condition as CO_2-OCM, $La_2O_2CO_3$ is formed at low temperatures only with the electric field imposed. $La_2O_2CO_3$ on LCAO is an important factor for CO_2-OCM in the electric field at low temperature. This catalytic reaction mechanism differs from previously reported mechanisms.

2.3.4 Effects of Ca-doped into $LaAlO_3$ catalyst

To ascertain the role of Ca doped in $LaAlO_3$ on the catalytic activity, we conducted activity tests by changing of the doped amounts of Ca in $LaAlO_3$ and the supported amounts of Ca on $La_{0.7}Ca_{0.3}AlO_{3-\delta}$ catalyst. Table 2-2 presents the results of catalytic activation tests for different substitution amounts of Ca in $LaAlO_3$, with field intensity fit to 94 V mm^{-1} . When the substitution amount of Ca in $La_{1-x}Ca_xAlO_{3-\delta}$ catalysts was increased to x=0.3, CH_4 and CO_2 conversion increased. A further increase in the Ca amount to x=0.5 decreased the catalytic activity. In addition, when the supported amounts of Ca on $La_{0.7}Ca_{0.3}AlO_{3-\delta}$ catalyst were increased, CH_4 and CO_2 conversion decreased. Furthermore, in the perspective of the relation between the BET specific surface area and the catalytic activity over $La_{1-x}Ca_xAlO_{3-\delta}$, the BET specific surface area was not an important factor in CO_2-OCM in the electric field. Moreover, XRD profile for $La_{1-x}Ca_xAlO_{3-\delta}$ as made and after applying the electric field were measured (shown in Figure 2-10–2-13) and XRD crystallite sizes of various Ca-doped

$LaAlO_3$ catalysts at perovskite (110) face were calculated by the Debye-Scherrer formula (shown in Table 2-3). As a result, the perovskite oxide structures for various Ca-doped $LaAlO_3$ catalysts were mostly unchanged.

Next, to elucidate the difference for CO_2 adsorption between Ca-doped into $LaAlO_3$ and Ca-supported on LCAO catalyst, CO_2-TPD was conducted using TG (as shown in Figure 2-14). Two peaks were observed in CO_2-TPD using TG. From the result of CO_2-TPD using the FT-IR and XRD profile, the peak at lower temperature derived from CO_2 adsorbent and $La_2O_2CO_3$ and the peak at higher temperature possibly derived from $CaCO_3$ decomposition. Therefore, when the amounts of Ca supported on LCAO catalyst increase, $CaCO_3$ was formed on LCAO catalyst. Moreover, $CaCO_3$ was coated on the active site for CO_2-OCM in the electric field by XRD measurement, as shown in Figure 2-15. Results show the importance for $La_{0.7}Ca_{0.3}AlO_{3-\delta}$ catalyst in CO_2-OCM in the electric field that Ca atoms incorporate into $LaAlO_3$ oxide structure, not generating $CaCO_3$.

2.4 Conclusion

Oxidative coupling of methane using carbon dioxide (CO_2-OCM) was conducted in an electric field. Results of the screening tests show that $La_{0.7}Ca_{0.3}AlO_{3-\delta}$ (LCAO) catalyst was the most appropriate catalyst in this reaction system, and it shows high activity even at 423 K. The C_2 hydrocarbon and syngas were dominant products. No other byproduct, such as oxygenates or carbon, was obtained on the catalyst. In addition, as a result of survey for the highest C_2 yield in CO_2-OCM in the electric field over LCAO catalyst, 7.4% was obtained at 348 K. To show the same catalytic activity by heating the catalyst, very high temperature was required, even at 1323 K in the conventional catalytic CO_2-OCM. The imposed current was correlated to with CH_4 conversion. The reaction rate depended on the CO_2 partial pressure by 0.7 order. Elucidating the adsorbed species from CO_2 on LCAO catalysts, CO_2 adsorbent and $La_2O_2CO_3$ are important for the progress of CO_2-OCM in the electric field. The rate-determined step in CO_2-OCM in the electric field is supposed to be desorption of intermediates. As the amounts of Ca doped into $LaAlO_3$ increased, the active site was presumed to increase. Furthermore, the Ca-doped effect of LCAO is that by which Ca atom was incorporated into the $LaAlO_3$ perovskite structure and generation of C_2 hydrocarbons was promoted.

References

[1] K. Otsuka, K. Jinro, A. Morikawa, The catalysts active and selective in oxidative coupling of methane, Chem. Lett. 14 (1985) 499–500.

[2] R. Pitchai, K. Klier, Partial oxidation of methane, Catal. Rev. Sci. Eng. 28 (1986) 13–88.

[3] C.-H. Lin, K.D. Campbell, J.X. Wang, J.H. Lunsford, Oxidative dimerization of methane over lanthanum oxide, J. Phys. Chem. 90 (1986) 534–537.

[4] K.D. Campbell, H. Zhang, J.H. Lunsford, Methane activation by the lanthanide oxides, J. Phys. Chem. 92 (1988) 750–753.

[5] J.S. Lee, S.T. Oyama, Oxidative coupling of methane to higher hydrocarbons, Catal. Rev. Sci. Eng. 30 (1988) 249–280.

[6] Y. Tong, M.P. Rosynek, J.H. Lunsford, Secondary reactions of methyl radicals with lanthanide oxides: Their role in the selective oxidation of methane, J. Phys. Chem. 93 (1989) 2896–2898.

[7] S.J. Korf, J.A. Roos, J.M. Diphoorn, R.H.J. Veehof, J.G. van Ommen, J.R.H. Ross, The selective oxidation of methane to ethane and ethylene over doped and un-doped rare earth oxide, Catal. Today 4 (1989) 279–292.

[8] V.R. Choudhary, V.H. Rane, Acidity/basicity of rare-earth oxides and their catalytic activity in oxidative coupling of methane to C_2-hydrocarbons, J. Catal. 130 (1991) 411–422.

[9] J.H. Lunsford, The catalytic oxidative coupling of methane, Angew. Chem. Int. Ed. Engl. 34 (1995) 970–980.

[10] Y. Sekine, K. Fujimoto, Oxidative coupling of methane in the gas phase: Simulation and reaction mechanism, Energy Fuels, 12 (1998) 828–829.

[11] A.G. Dedov, A.S. Loktev, Moiseev II, A. Aboukais, J.-F. Lamonier, I.N. Filimonov, Oxidative coupling of methane catalyzed by rare earth oxides: Unexpected synergistic effect of the oxide mixtures, Appl. Catal. A: Gen. 245 (2003) 209–220.

[12] M. Khodadadian, M. Taghizadeh, M. Hamidzadeh, Effects of various barium precursors and promoters on catalytic activity of Ba-Ti perovskite catalysts for oxidative coupling of methane, Fuel. Proc. Technol. 92 (2011) 1164–1168.

[13] V.H. Rane, S.T. Chaudhari, V.R. Choudhary, Comparison of the surface and catalytic properties of rare earth-promoted CaO catalysts in the oxidative coupling of methane, J. Chem. Technol. Biotechnol. 81 (2006) 208–215.

[14] K. Asami, T. Fujita, K. Kusakabe, Y. Nishiyama, Y. Ohtsuka, Conversion of methane with carbon dioxide into C_2 hydrocarbons over metal oxides, Appl. Catal. A: Gen. 126 (1995) 245–255.

[15] C. Chen, Y. Xu, G. Li, X. Guo, Oxidative coupling of methane by carbon dioxide: A highly C_2 selective La_2O_3/ZnO catalyst, Catal. Lett. 42 (1996) 149–153.
[16] K. Asami, K. Kusakabe, N. Ashi, Y. Ohtsuka, Synthesis of ethane and ethylene from methane and carbon dioxide over praseodymium oxide catalysts, Appl. Catal. A: Gen. 156 (1997) 43–56.
[17] Y. Wang, Y. Takahashi, Y. Ohtsuka, Remarkable enhancing effect of carbon dioxide on the conversion of methane to C_2 hydrocarbons using praseodymium oxide, Chem. Lett. 56 (1998) 203–206.
[18] Y. Wang, Y. Takahashi, Y. Ohtsuka, Carbon dioxide as oxidant for the conversion of methane to ethane and ethylene using modified CeO_2 catalysts, J. Catal. 186 (1999) 160–168.
[19] Y. Wang, Y. Ohtsuka, Mn-based binary oxides as catalysts for the conversion of methane to C_2 hydrocarbons with carbon dioxide as oxidant, Appl. Catal. A: Gen. 219 (2001) 183–193.
[20] Y. Cai, L. Chou, S. Li, B. Zhang, J. Zhao, Selective conversion of methane to C_2 hydrocarbons using carbon dioxide over Mn-$SrCO_3$ catalysts, Catal. Lett. 86 (2003) 191–195.
[21] Y. Sekine, M. Tomioka, M. Matsukata, E. Kikuchi, Catalytic degradation of ethanol in an electric field, Catal. Today, 146(1-2) (2009) 183–187.
[22] Y. Sekine, M. Haraguchi, M. Tomioka, M. Matsukata, E. Kikuchi, Low-temperature hydrogen production by highly efficient catalytic system assisted by an electric field, J. Phys. Chem. A, 114 (2010) 3824–3833.
[23] Y. Sekine, M. Haraguchi, M. Matsukata, E. Kikuchi, Low temperature steam reforming of methane over metal catalyst supported on $Ce_xZr_{1-x}O_2$ in an electric field, Catal. Today, 171 (2011) 116–125.
[24] K. Tanaka, Y. Sekine, K. Oshima, Y. Tanaka, M. Matsukata, E. Kikuchi, Catalytic oxidative coupling of methane assisted by electric power over a semiconductor catalyst, Chem. Lett. 4 (2012) 351–353.
[25] K. Oshima, K. Tanaka, T. Yabe, Y. Tanaka, Y. Sekine, Catalytic oxidative coupling of methane with a dark current in an electric field at low external temperature, Int. J. Plasma Environ. Sci. Technol. 6 (2012) 266–271.
[26] K. Oshima, T. Shinagawa, Y. Sekine, Methane conversion assisted by plasma or electric field, J. Jpn. Petrol. Inst. 56 (2013) 11–21.
[27] K. Oshima, T. Shinagawa, M. Haraguchi, Y. Sekine, Low temperature hydrogen production by catalytic steam reforming of methane in an electric field, Int. J. Hydrogen Energy 38 (2013) 3003–3011.

[28] K. Oshima, T. Shinagawa, Y. Nogami, Y. Manabe, S. Ogo, Y. Sekine, Low temperature catalytic reverse water gas shift reaction assisted by an electric field, Catal. Today 232 (2014) 27–32.

[29] K. Sugiura, S. Ogo, K. Iwasaki, T. Yabe, Y. Sekine, Low-temperature catalytic oxidative coupling of methane in an electric field over a Ce-W-O catalyst system, Scientific Reports 6 (2016) 25154.

[30] B. Eliasson, C.-J. Liu, U. Kogelschatz, Direct conversion of methane and carbon dioxide to higher hydrocarbons using catalytic dielectric-barrier discharges with zeolites, Ind. Eng. Chem. Res. 39 (2000) 1221–1227.

[31] C. Liu, B. Xue, B. Eliasson, F. He, Y. Li, G.-H. Xu, Methane conversion to higher hydrocarbons in the presence of carbon dioxide using dielectric-barrier discharge plasmas, Plasma Chem. Plasma Proc. 21 (2001) 301–310.

[32] S. Kado, Y. Sekine, T. Nozaki, K. Okazaki, Diagnosis of atmospheric pressure low temperature plasma and application to high efficient methane conversion, Catal. Today 89 (2004) 47–55.

[33] S. Kado, K. Urasaki, Y. Sekine K. Fujimoto, Direct conversion of methane to acetylene or syngas at room temperature using non-equilibrium pulsed discharge, Fuel 82 (2003) 1377–1385.

[34] S. Kado, K. Urasaki, Y. Sekine, K. Fujimoto, T. Nozaki, K. Okazaki, Reaction mechanism of methane activation using non-equilibrium pulsed discharge at room temperature, Fuel 82 (2003) 2291–2297.

[35] S. Kado, K. Urasaki, H. Nakagawa, K. Miura, Y. Sekine, Methane coupling and reforming using non equilibrium pulsed discharge at room temperature: Catalyst-pulsed discharge combined system, ACS Books Util. Greenhouse Gas, 852 (2003) 303–313.

[36] S. Kado, Y. Sekine, K. Fujimoto, Direct synthesis of acetylene from methane by direct current pulse discharge, Chem. Commun. 24 (1999) 2485–2486.

[37] C.G. Vayenas, S. Bebelis, S. Neophytides, Non-faradaic electrochemical modification of catalytic activity, J. Phys. Chem. 92 (1988) 5083–5085.

[38] S. Bebelis, C.G. Vayenas, Non-faradaic electrochemical modification of catalytic activity. 1. The case of ethylene oxidation on Pt, J. Catal. 118 (1989) 125–146.

[39] P. Tsiakaras, C.G. Vayenas, Non-faradaic electrochemical modification of catalytic activity. VII. The case of methane oxidation on platinum, J. Catal. 140 (1993) 53–70.

[40] Yentekakis IV, Y. Jiang, Y. Neophytides, S. Bebelis, C.G. Vayenas, Catalysis, electrocatalysis and electrochemical promotion of the steam reforming of methane over Ni film and Ni-YSZ cermet anodes, Ionics 1 (1995) 491–498.

[41] A.D. Frantzis, S. Bebelis, C.G. Vayenas, Electrochemical promotion (NEMCA) of CH_4 and C_2H_4 oxidation on Pd/YSZ and investigation of the origin of NEMCA via AC impedance spectroscopy, Solid State Ionics 136–137 (2000) 863–872.

[42] V.G. Milt, R. Spretz, M.A. Ulla, E.A. Lombardo, J.G. Fierro, The nature of active sites for the oxidation of methane on La-based perovskites , Catal. Lett. 42 (1996) 57–63.

[43] T. Levan, M. Che, J.M. Tatibouët, M. Kermarec, Infrared study of the formation and stability of $La_2O_2CO_3$ during the oxidative coupling of methane on La_2O_3, J. Catal. 142 (1993) 18–26.

[44] C.T. Au, H. He, S.Y. Lai, C.F. Ng, The oxidative coupling of methane over $BaCO_3$/LaOBr—Catalysts of high ethylene yield, J. Catal. 163 (1996) 399–408.

[45] R.P. Taylor, G.L. Schrader, Lanthanum catalysts for methane oxidative coupling: a comparison of the reactivity of phases, Ind. Eng. Chem. Res. 30 (1991) 1016–1023.

[46] J.-L. Dubois, C.J. Cameron, Synergy between stable carbonates and yttria in selective catalytic oxidation of methane, Chem. Lett. 7 (1991) 1089–1092.

[47] T. Yang, L. Feng, S. Shen, Oxygen species on the surface of La_2O_3/CaO and its role in the oxidative coupling of methane, J. Catal., 145 (1994) 384–389.

Table 2-1 Catalytic activities for methane activity in an electric field over various $LaAlO_3$ oxide catalysts: 3.0 mA imposed current

Catalyst	Power / W	Field Intensity / V mm^{-1}	CH_4 Conv. / %	CO_2 Conv. / %	OCM Sel. / %	OCM Yield / %
$LaAlO_3$	spark discharge		3.1	2.9	17.4	0.5
$La_{0.7}Mg_{0.3}AlO_{3-\delta}$	spark discharge		2.3	1.7	18.6	0.4
$La_{0.7}Ca_{0.3}AlO_{3-\delta}$	7.5	177	10.4	14.2	19.6	2.0
$La_{0.7}Sr_{0.3}AlO_{3-\delta}$	3.0	137	4.8	6.2	12.7	0.6
$La_{0.7}Ba_{0.3}AlO_{3-\delta}$	4.2	127	11.0	16.4	8.6	0.9
$LaAl_{0.7}Ti_{0.3}O_{3-\delta}$	3.3	80	0.4	0.7	15.9	0.07
$LaAl_{0.7}Cr_{0.3}O_{3-\delta}$	3.3	103	0.1	0.1	60.6	0.03
$LaAl_{0.7}Mn_{0.3}O_{3-\delta}$	2.1	67	0.04	0.1	0	0
$LaAl_{0.7}Fe_{0.3}O_{3-\delta}$	1.8	57	0.4	0.01	0	0
$LaAl_{0.7}Co_{0.3}O_{3-\delta}$	4.2	137	8.1	11.7	1.7	0.1

Table 2-2 Catalytic activities for methane activity in an electric field over various Ca-doped $LaAlO_3$ and Ca-supported LCAO oxide catalysts: imposed current, 3.0 mA

Catalyst	Power / W	CH_4 Conv. / %	CO_2 Conv. / %	C_2 Sel. / %	C_2 Yield / %	BET specific surface area / $m^2\ g^{-1}$
$La_{0.9}Ca_{0.1}AlO_{3-\delta}$	3.6	3.4	2.0	20.6	0.7	12.3
$La_{0.8}Ca_{0.2}AlO_{3-\delta}$	3.9	2.8	3.0	37.7	1.1	9.6
$La_{0.7}Ca_{0.3}AlO_{3-\delta}$	7.5	10.4	14.2	19.6	2.0	9.6
$La_{0.6}Ca_{0.4}AlO_{3-\delta}$	6.5	1.6	0.8	26.9	0.4	5.3
$La_{0.5}Ca_{0.5}AlO_{3-\delta}$	6.0	0.4	0.6	37.4	0.2	11.2
1 wt%Ca/LCAO	5.1	7.7	10.8	22.3	1.7	7.3
2 wt%Ca/LCAO	4.8	3.3	2.0	32.0	1.1	8.1
5 wt%Ca/LCAO	5.7	4.7	4.1	28.6	1.3	4.0

Table 2-3 XRD crystallite size of various Ca-doped $LaAlO_3$ at perovskite (110) face in fresh and after CO_2-OCM in the electric field (after EF) using Debye-Scherrer formula

Catalyst		Crystallite size / nm
$La_{0.9}Ca_{0.1}AlO_{3-\delta}$	fresh	30.9
	after EF	32.9
$La_{0.8}Ca_{0.2}AlO_{3-\delta}$	fresh	32.2
	after EF	35.8
$La_{0.7}Ca_{0.3}AlO_{3-\delta}$	fresh	27.4
	after EF	28.1
$La_{0.6}Ca_{0.4}AlO_{3-\delta}$	fresh	29.1
	after EF	32.9
$La_{0.5}Ca_{0.5}AlO_{3-\delta}$	fresh	35.7
	after EF	38.2

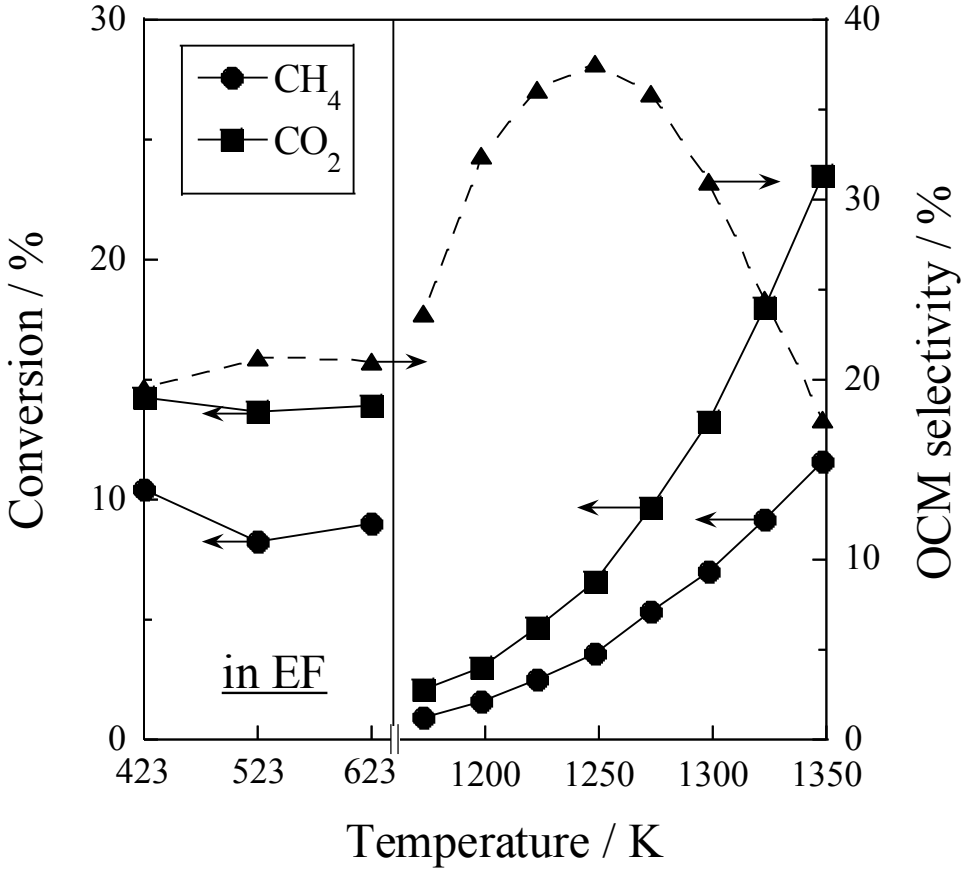

Figure 2-1 Comparison of the conversion and selectivity between conventional catalytic reaction and catalytic reaction in the electric field over $La_{0.7}Ca_{0.3}AlO_{3-\delta}$ catalyst: ●, CH_4 conversion; ■, CO_2 conversion; ▲, OCM selectivity; 3.0 mA imposed current.

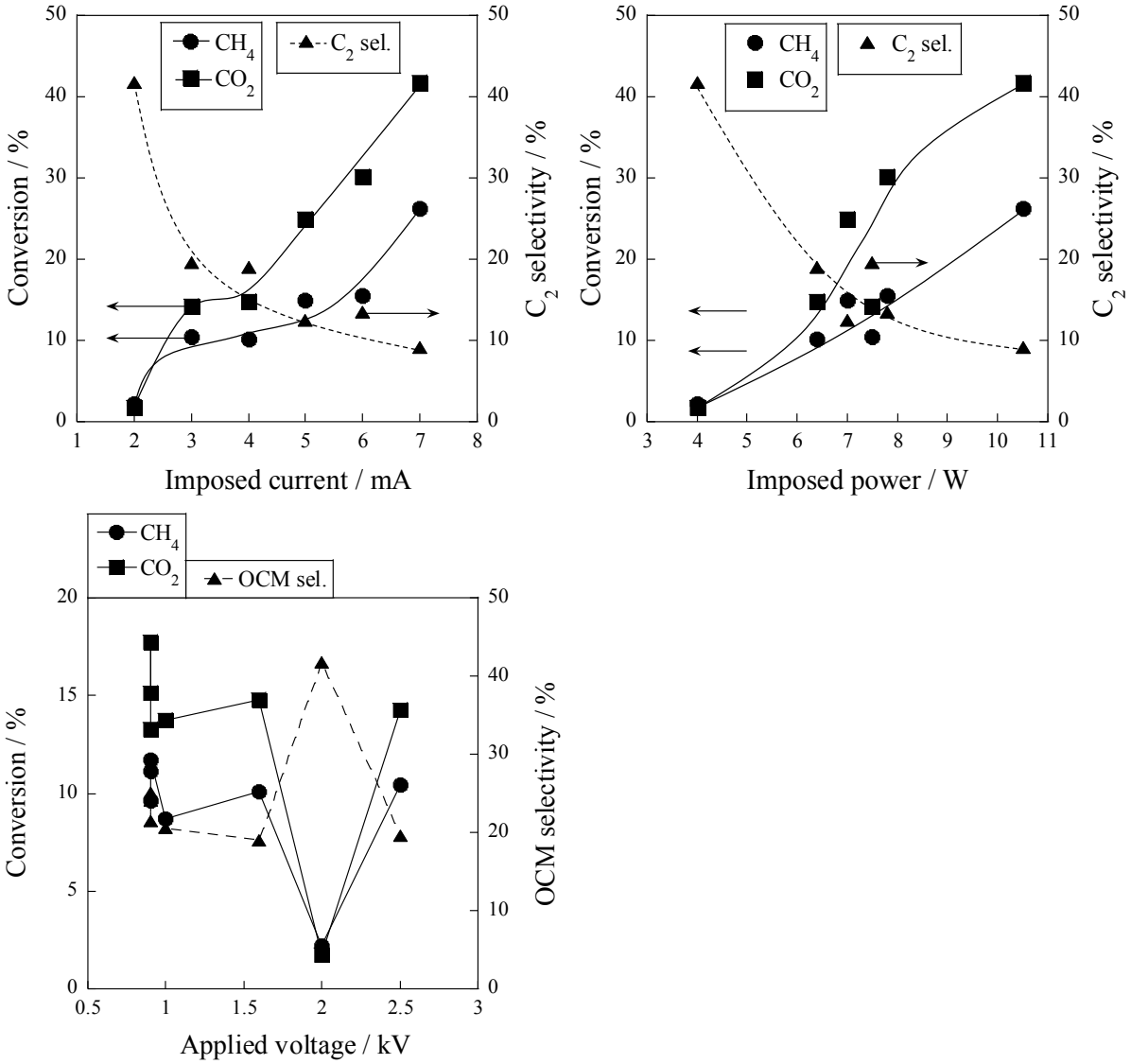

Figure 2-2 Effects of electrical factors (upper left, imposed current; upper right, imposed power; downside left, applied voltage) on the catalytic activity of methane and carbon dioxide conversion in the electric field over $La_{0.7}Ca_{0.3}AlO_{3-\delta}$ catalyst: ●, CH_4 conversion; ■, CO_2 conversion; and ▲, OCM selectivity.

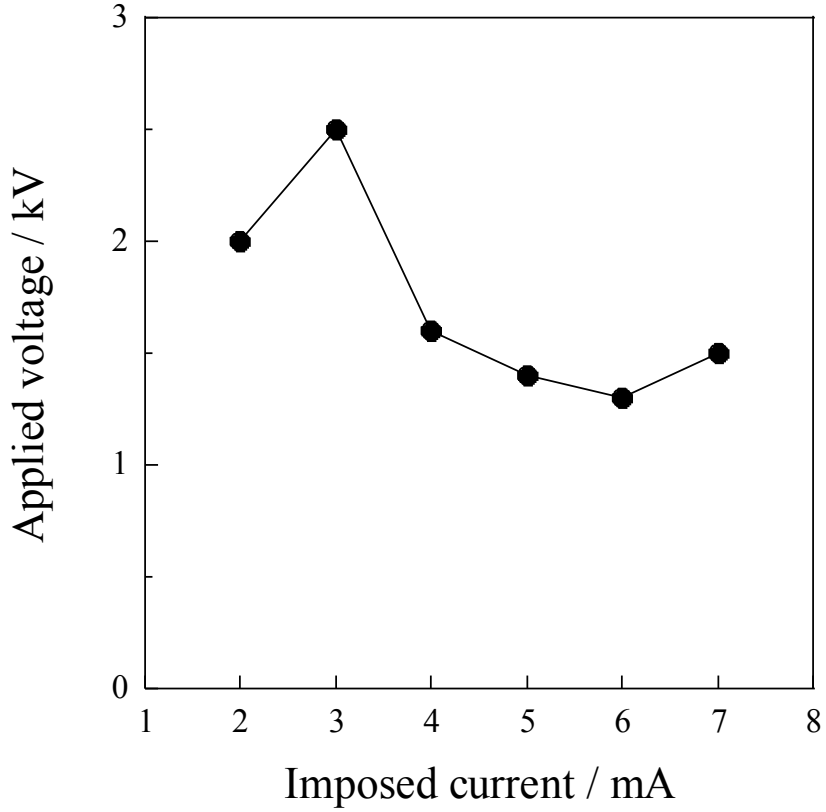

Figure 2-3 I-V profile on the catalytic reaction in the electric field.

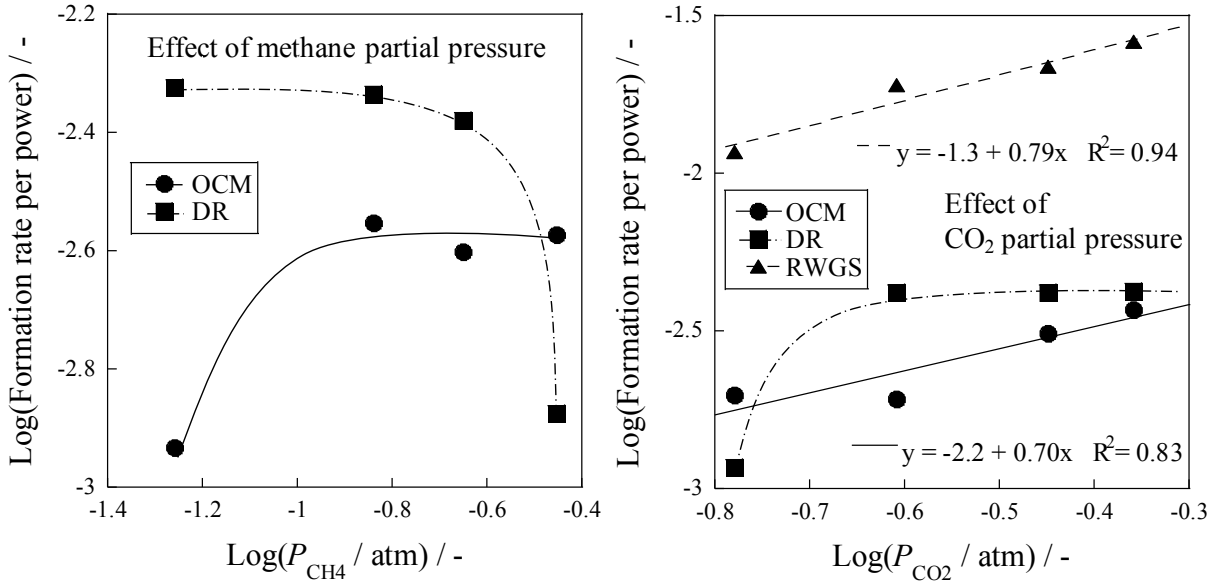

Figure 2-4 Calculation of reaction order in the electric field over $La_{0.7}Ca_{0.3}AlO_{3-\delta}$ catalyst, (left) for CH_4, (right) for CO_2: imposed current 3.0 mA; furnace temperature 423 K; ●, OCM reaction; ■, DR reaction; and ▲, RWGS reaction.

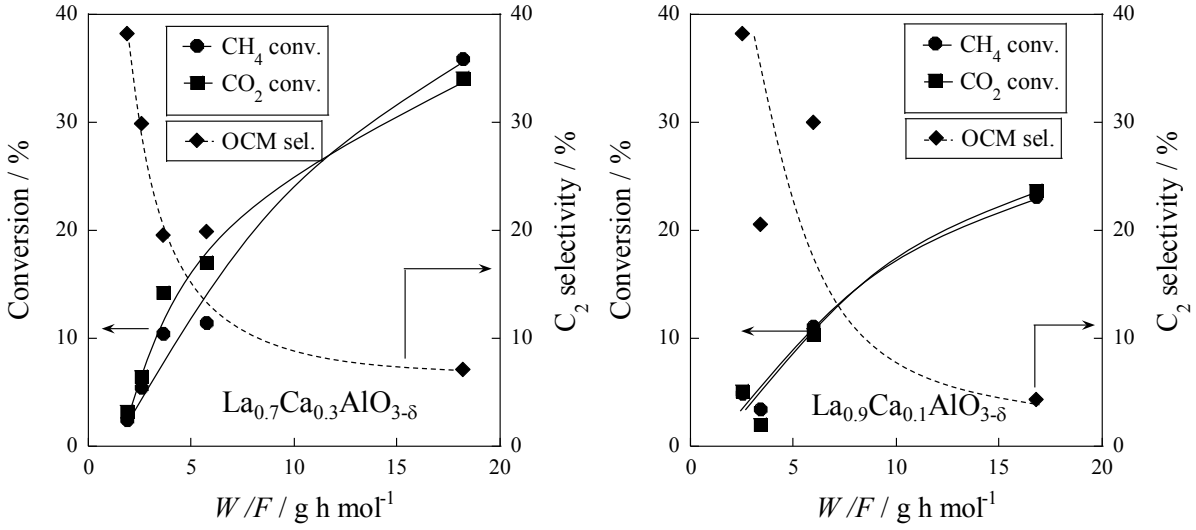

Figure 2-5 Influence of W/F_{CH4} on the catalytic activity for CO_2-OCM in the electric field over (left) $La_{0.7}Ca_{0.3}AlO_{3-\delta}$ and (right) $La_{0.9}Ca_{0.1}AlO_{3-\delta}$ catalyst: imposed current 3.0 mA; furnace temperature 423 K; ●, CH_4 conversion; ■, CO_2 conversion; ▲, OCM selectivity.

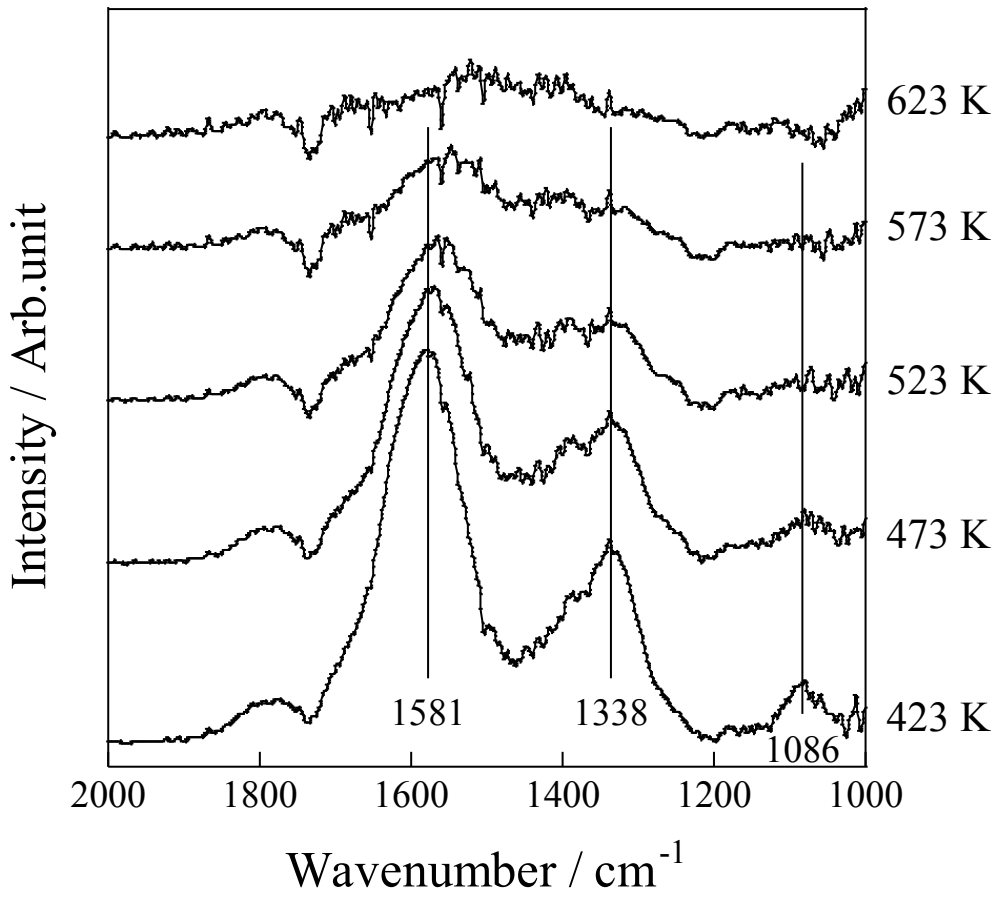

Figure 2-6 IR spectra during temperature programmed desorption of carbon dioxide over $La_{0.7}Ca_{0.3}AlO_{3-\delta}$ catalyst.

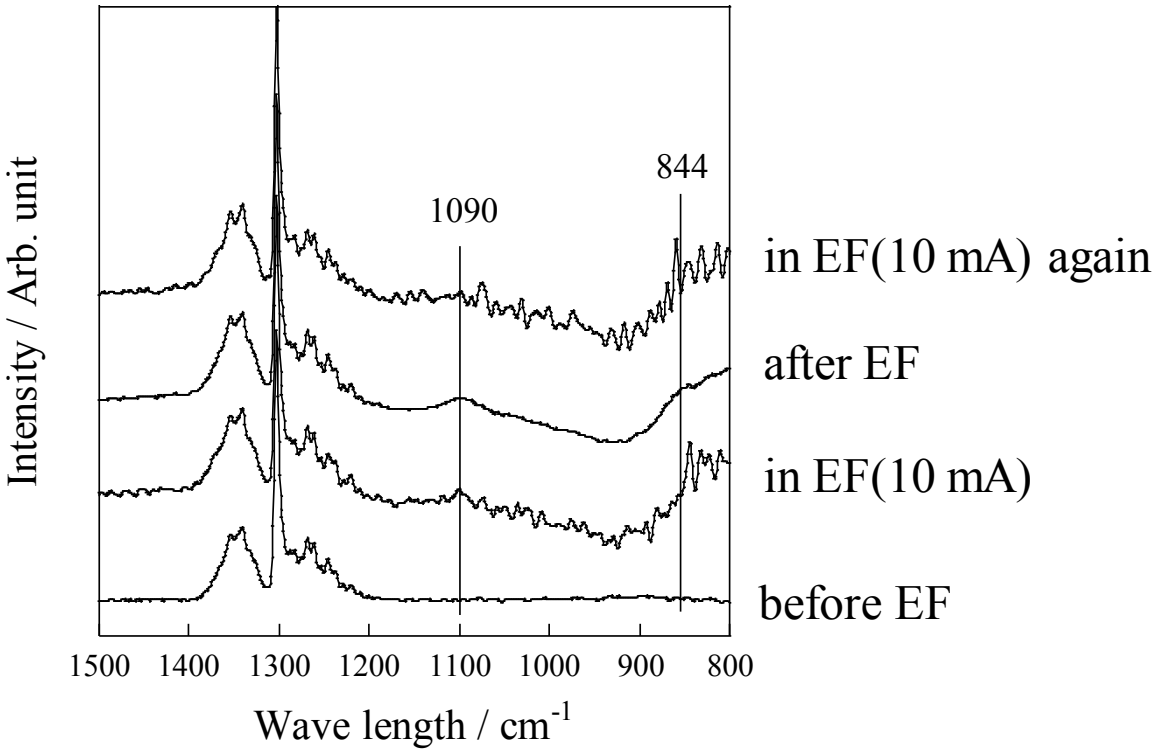

Figure 2-7 *In-situ* IR for CO_2-OCM in the electric field over $La_{0.7}Ca_{0.3}AlO_{3-\delta}$ catalyst.

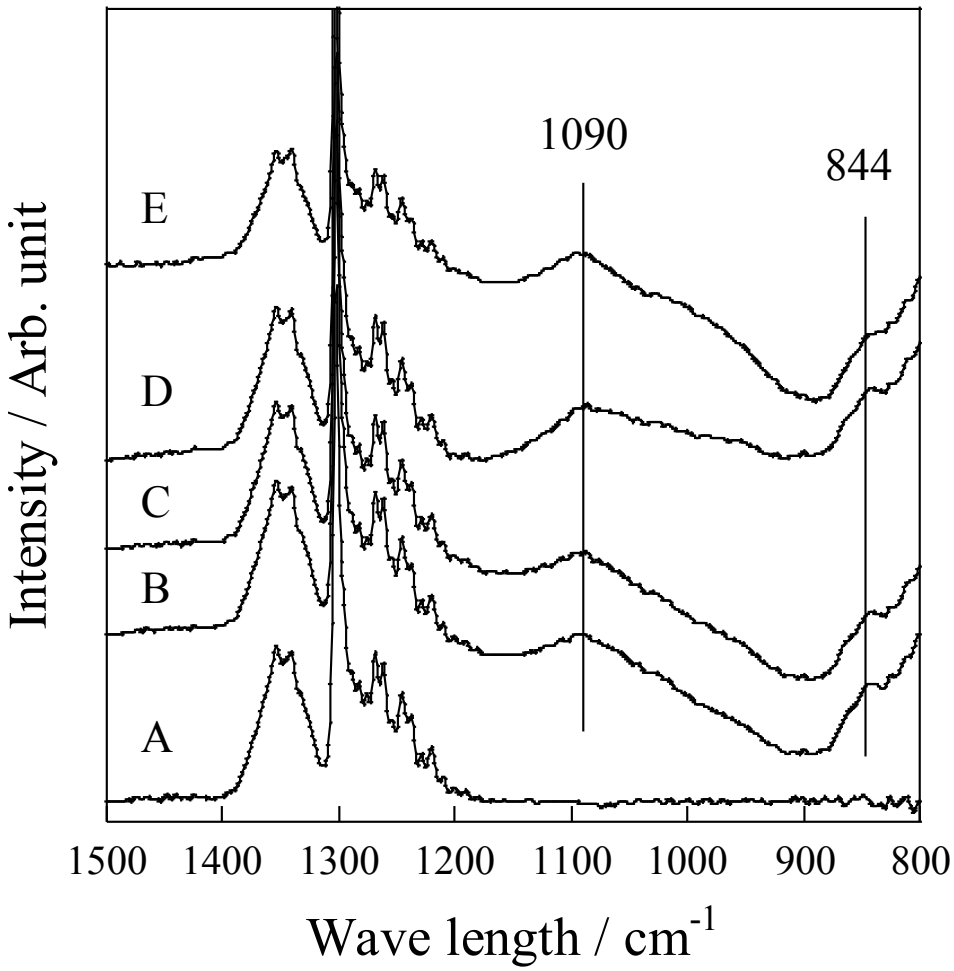

Figure 2-8 *In-situ* IR for CO_2-OCM in the electric field for changing the partial pressure of CO_2 over $La_{0.7}Ca_{0.3}AlO_{3-\delta}$ catalyst: (A) CH_4=50 mL min^{-1} before EF (electric field imposing), (B) CH_4=50 mL min^{-1} after EF , (C) CH_4:CO_2=45:5 mL min^{-1} after EF, (D) CH_4:CO_2=35:15 mL min^{-1} after EF, (E) CH_4:CO_2=25:25 mL min^{-1} after EF.

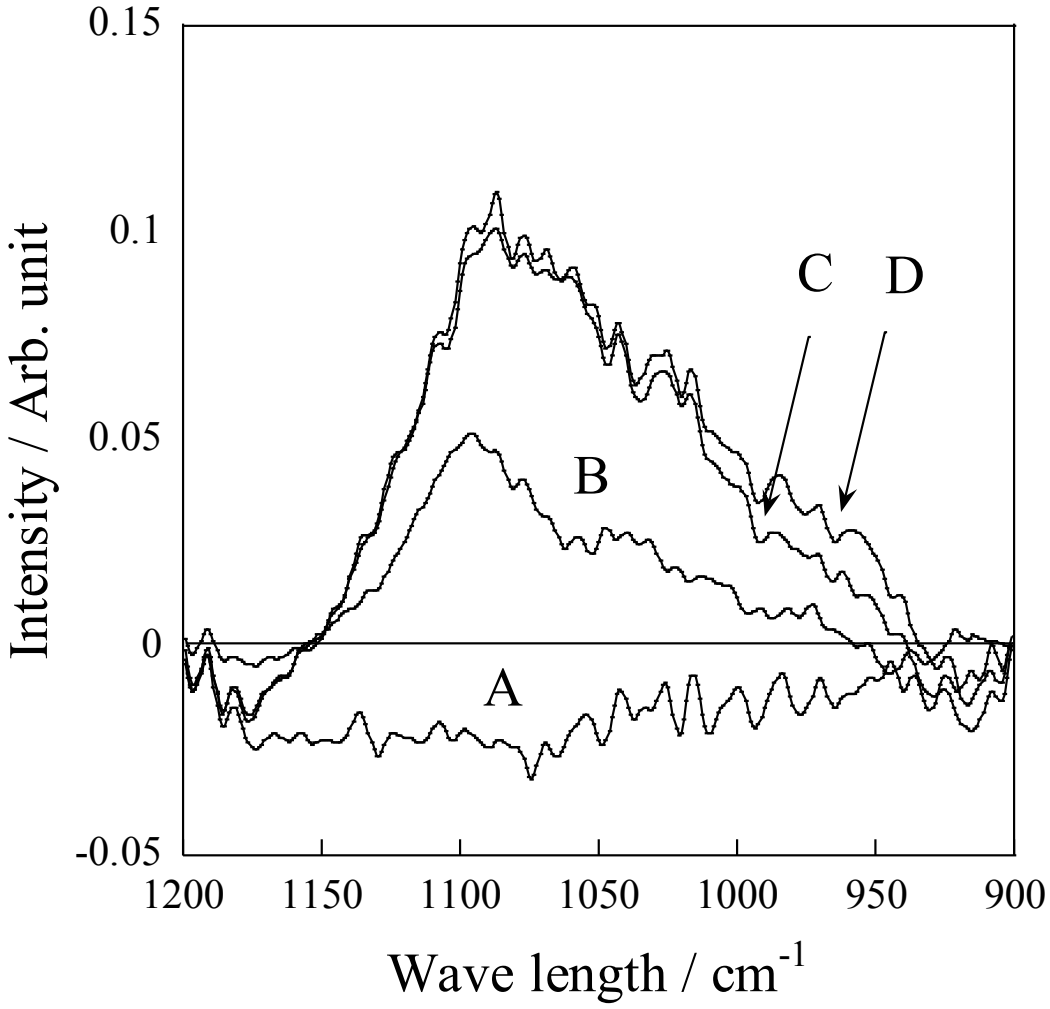

Figure 2-9 *In-situ* IR for CO_2-OCM in the electric field for changing the partial pressure of CO_2 over $La_{0.7}Ca_{0.3}AlO_{3-\delta}$ catalyst: (A) CH_4=50 mL min^{-1} before EF, (B) CH_4=50 mL min^{-1} after EF , (C) CH_4:CO_2=45:5 mL min^{-1} after EF, (D) CH_4:CO_2=35:15 mL min^{-1} after EF.

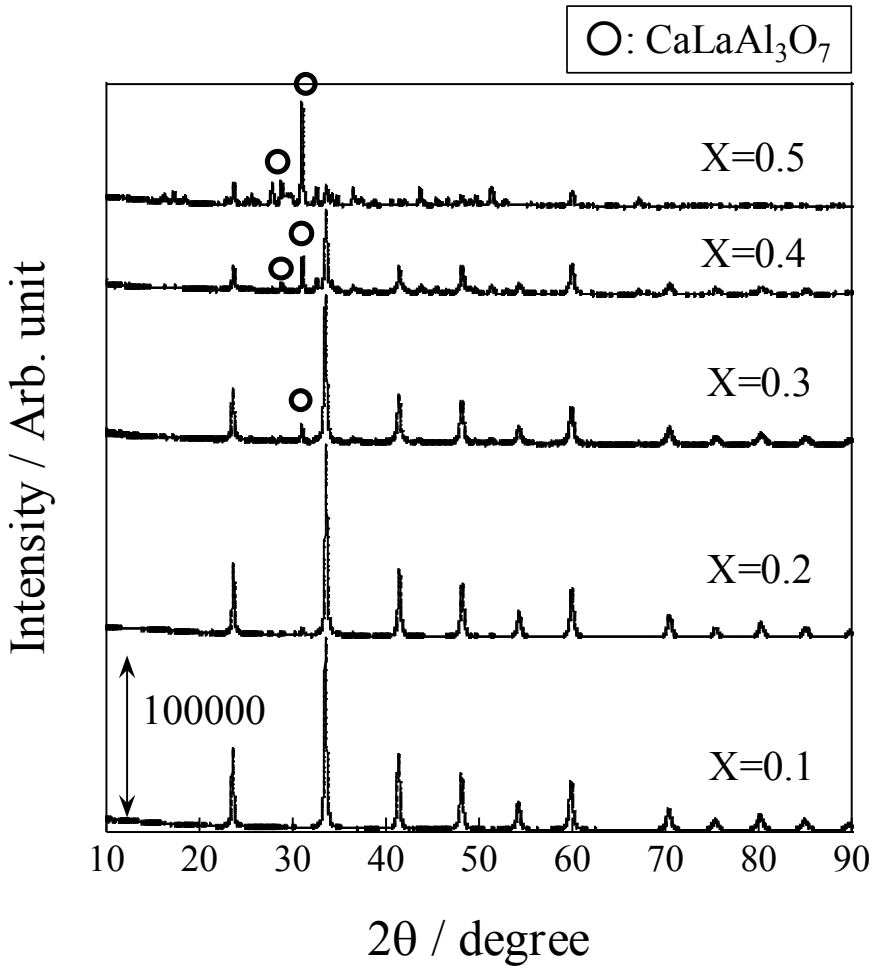

Figure 2-10 X-ray diffraction patterns for various $La_{1-X}Ca_XAlO_{3-\delta}$ catalysts.

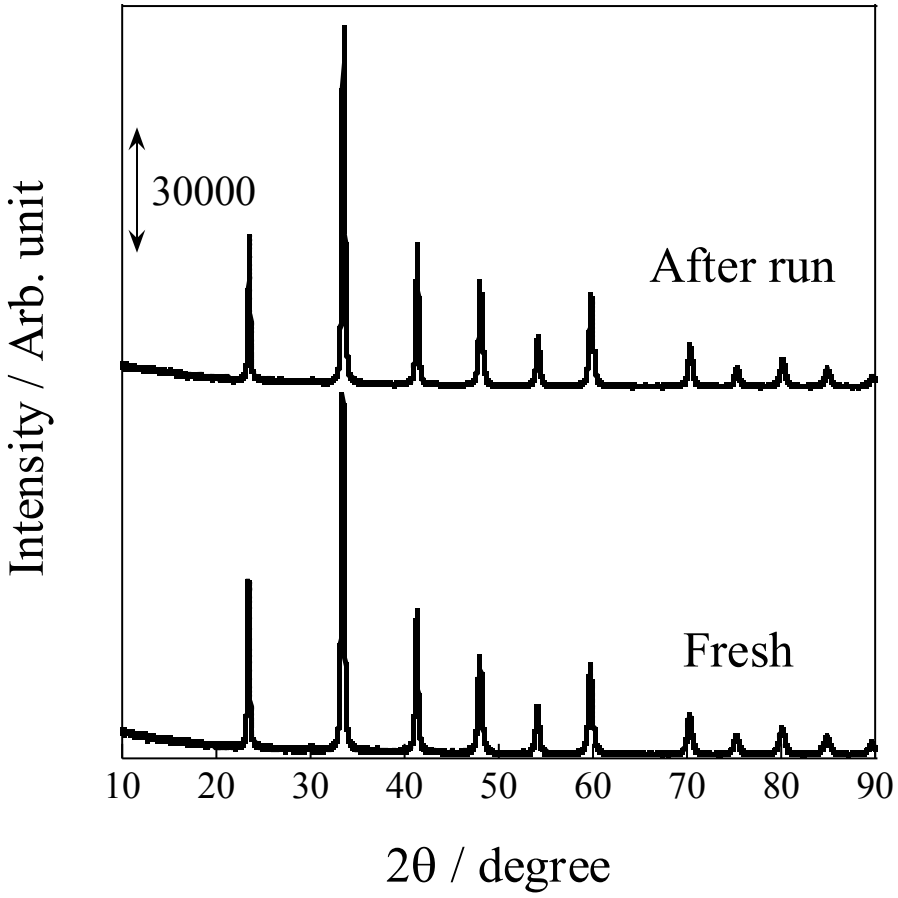

Figure 2-11 XRD profile over $La_{0.9}Ca_{0.1}AlO_{3-\delta}$ before/after the reaction

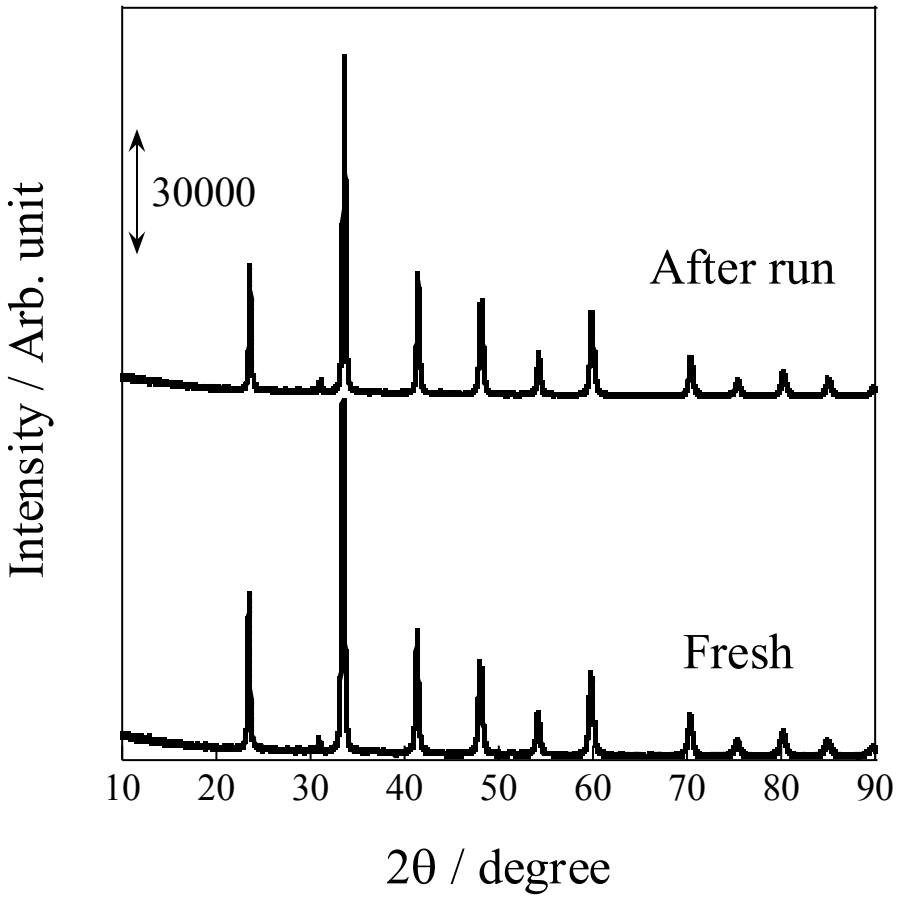

Figure 2-12 XRD profile over $La_{0.8}Ca_{0.2}AlO_{3-\delta}$ before/after the reaction

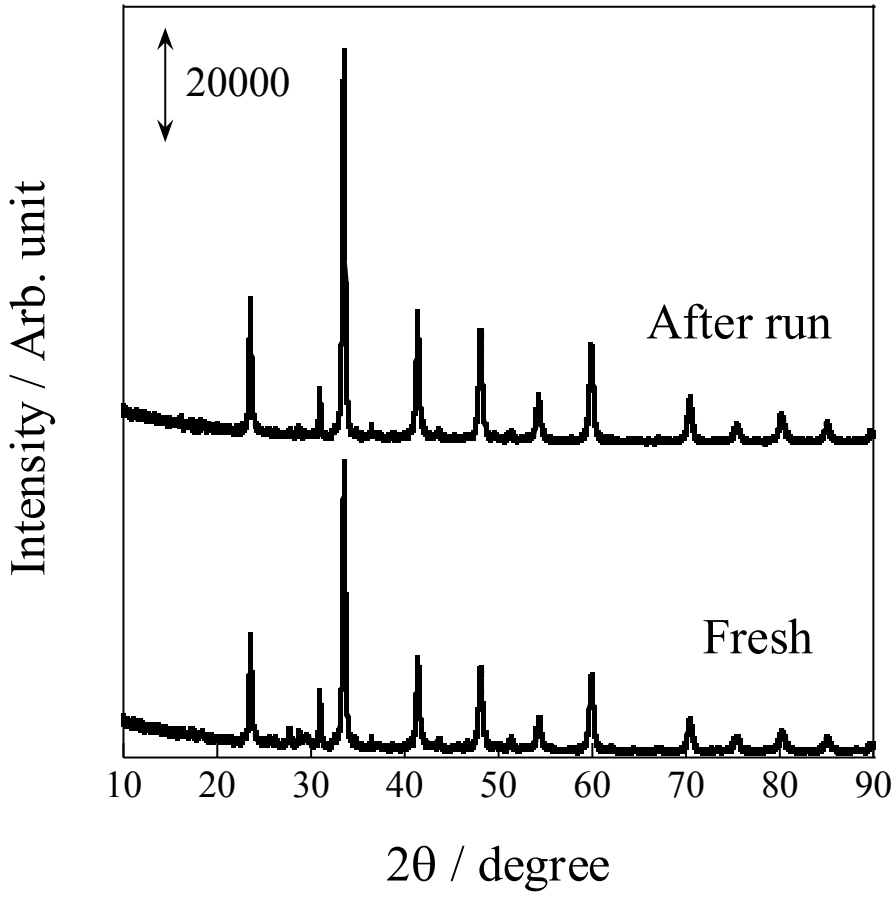

Figure 2-13 XRD profile over $La_{0.7}Ca_{0.3}AlO_{3-\delta}$ before/after the reaction

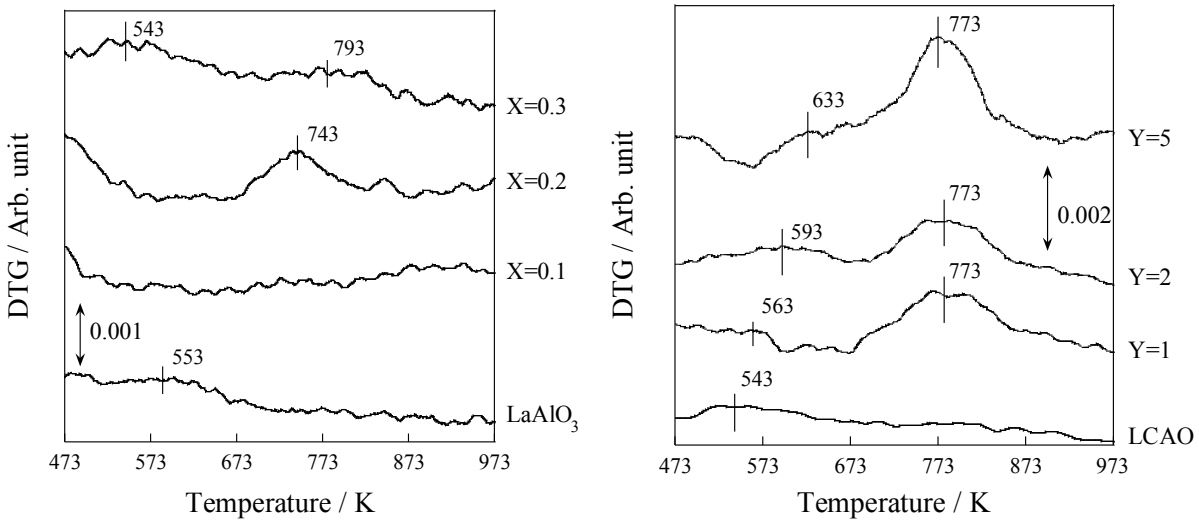

Figure 2-14 Results of thermogravimetry during temperature programmed desorption of carbon dioxide over (Left) various $La_{1-x}Ca_xAlO_{3-\delta}$ catalyst and (Right) various *y*-wt%Ca/LCAO catalysts.

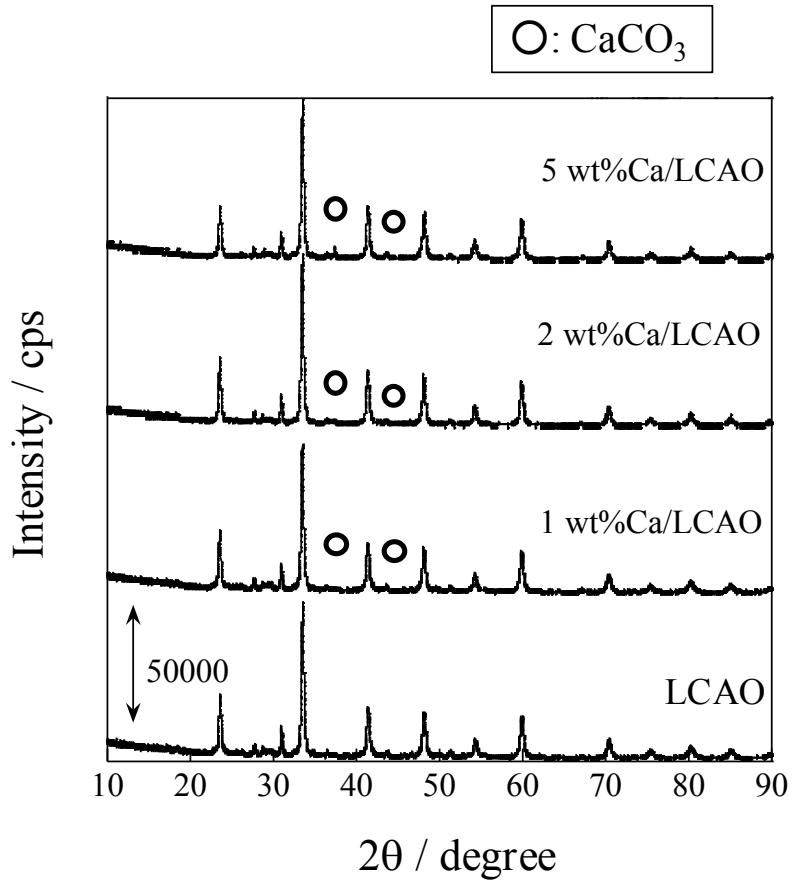

Figure 2-15 XRD profile over various supporting amounts of Ca on $La_{0.7}Ca_{0.3}AlO_{3-\delta}$

Appendix: XPS results

A-1 XPS results for various amounts of doped Ca in $LaAlO_3$ catalysts

In order to investigate the electron states of composed elements of various amounts of doped Ca in $LaAlO_3$ catalysts, XPS (X-ray photoelectron spectroscopy) was conducted. (as shown in the following figures: La $3d_{5/2}$ band, Figure A1; Ca 2p band, Figure A2; Al 2p band, Figure A3; C 1s band, Figure A4; O 1s band, Figure A5) [48-53] From the result of Figure A1, increasing Ca doped amounts in $LaAlO_3$ resulted in increasing the intensity of La carbonate peak, indicated the effect of carbonate pool for Ca sites. [18] On the other hand, the peak from La-O in perovskite oxide structure including the satellite peak remained unchanged. From the result of Figure A2, increasing Ca doped amounts up in $LaAlO_3$ up to 0.3 also resulted in increasing the intensity of Ca carbonate peak, but this peak decreased in 0.4. Combined with the result of XRD (Figure 10, shown again), the unpurified phase was not possibly suitable for generating the carbonate pool. From the result of Figure A3, increasing Ca doped amounts in $LaAlO_3$ up to 0.3 resulted in increasing the intensity of Al carbonate and hydroxide peaks, Al^{3+} ion. [54] On the other hand, in $La_{0.6}Ca_{0.4}AlO_{3-\delta}$, these structures did not form because the peaks from Al^{3+} ion were not observed. From the result of Figure A4, increasing Ca doped amounts in $LaAlO_3$ up to 0.3 resulted in increasing the intensity of the peak from -COO- unit. In $La_{0.6}Ca_{0.4}AlO_{3-\delta}$, the peak from carbon dioxide adsorbed on the catalyst surface remained observed. Finally, from the result of Figure A5, increasing Ca doped amounts in $LaAlO_3$ resulted in decreasing the ratio of surface carbon (O_{sur}), and increasing the ratio of carbonate and hydroxide thanks to increasing the basic sites. Also, from the result of the surface atom ratio calculated from XPS measurement (as shown in Table A1), more Ca atoms existed on the catalysis surface than in catalysts preparation.

A-2 XPS results for $La_{0.7}Ca_{0.3}AlO_{3-\delta}$ catalysts in various pretreatment conditions

In previous reports, CO_2-OCM proceeded in redox mechanism by CO_2 adsorption on the lattice defects over certain kinds of catalysts such as Ca-CeO_2. [18] So, we investigate the relationship between the lattice defect in $La_{0.7}Ca_{0.3}AlO_{3-\delta}$ catalyst and catalytic activities in the electric field from XPS measurements. XPS results for the catalysts before the reaction in various pretreatment conditions were shown in the following figures: La $3d_{5/2}$ band, Figure A6; Ca 2p band, Figure A7; Al 2p band, Figure A8; C 1s band, Figure A9; O 1s band, Figure A10. From the result of Figure A6, the Ca 2p peaks derived from carbonate for the catalysts in

O_2 and CO_2 preparation were higher than any other peaks. From the result of Figure A7, the Al 2p peak derived from hydroxide in O_2 preparation were higher than any other peaks. From the result of Figure A8, the C 1s peaks derived from hydroxyl group in Ar and H_2 preparation were higher, and the peaks derived from carbonate in CO_2 and O_2 preparation than any other peaks. Therefore, the electron states on the catalyst surface changed in various preparation conditions. Next, nonstoichiometric ratio of oxygen, denoted as δ, were calculated from XPS spectrum by the following equation and we investigated the relationship between δ and the catalytic activities. (as shown in Figure A11) [55]

$$\delta = 3 - \frac{2\,[O_{sur}]}{[La]+[Ca]+[Al]} \qquad \text{(eq. A1)}$$

(denoted [ ] as the surface concentration ratio of the perovskite cations calculated from XPS results)

As a result, increasing δ resulted in increasing CH_4 and CO_2 conversions, but C_2 selectivity decreased. This means that the oxygen defects which can be strongly adsorbed by CO2 increases, and DR reaction proceeded at the active sites.

Next, XPS results for the catalysts after the reaction in various pretreatment conditions were shown in the following figures: La $3d_{5/2}$ band, Figure A12; Ca 2p band, Figure A13; Al 2p band, Figure A14; C 1s band, Figure A15; O 1s band, Figure A16. As a result, after the reaction in the electric field, all the peaks derived from carbonate increased, compared to those before the reaction. These trends were in accordance with the result of in-situ IR. (Figure 7, shown again) From the result of Figure A16, the O 1s peaks derived from lattice oxygen (O_{lat}) decreased after the reaction in the electric field. Therefore, the recovery rate of oxygen defects by CO_2 in DR reaction may be law or this path may be irreversible. In order to investigate the redox mechanism, the catalytic tests in the electric field for changing time in various preparation conditions were conducted. (as shown in Figure A17) As a result, the recovery rate of oxygen defects was low and the catalytic activities decreased over the time. Also, the degradation rates of the catalytic activity in O_2 and CO_2 preparation were higher than in any other preparation. Therefore, the active sites for activating CH_4 easily decreased due to generate carbonate.

References:

[48] S. Badrinarayanan, A.B. Mandale, S.R. Sainkar, N.R. Pavaskar, V. Ramaswamy, The stability of the surface of La_2CuO_4 to reactions with adsorbed n-butyl amine: X-ray photoelectron spectroscopy study, J. Mat. Res. 9 (1994) 1140–1146.

[49] K. Tabata, Y. Hirano, E. Suzuki, XPS studies on the oxygen species of $LaMn_{1-x}Cu_xO_{3+\lambda}$, Appl. Catal. A: Gen. 170 (1998) 245–254.

[50] J.-C. Dupin, D. Gonbeau, P. Vinatier, A. Levasseur, Systematic XPS studies of metal oxides, hydroxides and peroxides, Phys. Chem. Phys. Chem. 6 (2000) 1319–1324.

[51] P.A.W. van der Heide, Systematic x-ray photoelectron spectroscopic study of $La_{1-x}Sr_x$-based perovskite-type oxides, Surf. Interface Anal. 33 (2002) 414–425.

[52] M.F. Sunding, K. Hadidi, S. Diplas, O.M. Løvvik, T.E. Norby, A.E. Gunnæs, XPS characterization of *in-situ* treated lanthanum oxide and hydroxide using tailored charge referencing and peak fitting procedures, J. Electron Spectrosc. 184 (2011) 399–409.

[53] R. Koirala, K.R. Gunugunuri, S.E. Pratsinis, P.G. Smirniotis, Effect of zirconia doping on the structure and stability of CaO-based sorbents for CO_2 capture during extended operating cycles, J. Phys. Chem. C 115 (2011) 24804–24812.

[54] E. Paparazzo, XPS, AES and EELS studies of Al surfaces, Vacuum 62 (2001) 47–60.

[55] N.A. Merino, B.P. Barbero, P. Eloy, L.E. Cadús, $La_{1-x}Ca_xCoO_3$ perovskite-type oxides: Identification of the surface oxygen species by XPS, Appl. Surf. Sci. 253 (2006) 1489–1493.

Table A1 Surface atom ratio from XPS measurement in various Ca-doped $LaAlO_3$.

Ca doped amounts	La	Ca	Al	O	C	Ca/(La+Ca)
0	13.7	0	13.1	58.5	14.7	0
0.1	8.2	2.3	13.8	58.7	17.1	0.22
0.2	7.1	4.1	11.9	58.7	18.2	0.36
0.3	5.7	5.0	10.7	52.2	26.4	0.47
0.4	4.3	6.0	10.6	51.2	27.8	0.58

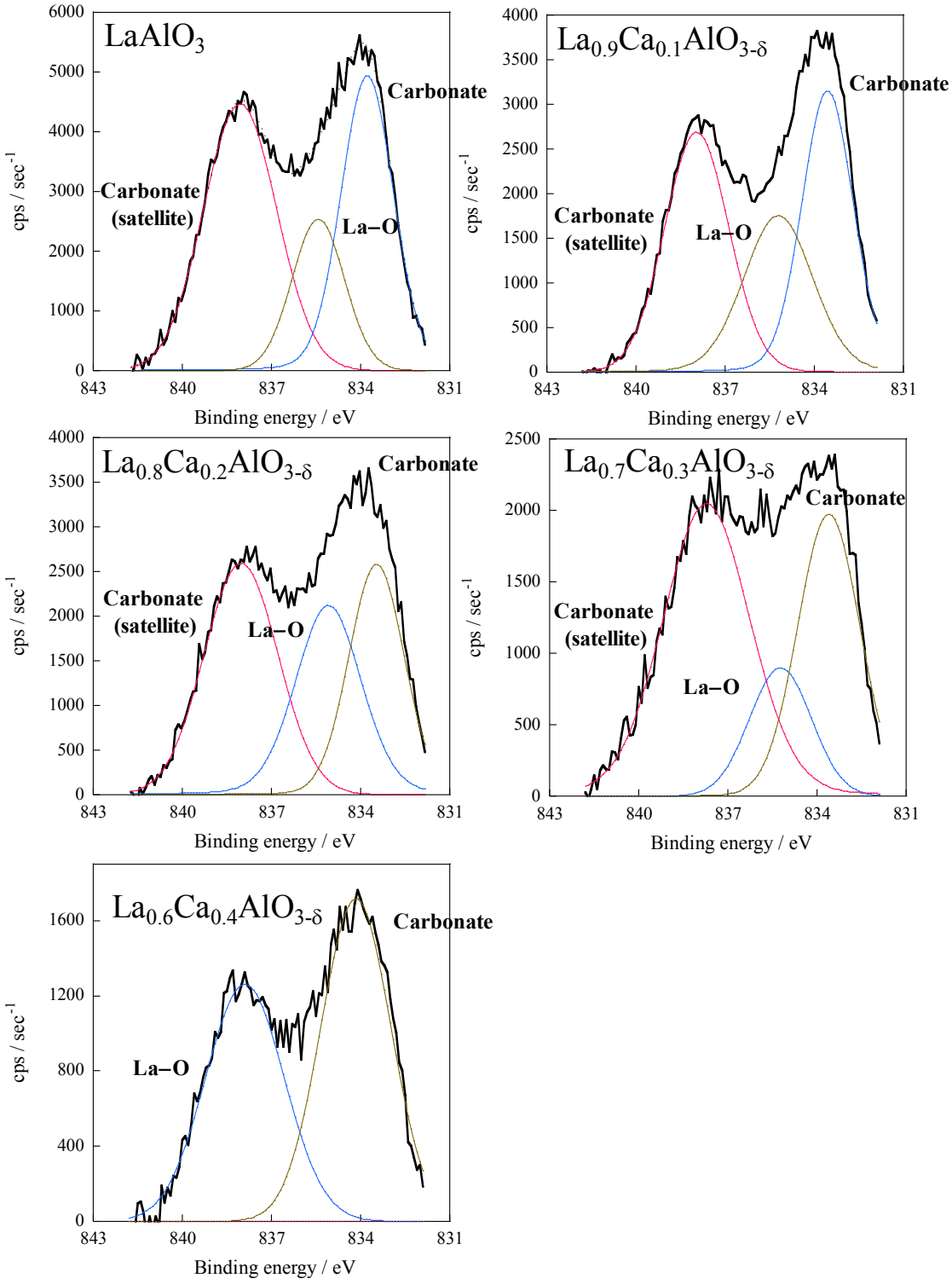

Figure A1 XPS spectra of La $3d_{5/2}$ band in various La perovskite oxides as made.

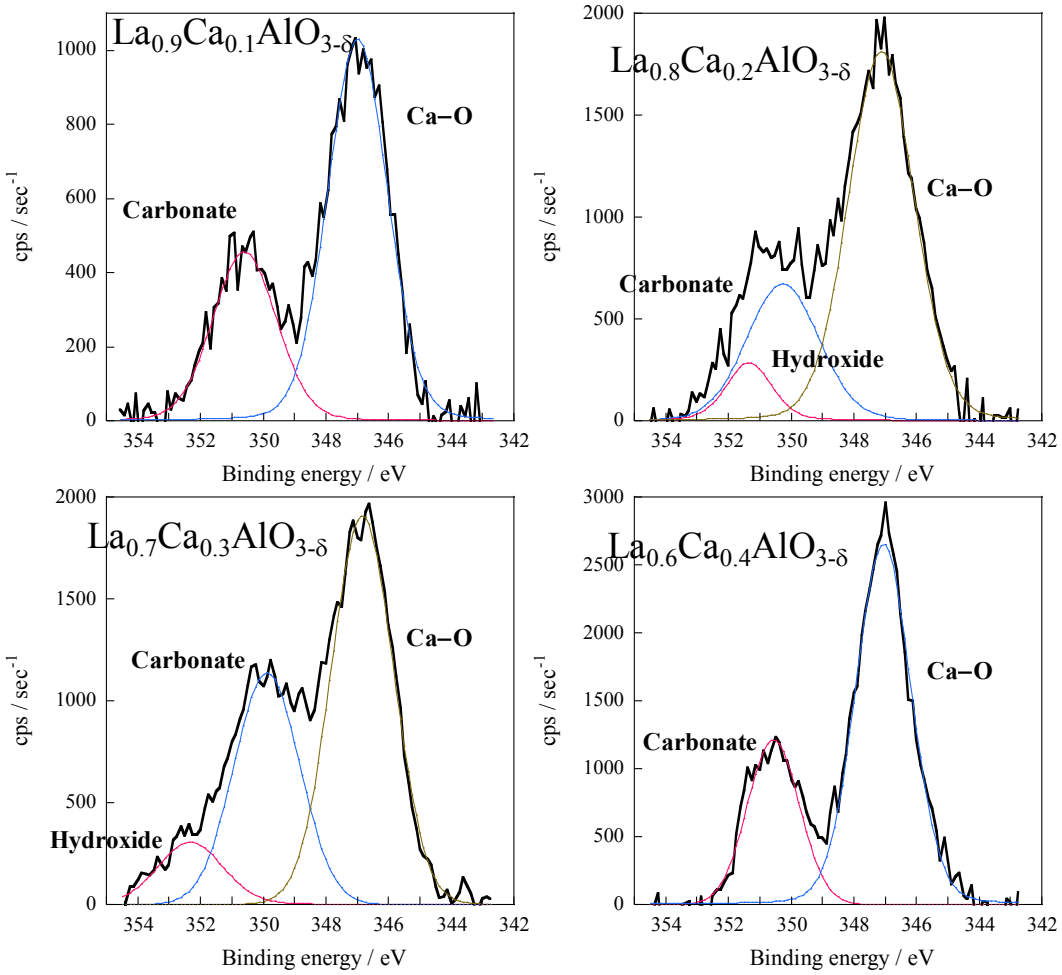

Figure A2 XPS spectra of Ca 2p band in various La perovskite oxides as made.

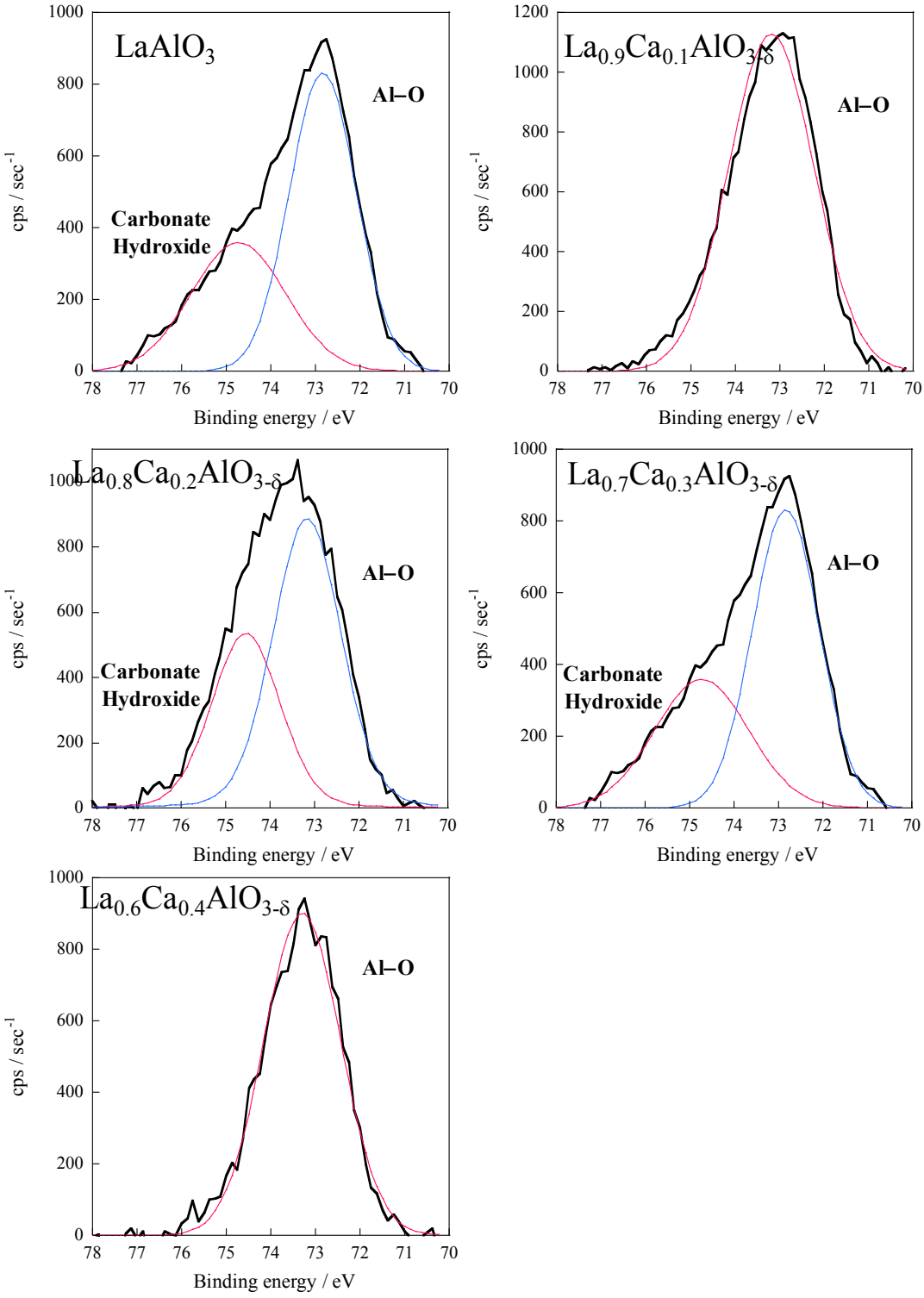

Figure A3 XPS spectra of Al 2p band in various La perovskite oxides as made.

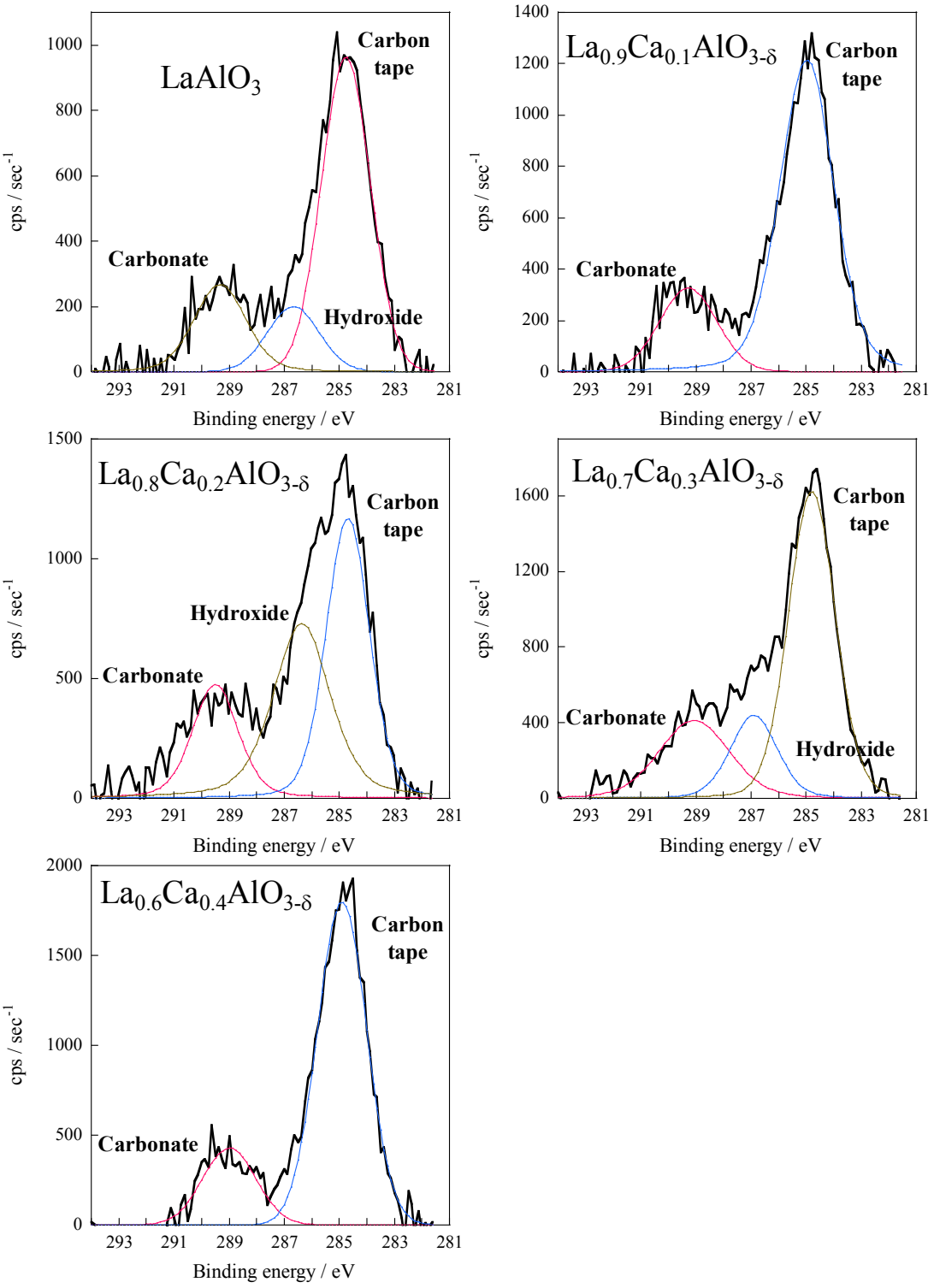

Figure A4 XPS spectra of C 1s band in various La perovskite oxides as made.

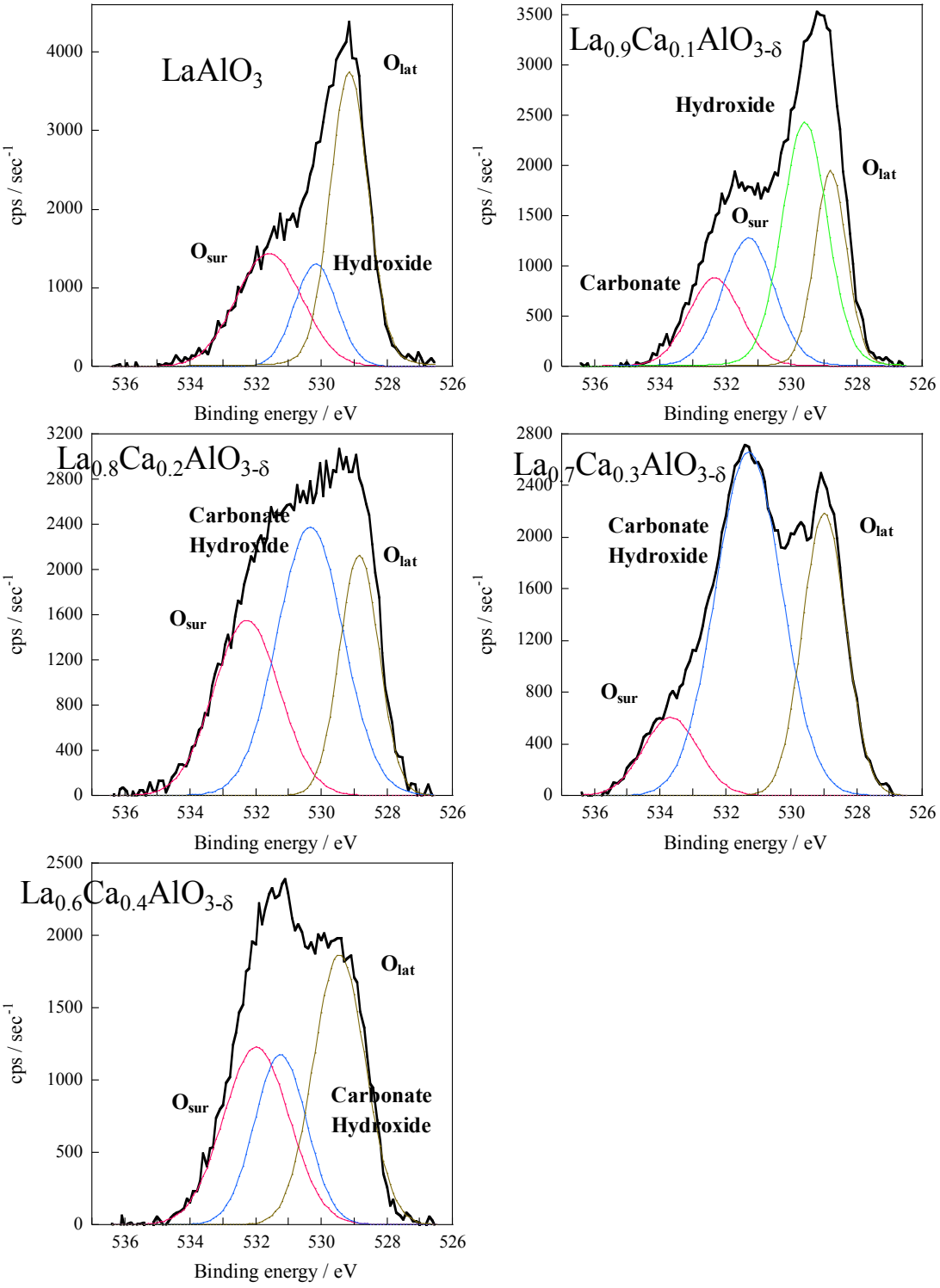

Figure A5 XPS spectra of O 1s band in various La perovskite oxides as made.

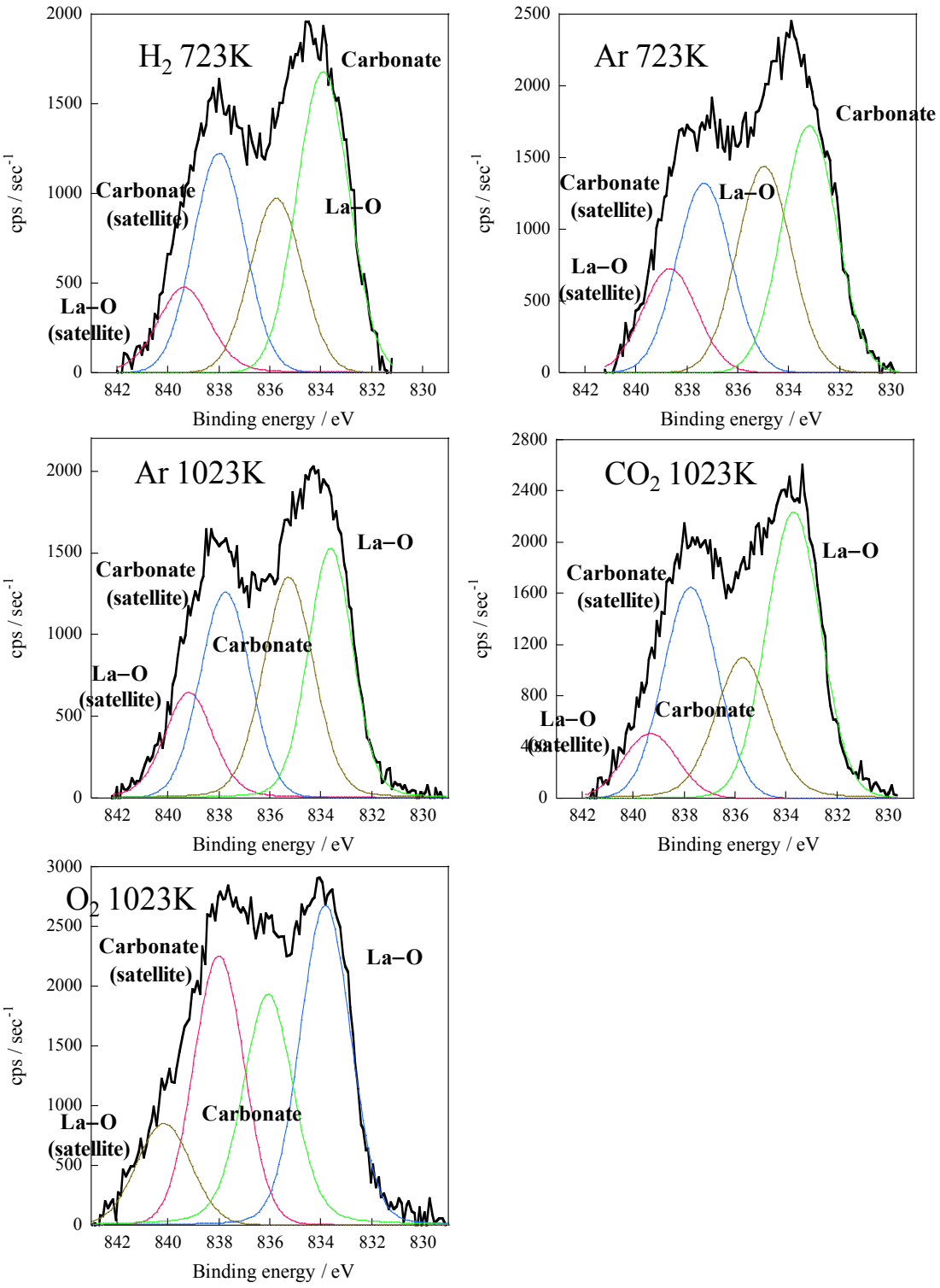

Figure A6 XPS spectra of La $3d_{5/2}$ band in $La_{0.7}Ca_{0.3}AlO_{3-\delta}$ in various preparation conditions.

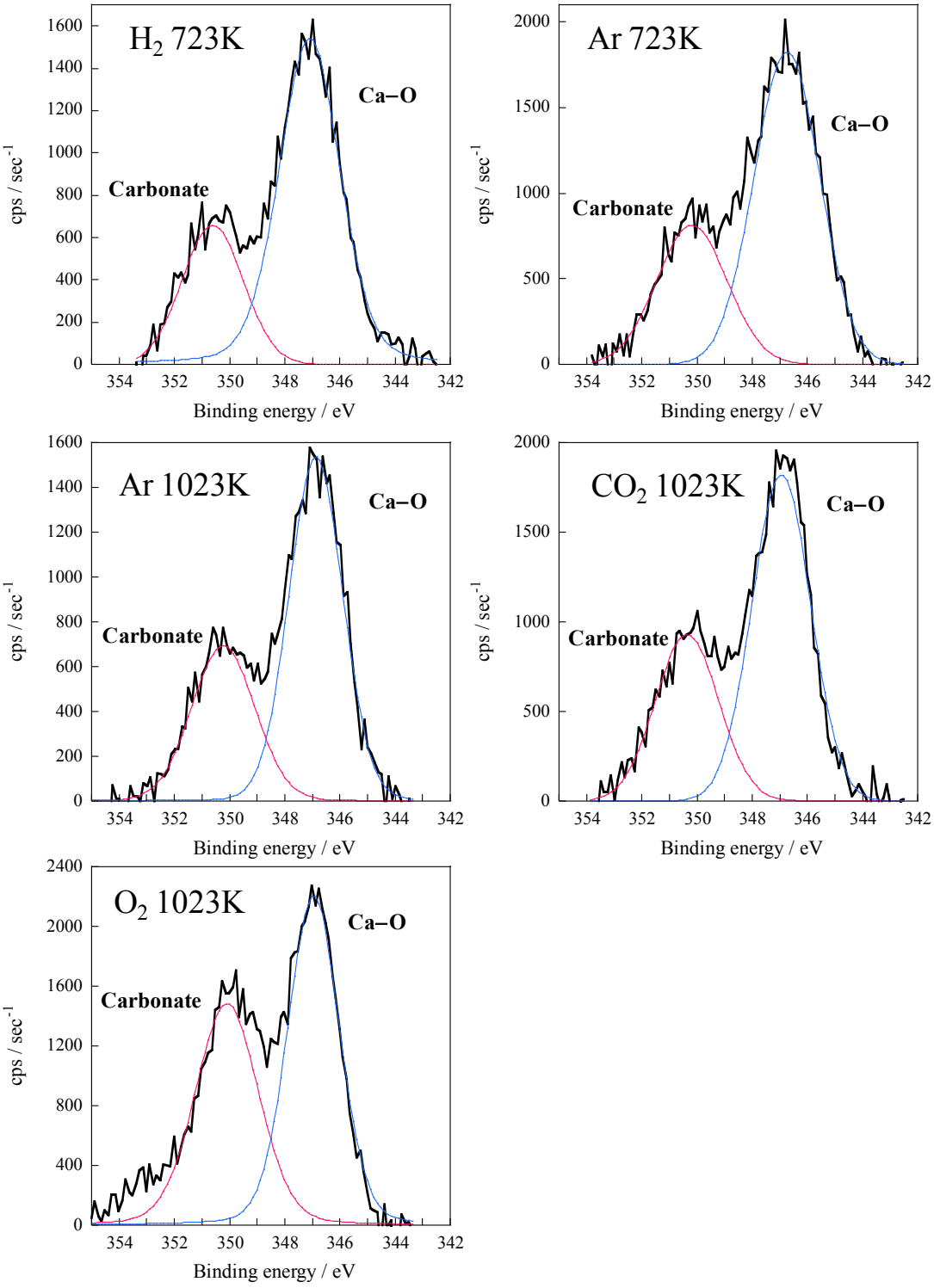

Figure A7 XPS spectra of Ca 2p band in $La_{0.7}Ca_{0.3}AlO_{3-\delta}$ in various preparation conditions.

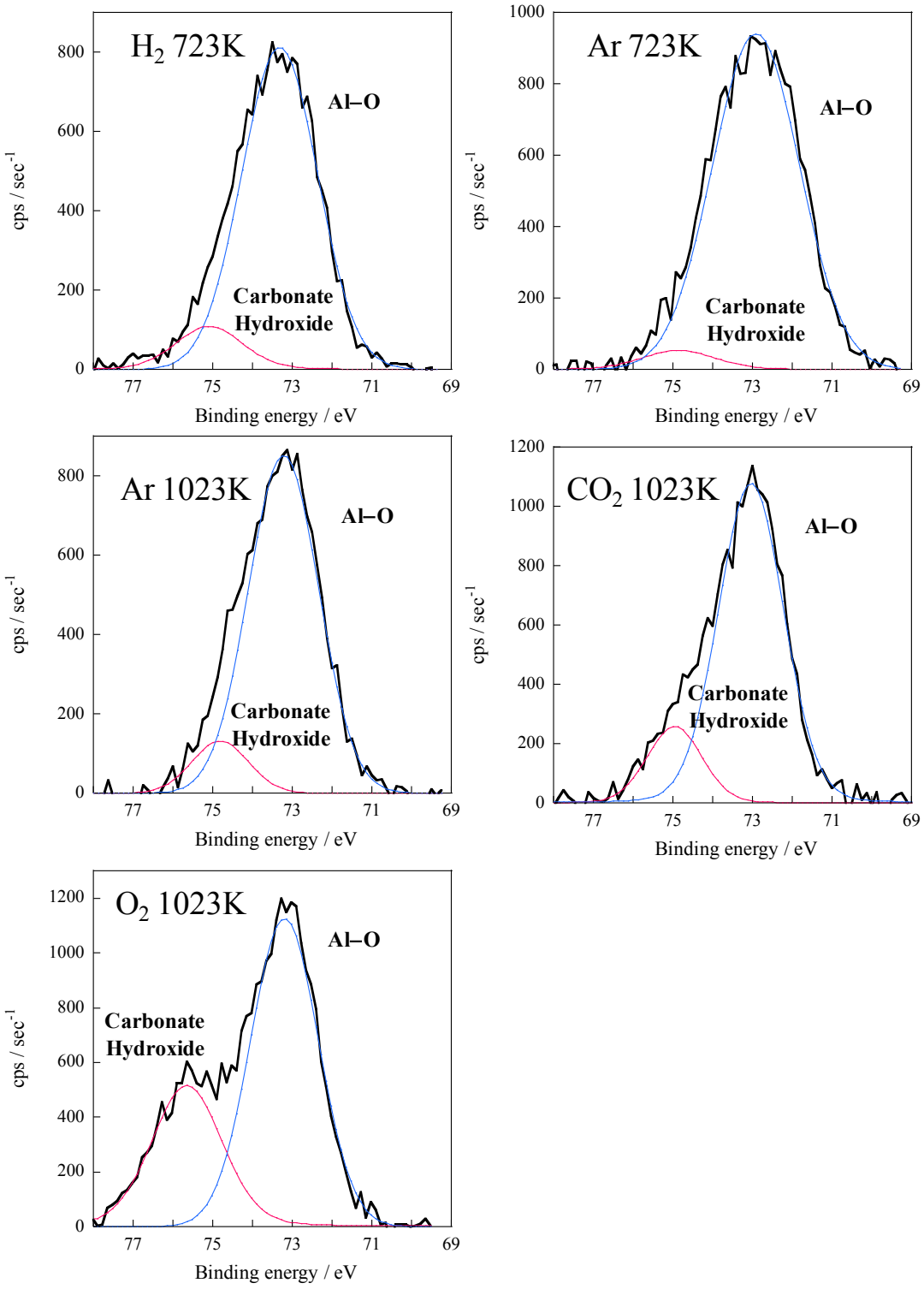

Figure A8 XPS spectra of Al 2p band in $La_{0.7}Ca_{0.3}AlO_{3-\delta}$ in various preparation conditions.

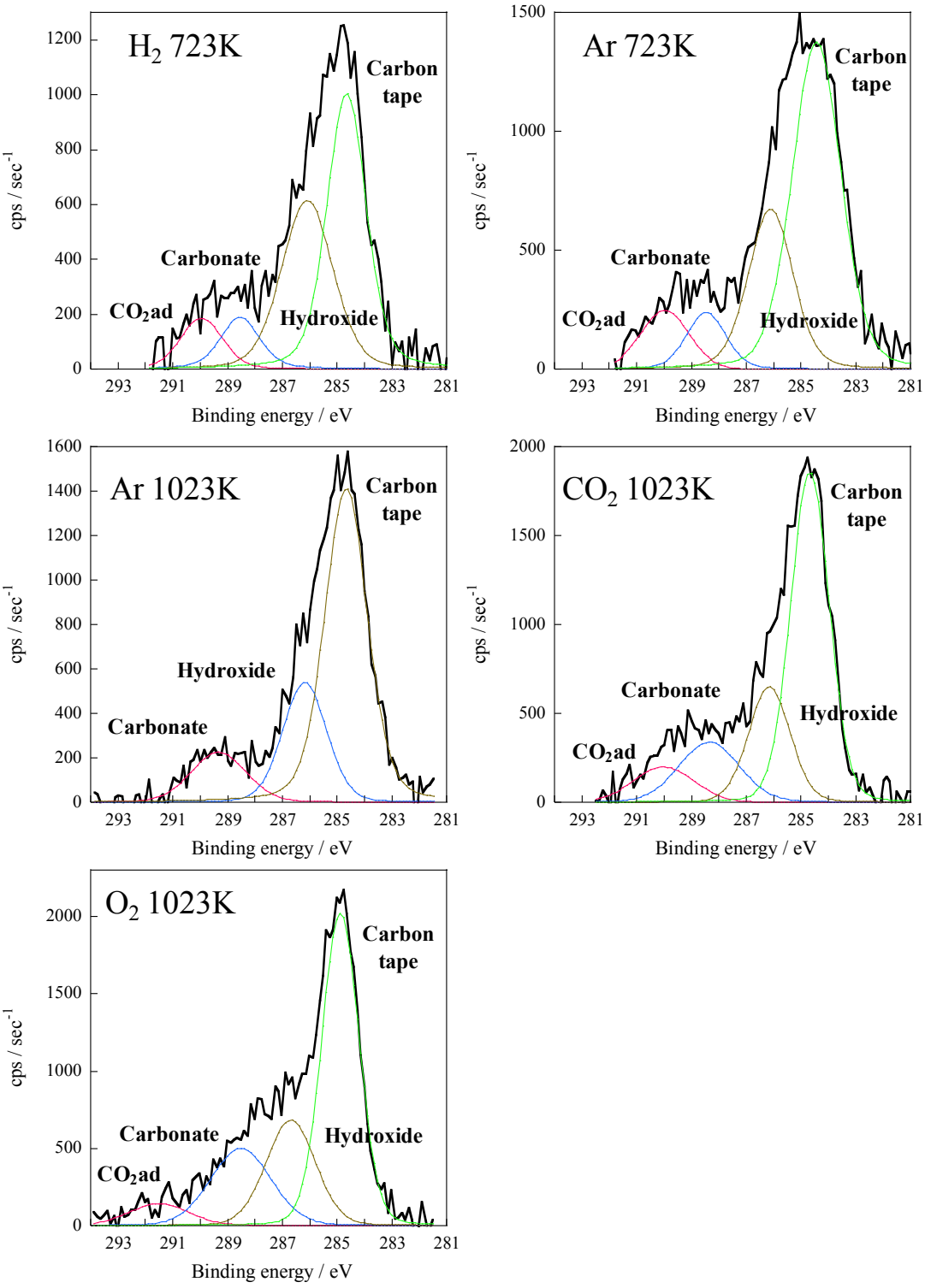

Figure A9 XPS spectra of C 1s band in $La_{0.7}Ca_{0.3}AlO_{3-\delta}$ in various preparation conditions.

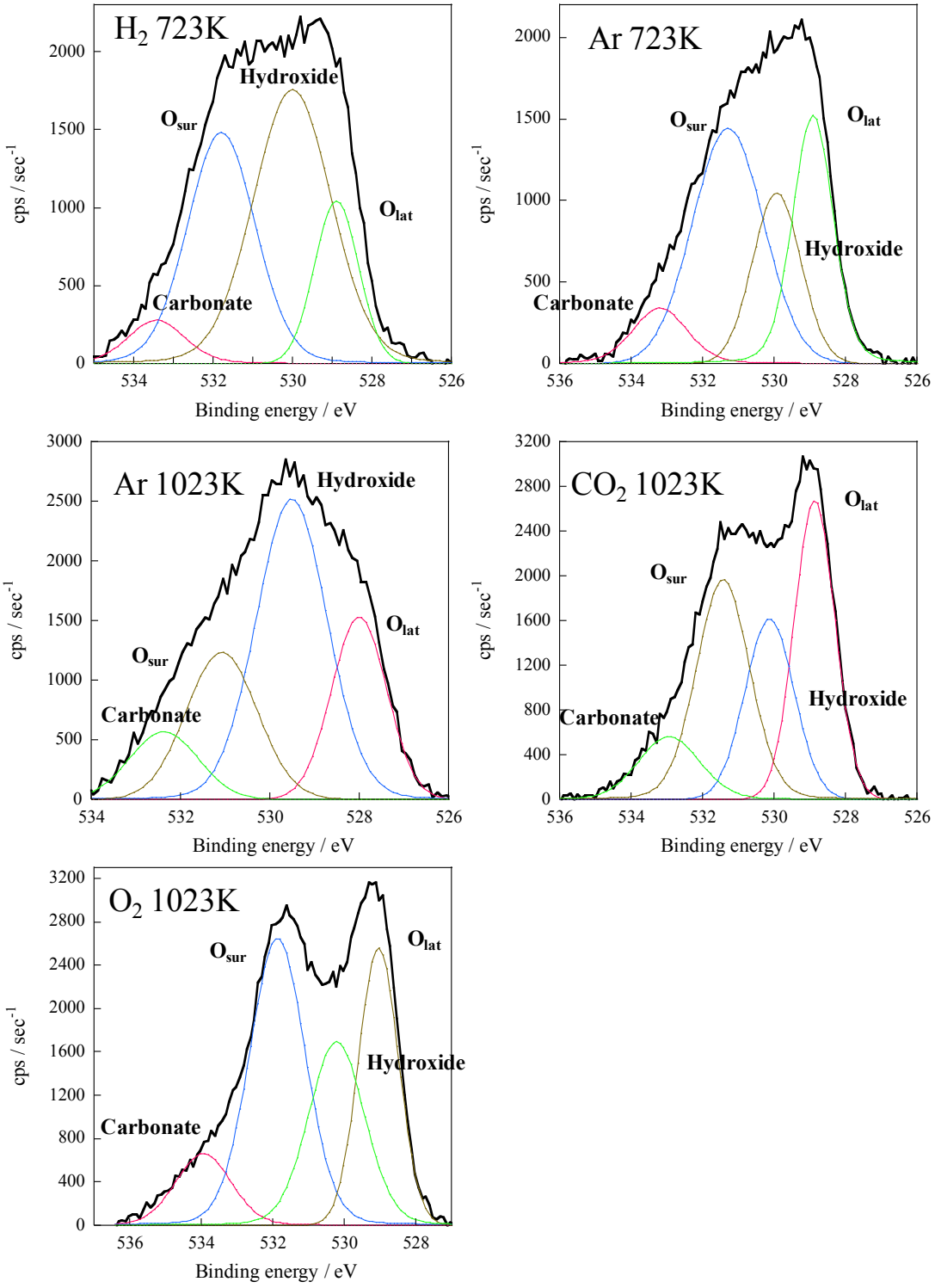

Figure A10 XPS spectra of O 1s band in $La_{0.7}Ca_{0.3}AlO_{3-\delta}$ in various preparation conditions.

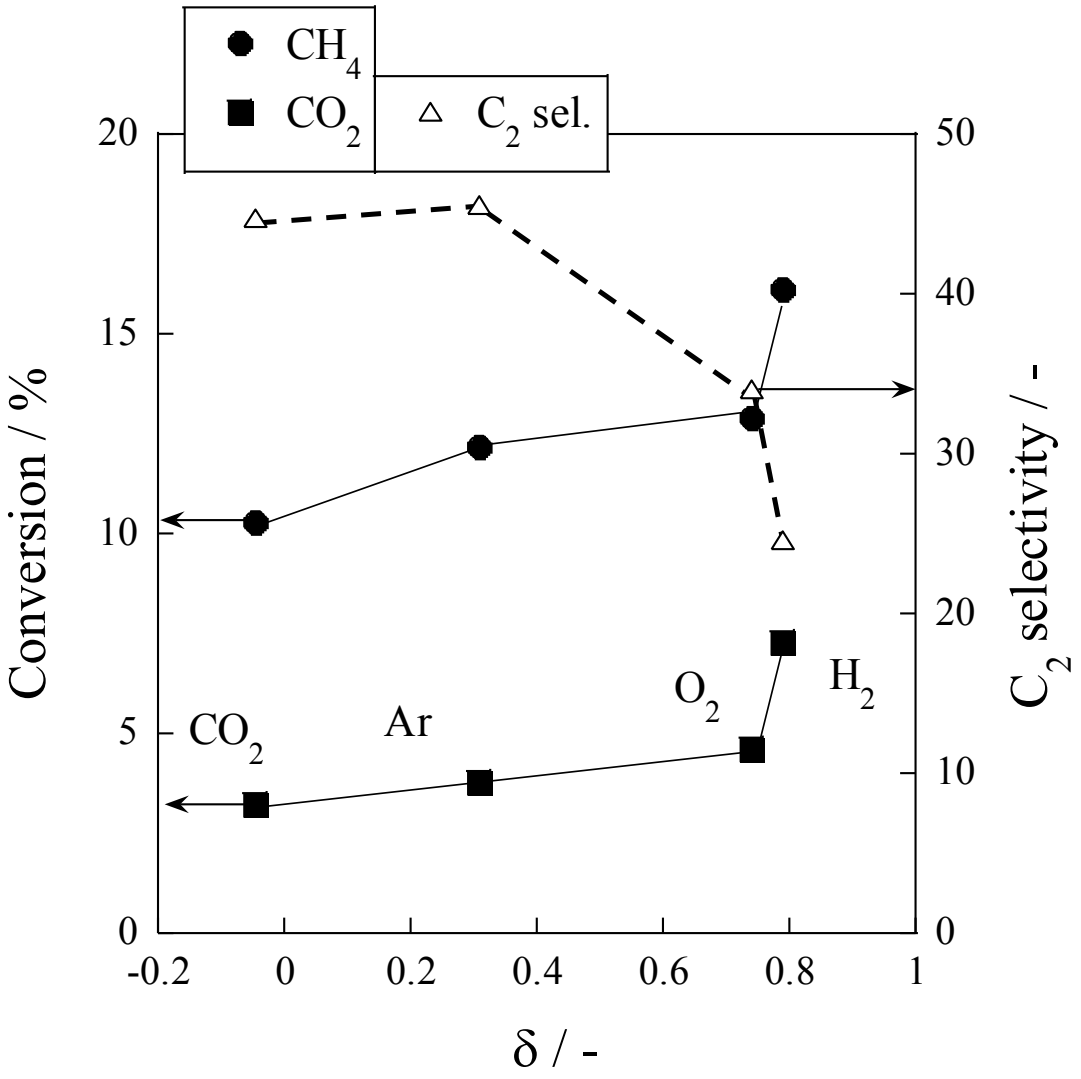

Figure A11 The interaction between oxygen non-stoichiometric property of δ and CO_2-OCM activity in the electric field over $La_{0.7}Ca_{0.3}AlO_{3-\delta}$ catalyst in various preparation method.

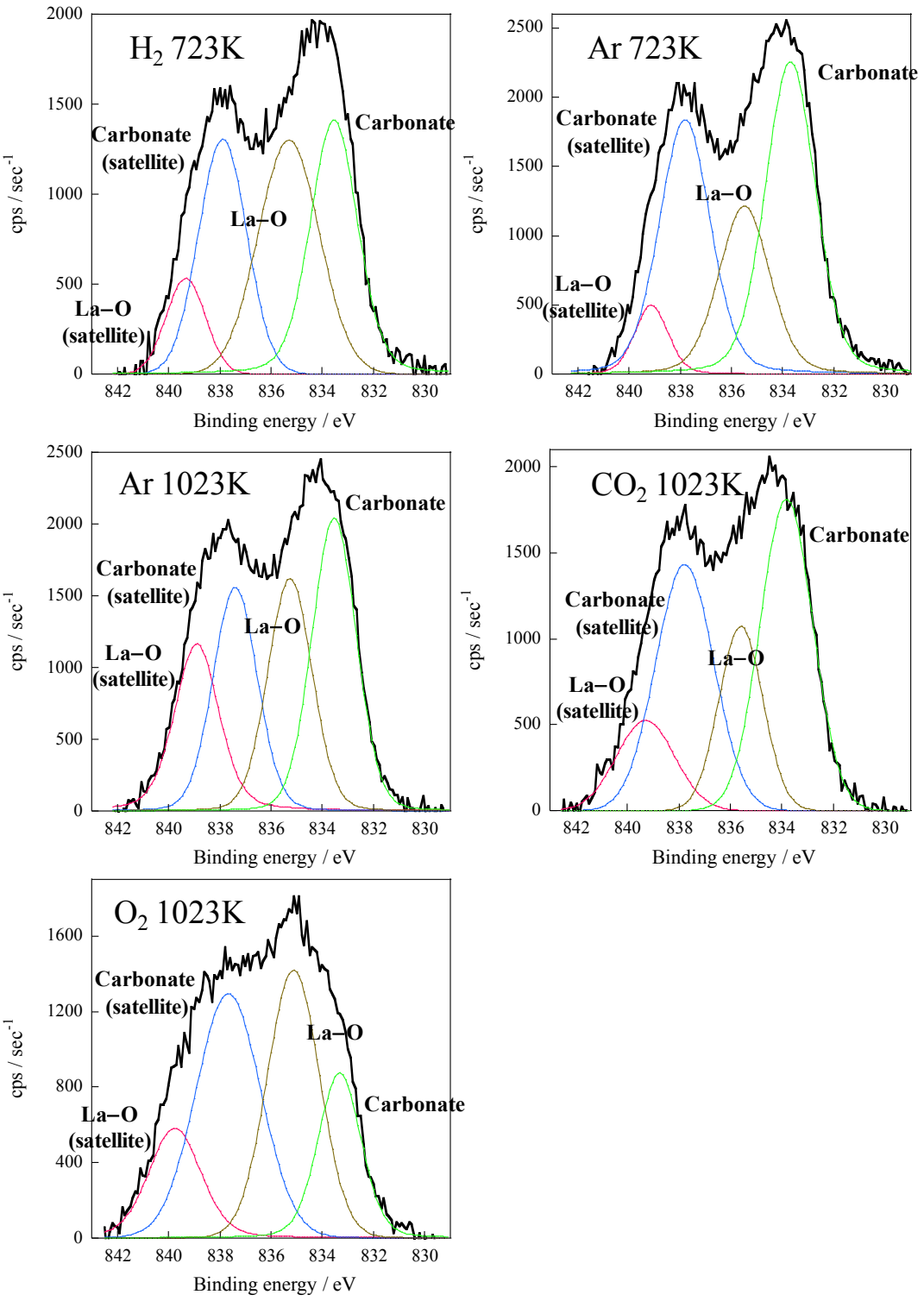

Figure A12 XPS spectra of La $3d_{5/2}$ band in $La_{0.7}Ca_{0.3}AlO_{3-\delta}$ in various preparation conditions after CO_2-OCM in the electric field.

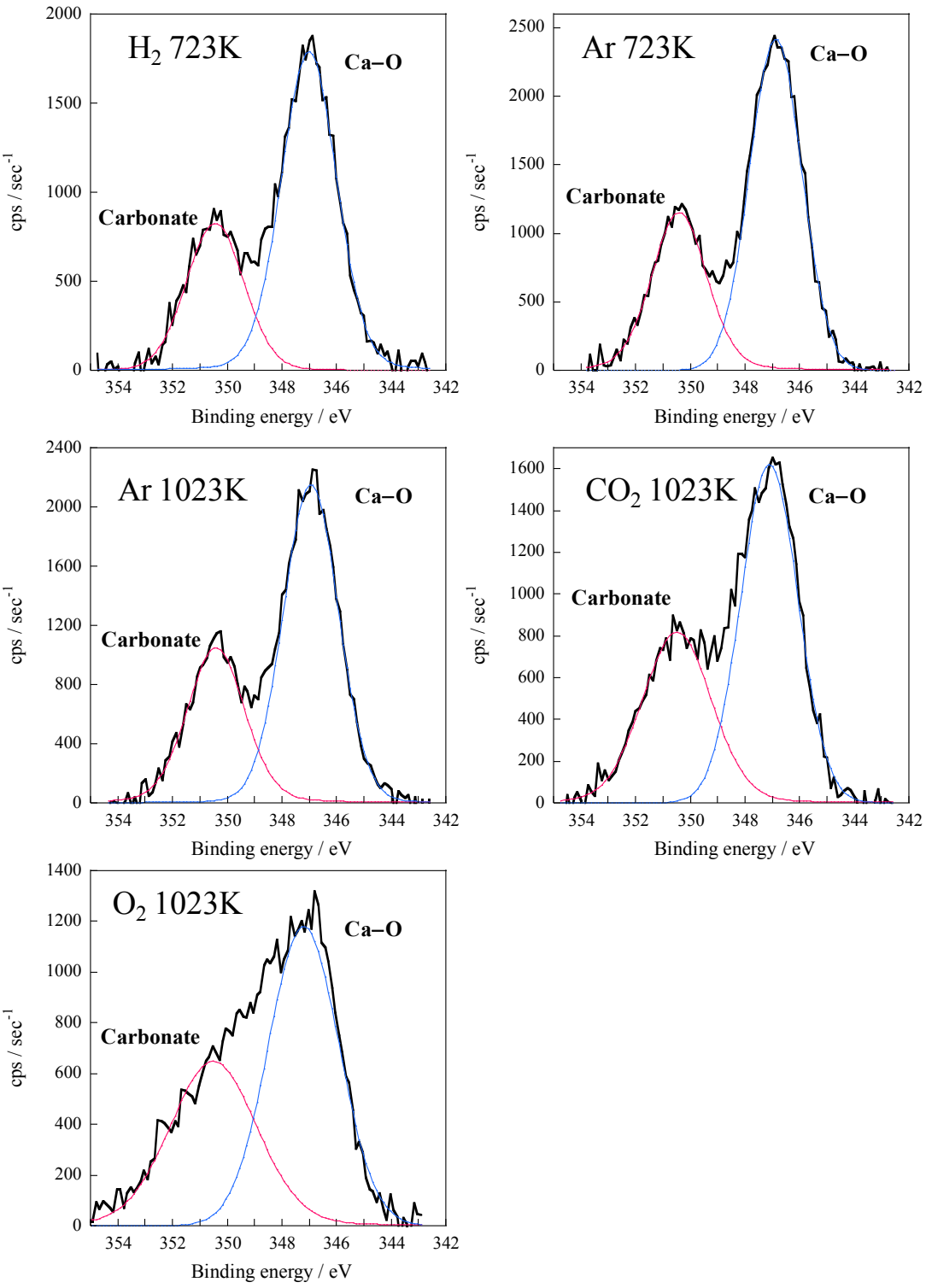

Figure A13 XPS spectra of Ca 2p band in $La_{0.7}Ca_{0.3}AlO_{3-\delta}$ in various preparation conditions after CO_2-OCM in the electric field.

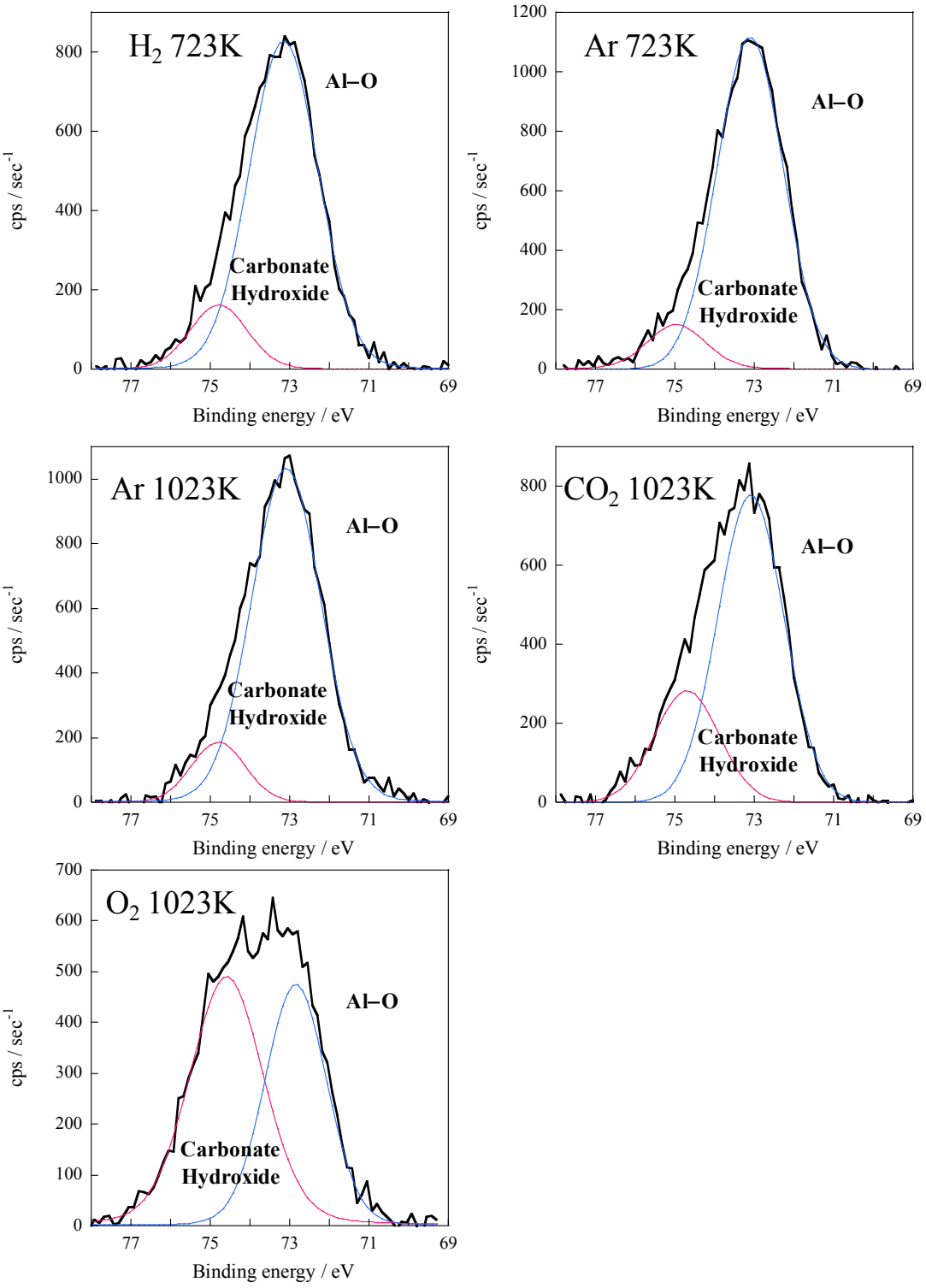

Figure A14 XPS spectra of Al 2p band in $La_{0.7}Ca_{0.3}AlO_{3-\delta}$ in various preparation conditions after CO_2-OCM in the electric field.

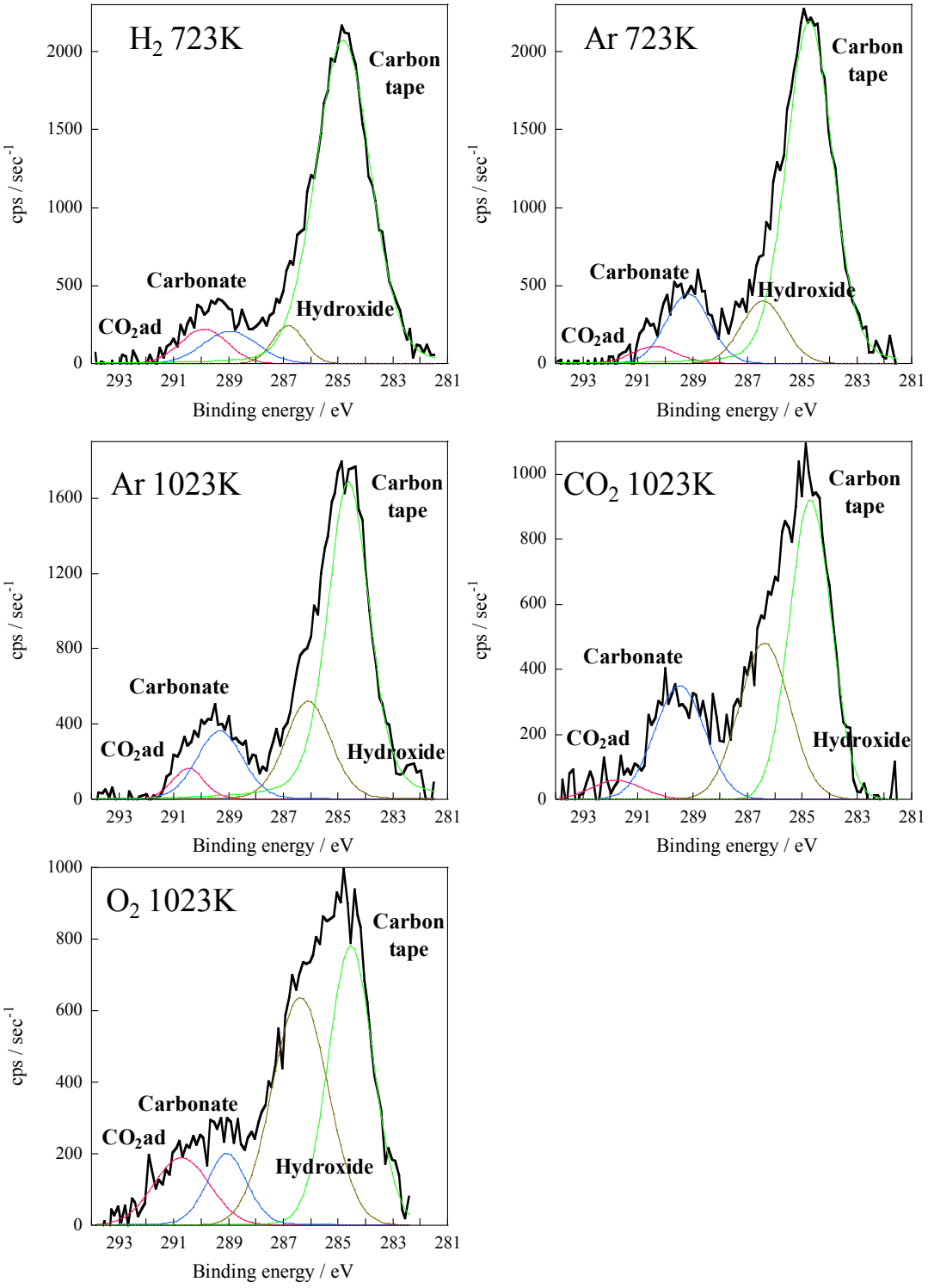

Figure A15 XPS spectra of C 1s band in $La_{0.7}Ca_{0.3}AlO_{3-\delta}$ in various preparation conditions after CO_2-OCM in the electric field.

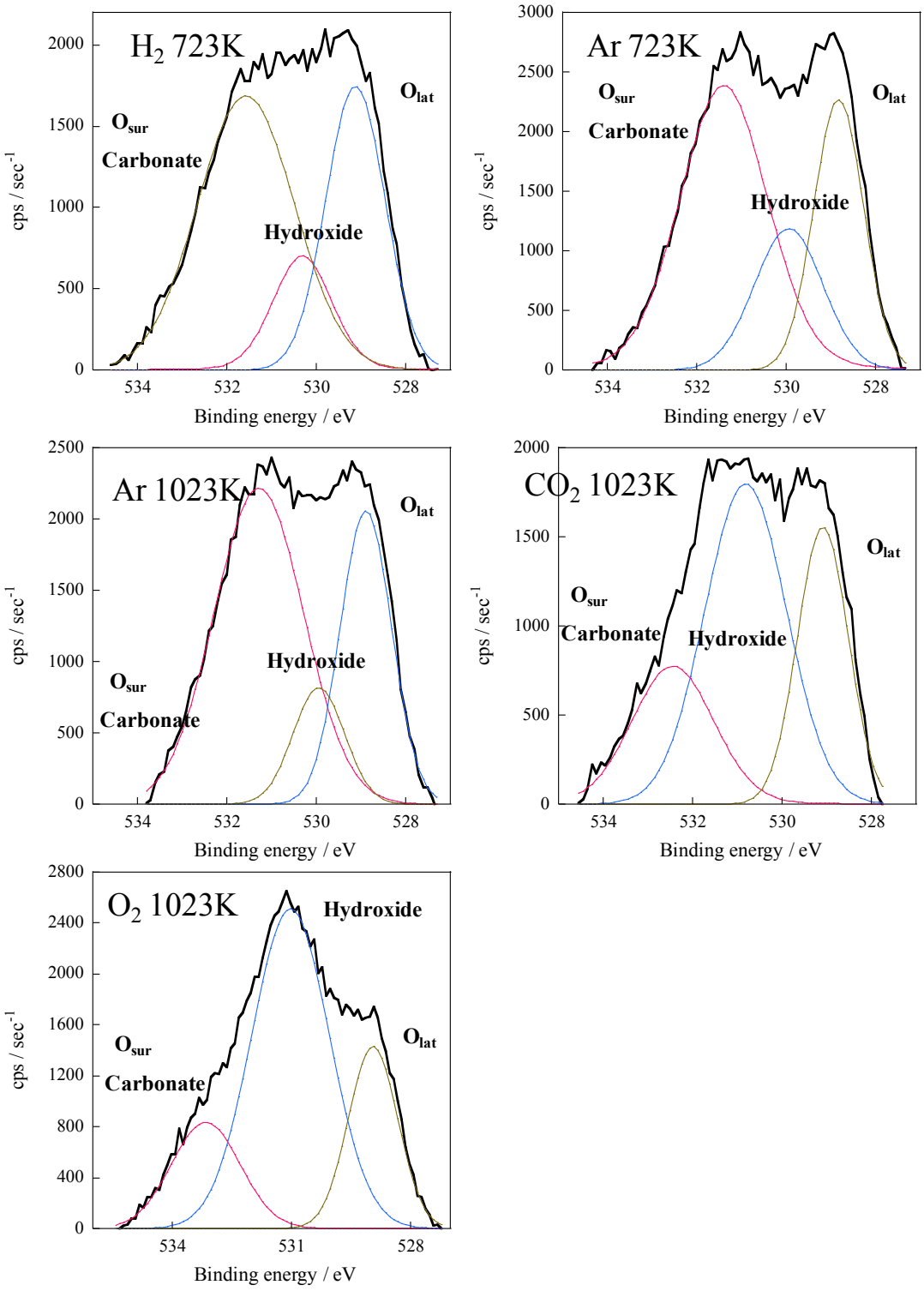

Figure A16 XPS spectra of O 1s band in $La_{0.7}Ca_{0.3}AlO_{3-\delta}$ in various preparation conditions after CO_2-OCM in the electric field.

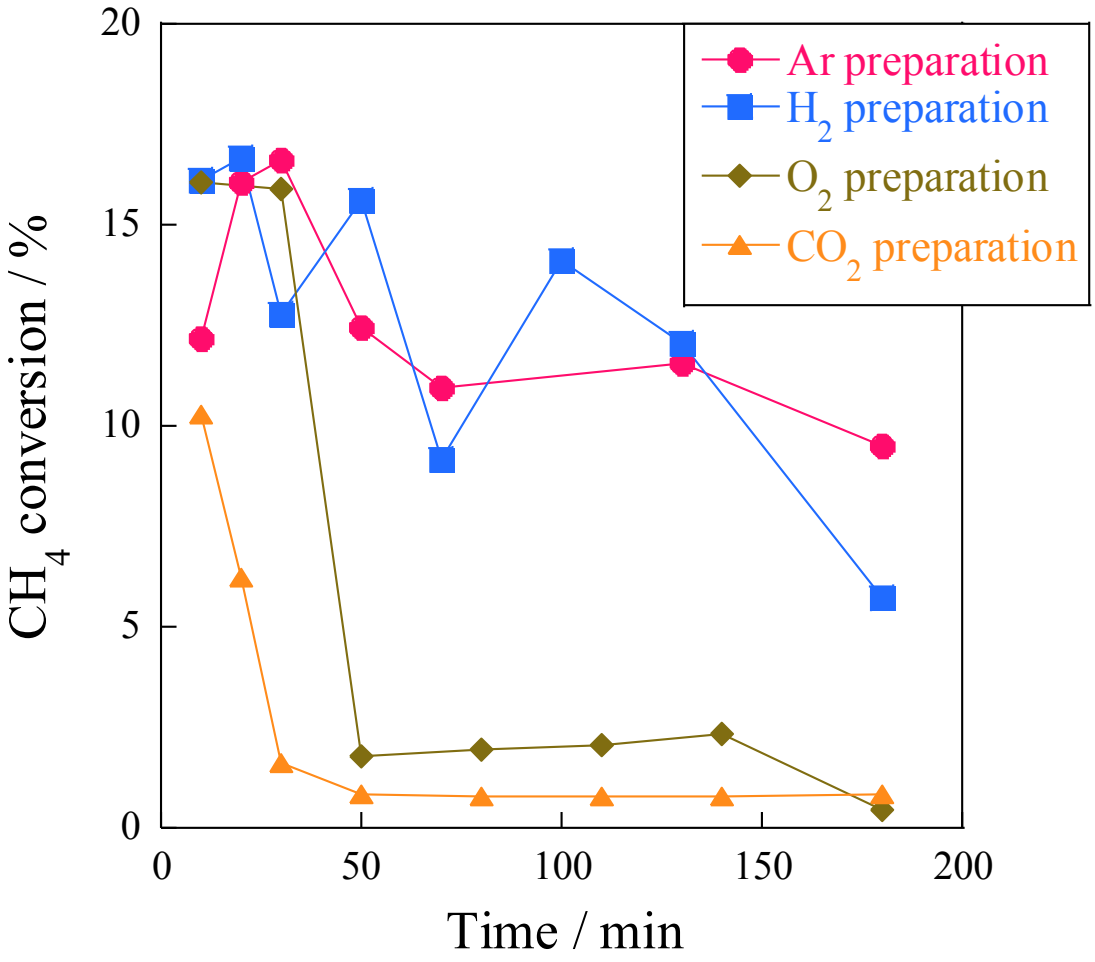

Figure A17 Time course dependence for CH_4 conversion over $La_{0.7}Ca_{0.3}AlO_{3-\delta}$ in various preparation conditions.

Chapter 3 Low-temperature dry reforming of methane to produce syngas in an electric field over La-doped Ni/ZrO_2 catalysts

3.1 Introduction

Methane, a major component of natural gas, is mainly used as an inexpensive and clean fuel. Recently, because of the "shale revolution," it has become readily available from various resources such as shale gas. The advent of new gas drilling technologies (fracking) has expanded the availability of natural gas from unconventional deposits [1]. In addition, biogas utilization is expanding along with the development of anaerobic fermentation processes from inedible plant raw materials [2, 3]. Efficient conversion processes for inexpensive methane to high value-added and easily transported liquid-phase products have been eagerly anticipated [4–6].

Syngas, a gas mixture of CO and H_2, production is an important step in the process of producing value-added products such as ammonia, methanol, alcohol and FT synthesis [7]. The cost for the syngas production is strongly dependent on the price and availability of methane, which generally determine the costs of downstream processes [8]. Today, common processes for the syngas production are steam reforming of methane (SRM), partial oxidation of methane (POx), auto-thermal reforming (ATR) and 'mixed reforming,' which is combined with SRM, POx, and ATR [9]. The process of dry (CO_2) reforming of methane (DRM) is ideally a 'green' process from the viewpoint of an environment and energy because both CH_4 and CO_2 are greenhouse gases [10, 11]. Biogas composed of CH_4 and CO_2 in almost equal proportions, which is produced from anaerobic fermentation of organic material, is useful as a raw material for the DRM reaction [12, 13]. As shown in eq. 1, DRM is an extremely endothermic reaction:

$$CH_4 + CO_2 \rightarrow 2CO + 2H_2 \qquad \Delta H^0_{298} = 247.2 \text{ kJ mol}^{-1} \qquad \text{(eq. 1)}$$

The syngas produced from DRM, with the H_2 : CO molar ratio equal to unity, is suitable for use as a feedstock from which to synthesize oxygenated hydrocarbons [14]. However, DRM necessitates high temperatures because it is an endothermic reaction; also, catalysts are deactivated by impurities such as hydrosulfides [15–17]. Particularly, carbon deposition on catalysts is unavoidable [18].

To suppress carbon deposition on catalysts caused by high temperature processing conditions, many researchers have investigated DRM over Ni or Co supported catalyst,

considering the aspects of high costs and limited availability of noble metals such as Rh, Pd, Pt, and Ir from an industrial standpoint [19–23]. Recently, a Ni-containing bimetallic catalyst has been investigated for use in reactions [24–31]. Although Ni catalyst is inexpensive and although it exhibits high catalytic activity for DRM, the carbon deposition on the Ni catalyst is crucially important. To suppress the carbon deposition, Pt or Co is added to the Ni-supported catalyst. Such bimetallic catalysts show higher catalytic activity and less carbon deposition [24, 27, 31].

Recently, the utilization of an electric field has been reported to lower reaction temperatures for several catalytic reactions [32–39]. One reaction is the catalytic reverse water gas shift reaction (RWGS: shown in eq. 2) in an electric field over metal supported La-ZrO_2 catalyst [38].

$$CO_2 + H_2 \rightarrow CO + H_2O \qquad \Delta H^0_{298} = 41.2 \text{ kJ mol}^{-1} \qquad \text{(eq. 2)}$$

In a conventional catalytic system, RWGS requires temperatures higher than 1000 K to achieve 50% CO_2 conversion in stoichiometric conditions. Screening for effective catalysts and catalyst-supports has revealed that Pt catalysts supported on La-ZrO_2 showed high catalytic activity for RWGS in an electric field at low temperatures. Stagg-Williams *et al.* also reported that Pt/La-ZrO_2 catalyst showed high catalytic activity for DRM in the conventional catalytic reaction because doped-La contributed to the thermal stability of the ZrO_2 structure [18, 40]. These results imply that the catalyst-supports might also be effective for DRM in the electric field. Other reaction is the catalytic methane steam reforming reaction (SRM) in an electric field (*electreforming*, ER) over Pd supported CeO_2 catalyst [41]. To elucidate the effects of an electric field on SRM, kinetic investigations and *operando*-DRIFTS measurements were conducted. Results of the kinetic analyses demonstrated that the water pressure dependency of the reaction rate increased during the application of the electric field and the reaction mechanism on ER was different from the conventional SRM. Also, from the results of *operando*-DRIFTS, proton conduction via adsorbed water on catalyst surface occurred with an electric field, known as the Grotthuss mechanism, and the surface protonics by the application of electric field served an important role in the enhancement of SRM. Referring these results, we conducted the reaction over metal supported La-ZrO_2 catalyst in the electric field.

The primary purpose of this study is to achieve high CH_4 and CO_2 conversion in producing syngas at low temperatures in an electric field over Ni-supported catalysts, with suppressed carbon deposition. First, screening tests were conducted of materials showing high CH_4 and

CO_2 conversion over various metal-supported rare-earth-doped zirconia catalysts in an electric field. Second, the effects of reaction temperature, imposed electric power and other electric parameters on the catalytic activity were examined. Third, a comparison of the amounts of carbon deposition between those of the conventional catalytic reaction (not imposing the electric field) and in the electric field were examined in a high CH_4 conversion condition under which carbon deposition readily occurred [42, 43] over Ni-supported La-doped zirconia (Ni/La-ZrO_2) catalyst. Finally, the effects of CH_4 and CO_2 on DRM in the electric field were investigated using results of tests in various CH_4 and CO_2 partial pressure conditions.

In summary, the catalyst of 1wt%Ni/10 mol%La-ZrO_2 showed high DRM activity even at 423 K of external temperature, at which no DRM proceeds in the conventional catalytic systems. By virtue of the low reaction temperature, low amounts of carbon deposition were confirmed even in conditions of high CH_4 conversion in the electric field. The imposed electric power was correlated to with the catalytic activities in the electric field. Syngas is producible at low temperature with high energy efficiency.

3.2. Experimental

3.2.1 Catalyst preparation

Catalyst-supports, 10 mol%X-ZrO_2 (X=La, Ce, Pr, Nd, Y) were prepared using a complex polymerized method. Each precursor was $ZrO(NO_3)_2 \cdot 2H_2O$, $La(NO_3)_3 \cdot 6H_2O$, $Ce(NO_3)_3 \cdot 6H_2O$, $Pr(NO_3)_3 \cdot 6H_2O$, $Pr(NO_3)_3 \cdot 6H_2O$ and $Y(NO_3)_3 \cdot 6H_2O$ (Kanto Chemical Co. Inc.). These precursors were dissolved into distilled water, with subsequent addition of citric acid and ethylene glycol. After condensation in a water bath at 353 K, the gel was stirred and heated to remove the water completely. Pre-calcination was conducted at 673 K for 2 h. Then calcination was conducted at 1123 K for 10 h in air flow. Then Fe, Co, Ni, Cu, Pd, or Pt was loaded on 10 mol%La-ZrO_2 (La-ZrO_2) supports with 1wt% as an active metal using an impregnation method. Precursors of respective elements were $Fe(NO_3)_3 \cdot 9H_2O$, $Co(NO_3)_2 \cdot 6H_2O$, $Ni(NO_3)_2 \cdot 6H_2O$, $Cu(NO_3)_2 \cdot 3H_2O$, $Pd(CH_3COO)_2$ and $Pt(NH_3)_4(NO_3)_2$ (Kanto Chemical Co. Inc.). Calcination was conducted at 973 K for 3 h. Unless noted otherwise, these catalysts are designated as Y/X-ZrO_2 (Y= Fe, Co, Ni, Cu, Pd, Pt).

3.2.2 Catalytic activity test

The experimental setup for catalytic activity tests with the application of an electric field is presented in Figure 3-1. Two stainless electrodes (2 mmϕ) were inserted into the reactor, with each end set as contacting the catalyst bed. A thermocouple was inserted to the catalyst bed to measure the reaction temperature in the catalyst bed. The charged amount of catalyst was 20 mg in tests for various CH_4 and CO_2 partial pressures, 100 mg in other activity tests, and 200 mg in high CH_4 conversion tests. In the screening tests, the feed gas was supplied at CH_4:CO_2:Ar = 1:1:2. The total flow rate was 100 mL min^{-1}. The value of W/F was about 1.6 $g_{\text{-cat}}$ h mol^{-1} (CH_4-based). For tests investigating the effects of reaction temperature, imposed electric power, and other electric parameters on the catalytic activities over Ni/La-ZrO_2 catalysts, the feed gas was supplied at CH_4:CO_2:Ar = 1:1:2, the total flow rate was 200 mL min^{-1}. In tests for changing contact times (W/F_{CH4}) for DRM in the electric field over Ni/La-ZrO_2, the gas composition was fixed to CH_4:CO_2:Ar = 1:1:2, and the total gas flow rate was changed, whereas the charged catalyst amount was fixed to 20 mg. In tests for investigating the carbon deposition resistance, the feed gas was supplied at CH_4:CO_2:Ar = 1:1:2, the total flow rate was 200 mL min^{-1} and the charged catalyst amount was 200 mg. Pre-treatment was conducted at 723 K for 30 min in Ar atmosphere in the screening tests, and at 1023 K for 30 min in H_2:Ar = 25:75, the total flow rate 100 mL min^{-1} in other tests. Although a furnace temperature was set at 423 K for all experiments, electrical conduction increased the temperature in the catalyst bed because of Joule heating. The measured reaction temperature is shown in each figure or table. The temperature was measured by thermo couples attached to the downside of the catalyst bed. A direct current (DC) high voltage power supply was used to impose the electric field. Application of the electric field was controlled using a current cut-off. The applied current was 3.0–12.0 mA. The applied voltage was monitored using a digital phosphor oscilloscope (TDS 2001C with a voltage probe P6015A; Tektronix Inc.). The applied voltage was determined by the catalyst characteristics, the electrode gap, and the atmosphere [44]. After passing a cold trap, products were analyzed using a GC-FID (GC-2014; Shimadzu Corp.) with a Porapak N packed column after methanation by Ru/Al_2O_3 catalyst (for analyses of CH_4, CO, CO_2, C_2H_4, C_2H_6) and a GC-TCD with a molecular sieve 5A packed column (for H_2 analysis). Conversion, selectivity, and yield were calculated using the following formulas.

$$CH_4 \text{ conv. } (\%) = \Sigma(F_{CO(CH_4)} + F_{C_2H_4} + F_{C_2H_6}) / S_{CH_4} \times 100 \quad \text{(eq. 3)}$$

$$CO_2 \text{ conv. } (\%) = F_{CO(CO_2)} / S_{CO_2} \times 100 \quad \text{(eq. 4)}$$

$$\text{CO sel. (\%)} = F_{CO(CH_4)} / \Sigma(F_{CO(CH_4)} + F_{C_2H_4} + F_{C_2H_6}) \times 100 \quad \text{(eq. 5)}$$

$$\text{CO yield (\%)} = CH_4 \text{ conv.} \times \text{CO sel.} / 100$$

$$= F_{CO(CH_4)} / S_{CH_4} \times 100 \quad \text{(eq. 6)}$$

$$\text{Power (W)} = \text{Applied current (mA)} \times \text{Applied voltage (kV)} \quad \text{(eq. 7)}$$

$$\text{Field Intensity (V mm}^{-1}\text{)} = \text{Applied voltage (kV)} / \text{Catalyst bed height (mm)} \quad \text{(eq. 8)}$$

$$H_2 / CO\ (-) = F_{H_2} / F_{CO} \quad \text{(eq. 9)}$$

$$\text{Faradaic number } (-) = (n_{CH_4} + n_{CO_2}) / n_e \quad \text{(eq. 10)}$$

In these equations, F denotes the product formation rate, S denotes the supply rate of the reactant, $CO(CH_4)$ and $CO(CO_2)$ respectively represent the produced amounts of CO derived from CH_4 and CO_2. The formation rates of products were calculated not from the products conversions, but from the composition of the outlet gas using GC-FID and GC-TCD. Also, n_M (M=CH_4, CO_2, electron) denotes the mole of consumed CH_4 and CO_2, and imposed electron calculated using applied current. The formation rate of $CO(CH_4)$ and $CO(CO_2)$ was calculated as presented below.

$$F_{CO(CH_4)} = (F_{CO} + F_{H_2}) / 4 \quad \text{(eq. 11)}$$

$$F_{CO(CO_2)} = (3F_{CO} - F_{H_2}) / 4 \quad \text{(eq. 12)}$$

Carbon balances were calculated from the supply rate for CH_4 and CO_2, and the products formation rate and the carbon balances were almost 100%.

3.2.3 Characterizations

For characterization of the catalysts, we used X-ray diffractometry (XRD, RINT-Ultima III; Rigaku Corp.) and scanning transmission electron microscopy (STEM, HF-2210; Hitachi Ltd.) for catalysts before and after the reactions for 3 h. The XRD patterns were measured using Cu-$K\alpha$ radiation. Anode voltage and anode current values were, respectively, 40 kV and 40 mA. Diffractograms were taken at 2θ angles for 10–90° with steps of 0.01°. Particle morphology was monitored using STEM. Amounts of carbon deposition on the catalyst after the reaction were measured using temperature programmed oxidation (TPO: 10%O_2/Ar; 100 mL min^{-1}) with an infrared gas analyzer (CGT-7000; Shimadzu Corp.). The BET specific surface area of catalyst was measured (Gemini VII 2390; Shimadzu Corp.). Before carrying out measurements, each sample was purged using He gas at 573 K for 1 h. The specific surface areas of the samples were calculated following the multi-point Brunauer–Emmett–

Teller (BET) procedure.

3.3 Results and discussion

3.3.1 Screening tests for DRM in an electric field

First, to discover suitable catalysts for methane and carbon dioxide conversion by DRM in an electric field, various metal-supported La-ZrO_2 (10 mol% La-doped ZrO_2) oxide catalysts were investigated to assess their catalytic activities. Various metal-doped ZrO_2 oxide catalysts were reported previously as good candidates for CH_4 and CO_2 conversion by oxidative coupling of methane using carbon dioxide [36]. Stabilized ZrO_2, various metal-doped ZrO_2 oxides such as Y, La, and Ce can retain a stable structure even at high temperatures [18]. Among various metal-doped ZrO_2 oxides, we selected La as a doping element because La-containing oxide showed high methane conversion in the electric field in our earlier studies [36, 44] and good activity for DRM in the conventional catalytic system (not imposing the electric field) [18, 45]. Table 3-1(A) presents experimentally obtained results on various metal-supported La-ZrO_2 catalysts for DRM in the electric field. The field intensity described in the table was calculated from the applied voltage per the catalyst bed height because the catalyst bed heights and the applied voltages differed depending on the nature of catalysts when a constant current (3.0 mA) was applied to the catalyst. The Faradaic number indicated the number of reacted molecules (CH_4 and CO_2) per electron. Increase in Faradaic number means more reactants are activated by the constant applied current. In these tables, the Faradaic number exceeded 20 for all catalysts. Therefore, DRM in the electric field was not a stoichiometric electrochemical reaction, but a catalytic reaction assisted by electrocatalytically. Among these catalysts, higher CH_4 and CO_2 conversions were obtained over Co/La-ZrO_2, Ni/La-ZrO_2, and Pt/La-ZrO_2 catalysts than other listed catalysts. Also, H_2/CO ratio shows the extent of sequential RWGS reaction progress. H_2 from DRM reacted with CO_2 and, CO and H_2O were produced. Therefore, when RWGS proceeds sequentially, H_2/CO ratio is lower than unity. The H_2/CO ratio over Co/La-ZrO_2 catalyst was 0.57, smaller than Ni/La-ZrO_2 (=0.83) and Pt/La-ZrO_2 (=0.80) catalysts. Smaller H_2/CO ratios indicate that RWGS reaction proceeded preferentially over Co/La-ZrO_2 catalyst than over Ni/La-ZrO_2 and Pt/La-ZrO_2 catalysts. In addition, the Faradaic numbers over Ni/La-ZrO_2 and Co/La-ZrO_2 catalysts were larger among other listed catalysts, i.e. higher energy efficiency. The electron efficiency over these two catalysts was prominently high among all catalysts. Therefore, we specifically examined the Ni/La-ZrO_2 catalyst for additional investigations considering high Faradaic

number (=252) and high H_2/CO ratio (=0.83).

To elucidate the role of doped metal in the support (i.e. La for Ni/La-ZrO_2), various stabilized zirconia, 10 mol% M-doped ZrO_2 (M=La, Ce, Pr, Nd, Y) were compared using Ni as a supported metal. Table 3-1(B) presents experimentally obtained results on 1wt% Ni/M-ZrO_2 catalysts. In this table, CO selectivity was eliminated because C_2 hydrocarbons such as ethane and ethylene as by-products were not found and CO selectivities over all listed catalysts were 100%. The table shows that CH_4 and CO_2 conversions over Ni/La-ZrO_2 and Ni/Pr-ZrO_2 catalysts were increased in comparison with Ni/ZrO_2 catalyst. XRD profiles for various metal-doped stabilized ZrO_2 supports were measured (shown in Figure 3-2) and XRD crystallite sizes of various metal-doped stabilized ZrO_2 supports at ZrO_2 (110) face were calculated using the Debye–Scherrer formula (shown in Table 3-2). As shown in Figure 3-2, monoclinic ZrO_2 phase was observed over ZrO_2 and Ce-ZrO_2. Tetragonal ZrO_2 phase was observed for other various metal-doped ZrO_2 catalysts. The crystalline sizes of La-ZrO_2 support were the smallest among various metal-doped ZrO_2 supports, i.e., the crystallinity of La-ZrO_2 support was lowest. The electrical conductivity of La-ZrO_2 support was lower than other metal-doped ZrO_2 supports, and applied voltage and imposed electric power over Ni/ZrO_2 catalyst were high. Also, CH_4 and CO_2 conversions showed higher values than those of other catalysts. Details of the relation between applied voltage and/or imposed electric power, and the catalytic activities will be discussed in the following section 3.3.

To optimize the supported amount of Ni on La-ZrO_2, various supported amounts of Ni on La-ZrO_2 catalysts were investigated to assess their catalytic activities for DRM in the electric field. Table 3-1(C) presents experimentally obtained results for these catalysts. When the supported amounts of Ni on La-ZrO_2 catalysts were increased to 1 wt%, CH_4 and CO_2 conversion increased monotonically. A further increase in the Ni-supported amounts to 10 wt% decreased the catalytic activity because the applied voltage and imposed electric power decreased, possibly because of increased density of surface Ni and changes in the current path.

From results of these tests, we inferred that 1wt%Ni/10 mol%La-ZrO_2 (Ni/La-ZrO_2) catalyst was the most appropriate catalyst among these oxides for DRM in the electric field. Regarding the catalyst stability, XRD profiles for Ni/La-ZrO_2 as made and after DRM reaction in the electric field (3 mA and 12 mA) showed a stable structure before and after the reaction (shown in Figure 3-3). Additionally, the crystalline size of ZrO_2 (110) and NiO (101) faces on Ni/La-ZrO_2 showed stable values before and after the reaction. Results show that Ni/La-ZrO_2 catalyst was stable for DRM in the electric field even after the reaction.

3.3.2 Catalytic activity and carbon deposition in the electric field

The electric field effects on the reaction were investigated through comparison of catalytic activity with/without imposing the electric field using Ni/La-ZrO_2 catalyst. Figure 3-4 presents results of CH_4 and CO_2 conversions (left side) and H_2/CO (right side) with/without imposition of the electric field at various temperatures. Reaction temperatures measured by the thermocouple were 694–943 K in conventional catalytic reactions and 535–955 K in the catalytic reaction with the electric field because of the Joule heating by imposition of the electric field. The DRM reaction proceeded even at low temperatures such as 535 K (423 K as the external temperature) when the electric field was applied, at which temperature no DRM proceeds in conventional catalytic systems. Furthermore, DRM selectivity in the electric field on 3 mA at 535 K was comparable to that in the conventional reaction at 800 K with the same CH_4 conversion. Results show that H_2/CO ratios were 0.77 in the electric field, and 0.35 in the conventional catalytic reaction. The DRM reaction more preferentially proceeded in the electric field than in the conventional catalytic reaction. DRM proceeded at markedly low temperatures by virtue of the application of the electric field. The RWGS reaction is an endothermic reaction. The equilibrium constant increases with increasing temperature, and RWGS did not proceed much in the electric field at 535 K. At the lower temperature region around 550 K, the temperature effect was negligible for the reaction in the electric field, so the Joule heating did not affect the catalytic activity in the electric field. The electrical modification of the catalyst was important for catalytic activity. The H_2/CO ratio decreased at temperatures from 650 K to 800 K in the electric field because the RWGS reaction proceeded at high temperatures. Regarding the increased H_2/CO ratio higher than 760 K, Swaan *et al.* reported the same results over various Ni supported catalysts (Ni/ZrO_2, Ni/La_2O_3, Ni-K/SiO_2, Ni-Cu/SiO_2, Ni/SiO_2-Al_2O_3) in the conventional catalytic system [46]. They reported that the product distributions and H_2/CO ratios for various CH_4 conversions over these catalysts in the same DRM reaction condition were measured, and the product distribution was dominated by the equilibrium of RWGS, irrespective of CH_4 conversion. Additionally, from the result of ref. [38], RWGS reaction did not proceed with the electric field at more than 593 K over Pt and Pd supported La-ZrO_2 catalysts. On the other hand, in Figure 3-4, CH_4 conversion proceeded with the electric field at around 600 K, that is, DRM reaction proceeded with the electric field and RWGS reaction was supposed to thermodynamically progress. Considering those discussion, the H_2/CO ratio increased by the equilibrium of RWGS above 800 K over Ni/La-ZrO_2 in the electric field (open symbols in Figure 3-4 right) like as the conventional catalytic system (closed symbols in Figure 3-4 right).

To investigate carbon deposition over Ni/La-ZrO_2 catalyst on DRM reaction in the electric field, the catalytic activity on DRM in the electric field was compared to that of the conventional reaction in conditions of high CH_4 conversion because carbon deposition on Ni supported catalyst is an unavoidable and crucially important difficulty that impedes industrial use. Table 3-3 presents experimentally obtained results for the catalytic activity in the electric field at external temperatures of 423 K and in conventional reaction at external temperatures of 1023 K for initial activity and after 140 min of the time course. In addition, Figure 3-5 presents pictures of carbon deposition in the reactor tube and around the electrode in the electric field (left side) and in the conventional reaction (right side) after 140 min. First, two reactions accounting for carbon deposition were the following: CO disproportionation (Boudouard reaction) is shown by eq. 13; CH_4 decomposition is shown by eq. 14.

$$2CO \rightarrow CO_2 + C_{(s)} \qquad \Delta H^0_{298} = -172.5 \text{ kJ mol}^{-1} \qquad \text{(eq. 13)}$$

$$CH_4 \rightarrow 2H_2 + C_{(s)} \qquad \Delta H^0_{298} = 74.0 \text{ kJ mol}^{-1} \qquad \text{(eq. 14)}$$

Gardner *et al.* reported that CO disproportionation occurred at temperatures higher than 623 K [47, 48]. Filamentous carbon was often formed during DRM reaction via CO disproportionation over Ni/γ-Al_2O_3 [47] and over Ni (110) single crystal [48]. Additionally, the apparent activation energy for producing the filamentous carbon was reported as 90–130 kJ mol^{-1}. From the viewpoint of Gibbs free energy, Wang *et al.* reported that CO disproportionation occurred below 973 K and that CH_4 decomposition occurred at temperatures higher than 830 K [15]. Investigation of carbon deposition behavior during DRM reaction was reported by Swaan *et al.* [46] and by Tsipouriari *et al.* [49, 50], independently, using isotope labeling and temperature programmed oxidation (TPO) to ascertain whether carbon deposition originated from CH_4 or from CO. Carbon deposits from CH_4 decomposition formed at an initial stage on the reaction, and the formed carbon exhibited weak interaction on the catalyst. However, the carbon deposits from CO disproportionation formed constantly during the reaction, and the formed carbon exhibited strong interaction on the catalyst. Additionally, most carbon deposits after the reaction originated from CO disproportionation.

Regarding the catalytic reaction without the electric field, much carbon deposition was observed, as shown in Table 3-3 and Figure 3-5(right). Most of the carbon was located at the bottom part of the reactor at 1023 K. In the inlet part of the catalyst bed, the concentration for CH_4 was high but the carbon deposition was not seen. Besides, in the outlet part of the catalyst bed, the concentration for CO was high and the carbon deposition was seen.

Therefore, it seemed to assume CO disproportionation at thermodynamic equilibrium in the outlet part at lower temperature, rather than the pyrolytic carbon deposition. In spite of the large amounts of carbon deposits in this case, CH_4 conversion did not change. Stagg-Williams *et al.* reported the same results over Pt/La-ZrO_2 catalyst [18]. Because of the basicity of La-ZrO_2 support, CO_2 was trapped easily on the catalyst support. Then the density of the CO_2 adsorption site near Pt metal particle presumably increased and the carbon deposits near the Pt metal particle were presumed to be cleaned by oxygen species derived from CO_2 dissociation on the catalyst support. As for CO_2 trap, activity tests for only CO_2 feed were conducted over Ni/La-ZrO_2 catalyst without the electric field at 823 K and with the electric field at 423 K after H_2 reduction preparation at 1023 K; CO_2 conversion without the electric field: 0.31%, with the electric field: 2.3%. As a result, CO was produced in both conditions and, therefore, CO_2 dissociation was occurred in our case. Considering their discussions, the carbon deposits near Ni metal particle on Ni/La-ZrO_2 catalyst were presumably cleaned, so the CH_4 conversion did not decrease. Additionally, as shown in Table 3-3, CO_2 conversion increased and the H_2/CO ratio decreased after 140 min. Hanley *et al.* reported the dissociation probability for CH_4, CO_2, and CO on the Ni surface [51–53]. The dissociation probability for CO is much higher than that for CH_4 and CO_2. The rate of CO disproportionation depends strongly on the temperature. The rate-determining step for CO disproportionation was reportedly CO dissociation, which occurs at temperatures higher than 623 K [54, 55]. Therefore, the amount of the carbon deposits after DRM in the electric field was low because the reaction temperature was lower than 623 K.

To elucidate the catalyst structure after DRM reaction in the electric field and to evaluate the carbon deposits on the catalyst, the surface structure for Ni/La-ZrO_2 catalyst was observed using STEM-EDX. The STEM images for as-made samples and after DRM in the electric field and EDX mappings for Zr, La, and Ni on each sample are presented in Figure 3-6. Although many whisker carbon filaments were observed even over the catalyst reacted in the electric field, as described in earlier reports [56–59], the amount of filamentous carbon is negligible small (1.5 mg/g-cat as shown in Table 3-3), and this filamentous carbon did not affect the catalytic activity on DRM in the electric field.

3.3.3 Electrical factors effects on catalytic activity in the electric field

To elucidate the electrical factors in catalytic activity tests, we investigated the effects of imposed electric power controlled by applied current on catalytic activity. Although we also confirmed the effects of applied voltage, no importance of voltage was found in this system.

Figure 3-7 presents results of CH_4 and CO_2 conversion as well as those for H_2/CO ratios obtained by changing the imposed electric power. Results show that CH_4 and CO_2 conversion depend on the imposed electric power. However, the H_2/CO ratio changed slightly when changing the imposed electric power. Oshima *et al.* showed the same results for increasing the imposed power promoted RWGS reaction over Pt and Pd supported La-ZrO_2 catalysts. [38] In addition, the relation between the applied current and applied voltage (I–V profile) for DRM in the electric field was investigated. Results are described in Figure 3-8. When the applied current was increased from 2 mA to 12 mA, the applied voltage did not follow Ohm's law. The applied voltage was affected by the adsorbed species and carriers on the catalyst.

3.3.4 Effects of CH_4 and CO_2 partial pressures on the catalytic activity in the electric field

To elucidate the catalytic reaction mechanism for DRM in the electric field over Ni/La-ZrO_2 catalyst, activity tests by changing CH_4 and CO_2 partial pressures (P_{CH4} and P_{CO2}) were conducted with/without imposing the electric field. Experiments for partial pressure dependence were conducted within the conversion of 2–4%. In such low conversions, these partial pressure conditions were within the dependence of the reaction rate in the perspective of the contact time, as shown in Figure 3-9. Table 3-4 presents each reaction order with/without an applied electric field. Figure 3-10 shows logarithmic plots for the formation rate of CO from CH_4, CO from CO_2, and H_2 by changing P_{CO2} for both cases. The reaction orders of CH_4 for the formation rate of "CO from CH_4" and "CO from CO_2" were zero for all cases. The reaction order of CH_4 for the formation rate of "H_2" was 0.26 without imposition of an electric field, and zero with imposition of an electric field. Results of the activity tests conducted with change of the partial pressure revealed that the formation rate r in DRM in the conventional catalytic system can be expressed as the following equation using rate constant k and partial pressure P.

$$\text{CO from } CH_4\text{: } r_1 = k_1 P_{CO2}^{0.05} \quad \text{(eq. 15)}$$

$$\text{CO from } CO_2\text{: } r_2 = k_2 P_{CO2}^{0.32} \quad \text{(eq. 16)}$$

$$H_2\text{: } r_3 = k_3 P_{CH4}^{0.26} P_{CO2}^{-0.42} \quad \text{(eq. 17)}$$

Formation rate r' in the electric field can be expressed as the following equation using rate constant k'.

$$\text{CO from } CH_4\text{: } r'_1 = k'_1 P_{CO2}^{0.22} \quad \text{(eq. 18)}$$

CO from CO_2: $r'_2 = k'_2 P_{CO2}^{0.30}$ (eq. 19)

H_2: $r'_3 = k'_3 P_{CO2}^{0.34}$ (eq. 20)

Comparison of the reaction order between reactions with/without electric field reveals that the reaction order for "CO from CO_2" was almost identical with/without imposing electric field. By imposing the electric field, the reaction order of CH_4 for "H_2" decreased from 0.26 to zero, and the reaction order of CO_2 for "CO from CH_4" increased 0.05 to 0.22. The reason for the low reaction order of CH_4 for "H_2" with imposition of electric field was presumed that imposing the electric field promoted CH_4 dissociation on the catalyst. Bradford *et al.* reported reaction orders over Ni/MgO (basic support) and Pt/ZrO_2 catalysts at lower temperatures of 673–723 K [60, 61]. In those cases, the reaction orders of CH_4 for all products were positive. In our study, the reaction temperatures for activity tests by changing partial pressures were higher than those in these reports. Therefore, CH_4 dissociation proceeded faster. In addition, zero orders in methane partial pressure with the electric field were possibly derived from the promotion for methane dissociative adsorption by the electric field. [41] It decreased the reaction order of CH_4. However, the reaction order of CO_2 for all products was mostly the same as those of Bradford's reports in the case without an electric field. The negative reaction order of CO_2 for "H_2" (i.e. =-0.42) is probably that the RWGS reaction proceeded at thermodynamic equilibrium, which consumed the H_2. Zhang *et al.* reported the reaction mechanism over Ni/La_2O_3 catalyst [62]. Hydrogen species move by spillover from dissociated CH_4 on the Ni metal surface onto the support. Also, CO_2 reacts to form formate species ($HCOO^-$). In addition the CO and hydroxyl species (OH^-) form via pyrolysis of the formate species. Considering this mechanism, the reasons for higher reaction orders of CO_2 for "CO from CH_4" and "H_2" are presumably that the imposed electric field activated CH_4 and the formate species, thereby promoting the surface reaction.

3.3.5 Energy efficiency of DRM in the electric field

To evaluate the energy efficiency during imposition of the electric field, the Faradaic number, the number of CH_4 and CO_2 molecules formed per electron supplied by the electric field, and the energy efficiency were calculated along with the endothermic enthalpy of the DRM reaction. Table 3-5 presents activity test results for various amounts of applied current including the values of the Faradaic number and energy efficiency. Results show that the Faradaic number was 88–252 in this reaction system. Therefore, the reaction was not only promoted electrochemically; it also proceeded catalytically in the electric field. Therefore, for

DRM in an electric field, syngas became producible at low external temperatures such as 423 K with high energy efficiency.

3.4 Conclusion

Dry reforming of methane (DRM) was conducted in an electric field. Results of the screening tests show that 1wt%Ni/10 mol%La-ZrO_2 (Ni/La-ZrO_2) catalyst was the most appropriate catalyst in this reaction system. Results also show high activity, even at 423 K (external temperature), at which temperature no DRM reaction proceeds in conventional catalytic systems. Additionally, high DRM selectivity, a high H_2/CO ratio, and low amounts of carbon deposition, even in conditions of high CH_4 conversion, were attributable to the low reaction temperature. The imposed electric power was correlated with the catalytic activities in the electric field. The DRM reaction rate in the electric field depended on the CO_2 partial pressure by 0.22 order for "CO from CH_4", 0.30 order for "CO from CO_2", and 0.34 order for "H_2". It was assumed that imposing the electric field presumably activated CH_4 and formate species, or promoted the surface reaction. Syngas became producible at low external temperatures, even at 423 K with high energy efficiency and without coke formation.

References

[1] Q. Wang, X. Chen, A.N. Jha, H. Rogers, Natural gas from shale formation – The evolution, evidence and challenges of shale gas revolution in United States, Renew. Sust. Energ. Rev. 30 (2014) 1–28.

[2] M. Aresta, A. Dibenedetto, I. Tommasi, Developing innovative synthetic technologies of industrial relevance based on carbon dioxide as raw material, Energy Fuels 15(2) (2001) 269–273.

[3] N.J. Themelis, P.A. Ulloa, Methane generation in landfills, Renew. Energ. 32 (2007) 1243–1257.

[4] J.H. Lunsford, The catalytic conversion of methane to higher hydrocarbons, Catal. Today 6 (1990) 235–259.

[5] J.R.H. Ross, A.N.J. van Keulen, M.E.S. Hegarty, K. Seshan, The catalytic conversion of natural gas to useful products, Catal. Today 30 (1996) 193–199.

[6] J.H. Lunsford, Catalytic conversion of methane to more useful chemicals and fuels: a challenge for the 21st century, Catal. Today 63 (2000) 165–174.

[7] A.P.E. York, T.C. Xiao, M.L.H. Green, J.B. Claridge, Methane oxyforming for synthesis gas, Catal. Rev.: Sci. Eng. 49(4) (2007) 511–560.

[8] A.S.K. Raju, C.S. Park, J.M. Norbeck, Synthesis gas production using steam hydrogasification and steam reforming, Fuel Proc. Technol. 90(2) (2009) 330–336.

[9] M.-S. Fan, A.Z. Abdullah, S. Bhatia, Catalytic technology for carbon dioxide reforming of methane to synthesis gas, ChemCatChem 1 (2009) 192–208.

[10] J. R. H. Ross, Natural gas reforming and CO_2 mitigation, Catal. Today 100 (2005) 151–158.

[11] D. Pakhare, J. Spivey, A review of dry(CO_2) reforming of methane over noble metal catalysts, Chem. Soc. Rev. 43 (2014) 7813–7837.

[12] U. Izquierdo, V.L. Barrio, J. Requies, J.F. Cambra, M.B. Guemez, P.L. Arias, Tri-reforming: A new biogas process for synthesis gas and hydrogen production, Int. J. Hydrogen Energy 38 (2013) 7623–7631.

[13] J.-M. Lavoie, Review on dry reforming of methane, a potentially more environmentally friendly approach to the increasing natural gas exploitation, Front. Chem. 2 (2014) 81.

[14] Z. Jiang, T. Xiao, V.L. Kuznetsov, P.P. Edwards, Turning carbon dioxide into fuel, Phil. Trans. R. Soc. A 368 (2010) 3343–3364.

[15] S.B. Wang, G.Q.M. Lu, G.J. Millar, Carbon dioxide reforming of methane to produce synthesis gas over metal-supported catalysts: State of the art, Energy Fuels 10 (1996) 896–904.

[16] M.C.J. Bradford, M.A. Vannice, CO_2 reforming of CH_4, Catal. Rev.: Sci. Eng. 41(1) (1999) 1–42.

[17] A.J. Brungs, A.P.E. York, J.B. Claridge, C. M.-Alvarez, M.L.H. Green, Dry reforming of methane to synthesis gas over supported molybdenum carbide catalysts, Catal. Lett. 70 (2000) 117–122.

[18] S.M. Stagg-Williams, F.B. Noronha, G. Fendley, D.E. Resasco, CO_2 reforming of CH_4 over Pt/ZrO_2 catalysts promoted with La and Ce oxides, J. Catal. 194 (2000) 240–249.

[19] Z. Zhang, X.E. Verykios, S.M. MacDonald, S. Affrossman, Comparative study of carbon dioxide reforming of methane to synthesis gas over Ni/La_2O_3 and conventional nickel-based catalysts, J. Phys. Chem. 100 (1996) 744–754.

[20] J.H. Bitter, K. Seshan, J.A. Lercher, On the contribution of X-ray absorption spectroscopy to explore structure and activity relations of Pt/ZrO_2 catalysts for CO_2/CH_4 reforming, Top. Catal. 10 (2000) 295–305.

[21] C. Song, W. Pan, Tri-reforming of methane: novel concept for catalytic production of industrially useful synthesis gas with desired H_2/CO ratios, Catal. Today 98 (2004) 463–484.

[22] L. Pino, A. Vita, F. Cipitì, M. Laganà, V. Recupero, Hydrogen production by methane tri-reforming process over Ni-ceria catalysts: Effect of La-doping, Appl. Catal. B: Environ. 104 (2011) 64–73.

[23] B. Nematollahi, M. Rezaei, M. Khajenoori, Combined dry reforming and partial oxidation of methane to synthesis gas on noble metal catalysts, Int. J. Hydrogen Energy 36 (2011) 2969–2978.

[24] K. Takanabe, K.I. Nagaoka, K. Aika, Improved resistance against coke deposition of titania supported cobalt and nickel bimetallic catalysts for carbon dioxide reforming of methane, Catal. Lett. 102 (2005) 153–157.

[25] J. Zhang, H. Wang, A.K. Dalai, Development of stable bimetallic catalysts for carbon dioxide reforming of methane, J. Catal. 249 (2007) 300–310.

[26] B. Steinhauer, M.R. Kasireddy, J. Radnik, A. Martin, Development of Ni-Pd bimetallic catalysts for the utilization of carbon dioxide and methane by dry reforming, Appl. Catal. A: Gen. 366 (2009) 333–341.

[27] D. San-José-Alanso, J. Juan-Juan, M.J. Illán-Gómez, M.C. Román-Martínez, Ni, Co and bimetallic Ni-Co catalysts for the dry reforming of methane, Appl. Catal. A: Gen. 371 (2009) 54–59.

[28] M. García- Diéguez, I.S. Pieta, M.C. Herrera, M.A. Larrubia, L.J. Alemany, Improved Pt-Ni nanocatalysts for dry reforming of methane, Appl. Catal A: Gen. 377 (2010) 191–199.

[29] I. Luisetto, S. Tuti, E.D. Bartolomeo, Co and Ni supported on CeO_2 as selective

bimetallic catalyst for dry reforming of methane, Int. J. Hydrogen Energy 37 (2012) 15992–15999.

[30] S. Özkara-Aydınoğlu, A.E. Aksoylu, A comparative study of the kinetics of carbon dioxide reforming of methane over Pt-Ni/Al_2O_3 catalyst: Effect of Pt/Ni ratio, Chem. Eng. J. 215-216 (2013) 542–549.

[31] H. Ay, D. Üner, Dry reforming of methane over CeO_2 supported Ni, Co and Ni-Co catalysts, Appl. Catal. B: Environ. 179 (2015) 128–138.

[32] Y. Sekine, M. Tomioka, M. Matsukata, E. Kikuchi, Catalytic degradation of ethanol in an electric field, Catal. Today 146(1-2) (2009) 183–187.

[33] Y. Sekine, M. Haraguchi, M. Tomioka, M. Matsukata, E. Kikuchi, Low temperature hydrogen production by highly efficient novel catalytic system assisted with electric field, J. Phys. Chem. A, 114 (2010) 3824–3833.

[34] Y. Sekine, M. Haraguchi, M. Matsukata, E. Kikuchi, Low temperature steam reforming of methane over metal catalyst supported on $Ce_XZr_{1-X}O_2$ in an electric field, Catal. Today 171 (2011) 116–125.

[35] K. Oshima, T. Shinagawa, M. Haraguchi, Y. Sekine, Low temperature hydrogen production by catalytic steam reforming of methane in an electric field, Int. J. Hydrogen Energy 38(7) (2013) 3003–3011.

[36] K. Oshima, K. Tanaka, T. Yabe, E. Kikuchi, Y. Sekine, Oxidative coupling of methane using carbon dioxide in an electric field over La-ZrO_2 catalyst at low external temperature, Fuel 107 (2013) 879–881.

[37] K. Oshima, T. Shinagawa, Y. Sekine, Methane conversion assisted by plasma or electric field –a review–, J. Jpn. Petrol. Inst. 56(1) (2013) 11–21.

[38] K. Oshima, T. Shinagawa, Y. Nogami, Y. Manabe, S. Ogo, Y. Sekine, Low temperature catalytic reverse water gas shift reaction assisted by an electric field, Catal. Today 232 (2014) 27–32.

[39] K. Sugiura, S. Ogo, K. Iwasaki, T. Yabe, Y. Sekine, Low-temperature catalytic oxidative coupling of methane in an electric field over a Ce-W-O catalyst system, Sci. Rep. 6 (2016) 25154.

[40] J.J Daniels, A.R. Arther, B.L. Lee, S.M. Stagg-Williams, Infrared spectroscopy study of CO and CO_2 on Ce- and La-promoted Pt/ZrO_2 catalysts, Catal. Lett. 103 (2005) 169–177.

[41] R. Manabe, S. Okada, R. Inagaki, K. Oshima, S. Ogo, Y. Sekine, Surface protonics promotes catalysis, Sci. Rep. in press.

[42] A.M. Gadalla, B. Bower, The role of catalyst support on the activity of nickel for reforming methane with CO_2, Chem. Eng. Sci. 43 (1988) 3049–3062.

[43] A.M. Gadalla, B. Bower, Carbon dioxide reforming of methane on nickel catalysts, Chem. Eng. Sci. 44 (1989) 2825–2829.

[44] K. Tanaka, Y. Sekine, K. Oshima, Y. Tanaka, M. Matsukata, E. Kikuchi, Catalytic oxidative coupling of methane assisted by electric power over a semiconductor catalyst, Chem. Lett. 41 (2012) 351–353.

[45] S. Sokolov, E.V. Kondratenko, M.-M. Pohl, U. Rodemerck, Effect of calcination conditions on time on-stream performance of $Ni/La_2O_3–ZrO_2$ in low- temperature dry reforming of methane, Int. J. Hydrogen Energy 38 (2013) 16121–16132.

[46] H.M. Swaan, V.C.H. Kroll, G.A. Martin, C. Mirodatos, Deactivation of supported nickel catalysts during the reforming of methane by carbon dioxide, Catal. Today 21 (1994) 571–578.

[47] D.C. Gardner, C.H. Bartholomew, Kinetics of carbon deposition during methanation of carbon monoxide, Ind. Eng. Chem. Prod. Res. Dev. 20(1) (1981) 80–87.

[48] D.W. Goodman, R.D. Kelley, T.E. Madey, J.T. Yates Jr., Kinetics of the hydrogenation of CO over a single crystal nickel catalyst, J. Catal. 63 (1980) 226–234.

[49] V.A. Tsipouriari, A.M. Efstathiou, Z.L. Zhang, X.E. Verykios, Reforming of methane with carbon dioxide to synthesis gas over supported Rh catalysts, Catal. Today 21 (1994) 579–587.

[50] V.A. Tsipouriari, X.E. Verykios, Carbon and oxygen reaction pathways of CO_2 reforming of methane over Ni/La_2O_3 and Ni/Al_2O_3 catalysts studied by isotopic tracing techniques, J. Catal. 187 (1999) 85–94.

[51] L. Hanley, Z. Xu, J.T. Yates Jr., Methane activation on Ni(111) at high pressures, Surf. Sci. 248 (1991) L265–L273.

[52] R. Rosei, F. Ciccacci, R. Memeo, C. Mariani, L.S. Caputi, L. Papagno, Kinetics of carbidic carbon formation from CO in the 10^{-6}-Torr range on Ni(110), J. Catal. 83(1) (1983) 19–24.

[53] C. Astaldi, A. Santoni, F.D. Valle, R. Rosei, Co dissociation and recombination reactions on Ni(100), Surf. Sci. 220(2-3) (1989) 322–332.

[54] J.G. McCarty, H. Wise, Hydrogenation of surface carbon on alumina-supported nickel, J. Catal 57(1979) 406–416.

[55] J.R. Rostrup-Nielsen, J.H.B. Hansen, CO_2-reforming of methane over transition metals, J. Catal 144 (1993) 38–49.

[56] L.J. E. Hofer, E. Sterling, J.T. McCartney, Structure of carbon deposited from carbon monoxide on iron, cobalt and nickel, J. Phys. Chem. 59(11) 1955 1153–1155.

[57] R.T.K. Baker, M.A. Barber, P.S. Harris, F.S. Feates, R.J. Waite, Nucleation and growth of

carbon deposits from the nickel catalyzed decomposition of acetylene, J. Catal. 26 (1972) 51–62.

[58] J.R. Rostrup-Nielsen, D. L. Trimm, Mechanisms of carbon formation on nickel-containing catalysts, J. Catal. 48 (1977) 155–165.

[59] S. Helveg, J. Sehested, J.R. Rostrup-Nielsen, Whisker carbon in perspective, Catal. Today 178 (2011) 42–26.

[60] M.C.J. Bradford, M.A. Vannice, Catalytic reforming of methane with carbon dioxide over nickel catalysts II. Reaction kinetics, Appl. Catal. A: Gen. 142 (1996) 97–122.

[61] M.C.J. Bradford, M.A. Vannice, CO_2 reforming of CH_4 over supported Pt catalysts, J. Catal. 173 (1998) 157–171.

[62] Z. Zhang, X.E. Verykios, S.M. MacDonald, S. Affrossman, Comparative study of carbon dioxide reforming of methane to synthesis gas over Ni/La_2O_3 and conventional nickel-based catalysts, J. Phys. Chem. 100 (1996) 744–754.

Table 3-1 Catalytic activities for DRM in an electric field over (A) various metal-supported La-ZrO_2 oxide catalysts, (B) various metal-doped Ni/M-ZrO_2 oxide catalysts, and (C) various loading amounts of Ni supported on La-ZrO_2 oxide catalysts: 3.0 mA applied current

(A)

Catalyst	Temp. / K	Power / W	Field Intensity / V mm^{-1}	CH_4 conv. / %	CO_2 conv. / %	CO sel. / %	CO yield / %	H_2/CO / –	Faradaic Number / –
La-ZrO_2	596	3.7	151	1.9	1.9	74.4	1.4	0.76	21
Fe/La-ZrO_2	649	3.5	228	6.9	14.6	91.2	6.3	0.23	119
Co/La-ZrO_2	619	4.5	292	20.3	31.2	99.4	20.1	0.57	252
Ni/La-ZrO_2	555	3.7	243	22.8	24.8	100	22.8	0.83	252
Cu/La-ZrO_2	626	3.9	256	3.9	3.6	88.5	3.5	0.99	42
Pd/La-ZrO_2	533	1.9	125	6.4	9.8	100	6.4	0.52	84
Pt/La-ZrO_2	580	4.1	271	21.0	23.6	100	21.0	0.80	238

(B)

Catalyst	Temp. / K	Power / W	Field Intensity / V mm^{-1}	CH_4 conv. / %	CO_2 conv. / %	H_2/CO / –	Faradaic Number / –
Ni/ZrO_2	560	3.0	182	15.2	18.6	0.77	184
Ni/La-ZrO_2	555	3.7	243	22.8	24.8	0.83	252
Ni/Ce-ZrO_2	545	2.1	143	13.2	17.2	0.75	171
Ni/Pr-ZrO_2	538	2.4	131	15.2	20.7	0.78	211
Ni/Nd-ZrO_2	498	2.1	137	12.5	15.0	0.88	158
Ni/Y-ZrO_2	496	2.4	170	12.4	17.8	0.75	145

(C)

Loading amount / wt%	Temp. / K	Power / W	Field Intensity / V mm^{-1}	CH_4 conv. / %	CO_2 conv. / %	CO sel. / %	CO yield / %	H_2/CO / –	Faradaic Number / –
0	596	2.3	153	1.9	1.9	74.4	1.4	0.76	21
0.5	653	4.8	314	16.0	20.7	100	16.0	0.78	203
1	555	3.7	245	22.8	24.8	100	22.8	0.83	252
2	503	1.7	115	9.0	11.0	100	9.0	0.84	109
5	471	1.1	76	4.3	4.8	100	4.3	0.87	45
10	482	1.1	71	3.0	4.3	100	3.0	0.65	36

Table 3-2 XRD crystallite size of various metal-doped ZrO_2 catalysts at a tetragonal ZrO_2 (110) face using the Debye–Scherrer formula

Catalyst	Crystallite size / nm
La-ZrO_2	8.2
Ce-ZrO_2	34.9
Pr-ZrO_2	23.3
Nd-ZrO_2	19.9
Y-ZrO_2	34.9

Table 3-3 Catalytic activities and amounts of carbon deposition under a high conversion condition on DRM with/without the electric field over 1wt%Ni/La-ZrO_2 oxide catalyst: 3.0 mA applied current, CH_4:CO_2:Ar = 1:1:2, total flow rate 20 mL min^{-1}

		Power / W	CH_4 conv. / %	CO_2 conv. / %	CO sel. / %	CO yield / %	H_2/CO / –	Carbon deposition / mg g-cat^{-1}
no imposing EF	initial	-	63.5	52.9	100	63.5	1.20	>39.6
	140 min.	-	64.0	77.0	100	64.0	0.81	
imposing EF	initial	8.1	74.5	85.3	100	74.5	0.87	1.5
	140 min.	6.9	77.2	87.6	100	77.2	0.88	

Table 3-4 Reaction orders obtained by changing partial pressures of reactants

Reaction order	no electric field		with electric field	
	P_{CH4}	P_{CO2}	P_{CH4}	P_{CO2}
Formation rate of CO from CH_4	0.0	0.05	0.0	0.22
Formation rate of CO from CO_2	0.0	0.32	0.0	0.30
Formation rate of H_2	0.26	-0.42	0.0	0.34

Table 3-5 Catalytic activities, energy efficiencies and Faradaic numbers on DRM in the electric field over 1wt%Ni/La-ZrO_2 catalyst with various applied currents

Current / mA	Voltage / kV	Power / W	Tcat [a] / K	Converion / % CH_4	Converion / % CO_2	H_2/CO / –	ΔHr [b] / J s^{-1}	Energy efficiency [c] / %	Faradaic number / -
3	1.2	3.7	555	22.8	24.8	0.83	0.9	24.6	252
4	0.8	3.2	541	15.1	18.0	0.85	0.5	15.3	132
5	0.8	4.0	559	18.7	20.6	0.81	0.6	14.8	125
6	0.6	3.6	556	17.8	21.1	0.86	0.7	20.8	103
7	0.8	5.6	584	33.7	42.9	0.78	1.7	29.9	131
8	0.6	4.8	558	25.4	32.1	0.79	1.2	25.3	114
12	0.4	5.0	576	30.2	36.1	0.79	1.6	31.5	88

[a] T_{cat}: temperature measured using a thermocouple attached to the catalyst bed

[b] ΔH_r: endothermic enthalpy of reaction for DRM

[c] Energy efficiency (%) = ΔH_r / input power×100

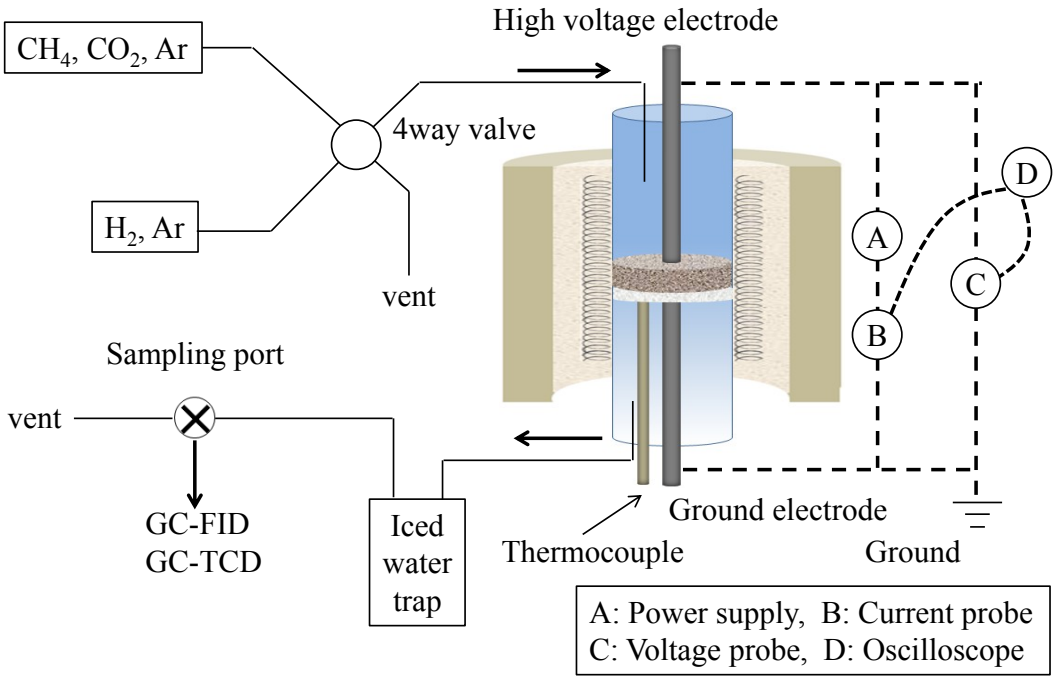

Figure 3-1 Schematic diagram of the experimental setup

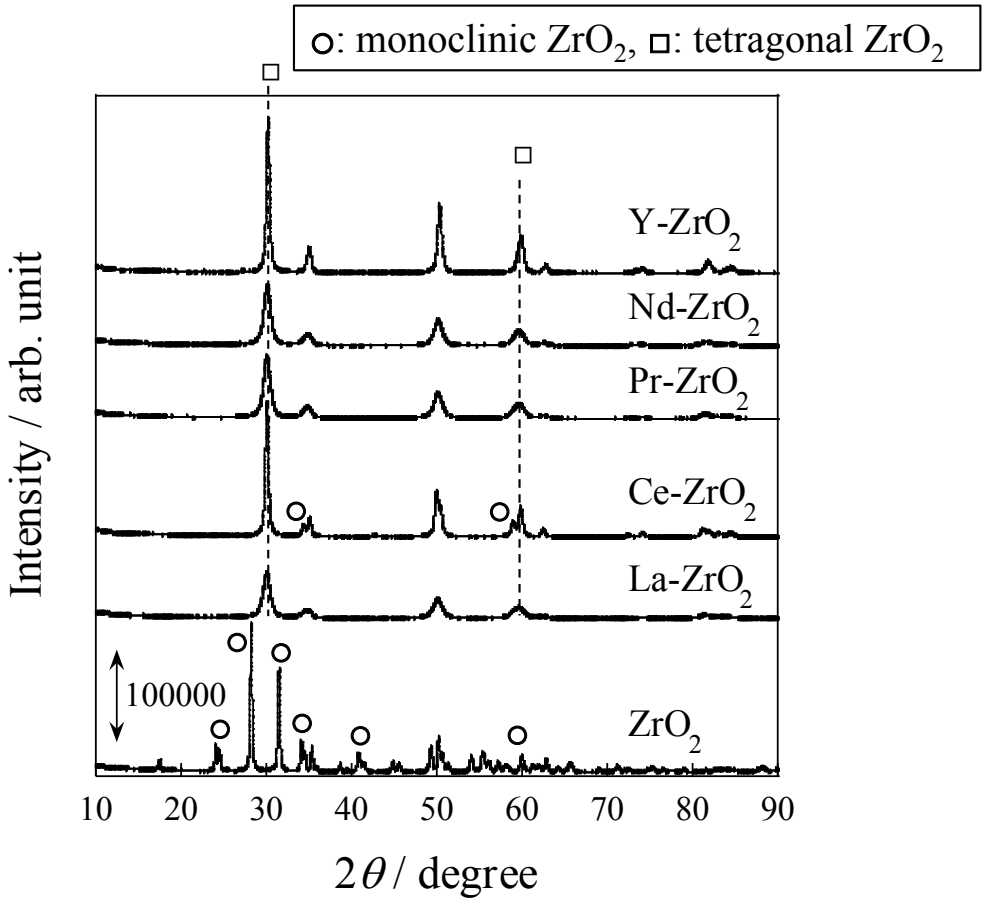

Figure 3-2 X-ray diffraction patterns for various metal-doped zirconia oxides.

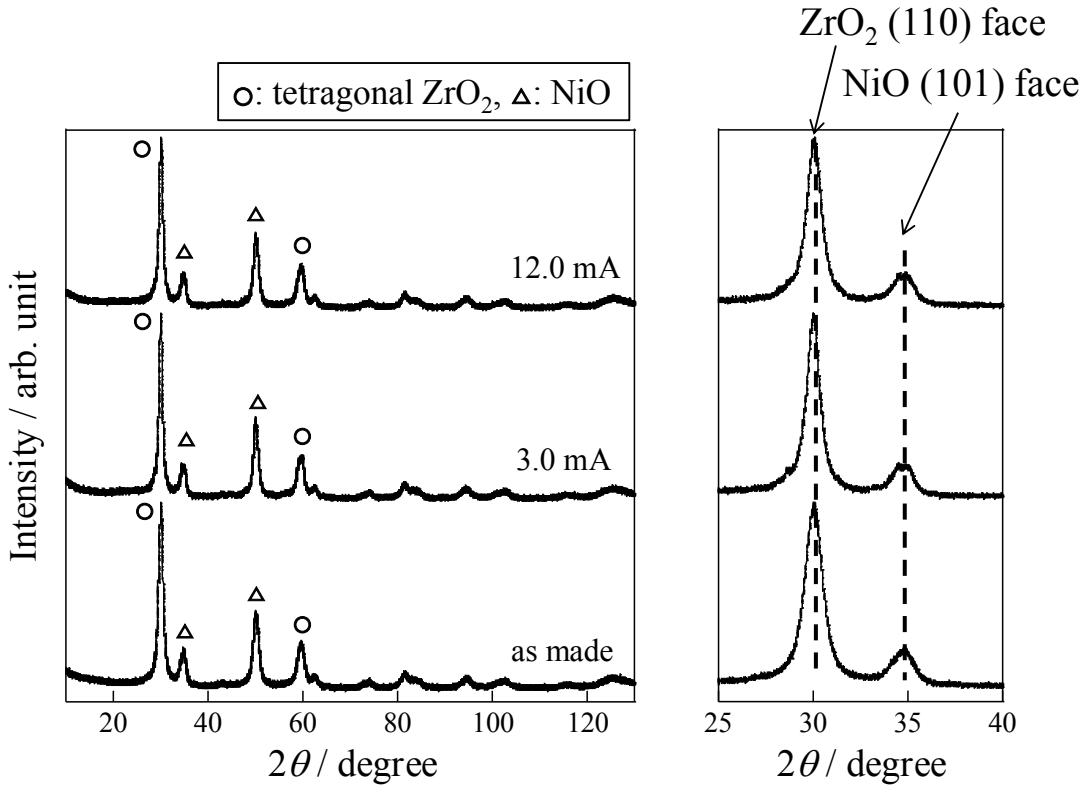

Figure 3-3 X-ray diffraction patterns for 1wt%Ni/La-ZrO_2 as made and after DRM in the electric field: 3.0 mA and 12.0 mA applied current.

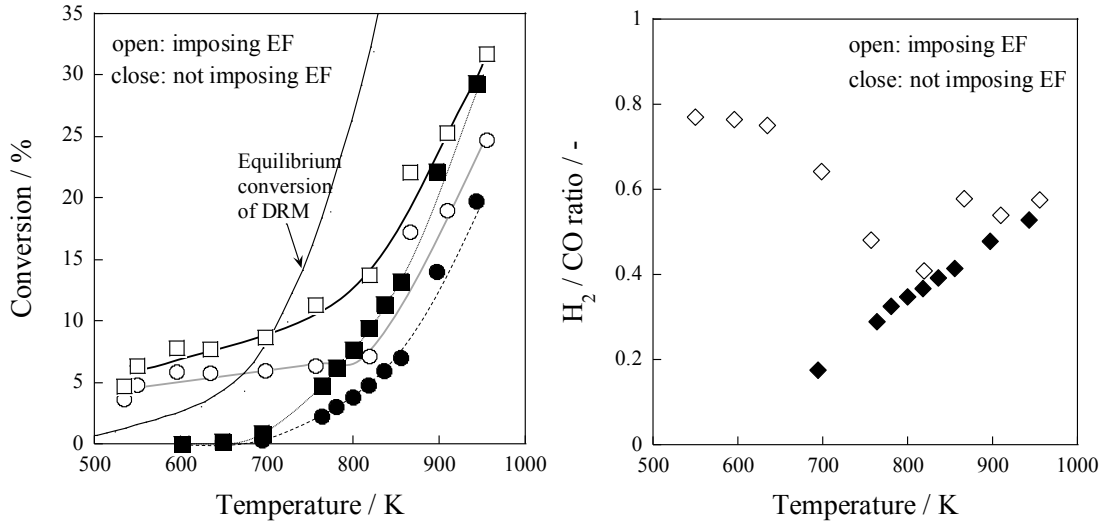

Figure 3-4 Comparison of the conversion and selectivity between conventional catalytic reaction and catalytic reaction in the electric field (EF) over 1wt%Ni/La-ZrO_2 catalyst: (Left) ○, CH_4 conversion; □, CO_2 conversion; (Right) ◇, H_2/CO ratio; 3.0 mA applied current

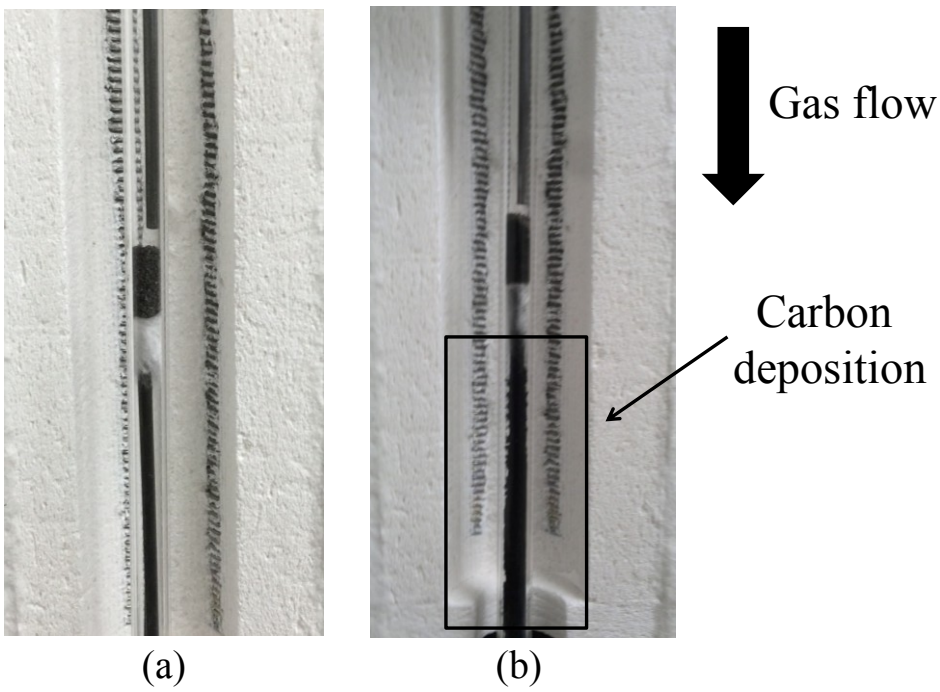

Figure 3-5 Carbon deposition in and around the reactor tube: (a) after DRM at 423 K in the electric field and (b) after DRM at 1023 K not imposing EF

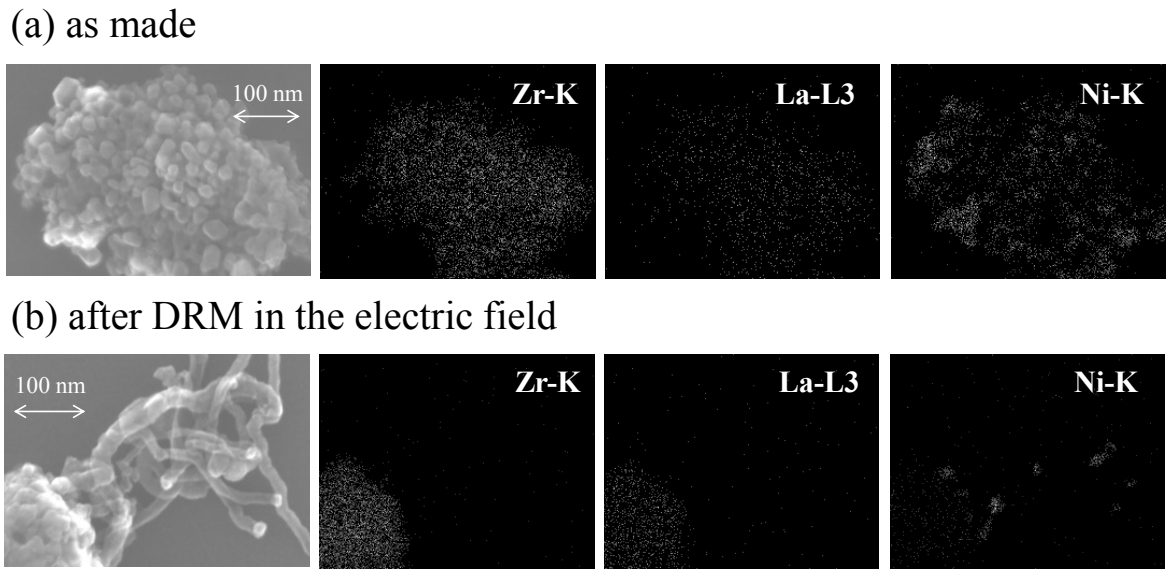

Figure 3-6 STEM images of 1wt%Ni/La-ZrO_2 (as made and after DRM in the electric field) and EDX mappings for Zr, La, and Ni.

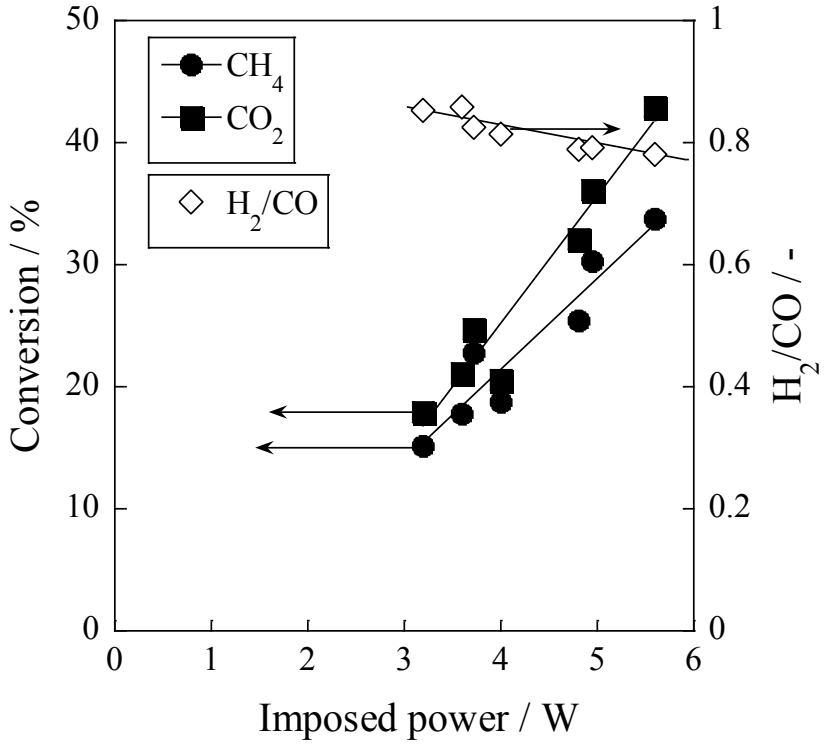

Figure 3-7 Effects of imposed electric power on the catalytic activity of DRM in the electric field over 1wt%Ni/La-ZrO_2 catalyst: ●, CH_4 conversion; ■, CO_2 conversion; and ◇, H_2/CO ratio

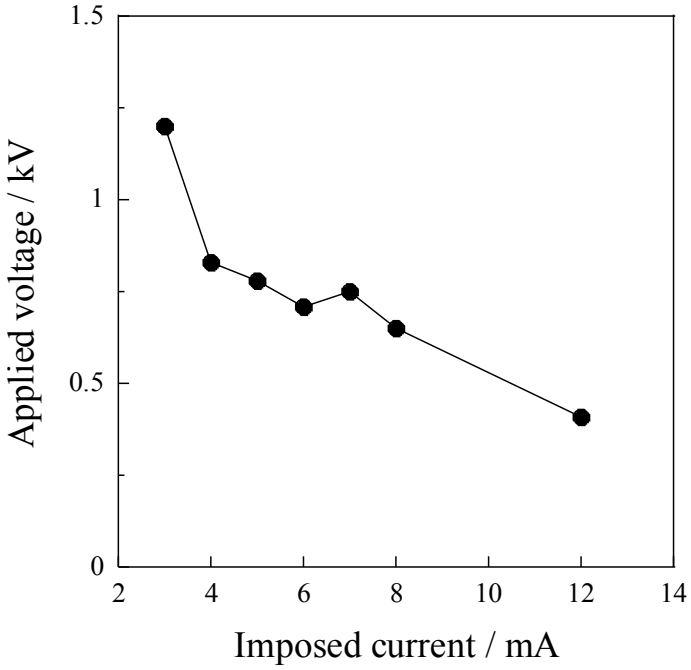

Figure 3-8 I-V profile on the catalytic reaction in the electric field.

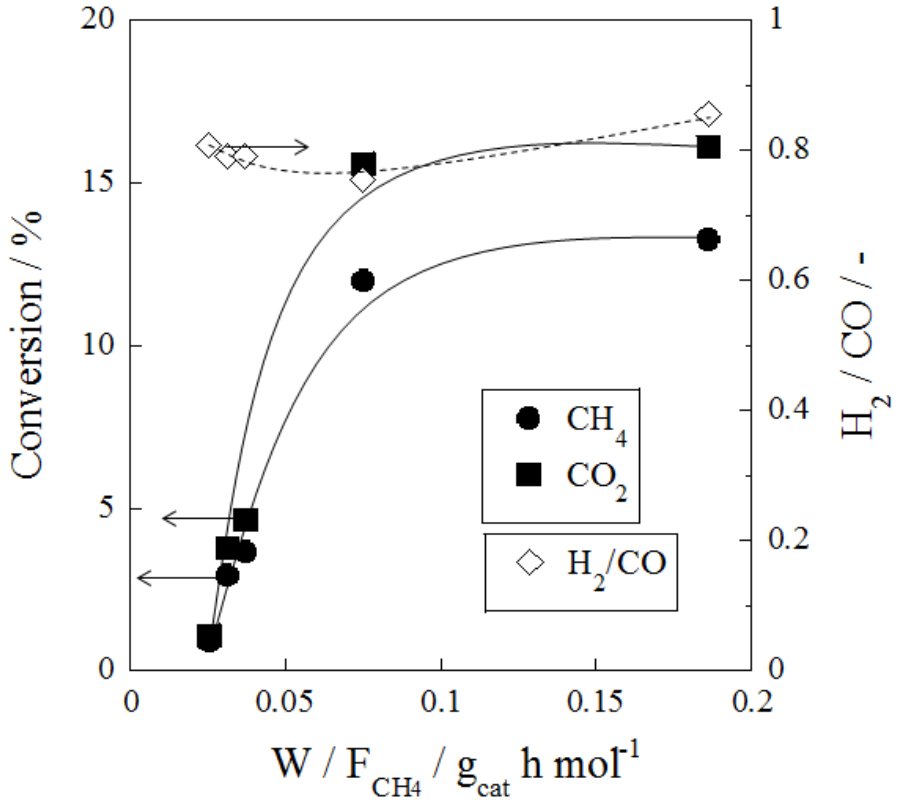

Figure 3-9 DRM catalytic activities depending on the contact time over 1wt%Ni/La-ZrO_2 catalyst: ●, CH_4 conversion; ■, CO_2 conversion; and ◇, H_2/CO ratio

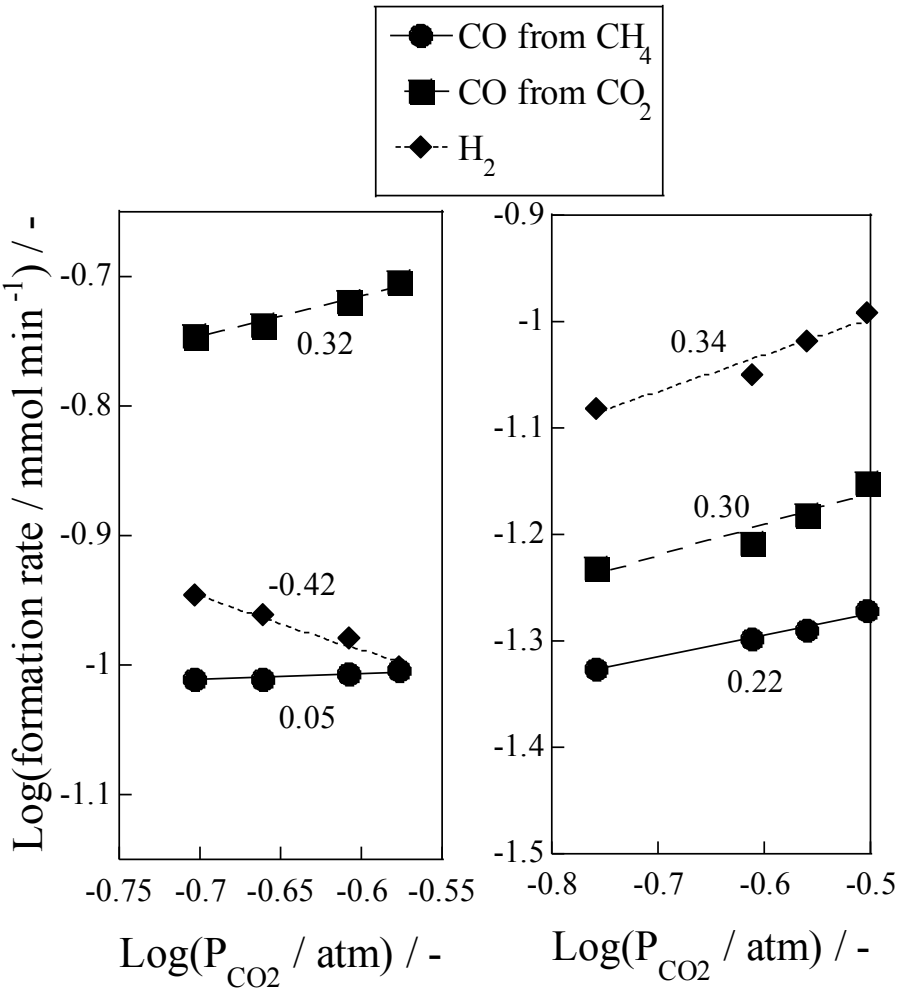

Figure 3-10 Effects of CO_2 partial pressure on the reaction rate for determining reaction order for DRM over 1wt%Ni/La-ZrO_2 catalyst: (left) in the conventional reaction (not imposing EF) at 823 K and (right) in the electric field at 823 K

Chapter 4 Other reactions

4.1 Oxidative coupling of methane using dioxide in an electric field over various metal doped ZrO_2 catalysts

4.1.1 Introduction

In this section, the tests for changing the residence time in various imposed currents and the activation tests for only CO_2 feed were conducted in order to investigate the detail reaction mechanism in oxidative coupling of methane using CO_2 (CO_2-OCM) in an electric field over 10 mol%-La doped ZrO_2 catalyst, which was reported by our groups before. [1] Additionally, in order to further improve CO_2-OCM activity in the ZrO_2 catalyst system, we conducted CO_2-OCM in the electric field over various alkali earth metal doped ZrO_2 catalysts. As a result of screening tests for various alkali earth metal doping catalysts, CH_4 conversion over Ba doped ZrO_2 catalyst was almost the same as that over La doped ZrO_2 catalyst but C_2 selectivity was lower. Therefore, the main object of this study was for elucidating the important factor of producing the CO_2-OCM reaction in the electric field over ZrO_2 catalyst system by comparing it to the catalytic activity over various alkali earth metal supported ZrO_2 catalysts and conducting XRD measurement.

4.1.2 Experimental

4.1.2.1 Catalyst preparation

CaO, SrO, BaO and various metal doped ZrO_2 (M-ZrO_2: M=Ca, Sr, Ba, La) catalysts were prepared using a complex polymerized method based on the Pechini method, as shown in Figure 4-1-1. Each of the nitrate precursors were dissolved into distilled water, with subsequent addition of citric acid and ethylene glycol. After condensation in a water bath at 353 K, the gel was stirred and heated to remove the water completely. Pre-calcination was conducted at 673 K for 2 h. Then calcination was conducted at 1123 K for 10 h in air flow. Next, supported alkali earth metals were loaded on various M-ZrO_2 catalysts with 10 wt% as an active metal using a water impregnation method. Precursors of respective elements were nitrate. Calcination was conducted at 973 K for 3 h.

4.1.2.2 Catalytic activity

Catalytic activity tests in the electric field were performed using a quartz tube (6 mm o.d.) reactor. The charged amount of the catalyst was 100 mg or 200 mg. The reaction temperature was 423 K. Products were dried in a cold trap and were subsequently analyzed using a GC-FID (GC-2014; Shimadzu Corp.) with a Porapak N-packed column after methanation by Ru/Al_2O_3 catalyst for analyses of CO, CH_4, and CO_2, C_{2+}hydrocarbons, and for GC-TCD (GC-2014; Shimadzu Corp.) with a molecular sieve 5A packed column for analyses of H_2 and CH_4. The electric field was applied on the catalyst using a DC high-voltage power supply. The field was controlled using a constant input current. The impressed voltage depended on the electric characteristics of the catalyst and the gas condition characteristics. Calculation methods were described in Chapter 2, section 2.2.5. The flow rate of raw gas was set up as CH_4:CO_2:Ar = 25:25:50, with a total flow rate of 100 mL min^{-1} insofar as there is no particular remark stating otherwise. In tests for changing the residence time, the flow rate ratio was fixed to CH_4:CO_2:Ar = 1:1:2, changing the total flow rate from 20 mL min^{-1} to 200 mL min^{-1}.

4.1.3 Results and discussion

4.1.3.1 The residence time dependence in CO_2-OCM over 10 mol%La-ZrO_2 catalyst

First, in order to obtain the more catalytic activity and investigate the reaction mechanism in CO_2-OCM in the electric field, tests for changing the residence time over the 10 mol%La-ZrO_2 catalyst were conducted in various imposed current conditions (3, 5, 7 mA). Results are shown in Figure 4-1-2. Also, results of the residence time dependence of the distribution for C_2 products, denoted as a C_2H_4/C_2H_6 ratio, in various imposed current conditions were shown in Figure 4-1-3. As shown in Figure 4-1-2, increasing the residence time resulted in decreasing OCM selectivity as the same trends in previous reports. [4] Additionally, from the result in Figure 4-1-3, increasing the residence time progressed the sequential reaction, possibly dry reforming of methane (DR), of C_2 products because of the increasing C_2H_4/C_2H_6 ratio. Otherwise, increasing the imposed current resulted in increasing the gradient for both CH_4 and CO_2 conversion and OCM selectivity drastically decreased in low residence time conditions. This was possibly because both CH_4 and CO_2 conversion depended on kinetic control in a low imposed current condition but the sequential reaction was not suppressed in a high imposed current condition due to an increase in the partial

pressure of C_2 products, which more easily reacted with CO_2 than methane. Therefore, the most appropriate reaction condition for CO_2-OCM in the electric field was in an imposed 3 mA current and high residence time: the C_2 yield was 4.0% in CH_4:CO_2:Ar = 5:5:10, the total flow rate was 100 mL min^{-1}; and the catalyst weight was 300 mg. In the conditions of higher residence time, the imposed electric field became unstable. Thus, the above mentioned reaction condition was possibly the most suitable over the 10 mol%La-ZrO_2 catalyst. Next, results of the residence time dependence of the reaction selectivity as OCM, DR and reverse water gas shift reaction (RWGS) in the CO_2-OCM reaction condition in the electric field in an imposed 3 mA current were also shown in Figure 4-1-4. As a result, the reaction selectivity for DR and RWGS increased as the residence time increased. These trends in the electric field were the same as previous reports in the conventional catalytic reaction. [5] Next, results of the residence time dependence of the CH_4 and CO_2 conversion per input current in various imposed current conditions were shown in Figure 4-1-5. As a result, CH_4 and CO_2 conversion increased as the residence time increased due to the synergistic effect for the catalyst and electric field, not due to the electrochemical reaction.

Next, we focused on the lower residence time area. Results of the residence time dependence of the CH_4 conversion in the lower residence time area were shown in Figure 4-1-6. As a result, another reaction probably proceeded before the reaction for CH_4 and CO_2 because the intercept for the approximate straight line was negative and the consumption rate decreased. The possible reaction is the degradation of CO_2 as follows:

$$CO_2 \rightarrow CO + 1/2\ O_2 \qquad \text{eq. 1-1}$$

In order to investigate the side reaction for the degradation of CO_2, tests for only CO_2 feed, diluted by Ar, in the electric field were conducted in the lower residence time area. Results of the residence time dependence of CO_2 conversion (left side) and the consumption rate for CO_2 (right side) in the lower residence time area were shown in Figure 4-1-7. As a result, only the degradation of CO_2 proceeded because the approximate straight line passed through the origin of the coordinate axes and the consumption rate for CO_2 was constant in this area. Additionally, in order to confirm the degradation of CO_2 proceeded in the conventional catalytic reaction, not the imposed electric field, tests for the temperature dependence of CO_2 conversion were conducted, as shown in Figure 4-1-8. As a result, the degradation of CO_2 progressed exceeding 1123 K to some extent. Compared with the results in Figure 4-1-7, the degradation of CO_2 was activated by applying the electric field. The degradation of catalytic activity was not observed because the tests were conducted over no metal supported catalysts

and active oxygen species functioned as counter reactants were not produced. In our case, surface oxygen ion defects ($V_O^{\cdot\cdot}$) and CO_2 on 10 mol%La-ZrO_2 oxide catalysts reacted as the CO_2 decomposition, and active oxygen species functioned as counter reactants decreased as the reaction progressed. (as shown in eq. 2)

$$CO_2 + V_O^{\cdot\cdot} \rightarrow CO + O_{lat} \qquad \text{eq. 1-2}$$

In order to investigate the effect of this reaction on CO_2-OCM in the electric field, the formation rate of O_2 calculated from that of products (upper side) was compared to that derived from the degradation of CO_2 (down side), as shown in Table 4-1-1. As a result, O_2 derived from the CO_2 decomposition possibly reacted with CH_4 to form C_2 hydrocarbons because the formation rate of O_2 derived from the CO_2 decomposition was higher than the formation calculated from that of products. Additionally, the effect of the CH_4 reaction was not ignored because the formation rate of CO in CO_2-OCM was different from that in the CO_2 decomposition.

4.1.3.2 Screening tests over various ZrO_2 catalysts

In order to obtain higher CO_2-OCM activity than described before, screening tests over various metal doped ZrO_2 catalysts were conducted in the electric field. As shown in Figure 4-1-9, the side reaction such as the DRM reaction thermodynamically proceeded more than the CO_2-OCM reaction at a higher temperature. Therefore, lower reaction temperature was important for producing the CO_2-OCM reaction. In the screening tests over various ZrO_2 catalysts, the alkali earth metal doped ZrO_2 catalyst showed higher CO_2-OCM activity than the ZrO_2 catalyst, especially the 10 mol%Ba-ZrO_2 catalyst that had the same activity for the 10 mol%La-ZrO_2 catalyst. Therefore, activation tests for changing the substitution amounts of Ba in the Ba doped ZrO_2 catalyst system were conducted in the electric field, as shown in Table 4-1-2. As a result, the highest OCM yield was obtained over the BaO catalyst but the stability of the Ba doped ZrO_2 catalyst was higher than BaO. In order to elucidate the structural effect of Ba doped into ZrO_2, XRD measurements for various amounts of Ba doped ZrO_2 catalysts were conducted, as shown in Figure 4-1-10. From the result, the tetragonal phase of ZrO_2 was observed to be the same as the La doped ZrO_2, previously reported. [1] Increasing the amounts of doped Ba in ZrO_2 resulted in increasing the intensity for $BaZrO_3$ phase and this unpurified structure possibly lowered CO_2-OCM activity.

Next, screening tests over various alkali earth metal supported ZrO_2, Sr or Ba doped ZrO_2 catalysts were conducted in the electric field. Results are summarized in Table 4-1-3. As a result, in various alkali earth metal supported ZrO_2 catalysts, the initial activity was higher than the ZrO_2 catalyst but the catalytic activity degraded quickly. These trends were the same over Sr or Ba doped ZrO_2 supports. Therefore, metal supported ZrO_2 catalysts were not suitable in CO_2-OCM in the electric field.

4.1.4 Conclusion

Oxidative coupling of methane using carbon dioxide (CO_2-OCM) was conducted in an electric field. Upon investigating for the residence time dependence in CO_2-OCM over the 10 mol%La-ZrO_2 catalyst, the most appropriate reaction condition for the reaction in the electric field was in an imposed 3 mA current and high residence time: the C_2 yield was 4.0% in CH_4:CO_2:Ar = 5:5:10, the total flow rate was 100 mL min^{-1};and the catalyst weight was 300 mg. As a result of investigating the effect of CO_2 degradation on CO_2-OCM in the electric field, O_2 derived from the CO_2 decomposition possibly reacted with CH_4 to form C_2 hydrocarbons. Otherwise, results of the screening tests over various ZrO_2 catalysts show that 10 mol%Ba-ZrO_2 was the most appropriate catalyst in this reaction system, and it shows high activity even at 423 K. However, the structure was unstable in CO_2-OCM in the electric field and metal supported ZrO_2 catalysts were not suitable in CO_2-OCM in the electric field.

Reference

[1] K. Oshima, K. Tanaka, T. Yabe, E. Kikuchi, Y Sekine, Oxidative coupling of methane using carbon dioxide in an electric field over La–ZrO_2 catalyst at low external temperature, Fuel 107 (2014) 879–881.

[2] K. Pokrovski, K. T. Jung, A.T. Bell, Investigation of CO and CO_2 adsorption on tetragonal and monoclinic zirconia, Langmuir 17 (2001) 4297–4303.

[3] N.A. Merino, B.P. Barbero, P. Eloy, L.E. Cadús, $La_{1-x}Ca_xCoO_3$ perovskite-type oxides: Identification of the surface oxygen species by XPS, Appl. Surf. Sci. 253 (2006) 1489–1493.

[4] K. Oshima, K. Tanaka, T. Yabe, Y. Tanaka, Y. Sekine, Catalytic oxidative coupling of methane with a dark current in an electric field at low external temperature, Int. J. Plasma Eng. Sci. Technol. 6 (2012) 266–271.

[5] K. Asami, T. Fujita, K. Kusakabe, Y. Nishiyama, Y. Ohtsuka, Conversion of methane with carbon dioxide into C_2 hydrocarbons over metal oxides, Appl. Catal. A. 126 (1995) 245–255.

Table 4-1-1 Evaluation of the CO_2 degradation for CO_2-OCM on the 10 mol% La-ZrO_2 catalyst in the electric field.

$CH_4/CO_2/Ar$	W/F	CO_2 conv.	Formation rate / mmol/min			
Flow rate / mL min^{-1} / g-cat h mol^{-1}		/ %	CO from CO_2	C_2H_4	C_2H_6	O_2(calculation)
15_15_30	5.41	8.44	0.050	0.0023	0.0024	0.0035
25_25_50	2.95	7.64	0.073	0.0036	0.0040	0.0055
35_35_70	2.44	3.66	0.062	0.0030	0.0039	0.0050
45_45_90	1.84	1.98	0.039	0.0023	0.0036	0.0041

CO_2/Ar	W/F	CO_2 conv.	Formation rate / mmol/min	
Flow rate / mL min^{-1} / g-cat h mol^{-1}		/ %	CO	O_2(calculation)
15_30	5.70	3.15	0.025	0.012
25_50	3.50	1.95	0.025	0.012
35_70	2.41	1.23	0.023	0.011
45_90	1.86	1.02	0.024	0.012

Table 4-1-2 Results of the activation test of various Ba doped ZrO_2 catalysts in the electric field.

	Voltage/V	CH_4 Conv. / %	CO_2 Conv. / %	OCM Sel. / %	OCM Yield / %	C_2H_4/C_2H_6 / -	Power / W	IEP dens. / W・mm^{-1}
ZrO_2	1400	7.44	12.3	13.3	0.99	0.67	7.0	0.83
10mol%Ba-ZrO_2	1000	4.00	9.6	19.3	0.77	1.02	5.0	0.45
50mol%Ba-ZrO_2	800	8.3	12.6	6.09	0.51	1.03	4.0	0.45
70mol%Ba-ZrO_2	2600	41.5	59.9	1.30	0.54	1.48	13.0	0.59
BaO	1200	3.18	1.65	39.1	1.24	1.08	6.0	0.30

Table 4-1-3 Results of the activation test of various alkali earth metal catalysts supported on ZrO_2 in the electric field.

	Voltage/V	CH_4 Conv. / %	CO_2 Conv. / %	OCM Sel. / %	OCM Yield / %	C_2H_4/C_2H_6 / -	Power / W	IEP dens. / W・mm^{-1}
10 wt%Ca/ZrO_2	1800	1.5	1.4	34.2	0.51	0.40	5.4	0.40
10 wt%Sr/ZrO_2	1800	7.4	11.9	20.5	1.52	1.17	5.4	0.47
10 wt%Ba/ZrO_2	800	2.5	3.2	18.4	0.45	0.61	4.0	0.36
ZrO_2	2200	7.2	11.8	10.6	0.77	0.58	6.6	0.79
10wt%Ba/10mol%Ba-ZrO_2	1500	13.4	17.8	3.61	0.48	1.49	4.5	0.45
10mol%Ba-ZrO_2	2200	7.0	16.7	20.5	1.44	1.0	6.6	0.65
10wt%Sr/10mol%Sr-ZrO_2	900	4.9	6.8	10.0	0.49	0.9	2.7	0.27
10mol%Sr-ZrO_2	2000	10.0	17.0	14.0	1.40	1.01	6.0	0.59

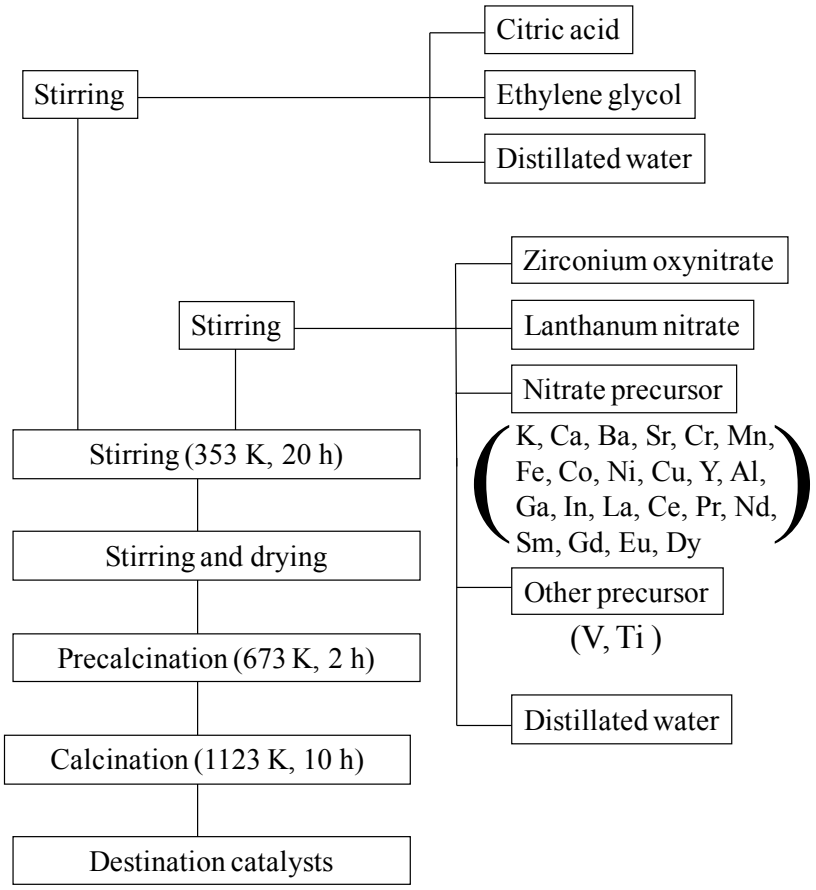

Figure 4-1-1 Preparation of various catalysts by complex polymerized method

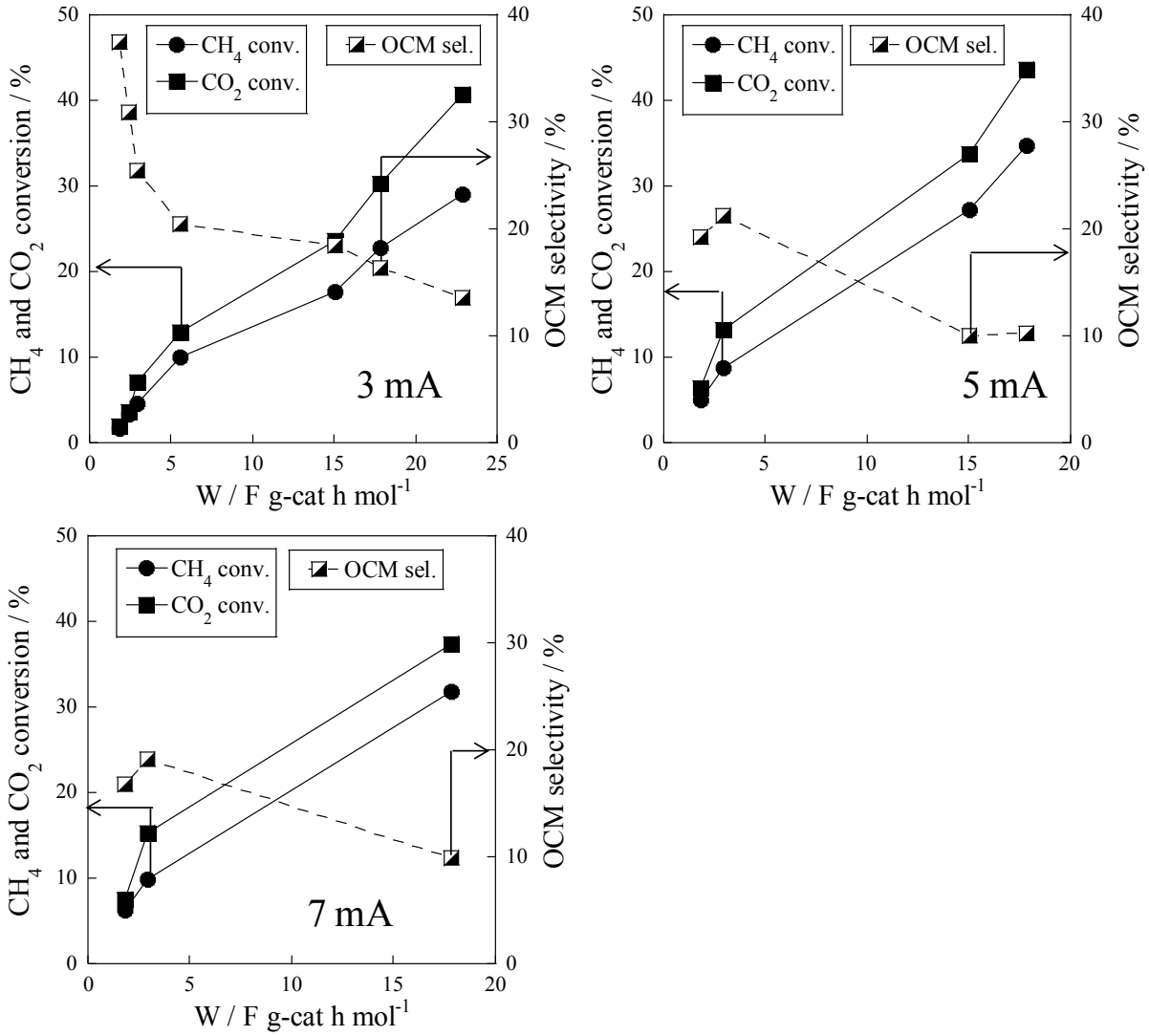

Figure 4-1-2 Effect of the residence time on the conversion and selectivity for the CO_2-OCM reaction over the 10 mol% La-ZrO_2 catalyst in the electric field, imposing various current (3,5,7 mA): ; ●, CH_4 conversion; ■, CO_2 conversion; ◪, OCM selectivity.

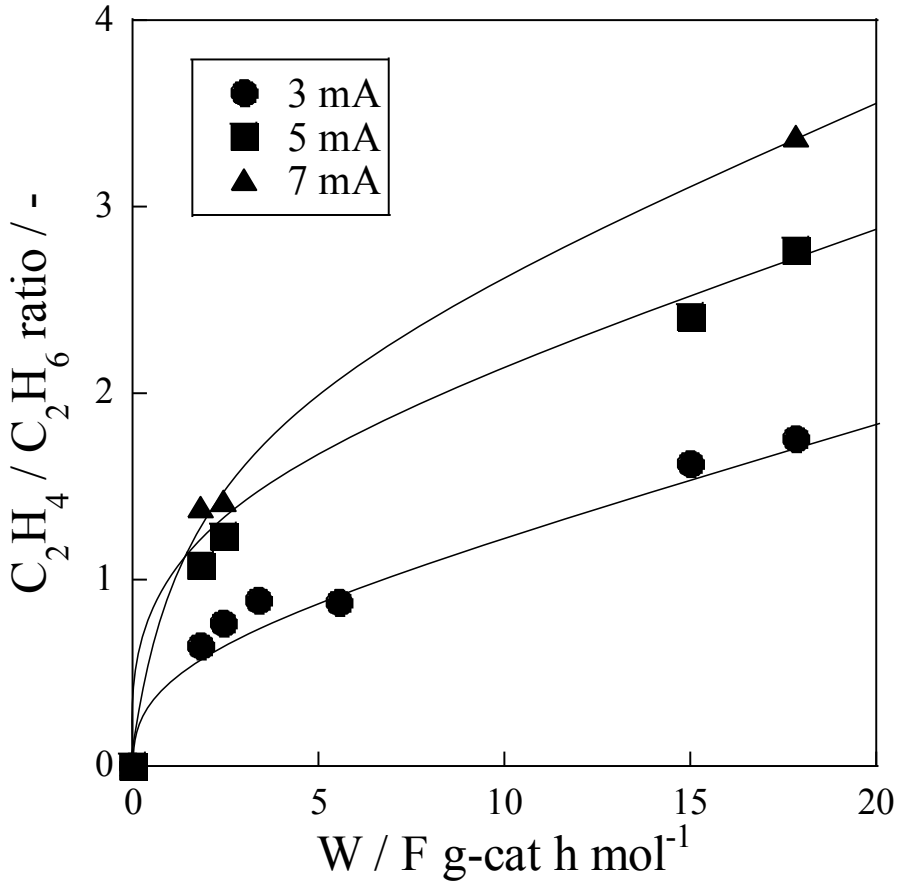

Figure 4-1-3 Effect of the residence time on the C_2H_4 / C_2H_6 ratio for the CO_2-OCM reaction over the 10 mol% La-ZrO_2 catalyst in the electric field, imposing 3 mA current.

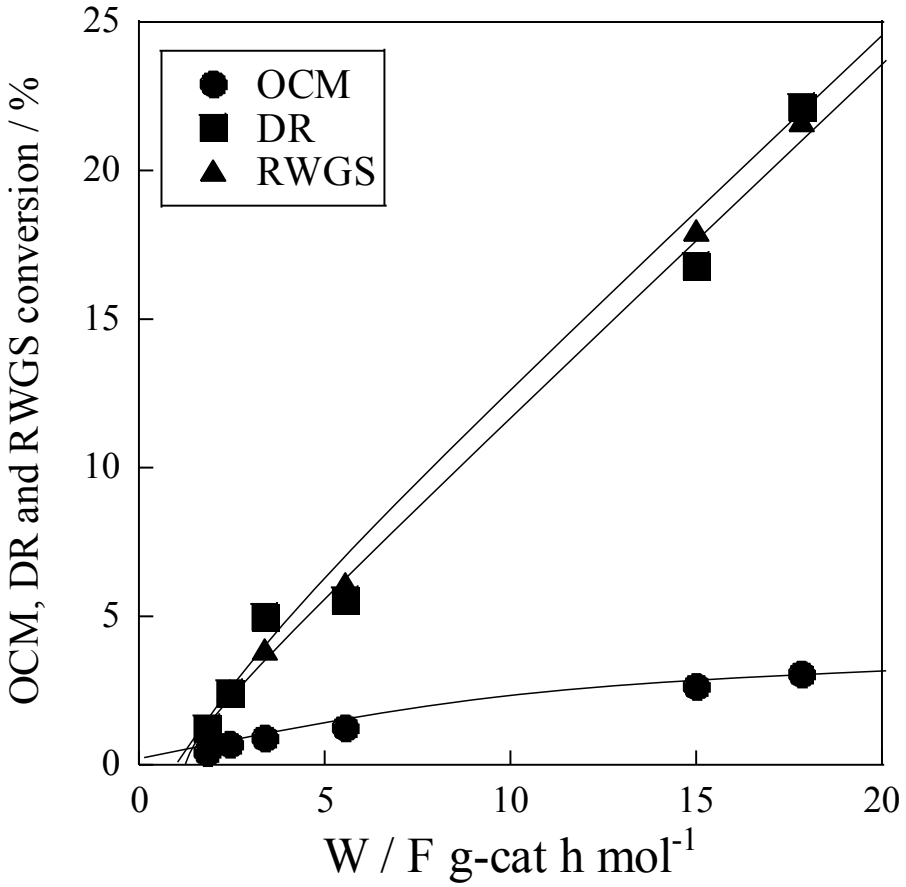

Figure 4-1-4 Effect of the residence time on the various conversion for OCM, DR and RWGS in the CO_2-OCM condition over the 10 mol% La-ZrO_2 catalyst in the electric field, imposing 3 mA current.

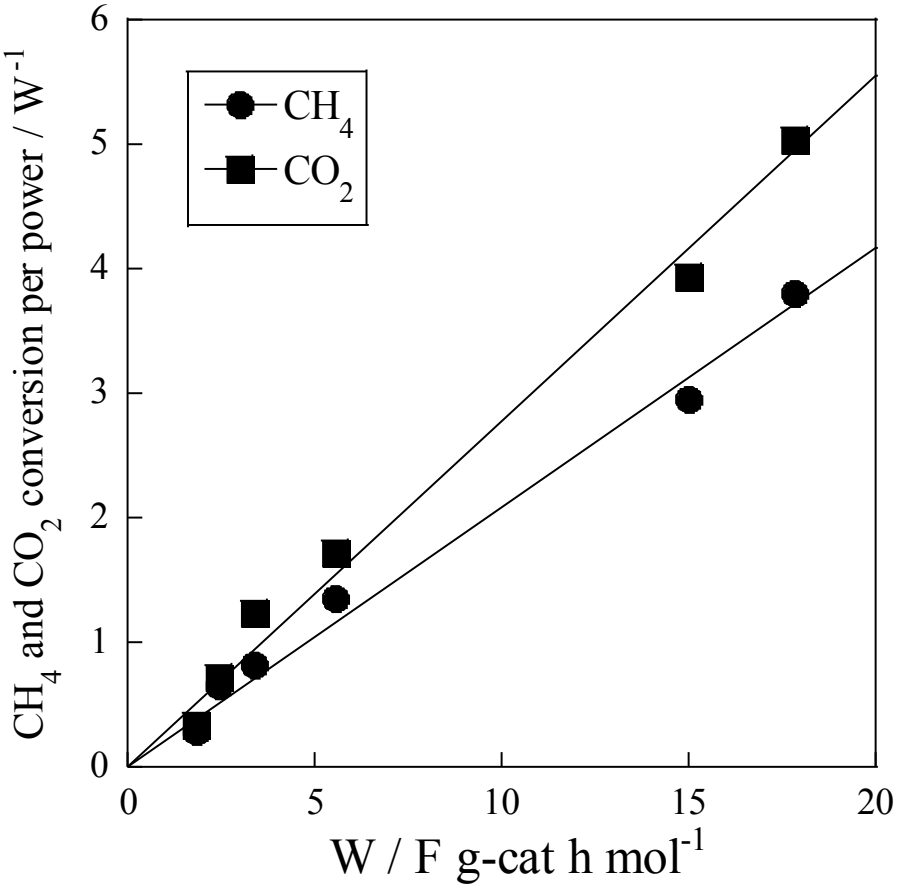

Figure 4-1-5 Effect of the residence time on the conversion per power for the CO_2-OCM over the 10 mol% La-ZrO_2 catalyst in the electric field, imposing 3 mA current.

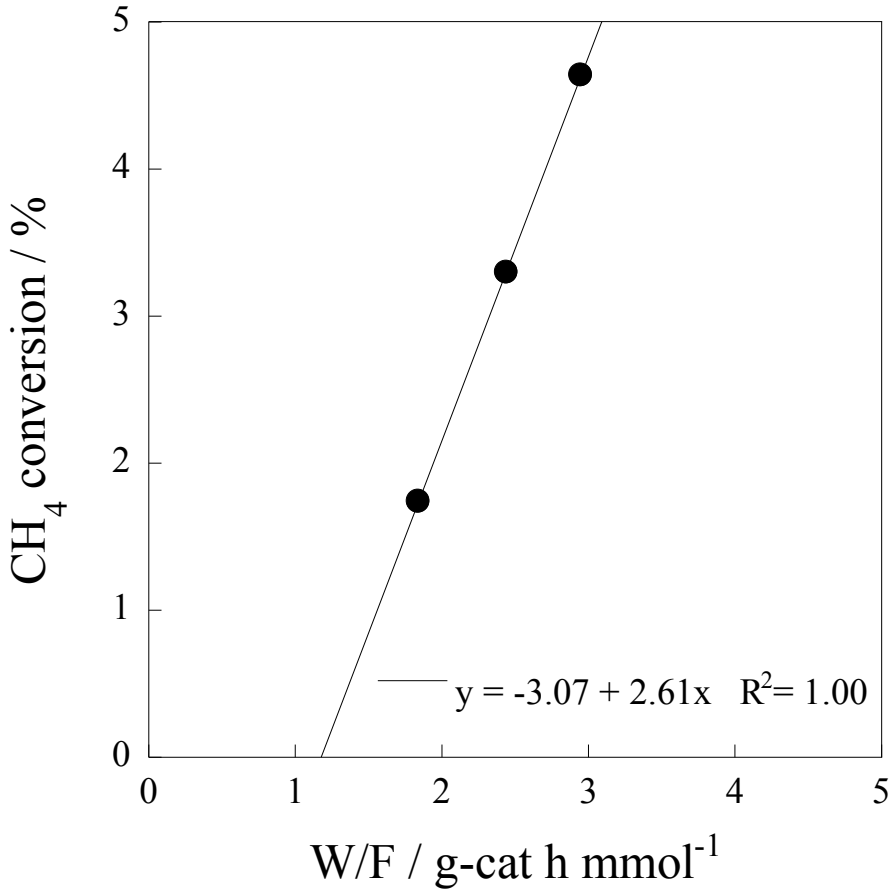

Figure 4-1-6 Effect of the residence time on the CH_4 conversion for the CO_2-OCM over 10 mol% La-ZrO_2 catalyst in the electric field, imposing 3 mA current.

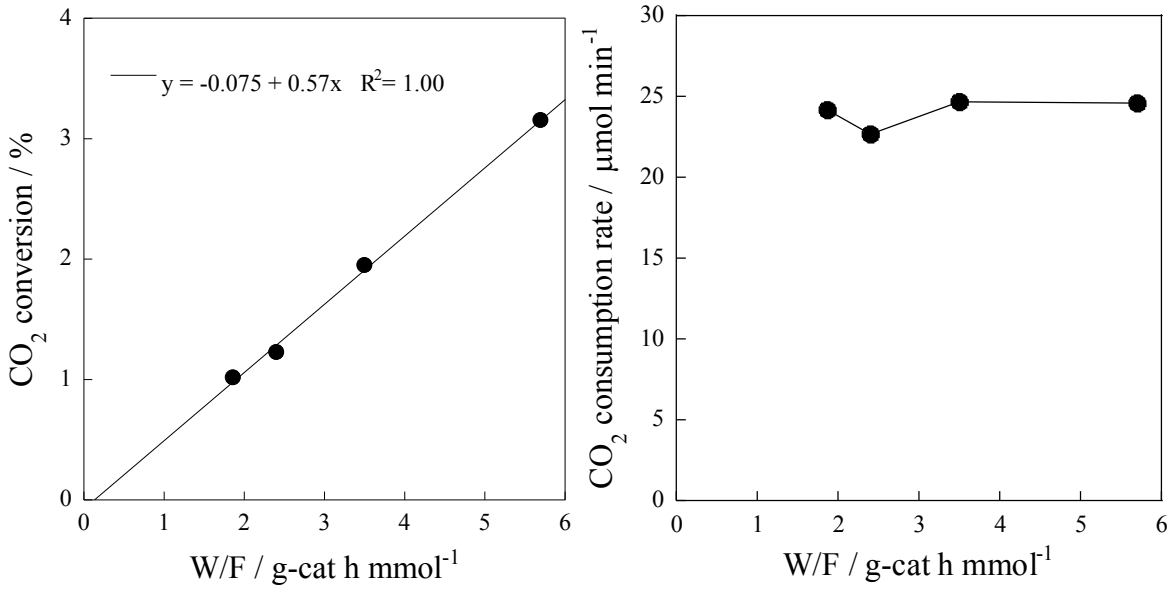

Figure 4-1-7 Effect of the residence time on the CO_2 conversion (Left) and consumption rate (Right) for the CO_2-OCM reaction over 10 mol% La-ZrO_2 catalyst in the electric field, imposing 3 mA current.

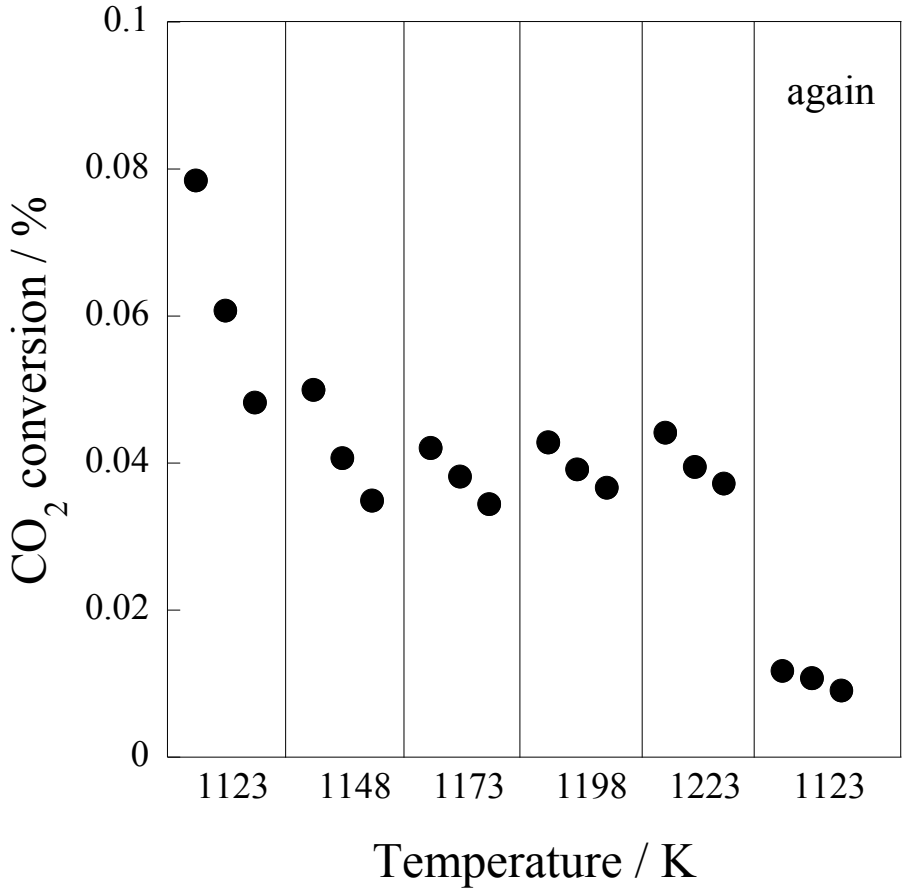

Figure 4-1-8 Temperature dependence of CO_2 conversion for the CO_2-OCM reaction over 10 mol% La-ZrO_2 catalyst in the conventional reaction.

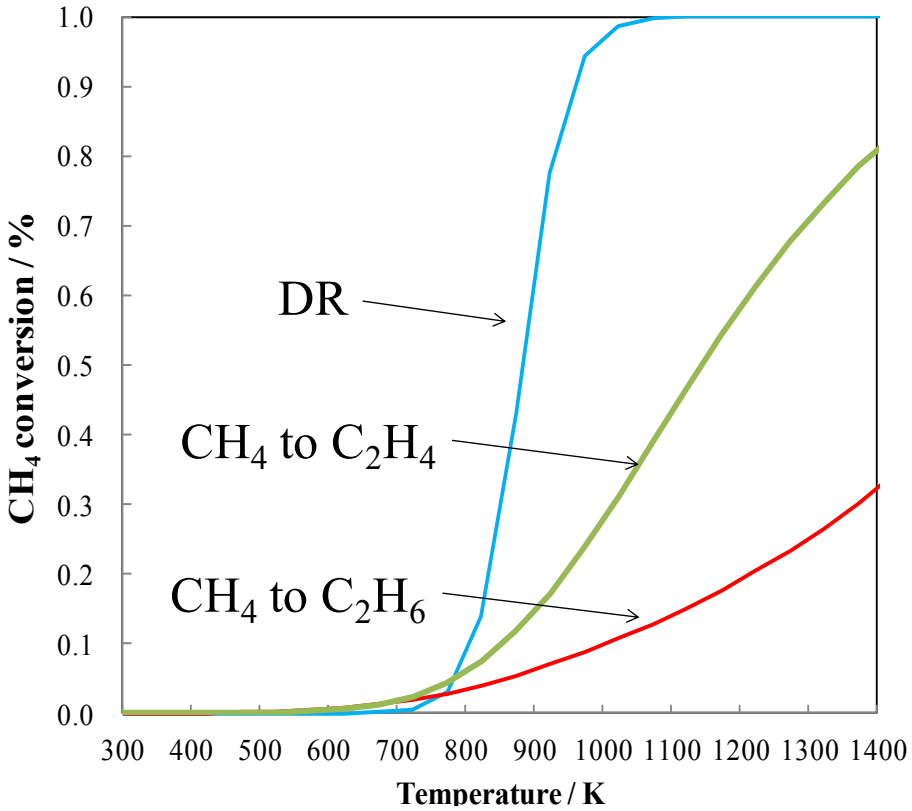

Figure 4-1-9 Equilibrium conversion of CO_2-OCM (products; C_2H_4 and C_2H_6) and DR at CH_4:CO_2:Ar = 25:25:50; total flow: 100 mL min^{-1}.

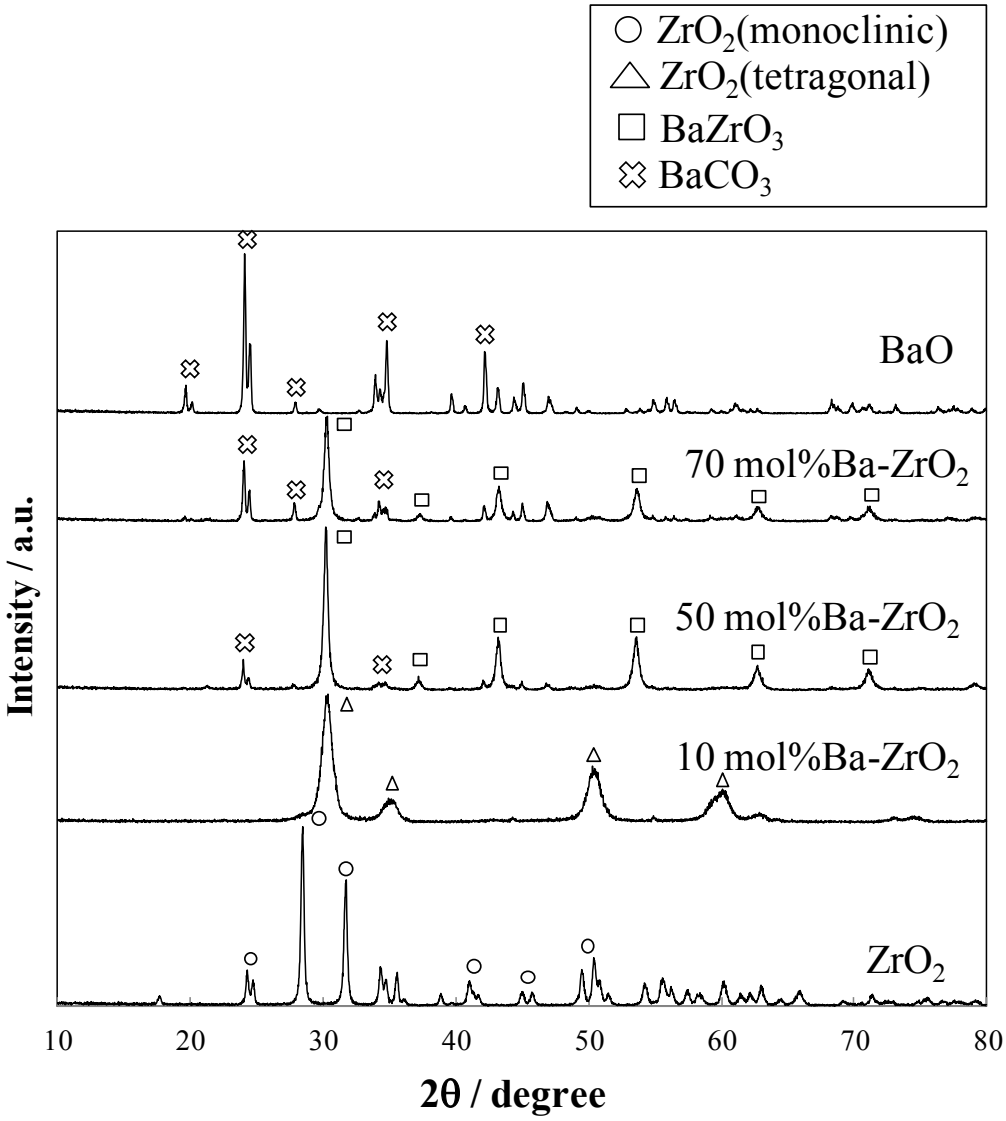

Figure 4-1-10 XRD pattern of various Ba doped zirconium oxide catalysts.

4.2 Oxidative coupling of methane in an electric field over various polyoxo-methalate (POM) supported CeO_2 catalysts

4.2.1 Introduction

In this research, we focused on Keggin−type heteropolyacids as good candidate catalysts for OCM catalytic activity in the electric field. Keggin-type heteropolyacid is a kind of anionic cluster and have a unique multi-electron redox characteristic, which enabled easy electron transportations. Additionally, the base structure of a Keggin-type heteropolyacid is Mo or W and the different metal doped oxides into the structure such as V, Fe and Ru are known to indicate a unique multi-electron redox characteristics. However, Keggin-type heteropolyacid is known to be weak in high temperature conditions, that is, collapsed at 573−673 K. Therefore, the Keggin-type heteropolyacid is difficult to utilize as catalysts in a high temperature reaction. Now, we conducted oxidative coupling of methane (OCM) in an electric field over mixed catalysts with heteropolyacid and CeO_2, which had good electron conductivity, at lower temperature to the extent for not collapsing the structure. In this work, screening tests over various heteropolyacid catalysts on CeO_2 were conducted and the structure of active sites for OCM in the electric field was investigated.

4.2.2 Experimental

4.2.2.1 Catalyst preparation

Keggin-type heteropolyacids of tetrabutylammonium (TBA) as cation were synthesized by the method described in Figure 4-2-1. [6,7] In this procedure, precursors of Mo and W as addendum parts were $Na_2MoO_4{\cdot}2H_2O$ (Kanto Chemical Inc.) and $Na_2WO_4{\cdot}2H_2O$ (Kanto Chemical Inc.), and a precursor of P as hetero parts was $NaH_2PO_4{\cdot}2H_2O$ (Kanto Chemical Inc.) Additionally, precursors of V as doped differential metal in heteropolyacids were V_2O_5 (Kanto Chemical Inc.) Each of the precursors was prepared in the water solvent of 0.5 M Na_2MoO_4, 1.0 M Na_2WO_4, 1.0 M NaH_2PO_4 and 1.0 M V_2O_5/1.5 M NaOH. Next, the prepared aqueous solutions of the Mo base were stirred for 3 h at 353 K and that of W were stirred for 2 days at 353 K. Next, in order to isolate heteropolyacids as solids, the above mentioned aqueous solutions were added into $[CH_3(CH_2)_3]_4NBr$ (TBA, Kanto Chemical Inc.) and a heteropolyacid crystal was collected by the suction type filter equipment. After washing the heteropolyacid crystal with distilled water and ethanol, Keggin-type heteropolyacids of

TBA (Tetra butyl ammonium-polyoxomethalate, TBA-POM) as cations were obtained by drying all over night in oven at 393 K. TBA-POMs in this reports were denotes as TBA-$PMo_{12-x}V_xO_{40}$, TBA-$PW_{12-x}V_xO_{40}$ (x = 0–2).

Keggin-type TBA-HPAs supported on CeO_2 (JRC-CEO-1) catalysts were prepared by impregnation with acetone as the impregnation solvent. The loading amount of TBA-HPAs was 40 wt%. First, acetone (30 mL) and CeO_2 (0.6 g) were added to a 300 mL eggplant flask and were stirred for 2 h using a rotary evaporator. Subsequently, TBA-HPAs (0.4 g) dissolved into acetone (10 mL) were added to the flask and were stirred for 2 h again. The resulting suspension was dried. Then the resulting solid was dried overnight at 393 K. [11]

WO_3/CeO_2 catalyst containing 11.9 wt% W was prepared using impregnation with water as the impregnation solvent, as described in a previous report. [8] An ammonium metatungstate hydrate ($(NH_4)_6H_2W_{12}O_{40}\cdot H_2O$, Kanto Chemical Inc.) was used as a precursor. After impregnation, the resulting suspension was dried. Next, the obtained solid was dried at 393 K all of them overnight, followed by calcination for 3 h in air at 773 K under a ramping rate of 0.5 K min^{-1}.

A $Ce_2(WO_4)_3/CeO_2$ catalyst containing 11.9 wt% W was prepared by impregnating CeO_2 with an aqueous solution of ammonium metatungstate hydrate using a similar method to that for WO_3/CeO_2, except that the calcination temperature was 1173 K. Unsupported $Ce_2(WO_4)_3$ was prepared using a complex method combining EDTA (ethylenediaminetetracetic acid, Kanto Chemical Inc.) and citrate acids, as described in previous reports. (as shown in Figure 4-2-2) [9,12] The pH was controlled by adding a water solution of ammonia. The obtained solution was stirred by the gel composition at 353K. The gel composition was dried at 393 K overnight, followed by calcination for 5 h in air at 1273 K under a ramping rate of 5 K min^{-1}. The mole ratio for EDTA, citric acid and all metal ions was prepared as 1:1.5:1.

4.2.2.2 Activation tests

Catalytic activity tests were conducted with a fixed bed flow-type reactor equipped with a quartz tube (4.0 mm i.d.). The catalyst particle size was arranged as 355–500 μm. The charged amount of the catalyst was 100 mg. The flow rate of raw gas was set up as CH_4:O_2:Ar = 25:15:60, with a total flow rate of 100 mL min^{-1} insofar as there is no particular remark stating otherwise. The effect of the residence time (W/F_{CH4}) was investigated by changing the total flow rate. The standard W/F_{CH4} was 1.6 g_{cat} h mol^{-1}. For the reaction in the electric field, two stainless steel electrodes (2.0 mm o.d.) were inserted contiguously into the catalyst bed in the reactor. The electric field was controlled using a constant current (3, 5, or 7 mA) with a

DC power supply. The imposed voltage depended on the electric properties of the catalyst. Current and voltage profiles were measured using an oscilloscope (TDS 3052B; Tektronix Inc.). The reactor temperature was set to 423 K to avoid the condensation of water produced by the reactions, except for reactions that used no electric field. Product gases after passing a cold trap were analyzed using GC-FID (GC-14B; Shimadzu Corp.) with a Porapak N packed column and methanizer (Ru/Al_2O_3 catalyst), and using a GC-TCD (GC-2014; Shimadzu Corp.) with a molecular sieve 5A packed column. The respective calculation formulae for conversion, C_2 yield, C_2 selectivity, and Faradaic number in this study are shown below (from eq. 2-1 to eq. 2-5).

$$CH_4 \text{ Conversion (\%)} = \frac{\text{Carbon moles of } (CO,\ CO_2,\ C_2H_4,\ C_2H_6 \text{ and } C_2H_2)}{\text{Carbon moles of input methane}} \times 100 \qquad \text{eq. 2-1}$$

$$O_2 \text{ Conversion (\%)} = \frac{\text{Consumption moles of } O_2}{\text{Input oxygen moles}} \times 100 \qquad \text{eq. 2-2}$$

$$C_2 \text{ Yield (\%, C-based)} = \frac{\text{Carbon moles of } (C_2H_4,\ C_2H_6 \text{ and } C_2H_2)}{\text{Carbon moles of input methane}} \times 100 \qquad \text{eq. 2-3}$$

$$C_2 \text{ Selectivity (\%, C-based)} = \frac{C_2 \text{ Yield}}{CH_4 \text{ Conversion}} \times 100 \qquad \text{eq. 2-4}$$

$$\text{Faradaic number} = \frac{\text{Carbon moles of reacted methane}}{\text{Moles of input electron}} \qquad \text{eq. 2-5}$$

A periodic operation test was conducted to elucidate surface active species on the catalyst in the following steps. In the first step, oxygen and Ar were supplied to the reactor with an electric field for 10 min for oxidation of the catalyst surface. For the second step, residual oxygen in the gas phase of the reactor was removed with Ar purge for 5 min. For the third step, methane and Ar were supplied to the reactor with an electric field for 12 min to evaluate the oxidation catalysis of the surface oxygen species on the catalyst. As the final step, an Ar purge was conducted for 20 min to remove all residual gases. The steps described above were repeated for three cycles. Product gases were analyzed at 5 min after the oxygen＋Ar supply, and at 2 min or 12 min after the methane＋Ar supply (CO_x and desorbed CH_4 were detected at 5 min after the oxygen＋Ar supply and no products were detected at 12 min after the methane＋Ar supply). The gas flow rate was O_2 : Ar = 1 : 10, the total flow rate was 55 mL min^{-1} (for oxidation of the catalyst surface) and CH_4 : Ar = 1 : 10 or 1 : 2, the total flow rate was 55 or 75 mL min^{-1} (for oxidation of supplied methane by surface oxygen species). The reactor temperature was fixed at 473 K. The imposed current was set at 3.0 or 7.0 mA.

4.2.2.3 Characterization

In order to investigate Keggin-type heteropolyacid catalysts supported on CeO_2 and the catalyst structure after the reaction, FT-IR (Fourier transform infrared spectrometer; FT-IR/6100, Jasco Corp.) measurement was conducted. The measuring range for FT-IR was 500-4000 cm^{-1}. The measurement sample was prepared by the KBr pellet method: the sample was held by two KBr plates and shaped as a 5 mmφ disk by a press-forming container.

In order to investigate the catalyst structure before/during/after the reaction, *ex-situ* and *in-situ* Raman measurements in the electric field were conducted using a Raman spectrometer. (NRS-1000; Jasco Corp.; 532 nm) *In-situ* measurement was conducted with a hand-made glass reactor and gold wire electrodes. The reactant feed gases were supplied with canned standard gases (CH_4(0.995%)+Ar and/or O_2(99.9%)). The electric field was imposed using a constant current at 6.0 mA. Raman spectra for catalyst heated at the reaction temperature (603–703 K) without an electric field were also observed to elucidate the effect of Joule heating on the catalyst structure. A Ni-Cr wire was inserted into the sample for heating by resistance heating.

In order to investigate the catalyst structure before/after the reaction, XRD measurement (RINT-Ultima III; Rigaku Corp. or Smart Lab; Rigaku Corp.) was conducted. The XRD patterns were measured using Cu-*K*α radiation. Anode voltage and anode current values were, respectively, 40 kV and 40 mA. Diffractograms were taken at 2θ angles for 5–80° with steps of 10 ° min^{-1}. The crystal structure from XRD patterns was assigned by an online database (http://crystdb.nims.go.jp/), provided by Atom Work in National Institute for Materials Science (NIMS), and previous reports. [13]

X-ray absorption fine structure (XAFS) spectra of Mo-K, V-K, W-L_3 and Ce-K edges were recorded in the transmission method on BL14B2 in SPring-8 (Hyogo, Japan). Catalysts treated in the reaction condition were ground into powder and were pressed into pellets. Then, pellets were packed into gas-barrier bags. The pellets were diluted with BN in a dry condition and pulverized by a planetary ball mill (P-6; FRITSCH Corp.) with the rotation rate of 200 rpm for 10 min twice and to adjust for XAFS measurement. EXAFS analysis and curve fitting were performed using software (Athena ver. 0.8.056; Artemis ver. 0.8.012). The Ce-K edge of *in-situ* XAFS on a $Ce_2(WO_4)_3/CeO_2$ catalyst were conducted in the same way: an imposed current at 6.0 mA, a reaction temperature at 423 K, the reactant gas composition of O_2 as 12.8 mL min^{-1} and N_2 as 58.4 mL min^{-1}.

DRIFTS measurements on a $Ce_2(WO_4)_3/CeO_2$ catalyst were conducted using FT-IR (FT-IR/ 6100; Jasco Corp.) with an MCT detector and a diffuse reflectance infrared fourier

transform spectroscopy reactor cell (DR-600Ai; Jasco Corp.) with ZnSe windows for 50 times with a resolution of 4.0 cm^{-1} at 450–4000 cm^{-1}. The flow rate of the reactant gas was CH_4:O_2:Ar = 2:1:57, the total flow of 60 mL min-1, and the imposed current was 2.0–6.0 mA.

4.2.3 Results and discussion

4.2.3.1 OCM reaction in the electric field over TBA-PMo/CeO_2 catalysts

To discover suitable catalysts in OCM reaction in the electric field over POM catalysts, the screening tests for TBA-$PMo_{12-x}V_x/CeO_2$ (x = 0–2) catalysts were conducted. First, to confirm the synthesis of TBA-$PMo_{10}V_2$ and 40 wt%TBA-$PMo_{10}V_2/CeO_2$, FT-IR was conducted as shown in Figure 4-2-3. Consequently, the synthesis of these oxides was accomplished. Then, various supported amounts of TBA-$PMo_{10}V_2$ on CeO_2 catalysts were investigated to assess their catalytic activities for the OCM reaction in the electric field with an imposed power at 7.0 mA and at room temperature (as shown in Figure 4-2-4). Consequently, we inferred that a 40wt% TBA- $PMo_{10}V_2/CeO_2$ catalyst was the most appropriate catalyst among these oxides for OCM in the electric field. In order to decide the appropriate O_2 pressure, tests for changing the partial pressure of O_2 over a 40wt% TBA-$PMo_{10}V_2/CeO_2$ catalyst were conducted; the CH_4 flow was fixed to 0.25 atm, and the imposed current was 7.0 mA. (as shown in Figure 4-2-5) As a result, the electric field was not applied stably and the most appropriate O_2 partial pressure was decided to be 0.15 atm. Next, Table 4-2-1 shows the results of tests for 40 wt% TBA-$PMo_{12-x}V_x/CeO_2$ (x = 0–2) catalysts on 5.0 mA at 423 K. As a result, although the OCM reaction did not proceed (C_2 selectivity: 0.2%, CO_2 selectivity: 98.5 %) and complete combustion proceeded over the CeO_2 catalyst, and the OCM reaction proceeded over TBA-$PMo_{12-x}V_x/CeO_2$ catalysts thanks to the unique surface structure. Next, to investigate the unique surface structure after the imposed electric field, the OCM reaction in the conventional catalytic system, when not applying the electric field, over TBA-$PMo_{12-x}V_x/CeO_2$ catalysts was conducted at 473-873 K. (as shown in Figure 4-2-6) Figure 4-2-6 also indicates results of tests in the electric field (imposed current: 3.0 mA, at 423 K.) As a result, the OCM reaction did not proceed even at 873 K, when the electric field was not imposed. Therefore, the synergistic effect on TBA-$PMo_{12-x}V_x/CeO_2$ catalysts and the electric field played an important role in producing the OCM reaction.

In order to elucidate the formation of active oxygen species on the catalyst surface in the electric field, periodic tests of CH_4 and O_2 were conducted; the imposed current was 3.0 mA over a 40 wt%TBA-$PMo_{10}V_2/CeO_2$ catalyst (as shown in Figure 4-2-7) and over a CeO_2

catalyst (as shown in Figure 4-2-8.) From the results in Figure 4-2-7, high C_2 selectivity (above 90%) was obtained over a 40 wt%TBA-$PMo_{10}V_2/CeO_2$ catalyst even after the second or third cycles of the tests. Low C_2 selectivity was shown after the first cycle of the test probably due to combustion of hydrocarbons. On the other hand, from the results in Figure 4-2-8, C_2 hydrocarbons were not produced in periodic tests over a CeO_2 catalyst. Therefore, active oxygen for proceeding highly selective OCM reaction on a TBA-$PMo_{10}V_2/CeO_2$ catalyst were supposed to be formed on the surface.

In order to elucidate the catalytic surface before/after OCM reaction in the electric field, FT-IR measurement was conducted on a 40wt%TBA-$PMo_{10}V_2/CeO_2$ catalyst. Figure 4-2-9 indicates the results of the spectrum before/after the reaction and Figure 4-2-10 indicates those of the periodic tests of CH_4 and O_2. From the result of Figure 4-2-9, the peak assigned to heteropolyacid at 700−1200 cm^{-1} disappeared after the reaction in the electric field. From the result of Figure 4-2-10, the heteropolyacid structure collapsed in the OCM reaction (CH_4 and O_2) by the imposed electric field, as well as because the heteropolyacid structure already collapsed after the first cycle of the test. In order to investigate the effect of CH_4 on the heteropolyacid structure in the electric field, FT-IR measurements were conducted in only CH_4 flow in the electric fields at 473 K (as shown in Figure 4-2-11) and 673 K (Figure 4-2-12). From the results of Figure 4-2-11, the heteropolyacid structure did not collapse by the imposed electric field because the structure was stable even after the reaction at 473 K in the electric field. On the other hand, from the results of Figure 4-2-11, the heteropolyacid structure collapsed in the electric field at 673 K. Therefore, a higher reaction temperature was a major factor for the collapsed heteropolyacid structure. Additionally, Raman (Figure 4-2-13), XRD (Figure 4-2-14), XAFS (Figure 4-2-15–Figure 4-2-17) measurements were conducted for evaluating the catalyst structure before/after the reaction in the electric field. As a result of various characterizations, the heteropolyacid structure collapsed after the reaction, and MoO_3 and mixed oxides of Mo and Ce were generated. Therefore, the new structure derived from the 40wt%TBA-$PMo_{10}V_2$ on CeO_2 oxide in the electric field possibly played an important role in progressing OCM reaction.

In order to elucidate the effect of Mo or V on the 40 wt%TBA-$PMo_{10}V_2/CeO_2$ catalyst, catalytic activity tests over Mo or V supported on CeO_2 catalysts were conducted, as shown in Table 4-2-2. The amounts of Mo or V were prepared in the same way as those of 40 wt%TBA- $PMo_{10}V_2O_{40}/CeO_2$. As a result, Mo or V supported on CeO_2 catalysts indicated OCM activity in the electric field but the activities were lower than that over the 40 wt%TBA-$PMo_{10}V_2/CeO_2$ catalyst. Therefore, Mo and/or V oxides, and mixed oxides of Ce were the active sites in the OCM reaction and the heteropolyacids functioned as precursors for

highly dispersing the active sites.

4.2.3.2 OCM reaction in the electric field over TBA-PW/CeO_2 catalysts

In our submitted papers [11], we reported that the 40 wt%TBA-PW_{12}/CeO_2 catalyst indicated high OCM activity at 423 K (CH_4 conversion: 14.9%, C_2 selectivity: 43.4%, C_2 yield: 6.4%, 3mA) in the electric field, and a synergetic effect between the $Ce_2(WO_4)_3$ structure and electric field created the active oxygen species for selective oxidation of methane. In further studies, the activity tests over a 40 wt%TBA-PW_{12}/CeO_2 catalyst were conducted in the conventional reaction at 573−1073 K as an external temperature without the imposing electric field, as shown in Figure 4-2-18. On the other hand, lower OCM activity was indicated even at 1073 K: CH_4 conversion: 14.9% and C_2 selectivity: 43.4%. Therefore, the synergistic effect on a TBA-PW_{12}/CeO_2 catalyst and the electric field played an important role in producing the OCM reaction. Next, in order to elucidate the formation of active oxygen species on the catalyst surface in the electric field, periodic tests of CH_4 and O_2 were conducted over a TBA-PW_{12}/CeO_2 catalyst with an imposed 7.0 mA current at 473 K, as shown in Figure 4-2-19. As a result, high C_2 selectivity exceeding 55% was stably indicated even after 8 cycles of the periodic tests. Therefore, active oxygen for proceeding highly selective OCM reaction on a TBA-PW_{12}/CeO_2 catalyst possibly formed on the surface. On the other hand, C_2 products were not generated over a CeO_2 catalyst in the same periodic test. Thus, the heteropolyacid supported on CeO_2 possibly generated the reactive oxygen species for producing the selective OCM reaction in the electric field.

In order to evaluate the catalyst structure before/after the reaction in the electric field, Raman (Figure 4-2-20), XRD (Figure 4-2-21), XPS (Figure 4-2-22) and XAFS (Figure 4-2-23) measurements were conducted on the TBA-PW_{12}/CeO_2 catalyst. From the result of Raman and XRD measurements, the heteropolyacid structures were collapsed, and CeO_2, WO_3 and $Ce_2(WO_4)_3$ were generated after the reaction in the electric field. As shown in Figure 4-2-22, only Ce^{4+} peaks were observed on the catalyst before the reaction but Ce^{3+} peaks were also observed after the reaction. Additionally, as shown in Figure 4-2-23, the peaks derived from the W–O–W of the heteropolyacid structure at 3–4 Å in the EXAFS range were observed on the catalyst before the reaction. On the other hand, the peaks derived from the W–O–W of the heteropolyacid structure disappeared and new peaks possibly derived from tungsten oxide and mixed oxides of Ce and W at 1–2 Å were observed on the catalyst after the reaction. Therefore, the $Ce_2(WO_4)_3$ structure was generated after the reaction.

4.2.3.3 OCM reaction in the electric field over $Ce_2(WO_4)_3/CeO_2$ catalyst

In our submitted papers [11], we reported that the $Ce_2(WO_4)_3$ structure was the reactive site for OCM reaction in the electric field. Additionally, in order to elucidate the catalytic activity over a WO_3 unit, the activity tests over the WO_3 catalyst was conducted at 673 K in the electric field, as shown in Table 4-2-3. As a result, the WO_3 catalyst did not indicate OCM activity at 673 K and the reactive oxygen species for proceeding selective OCM reaction were not produced over the WO_3 catalyst in the electric field.

Next, we also reported that the $Ce_2(WO_4)_3/CeO_2$ structure indicated high OCM activity in the electric field and low OCM activity in the conventional catalytic reaction without the electric field. In order to elucidate a $Ce_2(WO_4)_3$ supported effect on CeO_2, tests for changing the amounts of supported W species were conducted at 423 K with an imposing 3.0 mA current, as shown in Table 4-2-4. As a result, increasing the amount of supported W species resulted in increasing C_2 selectivity but decreasing CH_4 conversion because the active sites of the $Ce_2(WO_4)_3$ structure increased while the surface site of CeO_2 decreased. Additionally, in order to elucidate Ce and W effects on the $Ce_2(WO_4)_3$ structure in the electric field, XAFS measurements were conducted, as shown in Figure 4-2-24–Figure 4-2-27. Figure 4-2-24 and Figure 4-2-25 indicated the Ce-K edge of *in-situ* and *ex-situ* XAFS results on $Ce_2(WO_4)_3/CeO_2$ in the electric field. From the result of XANES spectra, the electron state of Ce did not change before/after the reaction possibly because the peak for CeO_2 support was dominant in the catalyst. From the result of XAFS spectra, the peak for Ce decreased after the reaction in the electric field possibly due to the Debye-Waller factors of Joule heat from the electric field. Figure 4-2-26 showed the Ce-K edge of *ex-situ* XAFS results on CeO_2 and $Ce_2(WO_4)_3/CeO_2$. From the result of XANES, the peak on $Ce_2(WO_4)_3/CeO_2$ was difficult for distinguishing that on CeO_2 because the white line on $Ce_2(WO_4)_3/CeO_2$ was different from that on CeO_2.

In order to elucidate the absorbed species on the $Ce_2(WO_4)_3/CeO_2$ catalyst, we conducted *in-situ* DRIFT measurement in the electric field (imposed current: 2.0–6.0mA) at 423 K, as shown in Figure 4-2-28. From the results, the peaks for CH_4 were observed in the conventional reaction, and the peaks for CH_4, CO_2 and the reactive oxygen species such as superoxide (O_2^-) and peroxide (O_2^{2-}) were observed in the electric field. Additionally, the peak for the reactive oxygen species disappeared without the electric field. Therefore, the imposed electric field on $Ce_2(WO_4)_3/CeO_2$ catalyst played an important role in producing the OCM reaction.

In order to investigate the W–O behaviour in the $Ce_2(WO_4)_3/CeO_2$ catalyst, we conducted

in-situ Raman measurement in the electric field (imposed current: 6.0 mA) at room temperature, as shown in Figure 4-2-29. As a result, the peak for W–O in the $Ce_2(WO_4)_3/CeO_2$ catalyst decreased in the CH_4 flow possibly because CH_4 reacted with the active oxygen species derived from W–O in the $Ce_2(WO_4)_3/CeO_2$ structure. Additionally, the peak for W–O in the catalyst changed depending on the time in CH_4 and O_2 flow possibly because cycles of consumption and regeneration for oxygen species on a $Ce_2(WO_4)_3$ catalyst were repeated by redox mechanism and the bond of W–O in the catalyst lengthened by the imposed electric field because the peak for W–O in the catalyst shifted to a lower wave number with the electric field. It was assumed that the bond of W–O in the catalyst lengthened, the bond of Ce–O in the Ce–O–W unit shrank, the electron of Ce atom was transferred to an O atom and the reactive oxygen for OCM was generated.

4.2.4 Conclusion

Oxidative coupling of methane over various polyoxomethalate supported on CeO_2 catalysts were conducted in the electric field. In the 40 wt%TBA-$PMo_{10}V_2/CeO_2$ catalyst, Mo oxides and a mixed oxide with Mo and Ce were generated by the imposing electric field for producing high OCM activity. In the 40 wt%TBA-PW_{12}/CeO_2 catalyst, the $Ce_2(WO_4)_3$ structure played an important role as an active site in producing a selective OCM reaction in the electric field. These oxides possibly formed the reactive oxygen species suitable for OCM reaction such as superoxide (O_2^-) and peroxide (O_2^{2-}) by applying the electric field on the catalytic surface. In order to elucidate a $Ce_2(WO_4)_3/CeO_2$ structure by various characterizations, it was assumed that cycles of consumption and regeneration for oxygen species on $Ce_2(WO_4)_3$ catalyst were repeated by a redox mechanism, the bond of W–O in the catalyst lengthened by the imposed electric field, the bond of Ce–O in Ce–O–W unit shrank, the electron of Ce atom was transferred to an O atom and the reactive oxygen for OCM reaction was generated.

[6] T. Ueda, M. Komatsu, M. Hojo, Spectroscopic and voltammetric studies on the formation of Keggin-type V(V)−substituted tungstoarsenate(V) and −phosphate(V) complexes in aqueous and aqueous−organic solutions, Inorg. Chim. Acta. 344 (2003) 77−84.

[7] S. Himeno, N. Ishio, A voltammetric study on the formation of V(V)− and V(IV) −substituted molybdophosphate(V) complexes in aqueous solution, J. Electroanal. Chem. 451 (1998) 203−209.

[8] A.-S. Mamede, E. Payen, P. Grange, G. Poncelet, A. Ion, M. Alifanti, V.I. Pârvulescu, Characterization of WO_x/CeO_2 catalysts and their reactivity in the isomerization of hexane, J. Catal. 223 (2004) 1−12.

[9] M. Arab, A.L. L.-Moriyama, T.R. dos Santos, C.P. de Souza, J.R. Gavarri, C. Leroux, Strontium and cerium tungstate materials $SrWO_4$ and $Ce_2(WO_4)_3$: Methane oxidation and mixed conduction, Catal. Today. 208 (2013) 35−41.

[10] F.W.B. Lopes, M. Arab, H.P. Macedo, C.P. de Souza, J.F. de Souza, J.R. Gavarri, High temperature conduction and methane conversion capability of $BaCeO_3$ perovskite, Powder. Tech. 219 (2012) 186−192.

[11] K. Sugiura, S. Ogo, K. Iwasaki, T. Yabe, Y. Sekine, Low-temperature catalytic oxidative coupling of methane in an electric field over a Ce−W−O catalyst system, Sci. Rep. 6 25154 (2016) 1−9.

[12] B.O. Loopstra, H.M. Rietveld, Further refinement of the structure of WO_3, Acta Crystall. B-stru. 25(7) (1969) 1420−1421.

[13] L. H. Brixner, A.W. Sleight, C.M. Foris, Refined cell parameters of the Ln_2WO_6−type rare earth tungstates, J. Solid. State. Chem. 7 (1973) 418−421.

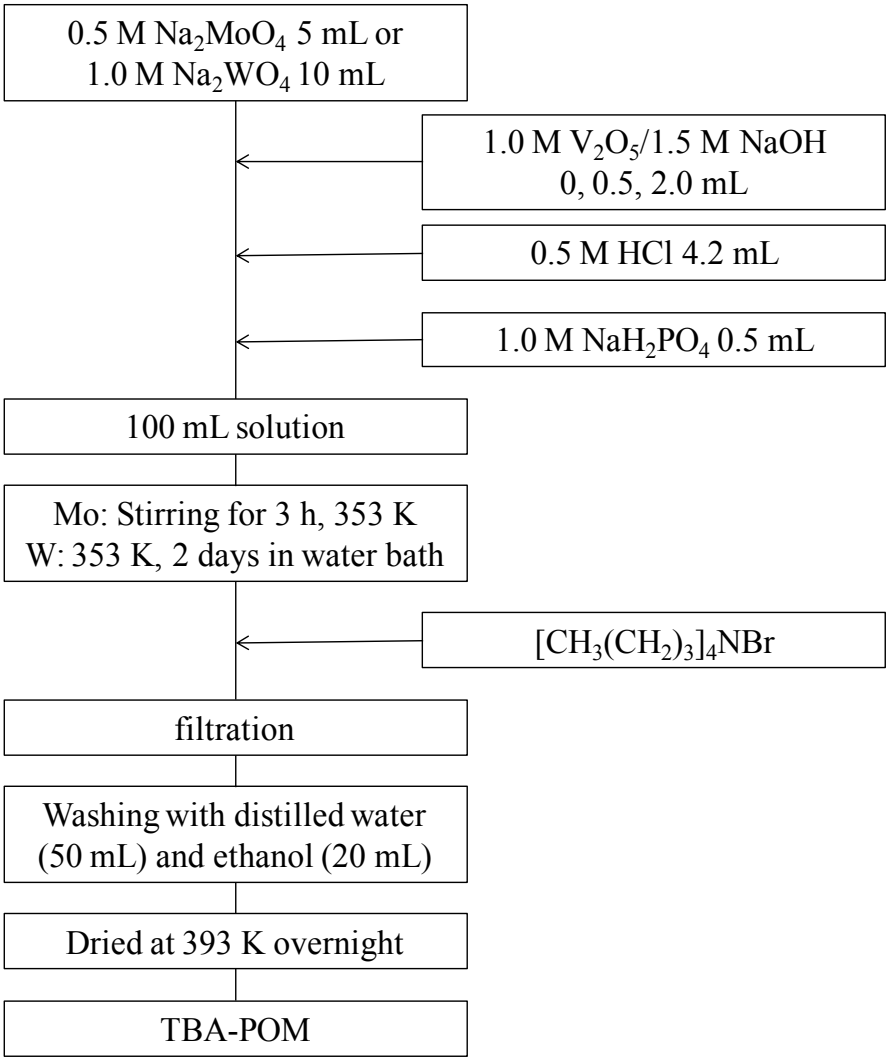

Figure 4-2-1 Preparation for the TBA-POM catalysts.

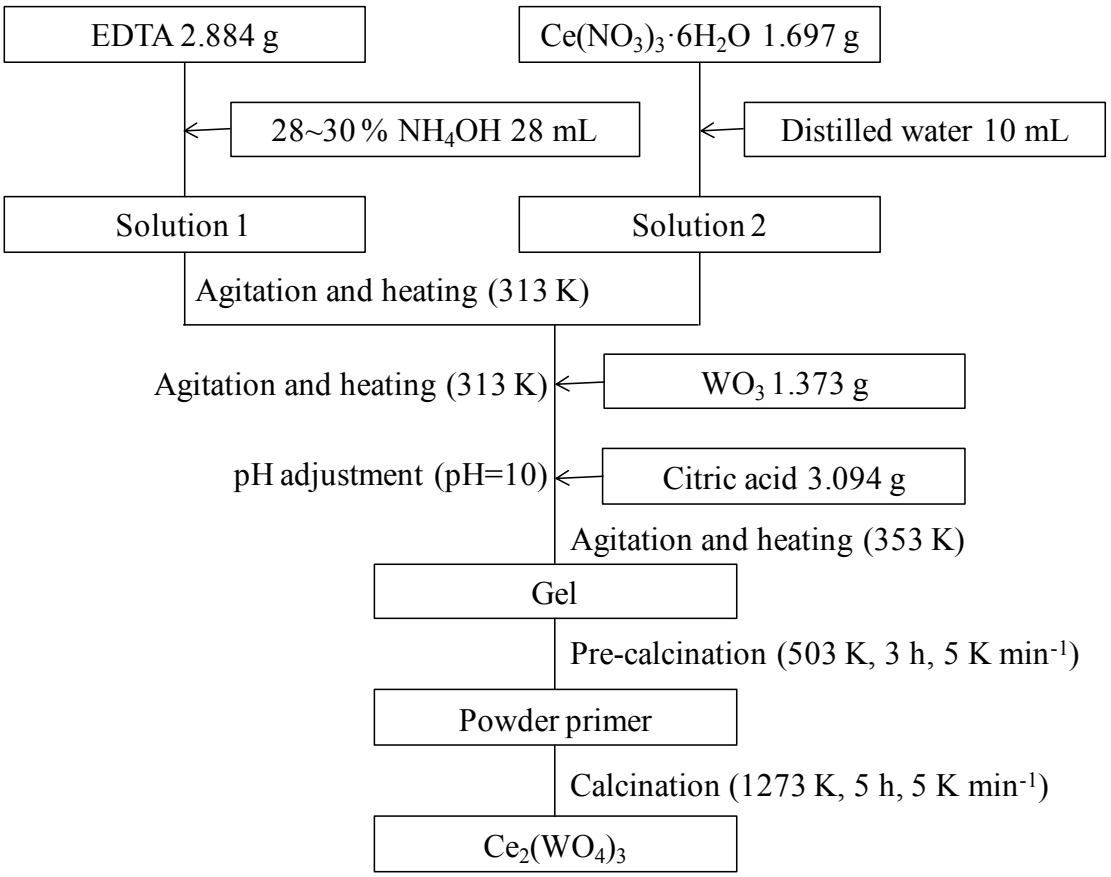

Figure 4-2-2 Preparation for $Ce_2(WO_4)_3$ using EDTA-citrate complexing method.

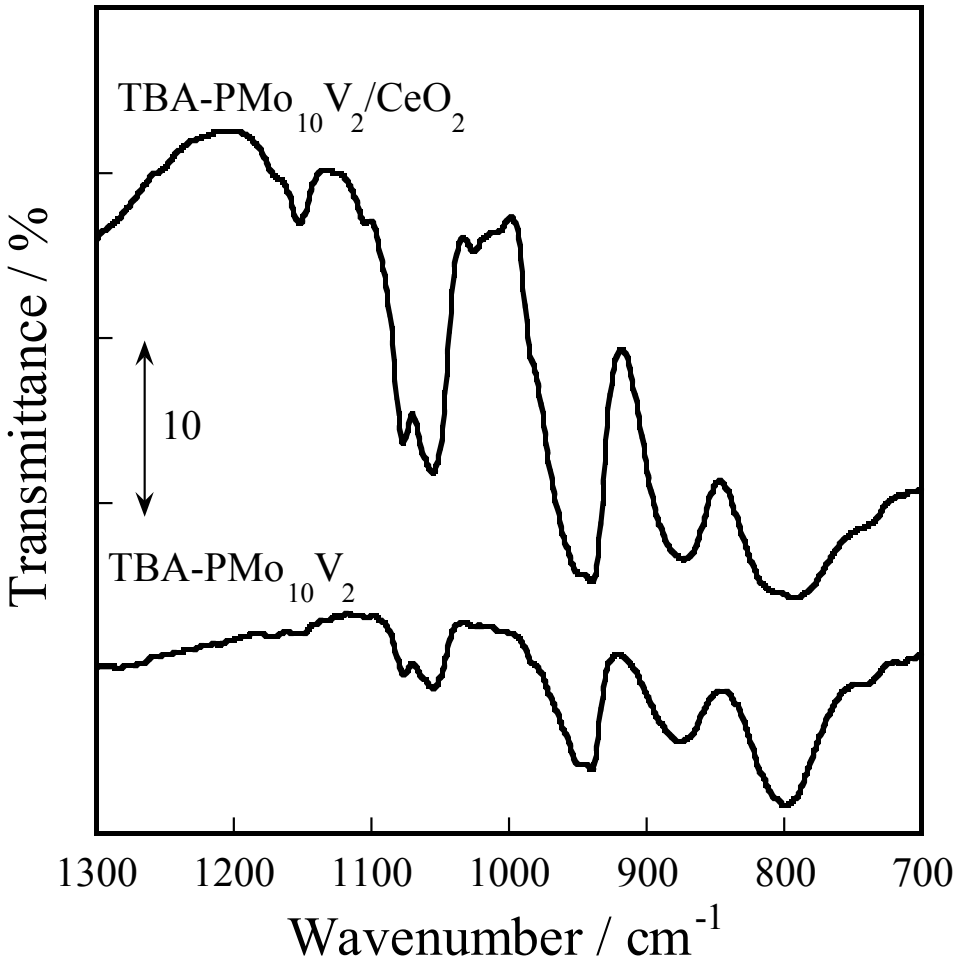

Figure 4-2-3 FT-IR spectra for TBA-$PMo_{10}V_2O_{40}$ and 40 wt%TBA-$PMo_{10}V_2O_{40}/CeO_2$ catalysts.

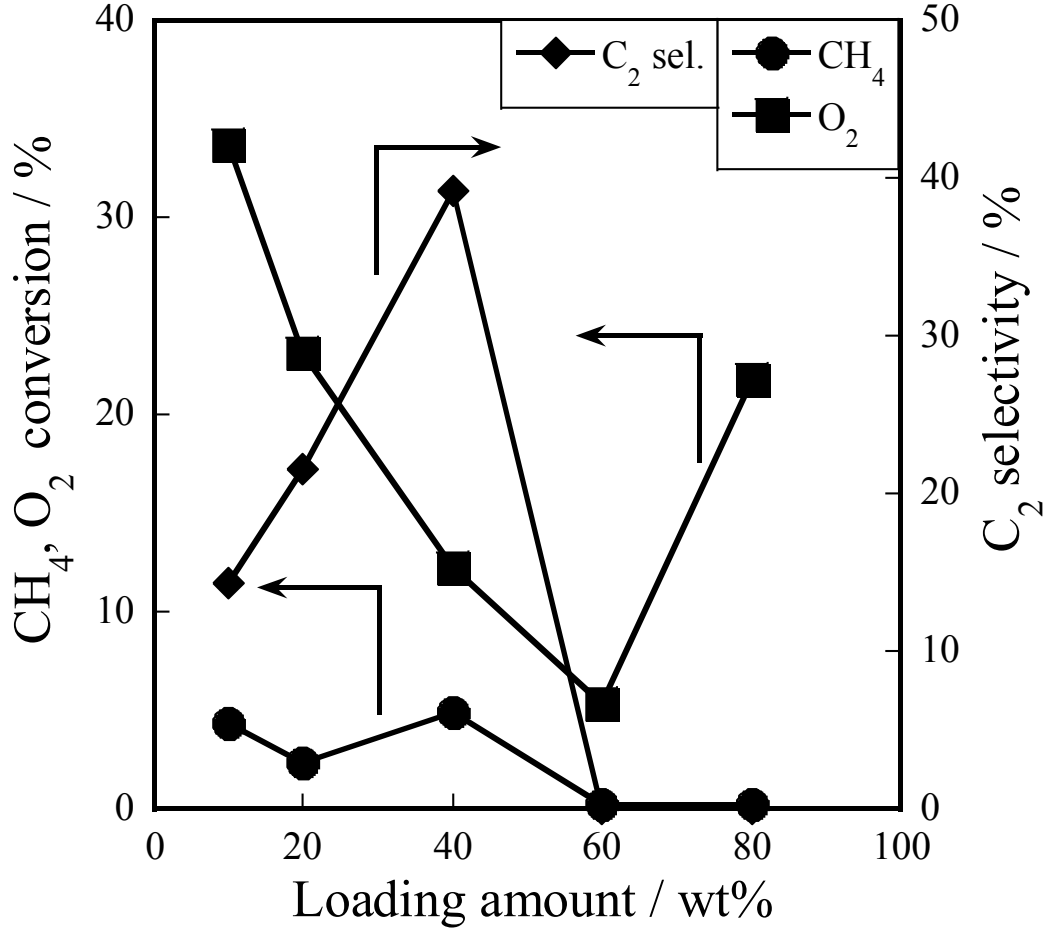

Figure 4-2-4 The effect of loading amount of TBA-$PMo_{10}V_2O_{40}$ to catalytic activity in the electric field; 7.0 mA; at room temperature; CH_4:O_2:Ar = 25:5:50; the total flow rate was 80 mL min^{-1}.

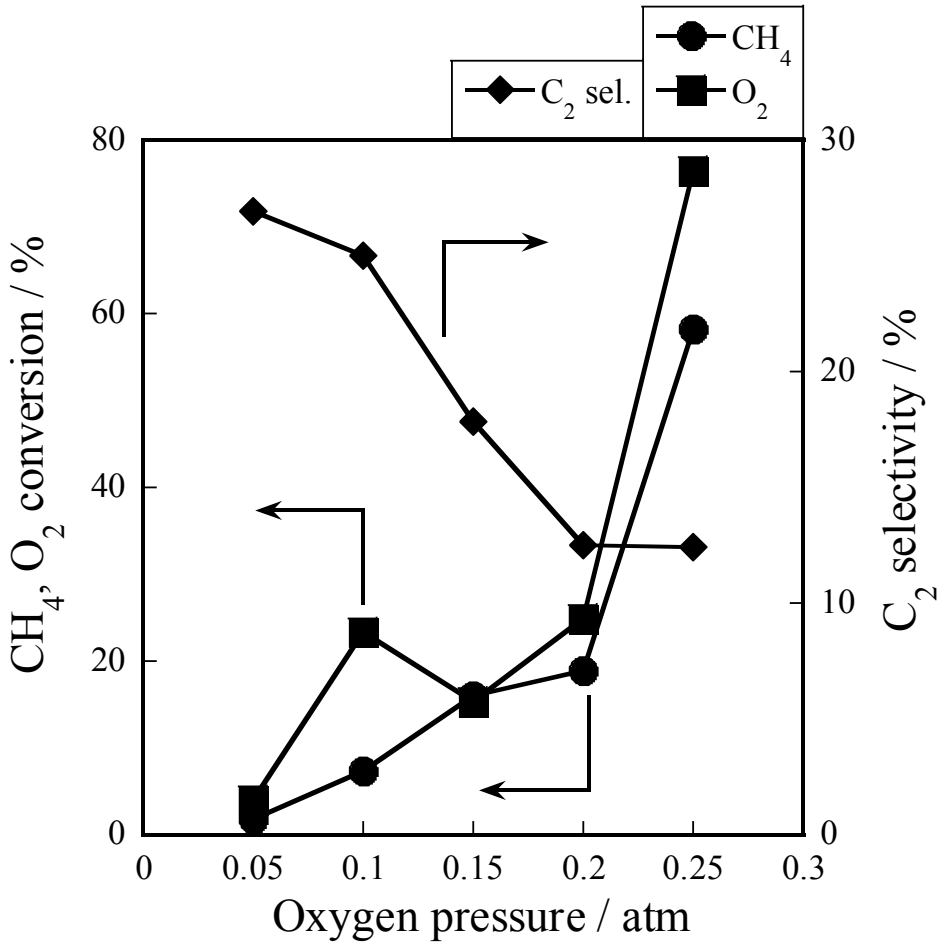

Figure 4-2-5 Oxygen pressure dependence on catalytic activities over 40 wt%TBA-$PMo_{10}V_2O_{40}/CeO_2$ in the electric field; 7.0 mA; 423 K; CH_4 flow rate, 25 mL min^{-1}.

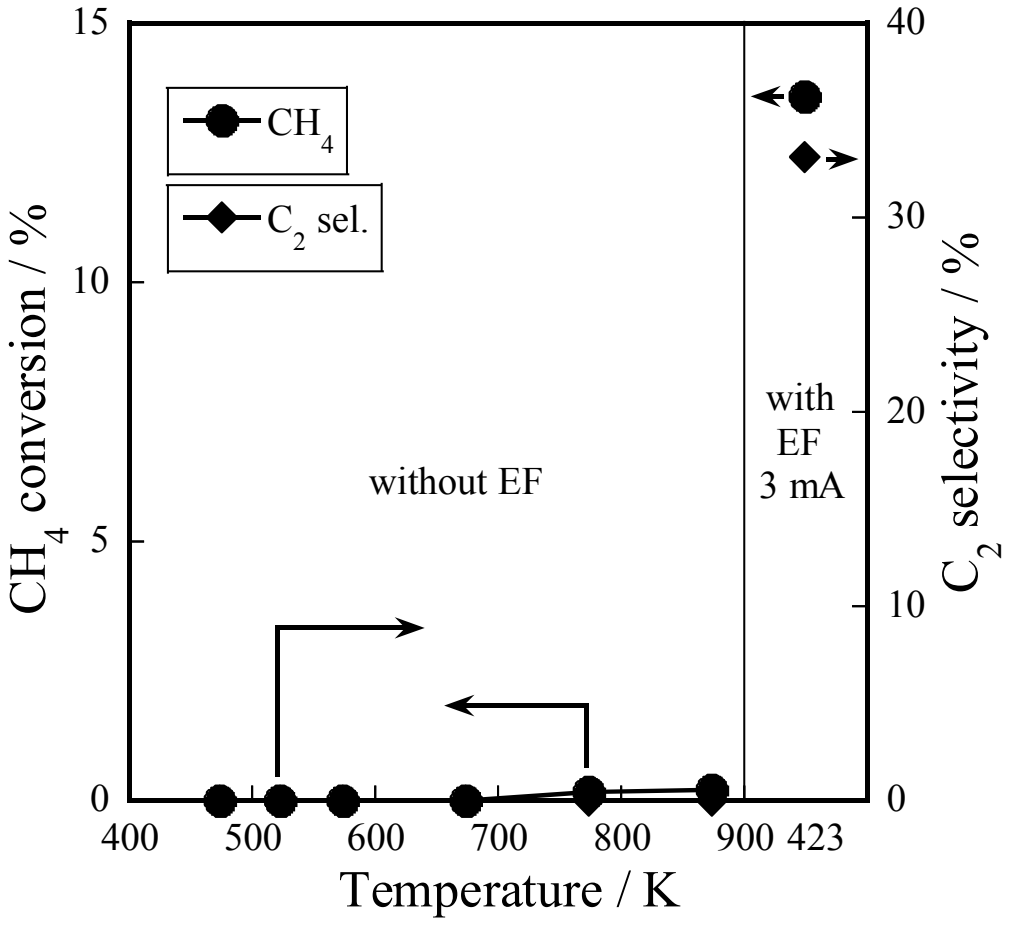

Figure 4-2-6 Temperature dependence on catalytic activity over 40 wt%TBA-$PMo_{10}V_2O_{40}$ /CeO_2 with and without the electric field; from 423 K to 873 K.

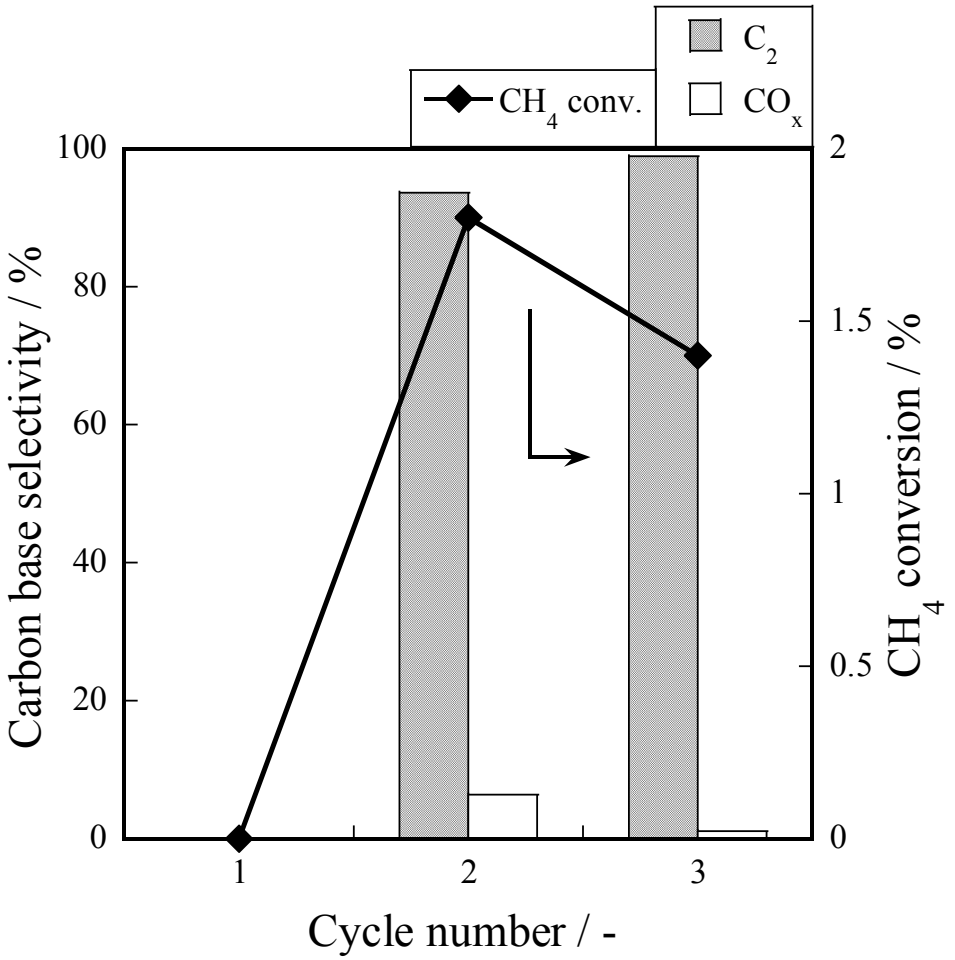

Figure 4-2-7 Results of periodic operation test (after 2 min from CH_4 flow) over 40 wt%TBA-$PMo_{10}V_2O_{40}/CeO_2$ in the electric field; 3.0 mA; 473 K; CH_4:Ar = 25:50, the total flow rate was 75 mL min^{-1}; O_2:Ar = 5:50, the total flow rate was 55 mL min^{-1}.

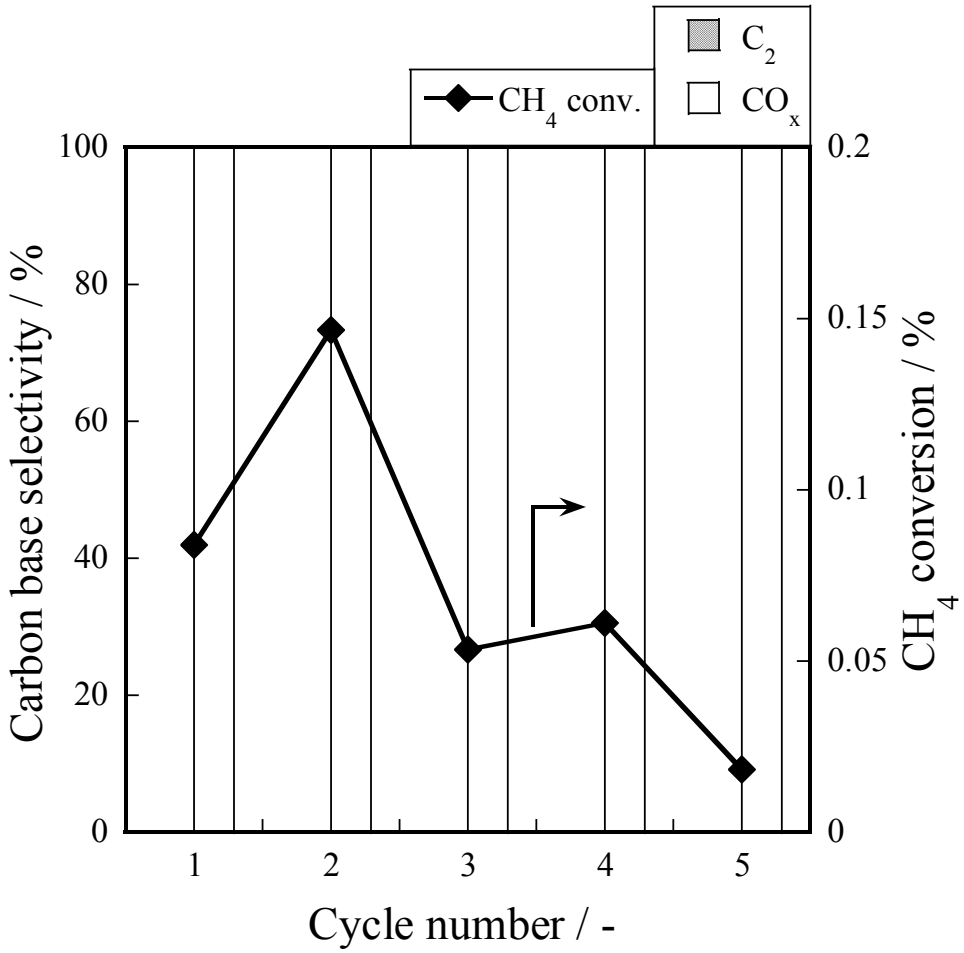

Figure 4-2-8 Results of periodic operation test (after 2 min from CH_4 flow) over CeO_2 in the electric field; 3.0 mA; 473 K; CH_4:Ar = 25:50, the total flow rate was 75 mL min^{-1}; O_2:Ar = 5:50, the total flow rate was 55 mL min^{-1}.

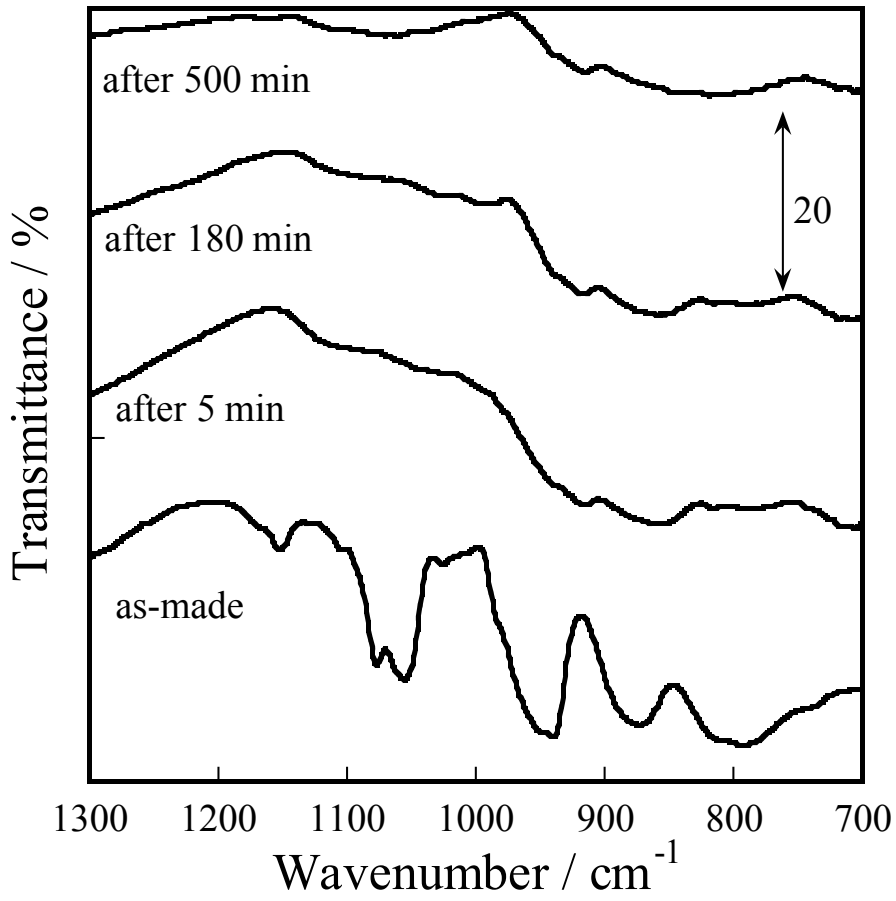

Figure 4-2-9 FT-IR spectra for various states of 40 wt%TBA-$PMo_{10}V_2O_{40}/CeO_2$ in as-made catalyst and the catalyst after catalytic activity tests with the electric field.

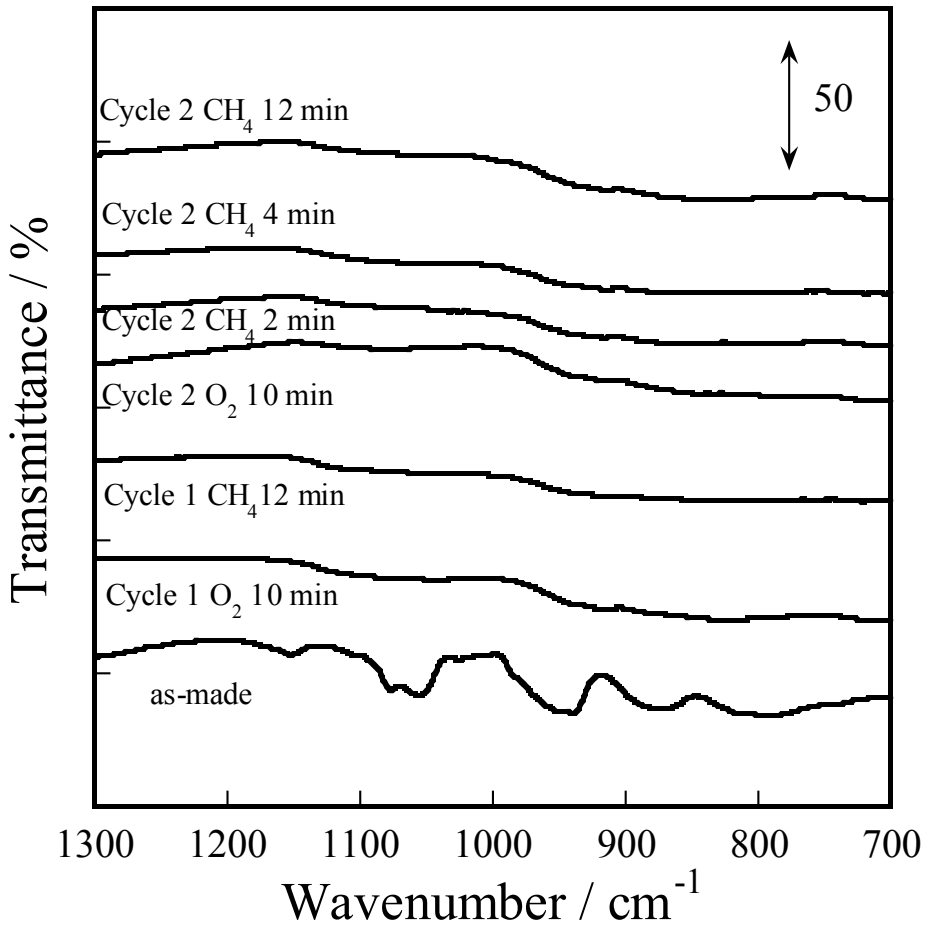

Figure 4-2-10 FT-IR spectra for various states of 40 wt%TBA-$PMo_{10}V_2O_{40}/CeO_2$ in as-made catalyst and the catalyst after periodic operation tests with the electric field.

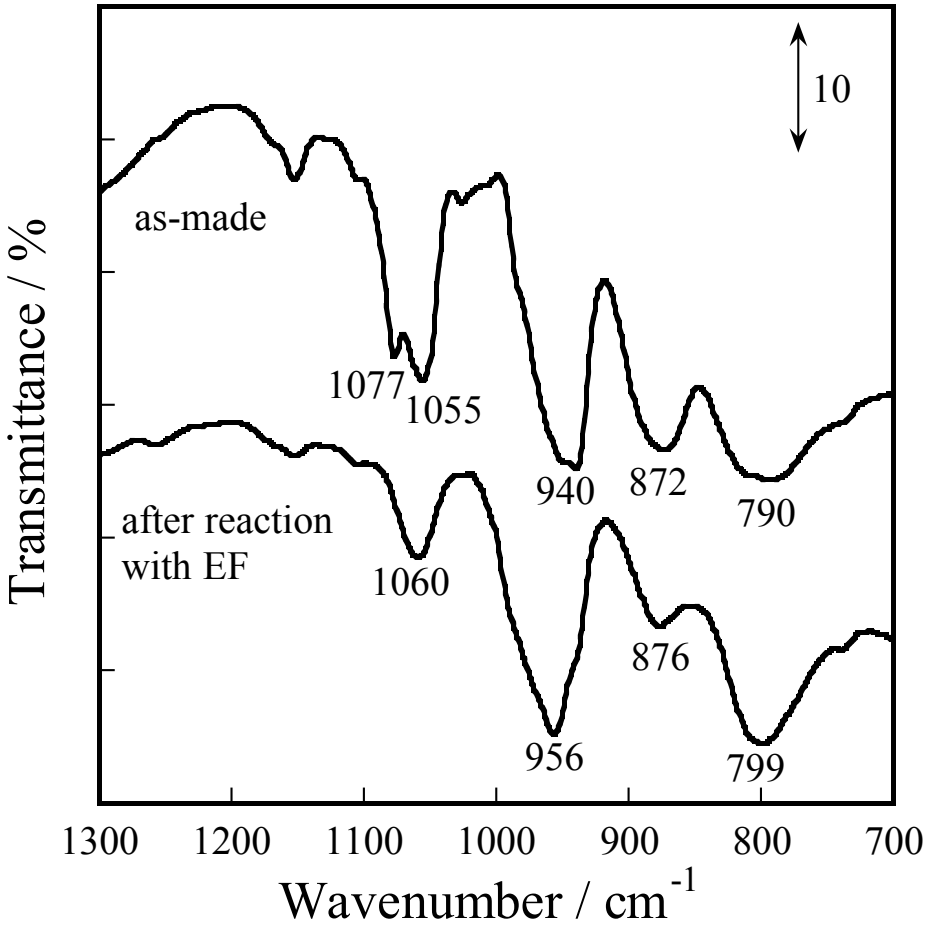

Figure 4-2-11 FT-IR spectra for various states of 40 wt%TBA-$PMo_{10}V_2O_{40}/CeO_2$ in as-made catalyst and the catalyst after CH_4 supply with the electric field at 473 K; CH_4:Ar = 25:50, the total flow rate was 75 mL min^{-1}.

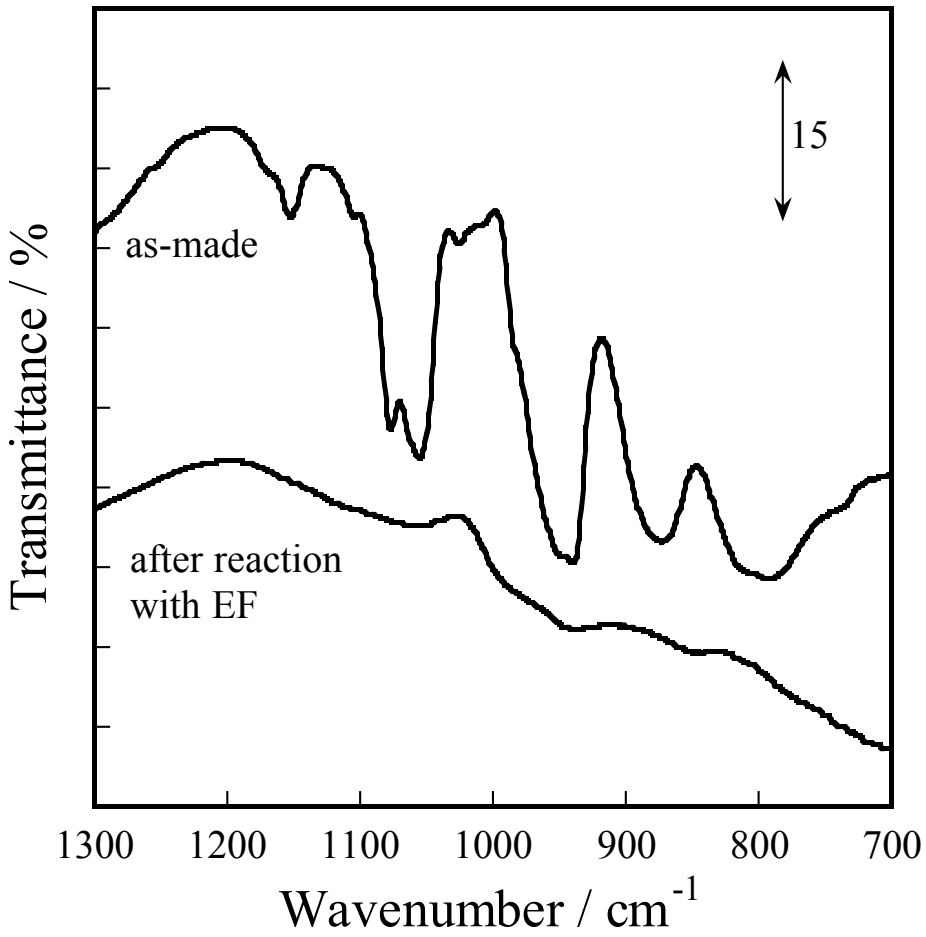

Figure 4-2-12 FT-IR spectra for various states of 40 wt%TBA-$PMo_{10}V_2O_{40}/CeO_2$ in as-made catalyst and the catalyst after CH_4 supply with the electric field at 673 K; CH_4:Ar = 25:50, the total flow rate was 75 mL min^{-1}.

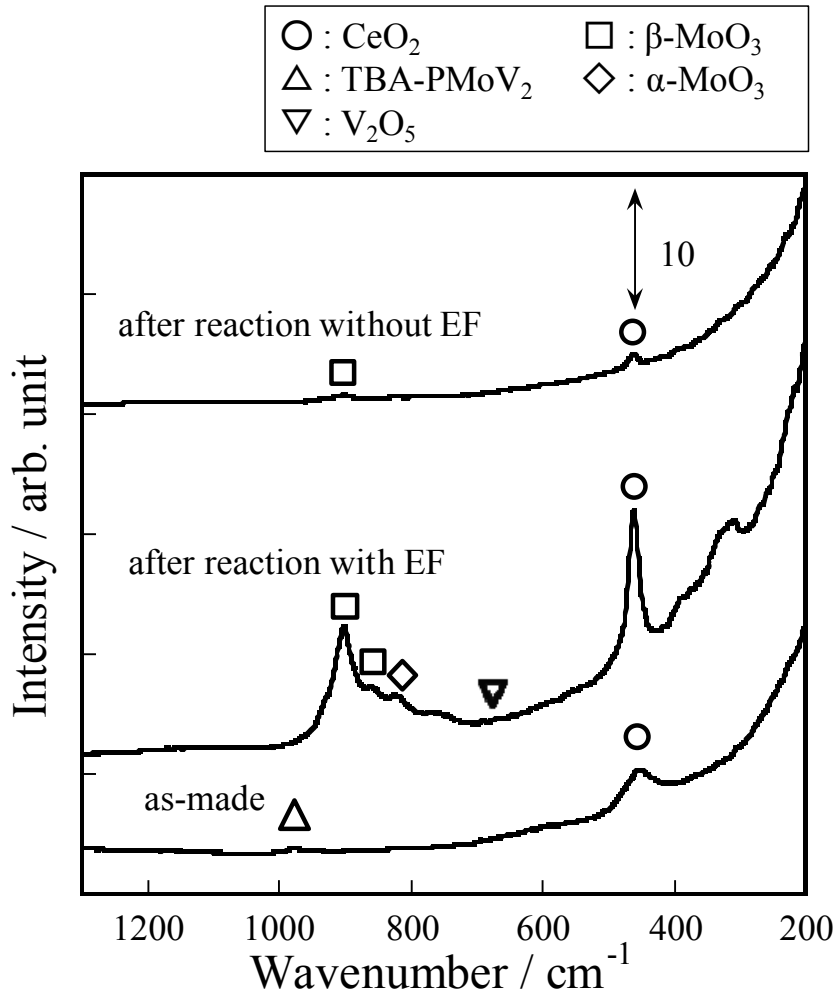

Figure 4-2-13 Raman spectra for various states of 40 wt%TBA-$PMo_{10}V_2O_{40}/CeO_2$.

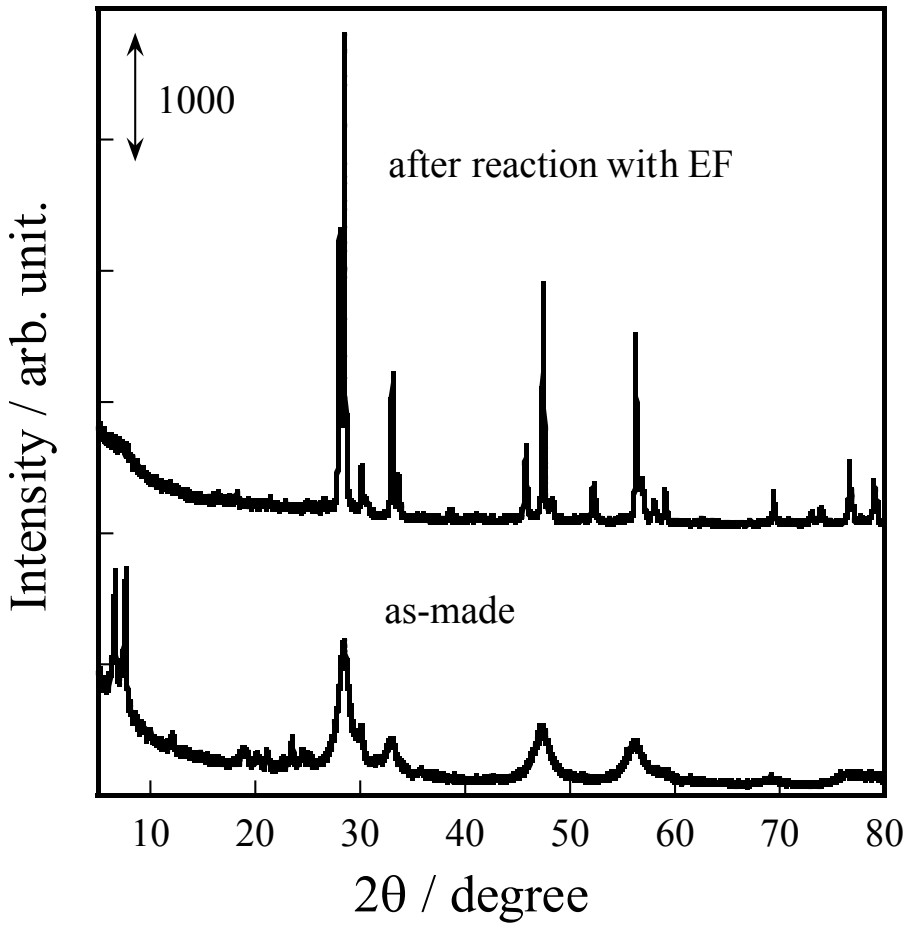

Figure 4-2-14 XRD patterns for various states of 40 wt%TBA-$PMo_{10}V_2O_{40}/CeO_2$.

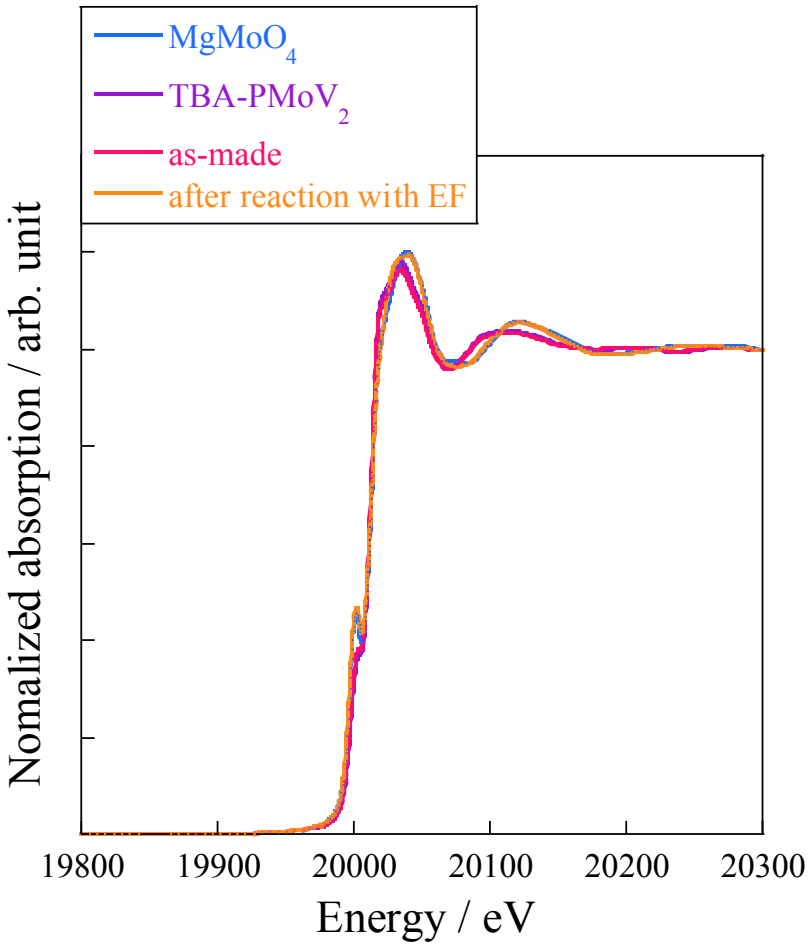

Figure 4-2-15 XANES spectra at Mo-K edge for $MgMoO_4$ as referred oxide and various states of 40 wt%TBA-$PMo_{10}V_2O_{40}$/CeO_2.

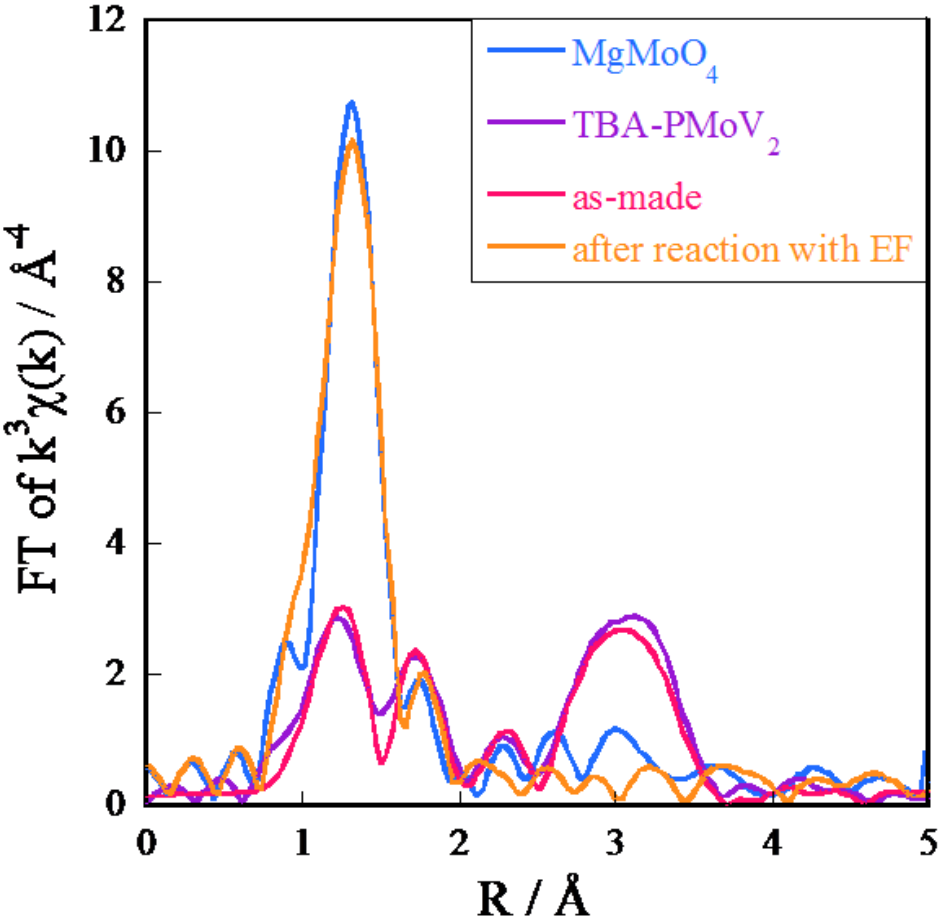

Figure 4-2-16 EXAFS spectra at Mo-K edge for $MgMoO_4$ as referred oxide and various states of 40 wt%TBA-$PMo_{10}V_2O_{40}$/CeO_2.

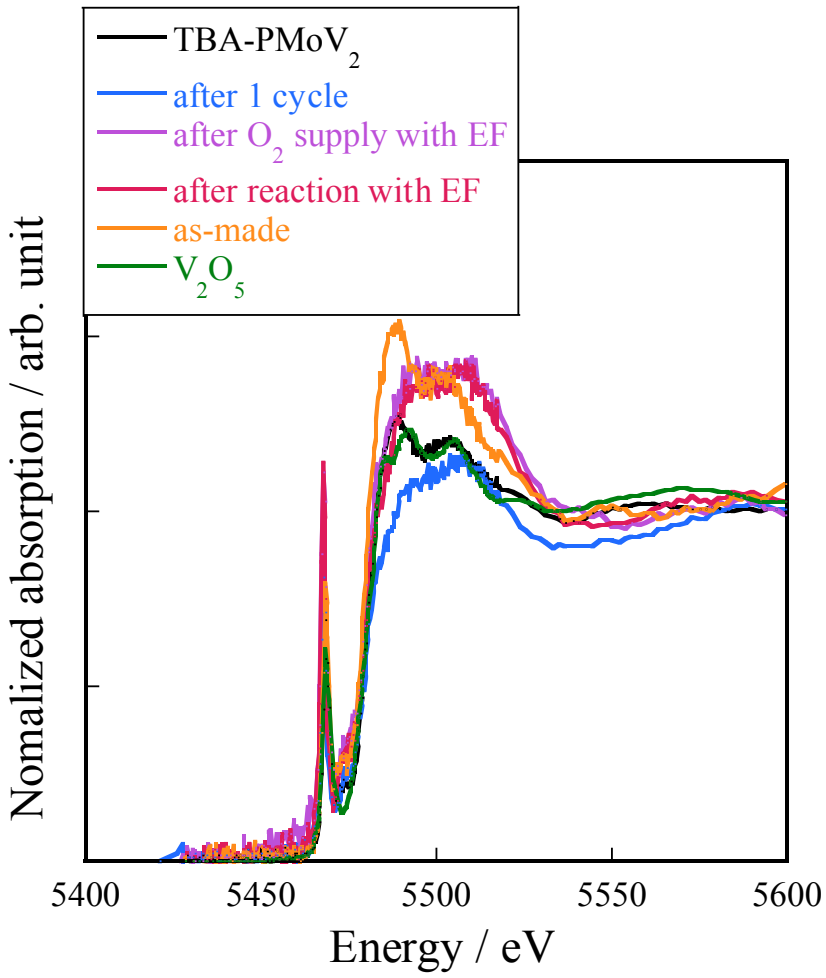

Figure 4-2-17 XANES spectra at V-K edge for V_2O_5 as referred oxide and various states of 40 wt%TBA-$PMo_{10}V_2O_{40}$/CeO_2.

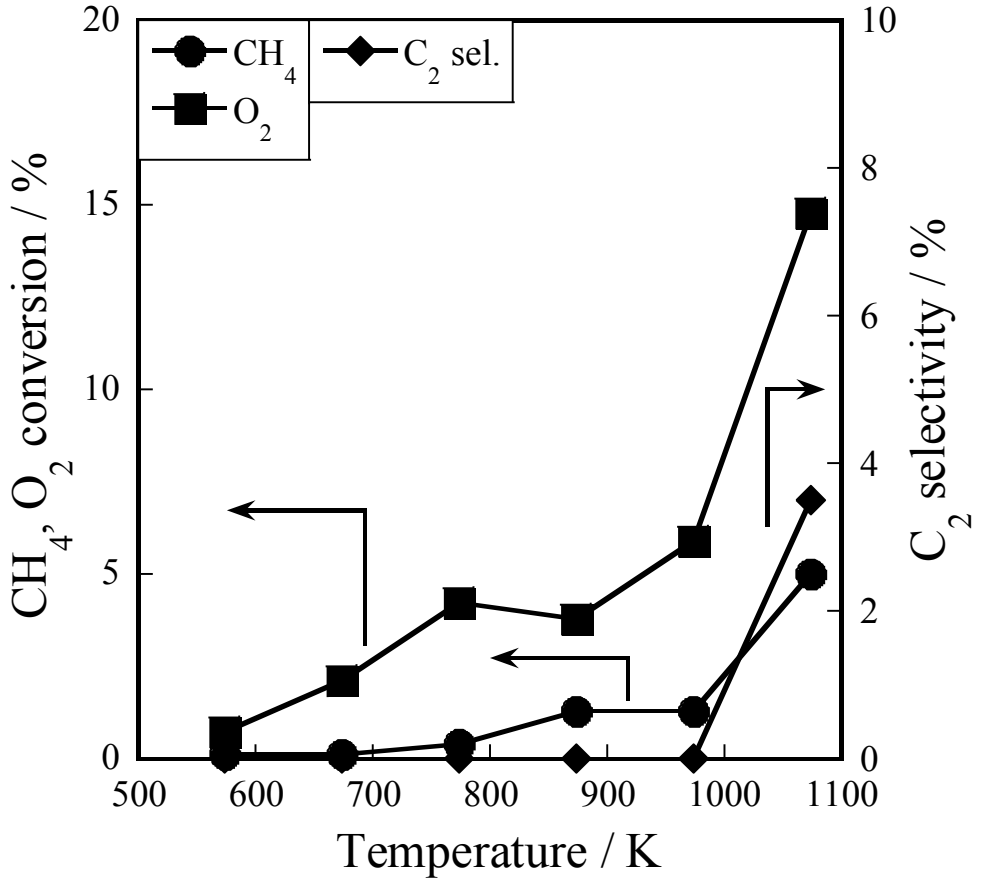

Figure 4-2-18 Catalytic activity over 40 wt%TBA-$PW_{12}O_{40}/CeO_2$ catalyst in various temperatures without the electric field; from 573 K to 1073 K..

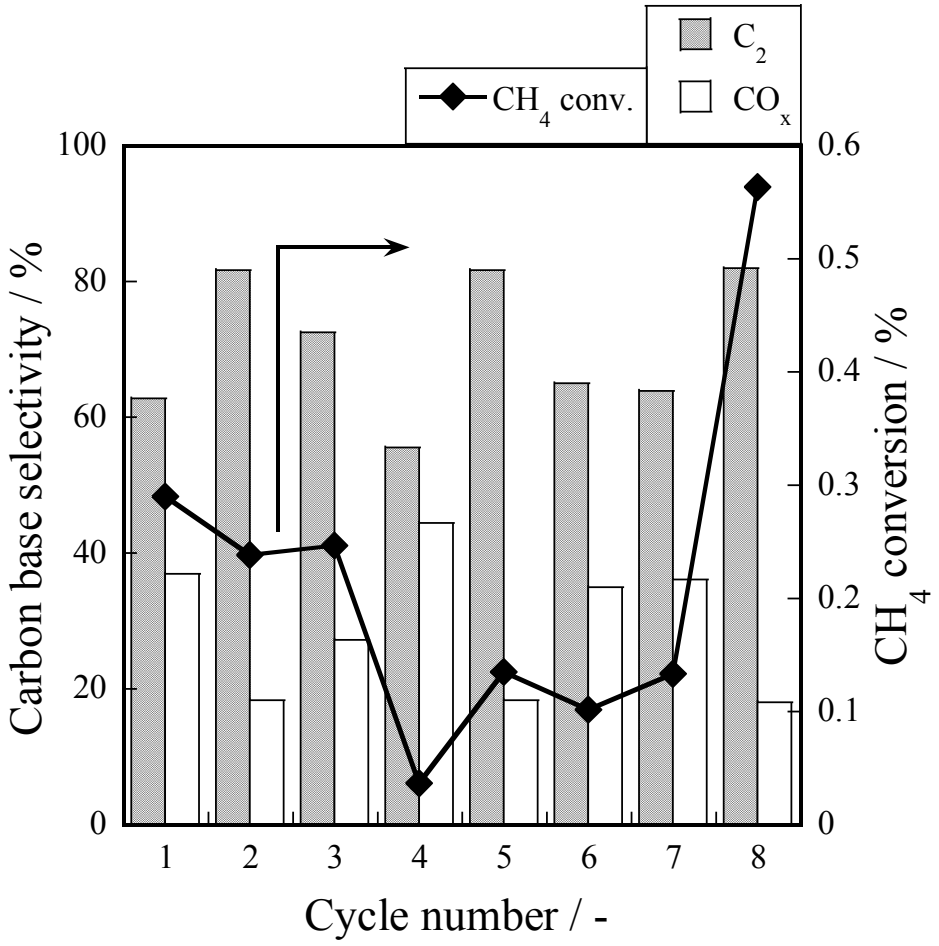

Figure 4-2-19 Results of periodic operation test (after 2 min from CH_4 supply) over 40 wt%TBA-$PW_{12}O_{40}/CeO_2$ in the electric field; 7.0 mA; 473 K; CH_4:Ar = 25:50, total flow rate : 75 mL min^{-1};O_2:Ar = 5:50, total flow rate: 55 mL min^{-1}.

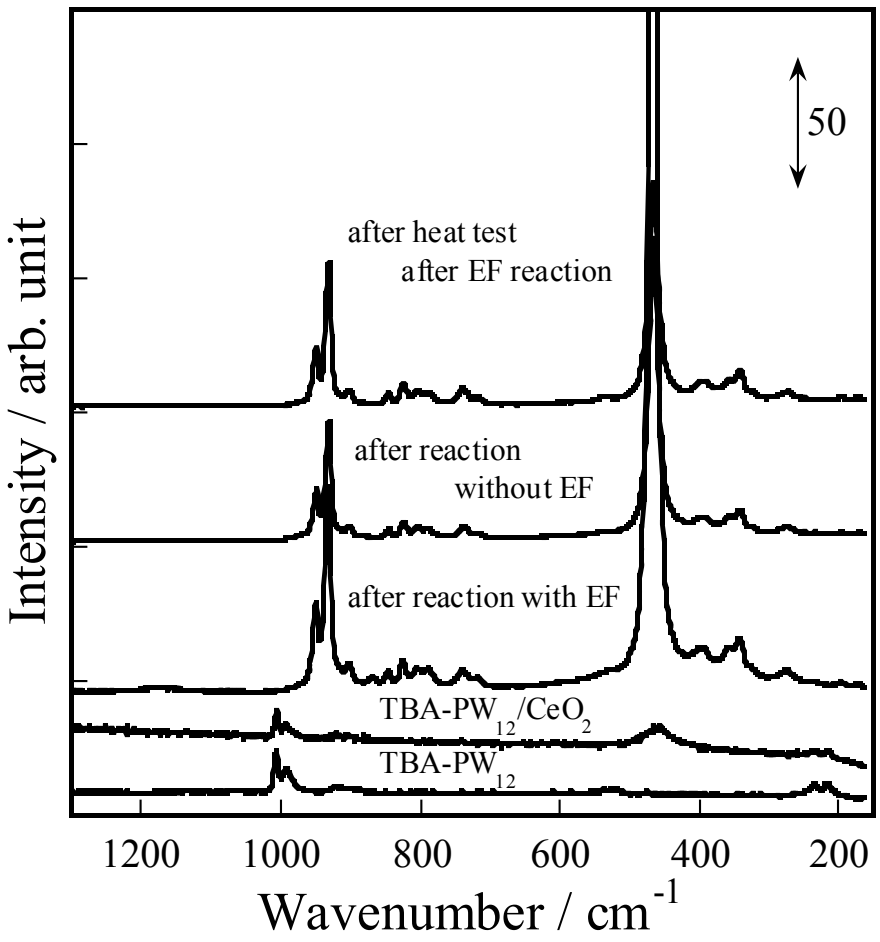

Figure 4-2-20 Raman spectra for various states of 40 wt%TBA-$PW_{12}O_{40}/CeO_2$.

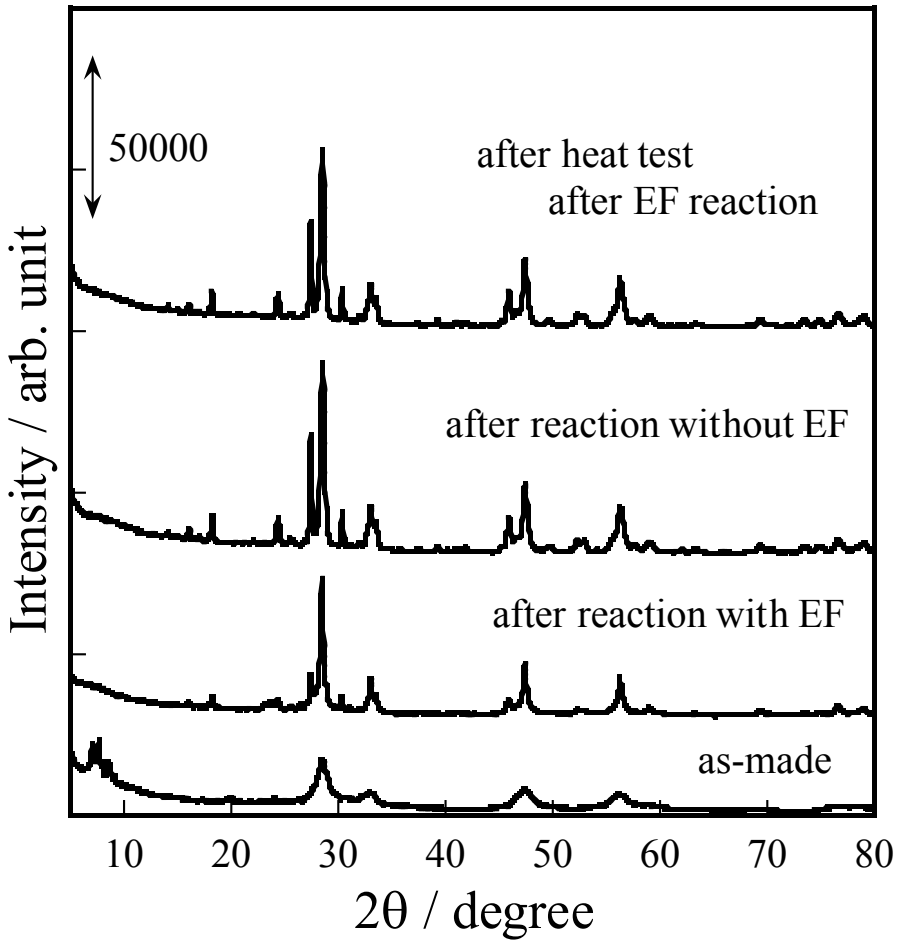

Figure 4-2-21 XRD patterns for various states of 40 wt%TBA-$PW_{12}O_{40}/CeO_2$.

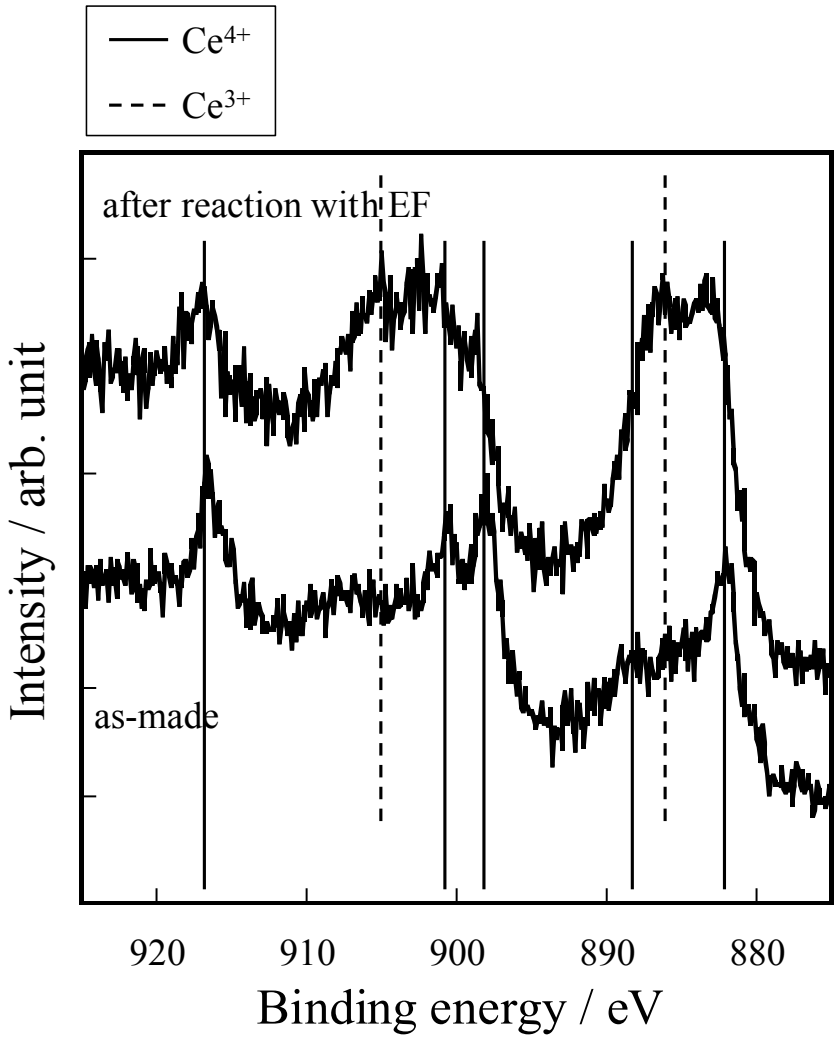

Figure 4-2-22 XPS spectra at Ce $3d_{5/2}$ in various states of 40 wt%TBA-$PW_{12}O_{40}$/CeO_2.

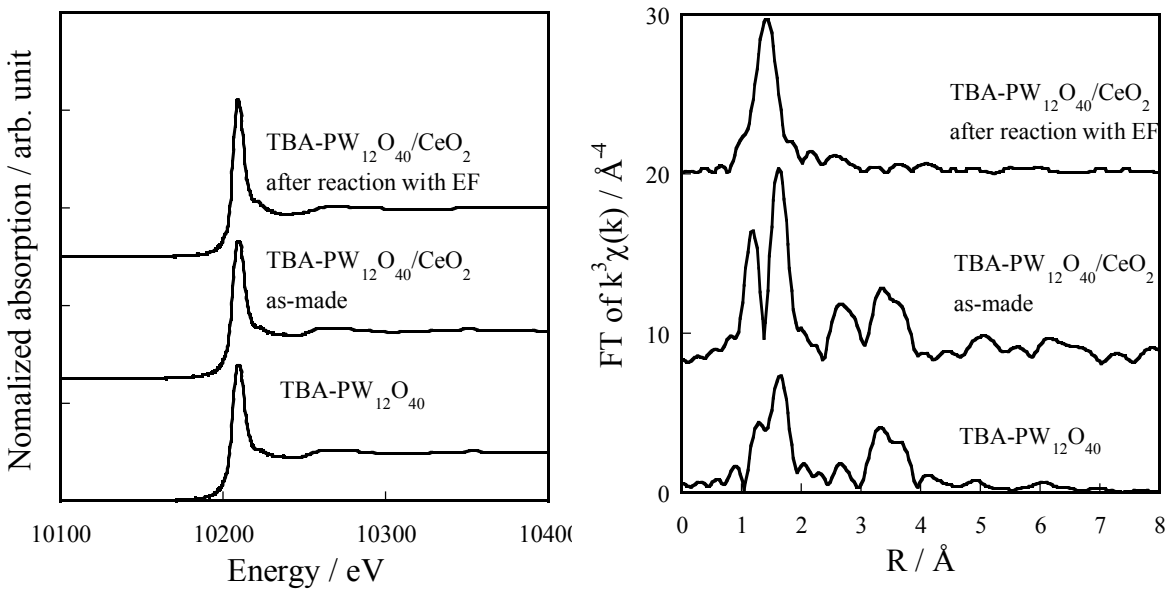

Figure 4-2-23 XANES (Left) and EXAFS (Right) spectra at W-L_3 edge in various states of 40 wt%TBA-$PW_{12}O_{40}/CeO_2$.

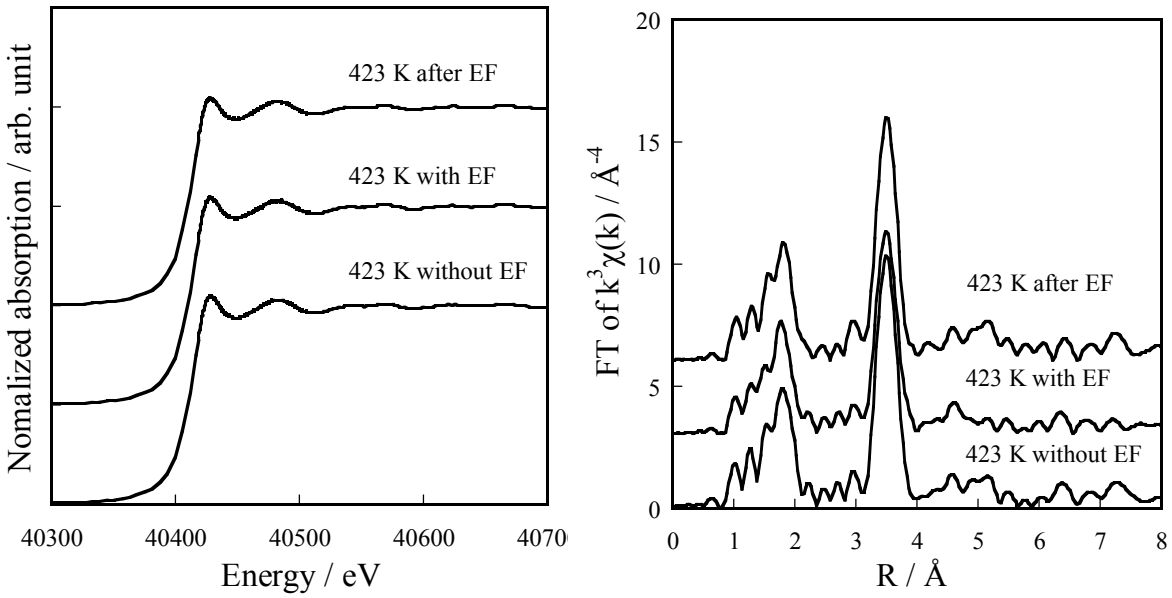

Figure 4-2-24 XANES and EXAFS spectra at Ce-K edge in various states of $Ce_2(WO_4)_3/CeO_2$ with and without electric field:6.0 mA; from 6.0 kV to 7.0 kV.

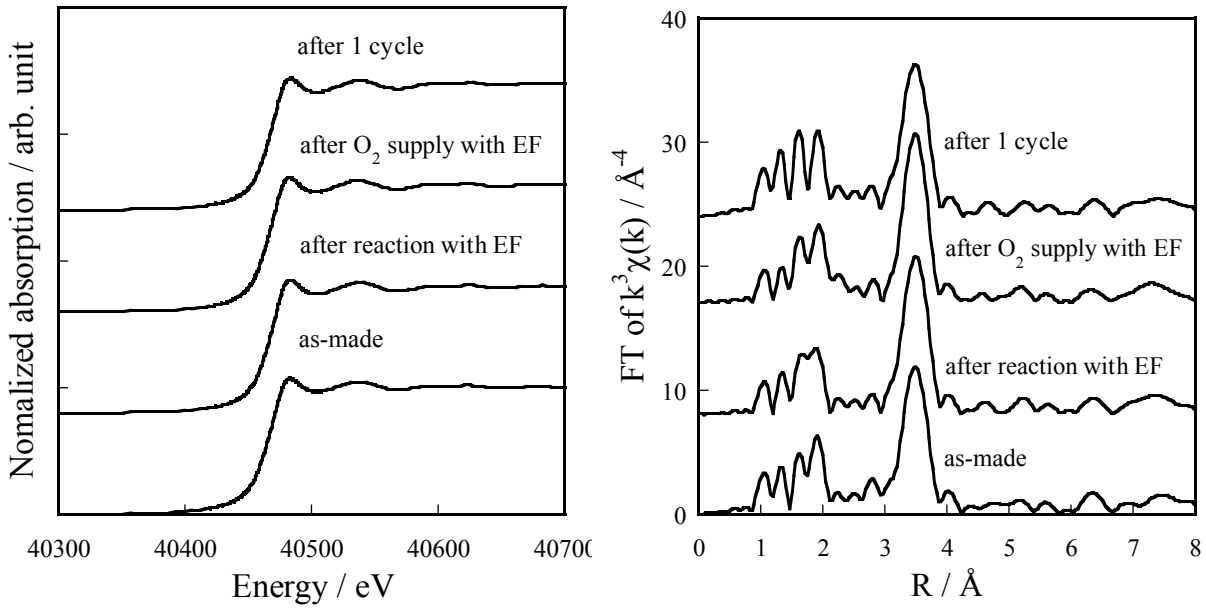

Figure 4-2-25 XANES and EXAFS spectra at Ce-K edge in various states of $Ce_2(WO_4)_3/CeO_2$.

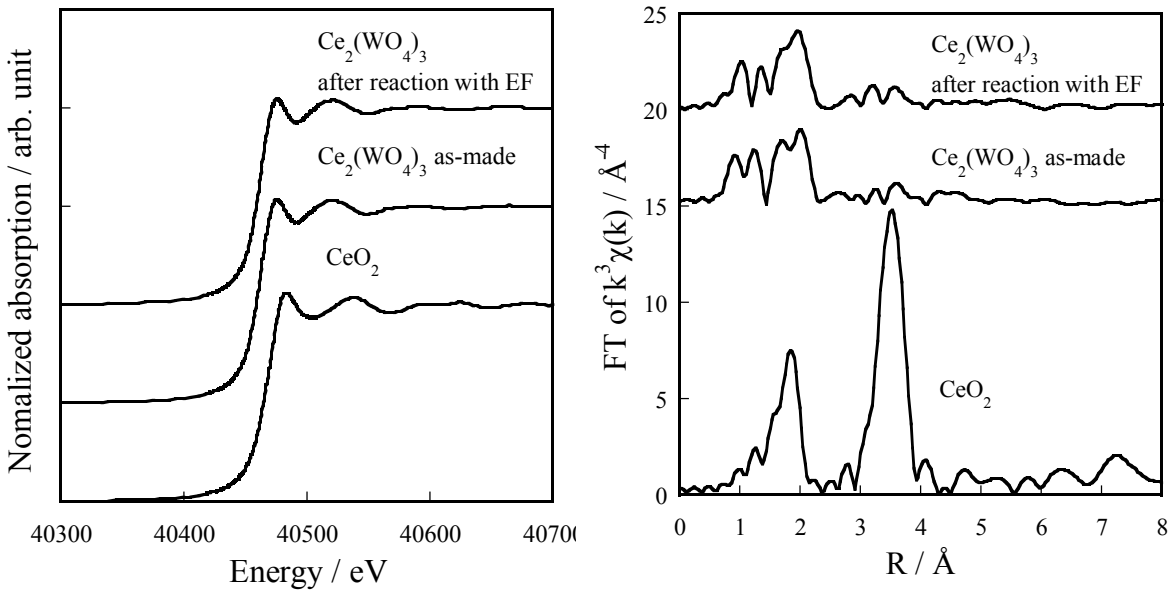

Figure 4-2-26 XANES and EXAFS spectra at Ce-K edge in CeO_2 and various states of $Ce_2(WO_4)_3$.

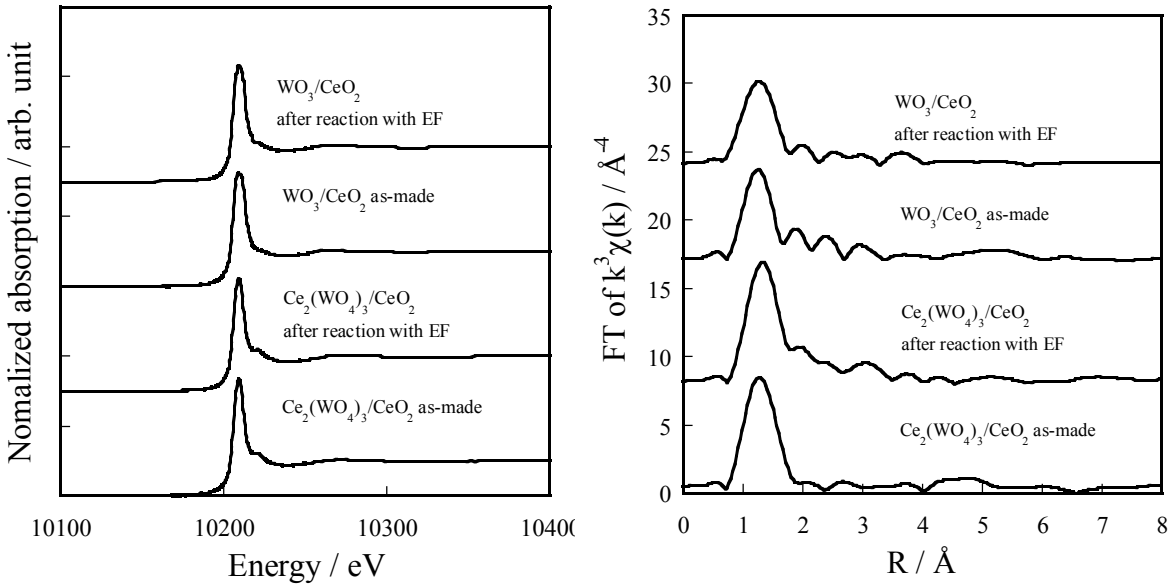

Figure 4-2-27 XANES and EXAFS spectra at W-L_3 edge in various states of $Ce_2(WO_4)_3/CeO_2$ and WO_3/CeO_2.

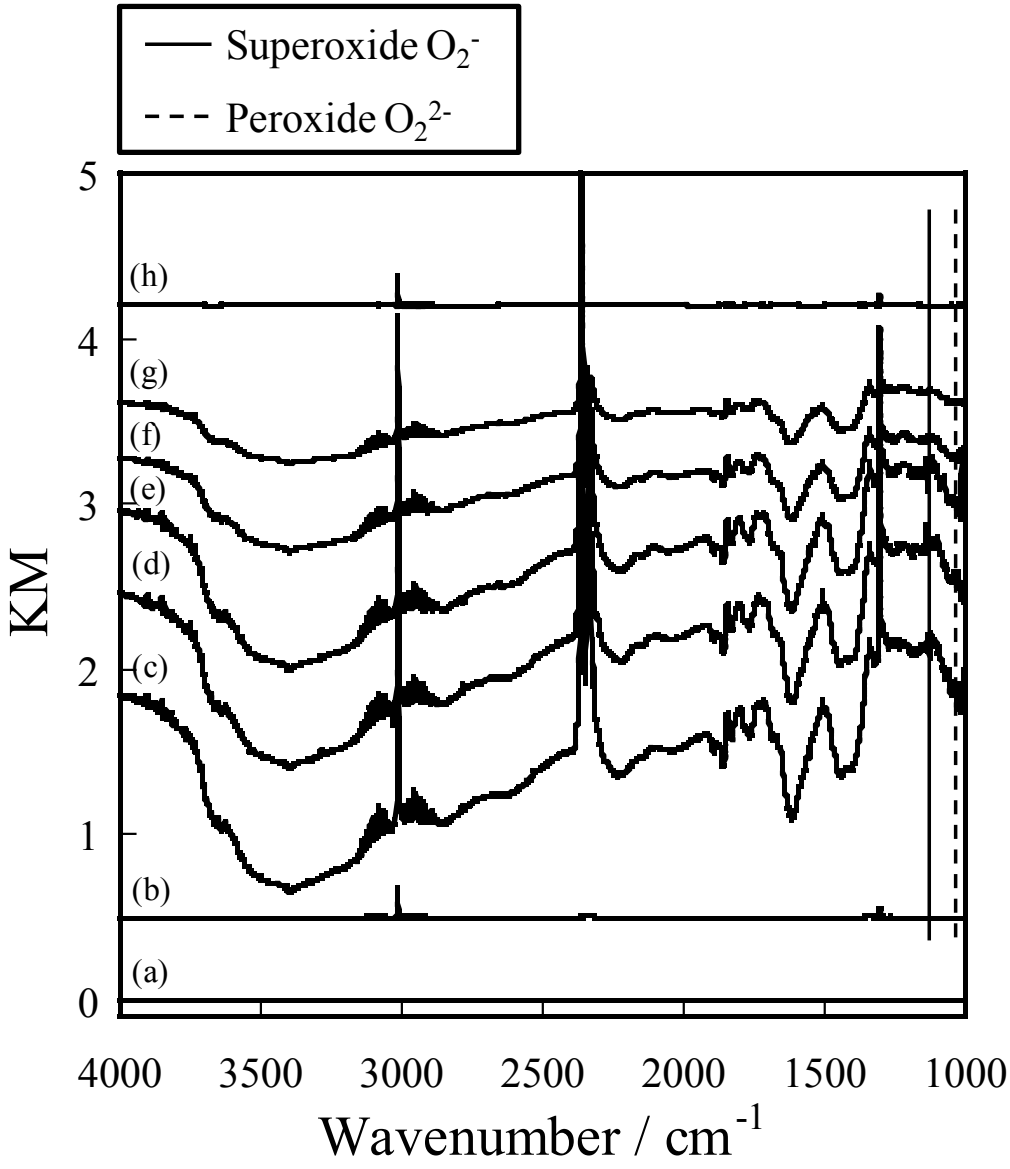

Figure 4-2-28 DRIFT spectra of various state of $Ce_2(WO_4)_3/CeO_2$ with and without electric field (423 K, CH_4:O_2:Ar = 2:1:57, total flow rate: 60 mL min^{-1}); (a) inert; (b) without EF; (c) 6.0 mA 430 V; (d) 5.0 mA, 460 V; (e) 4.0 mA, 660 V; (f) 3.0 mA, 660 V; (g) 2.0 mA, 760 V; (h) after reaction with electric field.

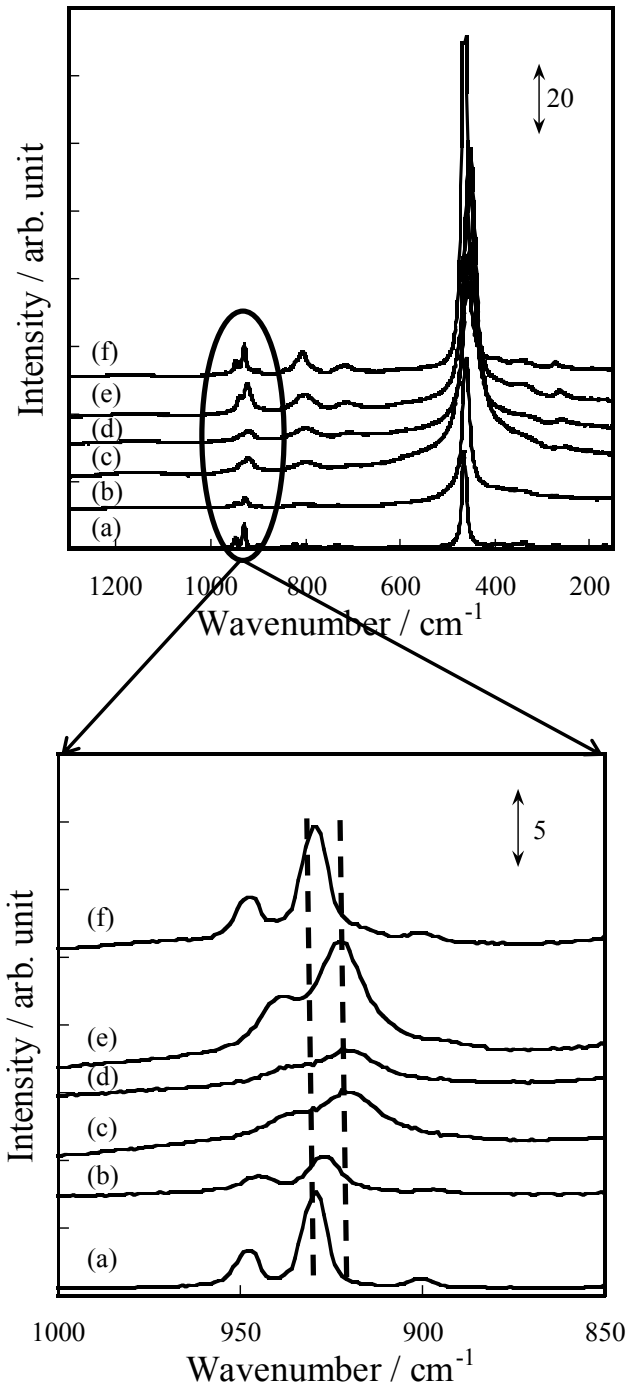

Figure 4-2-29 Raman spectra of $Ce_2(WO_4)_3/CeO_2$ with and without electric field. (a) inert at room temperature, (b) without EF in air at 603-703 K, (c) 6.0 mA in air (0.69 kV), (d) 6.0 mA in CH_4 (0.73 kV), (e) 6.0 mA in CH_4+O_2 (0.67 kV), (f) without EF after (e).

Table 4-2-1 Result of activity tests over TBA-$PMo_{12-x}V_xO_{40}/CeO_2$ in the electric field (x = 0~2); Feed gas CH_4:O_2:Ar = 25:15:60, total flow of 100 mL min^{-1}; imposed current: 5.0 mA; catalyst weight, 100 mg; furnace temperature, 423 K.

Catalysts	Voltage / V	CH_4 conv. / %	O_2 conv. / %	C_2 sel. / %	C_2 yield / %	Field intensity / V mm^{-1}
TBA-PMo_{12}/CeO_2	700	16.1	24.9	24.8	4.0	106
TBA-$PMo_{11}V_1/CeO_2$	800	20.6	26.3	30.0	6.2	129
TBA-$PMo_{10}V_2/CeO_2$	1100	20.4	27.4	27.5	5.6	159
CeO_2	100	28.2	100	0.2	0.1	20

Catalysts	Selectivity / C-%				
	CO	CO_2	C_2H_4	C_2H_6	C_2H_2
TBA-PMo_{12}/CeO_2	68.3	6.9	7.1	4.5	13.2
TBA-$PMo_{11}V_1/CeO_2$	62.3	7.8	7.2	3.7	19.1
TBA-$PMo_{10}V_2/CeO_2$	64.0	8.5	10.3	7.4	9.7
CeO_2	1.3	98.5	0.0	0.2	0.0

Table 4-2-2 Result of activity tests over Mo and/or V supported catalysts in the electric field; Feed gas CH_4:O_2:Ar = 25:15:60, total flow of 100 mL min^{-1}; imposed current: 3.0 mA; catalyst weight, 100 mg; furnace temperature, 423 K.

Catalysts	Voltage / V	CH_4 conv. / %	O_2 conv. / %	C_2 sel. / %	C_2 yield / %	Field intensity / V mm^{-1}
24.1 wt%Mo/CeO_2	700	7.1	10.4	28.3	2.0	149
3.3 wt%V/CeO_2	700	11.2	18.2	23.2	2.6	159
23.5 wt%Mo-2.49 wt%V/CeO_2	800	8.4	12.2	32.2	2.7	160
TBA-$PMo_{10}V_2/CeO_2$	1400	13.6	19.9	33.1	4.5	203

Catalysts	Selectivity / C-%				
	CO	CO_2	C_2H_4	C_2H_6	C_2H_2
24.1 wt%Mo/CeO_2	64.3	7.4	10.8	6.2	11.3
3.3 wt%V/CeO_2	52.1	24.8	8.5	4.7	9.9
23.5 wt%Mo-2.49 wt%V/CeO_2	61.0	6.8	12.1	6.6	13.5
TBA-$PMo_{10}V_2/CeO_2$	56.9	10.0	11.5	7.5	14.1

Table 4-2-3 Results of activity test over WO_3 in the electric field; Feed gas CH_4:O_2:Ar = 25:15:60, total flow of 100 mL min^{-1}; imposed current: 3.0–7.0 mA; catalyst weight, 100 mg; furnace temperature, 673 K.

Current / mA	Voltage / V	CH_4 conv. / %	O_2 conv. / %	C_2 sel. / %	C_2 yield / %	Field intensity / V mm^{-1}
3.0	0	0.0	12.9	0.0	0.0	0
5.0	100	0.0	15.4	0.0	0.0	29
7.0	100	0.0	15.5	0.0	0.0	29

Current	Selectivity / C-%				
/ mA	CO	CO_2	C_2H_4	C_2H_6	C_2H_2
3.0	0.0	0.0	0.0	0.0	0.0
5.0	0.0	0.0	0.0	0.0	0.0
7.0	100	0.0	0.0	0.0	0.0

Table 4-2-4 Dependence of W loading amount over $Ce_2(WO_4)_3/CeO_2$ in the electric field; Feed gas CH_4:O_2:Ar = 25:15:60, total flow of 100 mL min^{-1}; imposed current: 3.0 mA; catalyst weight, 100 mg; furnace temperature, 423 K.

W 1oading amount / wt%	Voltage / V	CH_4 conv. / %	O_2 conv. / %	C_2 sel. / %	C_2 yield / %	Field intensity / V mm^{-1}
11.9	900	13.7	17.5	37.8	5.2	225
28.6	800	10.7	12.6	47.1	5.0	186

W loading amount	Selectivity / C-%				
/ wt%	CO	CO_2	C_2H_4	C_2H_6	C_2H_2
11.9	55.8	6.5	10.2	5.5	22.1
28.6	48.8	4.1	18.3	11.6	17.2

Chapter 5 General conclusion

In this research, oxidative coupling of methane using carbon dioxide (CO_2-OCM) and dry reforming of methane (DRM) were conducted in an electric field for activating stable CH_4 and CO_2. Catalytic reaction in the electric field has been anticipated for producing these reactions which do not proceed in the conventional catalytic reaction without the imposed electric field, at lower temperature, solving various issues derived from the high reaction temperature such as carbon deposition and catalyst sintering, and improving energy efficiency for various catalytic processes.

In Chapter 2, CO_2-OCM reaction was conducted in an electric field. Results of the screening tests show that $La_{0.7}Ca_{0.3}AlO_{3-\delta}$ (LCAO) catalyst was the most appropriate catalyst in this reaction system, and it shows high activity even at 423 K with imposed 3 mA current. To show the same catalytic activity by heating the catalyst, very high temperature was required, even at 1323 K in the conventional catalytic CO_2-OCM. The reaction rate depended on the CO_2 partial pressure by 0.7 order. CO_2 adsorbent and $La_2O_2CO_3$ are important for the progress of CO_2-OCM in the electric field by *in-situ* IR measurement. Ca-doped effect of LCAO is that by which a Ca atom was incorporated into the $LaAlO_3$ perovskite structure and generation of C_2 hydrocarbons was promoted.

In Chapter 3, DRM reaction was conducted in an electric field. Results of the screening tests show that 1wt%Ni/10 mol%La-ZrO_2 (Ni/La-ZrO_2) catalyst was the most appropriate catalyst in this reaction system. Results also show high activity, even at 423 K (external temperature), at which temperature no DRM reaction proceeds in conventional catalytic systems. Additionally, high DRM selectivity, a high H_2/CO ratio, and low amounts of carbon deposition, even in conditions of high CH_4 conversion, were attributable to the low reaction temperature for suppressing CO disproportionation which occurred at exceeding 623 K. The imposed electric power was correlated with the catalytic activities in the electric field. The DRM reaction rate in the electric field depended on the CO_2 partial pressure by 0.22 order for "CO from CH_4", 0.30 order for "CO from CO_2", and 0.34 order for "H_2". Imposing the electric field presumably activated CH_4 and formate species, and also promoted the surface reaction. Electron efficiency was 88−252 $mol_{\text{-}CH4,CO2}/mol_{\text{-}e}$ and highly efficient, compared to electrochemical reaction (electron efficiency is 1). Syngas became producible at low external temperatures, even at 423 K with high energy efficiency and without coke formation.

In Chapter 4, CO_2-OCM reaction was conducted in an electric field over various metal doped ZrO_2 catalysts. Upon investigating the residence time dependence in the CO_2-OCM reaction over the 10 mol%La-ZrO_2 catalyst, the most appropriate reaction condition for the

reaction in the electric field was in an imposed 3 mA current and a high residence time: the C_2 yield was 4.0%. In order to investigate the effect of CO_2 degradation on the CO_2-OCM reaction in the electric field, O_2 derived from the CO_2 decomposition was possibly reacted with CH_4 to form C_2 hydrocarbons. In the same section, OCM reaction over various polyoxomethalate supported on CeO_2 catalysts were conducted in the electric field. In a 40 wt%TBA-$PMo_{10}V_2/CeO_2$ catalyst, Mo oxides and a mixed oxide with Mo and Ce were generated by the imposing electric field for producing high OCM activity. In a 40 wt%TBA-PW_{12}/CeO_2 catalyst, the $Ce_2(WO_4)_3$ structure played an important role as an active site in producing a selective OCM reaction in the electric field. It was assumed that cycles of consumption and regeneration for oxygen species on the $Ce_2(WO_4)_3$ catalyst were repeated by a redox mechanism, the bond of W–O in the catalyst lengthened by the imposed electric field, the bond of Ce–O in the Ce–O–W unit shrank, the electron of Ce atom was transferred to an O atom and the reactive oxygen for the OCM reaction was generated. Challenge for the future is to reveal the effects of the W–O bond expansion and the electron value change of Ce from Ce^{3+} to Ce^{4+} on activating CH_4 by collaboration with a computational chemistry.

Elucidation for the effect of the imposed electric field on the reaction of CH_4 and CO_2 such as CO_2-OCM and DRM reactions will make a substantial contribution and knowledge to further improvements of energy efficiency and expanding the availability for these reactions. Additionally, these works will become knowledge for applying an electric field to other catalytic reactions using CH_4 and CO_2.

早稲田大学　博士（工学）　学位申請　研究業績書

氏 名　矢部　智宏　　印

（2017 年　1 月　現在）

種 類 別	題名、　発表・発行掲載誌名、　発表・発行年月、　連名者（申請者含む）
○論文	矢部智宏, 「電場印加触媒反応における二酸化炭素を用いたメタン酸化カップリング」, *触媒*, 58, 5, 293-296, (2016).
○論文	T. Yabe, K. Mitarai, K. Oshima, S. Ogo, Y. Sekine, "Low-temperature dry reforming of methane to produce syngas in an electric field over La-doped Ni/ZrO_2 catalysts", *Fuel Proc. Technol.*, 158, 96-103 (2016).
○論文	K. Sugiura, S. Ogo, K. Iwasaki, T. Yabe, Y. Sekine, "Low-temperature catalytic oxidative coupling of methane in an electric field over a Ce-W-O catalyst system", *Scientific Reports*, 6, 25154, 1-9, (2016).
論文	K. Oshima, K. Tanaka, T. Yabe, E. Kikuchi, Y. Sekine, "Oxidative coupling of methane using carbon dioxide in an electric field over La-ZrO_2 catalyst at low external temperature", *Fuel*, 107, 879-881, (2013).
論文	K. Oshima, K. Tanaka, T. Yabe, Y. Tanaka, Y. Sekine, "Catalytic oxidative coupling of methane with a dark current in an electric field at low external temperature", *Int. J. Plasma Environ. Sci. Technol.*, 6(3), 266-271, (2012).
講演	T. Yabe, Y. Kamite, K. Sugiura, S. Ogo, Y. Sekine, "Low-temperature catalytic oxidative coupling of methane using carbon dioxide in an electric field over La perovskite oxide catalysts", the 46th Petroleum-Petrochemical Symposium of JPI, Kyoto, Japan, (November 2016).
講演	S. Ogo, K. Sugiura, K. Iwasaki, T. Yabe, R. Manabe, Y. Sekine, "Oxidative coupling of methane over polyoxometalate supported catalysts in an electric field at low temperature ", *Natural Gas Conversion Symposium 11*, Tromsø, Norway, (June 2016).
講演	小河脩平, 杉浦　圭, 岩崎晃聖, 矢部智宏, 関根　泰,「電場中でメタン酸化カップリングに高い活性を示すセリウムタングステート触媒の微細構造と電場の効果」, *第 117 回触媒学会討論会*, 大阪, 2016 年 3 月.
講演	岩崎晃聖, 杉浦　圭, 矢部智宏, 小河脩平, 関根　泰, 「Ce-W-O 系触媒を用いたメタン酸化カップリングにおける電場印加効果」, *第 117 回触媒学会討論会*, 大阪, 2016 年 3 月.
講演	矢部智宏, 杉浦　圭, 上手裕紀子, 小河脩平, 関根　泰,「異種カチオンドープ酸化物を触媒に用いた電場印加反応場における二酸化炭素を酸化剤とするメタン転換」, *第 41 回固体イオニクス討論会*, 札幌, 2015 年 11 月.

早稲田大学　博士（工学）　学位申請　研究業績書

種 類 別	題名、　発表・発行掲載誌名、　発表・発行年月、　連名者（申請者含む）
講演	岩崎晃聖, 杉浦　圭, 矢部智宏, 小河脩平, 関根　泰,「電場印加反応場においてメタン酸化カップリング活性を示す触媒構造」, *第 45 回石油・石油化学討論会*, 名古屋, 2015 年 11 月.
講演	上手裕紀子, 矢部智宏, 杉浦　圭, 小河脩平, 関根　泰, 「$La_{0.7}Ca_{0.3}AlO_{3-\delta}$を触媒とした電場印加触媒反応における二酸化炭素を用いたメタン酸化カップリング」, *第 45 回石油・石油化学討論会*, 名古屋, 2015 年 11 月.
講演	杉浦　圭, 岩崎晃聖, 矢部智宏, 小河脩平, 関根　泰, 「Keggin 型ポリオキソメタレートからの Ce-W 複合酸化物の合成とその電場印加反応場における酸化触媒特性」, *錯体化学会第 65 回討論会*, 奈良, 2015 年 9 月.
講演	岩崎晃聖, 杉浦　圭, 矢部智宏, 小河脩平, 関根　泰,「電場印加反応場で安定なリンタングステン酸セシウム塩担持触媒の合成とその酸化触媒特性」, *錯体化学会第 65 回討論会*, 奈良, 2015 年 9 月.
講演	矢部智宏, 杉浦　圭, 大島一真, 小河脩平, 関根　泰, 「$LaAlO_3$ 系酸化物を触媒とした電場中での二酸化炭素を用いたメタン酸化カップリングにおける Ca 添加効果」, *触媒学会第 116 回触媒討論会*, 三重, 2015 年 9 月.
講演	杉浦　圭, 岩崎晃聖, 矢部智宏, 小河脩平, 関根　泰,「セリウムタングステート触媒を用いた電場中でのメタン酸化カップリング」, *触媒学会第 116 回触媒討論会*, 三重, 2015 年 9 月.
講演	小河脩平, 杉浦　圭, 岩崎晃聖, 矢部智宏, 関根　泰,「低温・電場中でのメタン酸化カップリングに活性な触媒構造」, *触媒学会第 116 回触媒討論会*, 三重, 2015 年 9 月.
講演	御手洗健太, 大島一真, 矢部智宏, 小河脩平, 関根　泰,「Ni/La-ZrO_2 触媒における電場印加メタン炭酸ガス改質の反応機構解析」, *石油学会第 64 回研究発表会*, 東京, 2015 年 5 月.
講演	矢部智宏, 杉浦　圭, 御手洗健太, 大島一真, 小河脩平, 関根　泰,「電場印加反応場中における低温駆動メタン炭酸ガス改質」, *触媒学会第 115 回討論会*, 東京, 2015 年 3 月.
講演	矢部智宏, 杉浦　圭, 大島一真, 小河脩平, 関根　泰, 「$La_{0.7}Ca_{0.3}AlO_{3-\delta}$を触媒とした低温での電場中における二酸化炭素を用いたメタン酸化カップリング」, *触媒学会第 114 回触媒討論会*, 広島, 2014 年 9 月.

早稲田大学　博士（工学）　学位申請　研究業績書

種 類 別	題名、　発表・発行掲載誌名、　発表・発行年月、　連名者（申請者含む）
講演	T. Yabe, K. Sugiura, K. Oshima, S. Ogo, Y. Sekine, " Electrically promoted catalytic methane oxidative coupling with carbon dioxide over La-perovskite oxide catalysts", *The 248th ACS National Meeting*, San Francisco, America, (August 2014).
講演	T. Yabe, K. Oshima, Y. Sekine, " Oxidative coupling of methane with carbon dioxide assisted by an electric field", *The 6th Asia-Pacific Congress on Catalysis*, Taipei, China, (October 2013).
講演	杉浦　圭, 矢部智宏, 大島一真, 小河脩平, 関根　泰,「電場印加触媒反応によるメタンと二酸化炭素からの C2 炭化水素の合成」, *触媒学会第 113 回討論会*, 愛知, 2014 年 3 月.
講演	矢部智宏, 大島一真, 小河脩平, 関根　泰, 「電場アシスト触媒反応による二酸化炭素を用いたメタン酸化カップリング」, *触媒学会第 112 回触媒討論会*, 秋田, 2013 年 9 月.
講演	矢部智宏, 大島一真, 関根　泰, 「電場印加反応場による二酸化炭素を用いたメタン酸化カップリング」, *石油学会第 56 回研究発表会*, 東京, 2013 年 5 月.
著書	矢部智宏, 小河脩平, 関根　泰,「電場印加触媒反応によるメタンと二酸化炭素からの C2 炭化水素の合成」, *二酸化炭素を用いた化学品製造技術*, *S&T 出版*, 15-22, (2016).
著書	矢部智宏, 斎藤　晃, 小河脩平, 関根　泰, 「メタン転換・C1 化学におけるゼオライト」ナノ空間材料, *NTS*, 第 3 章 8 節, 288-295, (2016).
著書	矢部智宏, 小河脩平, 関根　泰, 「メタンの酸化的カップリング」, *ファインケミカル*, 8, 44, 5-9, (2015).
著書	矢部智宏, 真鍋　亮, 関根　泰, 「第 4 編第 1 章　シェール革命による石油化学原料生産への影響と今後の展望」, *シェールガス～開発・生産と石油化学～*, *NTS*, 229-240, (2014).

Acknowledgements

I would like to express my sincere gratitude to Prof. Yasushi Sekine (Waseda University), who is the chief examiner, for providing guidance with eagerness through dense discussions. I would like to be grateful to Prof. Takuro Katsufuji (Waseda University), Prof. Kenichi Oyaizu (Waseda University) and Dr. Hitoshi Mazaki (fellow in Central Technical Research Laboratory, JX Energy Corporation), who are the vice-chairman, for giving many valuable advices in my thesis defense. I would like to be grateful to Ass. Prof. Shuhei Ogo (Waseda University) for giving advices of research with sympathy. I would like to be grateful to Masami Kawaharabata, who is a secretary, for giving generous supports in a laboratory. I would like to express my sincere gratitude to Prof. Chang-jun Liu (Tianjin University) and Prof. Dapeng Cao (Tianjin University) for giving many advices and supports in a training course in an overseas laboratory. I would like to be grateful to Takahiro Gotoh (Materials Characterization Central Laboratory, Waseda University) for giving many assists for operations of various apparatus such as XRD and TEM. I would like to be grateful to Dr. Tetsuo Honma, Masashi Takagaki and Asuka Hirayama (Japan Synchrotron Radiation Research Institute, SPring-8) for giving many supports for XAFS measurements in BL14B2. Additionally, this work was supported by the Leading Graduate Program in Science and Engineering, Waseda University from MEXT, Japan. In this program, I would like to be grateful to the office staff for giving generous supports including the doctoral thesis defense. I would like to be grateful to Ass. Prof. Kazumasa Oshima (National Institute of Technology, Numazu College), Dr. Daiki Mukai (Nippon Steel & Sumikin Chemical Corporation), Dr. Kei Mukawa (Ministry of Economy, Trade and Industry) and Dr. Keisuke Tanaka for generous guidance for a fundamental research with sympathy. I would like to be grateful to Dr. Yukihiro Sugiura (Central Technical Research Laboratory, JX Energy Corporation) for giving advices from company's points of view. I would like to be grateful to Kei Sugiura, Kenta Mitarai, Yukiko Kamite, Ryo Manabe, Shigeki Okada, Kousei Iwasaki, Takuma Higo (Waseda University) and Rui Zhou (Tianjin University) for taking research such as experiments, catalyst preparations and *in-situ* measurements together. I would like to be grateful to Naomi Yabe and Erika Yabe, my family, for accepting to continue to the doctoral course and giving many supports. Finally, I would like to express my gratitude to all my teachers who put their faith in me and urged me to do better.

February, 2017

Tomohiro Yabe